

**Quantum State Engineering and Information  
Processing with Trapped Ions**

by

**Brian E. King**

B.Sc., Simon Fraser University, 1992

M.S., University of Colorado at Boulder, 1994

A thesis submitted to the  
Faculty of the Graduate School of the  
University of Colorado in partial fulfillment  
of the requirements for the degree of  
Doctor of Philosophy  
Department of Physics

1999

This thesis entitled:  
Quantum State Engineering and Information Processing with Trapped Ions  
written by Brian E. King  
has been approved for the Department of Physics

---

Dr. David Wineland

---

Prof. Eric Cornell

---

Dr. Christopher Monroe

Date \_\_\_\_\_

The final copy of this thesis has been examined by the signatories, and we find that both the content and the form meet acceptable presentation standards of scholarly work in the above mentioned discipline.

King, Brian E. (Ph.D., Physics)

Quantum State Engineering and Information Processing with Trapped Ions

Thesis directed by Dr. David Wineland

A single  ${}^9\text{Be}^+$  ion confined in an rf (Paul) trap may be used to realize two of the simplest quantum systems: the two-level system and the harmonic oscillator. The two-level system is comprised of two, ground-state hyperfine electronic levels. The trapping potential is harmonic, to a high degree of approximation, and so the ion's motion is that of a three-dimensional harmonic oscillator.

By coupling the ion's motional and electronic degrees of freedom, we can engineer entanglement between these systems. This allows us to study quantum mechanics, with all its peculiarities, in a well-controlled environment. For example, we can study the interactions of superposition states with the ion's environment, leading to a destruction of quantum superpositions. Furthermore, this system, when scaled up to several ions, may allow us to construct a simple "quantum computer," which promises exponential speed-up over any possible classical computer for some computational problems. Towards this goal, we have cooled two, trapped ions to their ground state of collective motion and have entangled their electronic degrees of freedom by using their joint motion to transfer entanglement between them.

## Dedication

To my parents, Basil and Lena King, who first taught me to look, and to wonder...

## Acknowledgements

*For my part, I know nothing with any certainty, but the sight of the stars makes me dream...* — V. Van Gogh

This thesis represents the culmination of a very lengthy journey: one which I have not — and could not have — travelled on my own. So I would like to take this opportunity to thank those who have gotten me to this point. I cannot separate, in my mind or in my memories, the research described in this thesis from the path which led to it. And so, my list of acknowledgements is a long one. Take solace, however, that this is a thesis and not an after-dinner speech, and so you have the opportunity to skip these pages entirely and hurry on to the “proper” content of this piece of writing! But, if you wish to see the names of those who have helped bring me to this point in my career and my life, read on...

I fear, in writing this, that I will have forgotten someone who ought to be included. If you're searching for your name, and do not find it, please blame my somewhat-fickle memory and not any lack of appreciation for you and your support. It seems almost inevitable that these lists miss some important names which they ought to, by all rights, include. I've tried my best to be comprehensive, but I doubt I'll escape the same fate as others.

But now, to start at the beginning...

Thanks to my mother, who taught me to listen, to read, and to learn. And to my father, who taught me to question, and to look out for the unobserved things in everyday

life. Thanks to both of them, for teaching me to always try my hardest without ever making me feel like I was under pressure. Whatever success I have had in this life is due to the beginnings which they gave me. Thanks also to my sisters, Lorraine, Sheila, and Deirdre, whose love, support, and advice have been unfailing. Especially to Sheila, who always encouraged my questions and imagination, and who taught me to pronounce “abominable!”

I also owe a debt of gratitude to my teachers, over the years. I have always been fortunate in having wonderful people from whom to learn, and supportive environments in which learning could take place. Special thanks to Sr. Alexis and to Bob DeJulius for creating and overseeing those environments. I also want to acknowledge in a special way Mrs. Mitchell, Mrs. Burns, and Mrs. Carlson, who helped me start out my academic career, and pointed it along the right path. Thanks, as well, to Frank Burns, Heather Cullen, Joe Cuddy (I know you’re watching, Fr. Joe!) and to Jocelyn Gagné. Jocelyn, you took my interest in physics, and nurtured it.

I cannot imagine a better undergraduate experience than the one I had at Simon Fraser. The physics and math courses I took there left me well-prepared for the rigours of graduate school, both in their breadth and in their depth. Again, a few names stand out in my mind. Thanks to Brian Thompson for teaching me the wonderful mysteries and discoveries inherent in mathematics. Thanks to Tony Arrott, for inspiration and for being a wonderful example of how to be a physicist with style and panache. Thanks to Leigh Palmer, for a good start in statistical mechanics — that course will stand out in my memory as the best I’ve ever had. Thanks to Albert Curzon, for rigour and compassion. Thanks to Partha, for stealing his child’s “tippy top,” and for being a wonderful teacher. Thanks to John Cochran, another wonderful teacher. I will always cherish the memories of the time he spent in the lab with me. I don’t believe I have ever had a better learning experience. And thanks to Bill Plischke, for good advice whenever I most needed it.

One of the best parts of my undergraduate experience at SFU was its excellent co-operative education programs. In particular, I'd like to acknowledge John Simms for all he did for the program and for me. That program gave me my first taste of research, and much invaluable experience. Thanks to the people at Science World, for great memories and for the job they do. Thanks to Nigel Stevenson, Bill Shin, Stazcik Burzynski and Peter Jackson, for all they taught me. Thanks, also, to Dave Huntley, for the exquisite care he always took in his work.

Before starting grad school, I took a year off. In retrospect, perhaps I should have spent that year pumping gas, or hauling coffee, or being a liftee. But instead, I had the wonderful experience of working for Barbara Frisken. Barb, thanks for all the good times, for all I learned from you about setting up and working in a physics lab, and for good advice over the years. Thanks, too, for what I can only assume must have been one hell of a letter of recommendation!

Thus far, I have acknowledged those who taught me in some sort of academic or research setting. But I have been molded and taught by many people of exceptional character whom I have been fortunate enough to call my friends. I have found out, over the years, that many people found high school to be a thoroughly unenjoyable experience. That could not have been further from the truth for me. "Thank you" to all of you who went through those years with me and made it such a great experience, especially those of you with whom I have been fortunate enough to keep in regular contact. In particular, to Sarah B., to Ed, to Ted, and to Kev.

Somehow, my fortune in friends continued on to my university days. My undergraduate experience would have been much poorer without the friendship of those I encountered during that time. I count myself as blessed to know people such as Gladys, Eric, Claudia, Sarah, Laura, and all the Science World folks. Thanks, also, to Dhavide. And to Eric — if anyone was ever in love with physics, it is you! Thank you for sharing that love of physics with me.

Though I have travelled far from Vancouver, those people always remain in my mind and in my heart.

Graduate school is not the easiest of times — especially those first two years. Although my emotional memories of that time have faded, and perhaps (I hope not!) I will eventually look back on them with rose-tinted glasses, I know that the only adjective that ever came close to describing those days was “hellish.” I’m sure that they would have been unbearable had I not been again blessed with the company of the incredible people who were stuck in the same boat as me. Thank you all. Aside from grad school (and sometimes, including it!), Boulder has been fun. Thanks to Orion, to Eric, to Keith, to Kristan, to Jim, to Julie, to Kim, and to all my other Boulder friends. Thanks to my roommates over the years — especially to Mas, Scott, and Rachel O. And to Julie, and Rachel P. — you helped me inestimably just by being yourselves at a time when I really needed that.

Thank you, Sarah.

I’ve never been a terribly single-minded person. In some ways, that has made grad school — especially in the world of JILA — very challenging. But I’ve always believed that even people with a broad range of interests may have something significant to contribute to physics. Time will tell. Nonetheless, I’d like to offer my thanks to those who created spaces for the “other” aspects of my self, and who shared in my expression of them. Thanks to everyone at UGGS, especially Tim, Adam, and Glenda. Thanks, as well, to those on the CU-UCSU JCSP (or DC, or CC, or SPC, or any of its other incarnations!), but especially to Susan Stafford, Kathryn Moerke (on whom I could always count for well-considered opinions), Ron Stump, and to Ali Vogt. Thanks to the wonderful people at the Mountain Sun, and to the folks at Trident. You people saved me...

I also wish to acknowledge all the people at CU who have helped me along the way, especially to Jinx Cooper (who taught us not to take it all so damn seriously), to

Peter Zoller (I couldn't have hoped for a better teacher of things quantum), to Dolores Wright, Susan Thompson, Linda Frueh, and all the other great people in the offices at Physics and at JILA, and to Earnest Rost (may you rest in peace, Ernie — thank you for being you).

And finally, we come to those people with whom I have had the wonderful opportunity to work over the past several years. Thanks, first, to John Wessels, Karen Belver, Wendy Ortega Henderson, Gwen Bennett, Dee-Anna Gibson, Norma Franklin, Eyvon Petty, and everyone in the Time and Frequency offices, and to Don Sullivan for making the Division such a terrific place to do research. “Thank you” to Leo Holberg, Fred Walls, W. David Lee, and all the other members of the Division for much help along the way. Thanks to John Lowe and his Engineering Support Group for invaluable assistance, and especially to Andrew Novick and Jason Heidecker.

The Ion Storage Group is a phenomenal learning environment and, although Dave and Chris (more on you guys later!) were my immediate supervisors, everyone was always willing to “explain it to the grad student,” and do it with patience and good humour. Wayne, John, and Jim: thank you from the bottom of my heart. I could not have asked for better teachers. Brana, the same goes for you. And thanks to all the post-docs: I learned something (many things!) from each of you. Steve Jefferts, Martin Poitsch, Amy Barton, Joseph Tan, John Miller, Pei Huang, Dana Berkeland, Brad King — I wouldn't have been able to make it without your help along the way. The same goes for my long-time office mate, Brent Young. Thanks, Brent, for all the help on so many fronts.

Max, Flavio, Travis, and Rob — thank you guys.

Finally, I come to the “Quantum Logic” group. Thanks, first, to Chris Monroe, who has been there from the start and has been responsible for my having such interesting physics to work with. Chris, I've learned a lot from you. We made a great team, and I'm glad to have worked with and for you. Thanks to Dawn Meekhof, who helped

me create a space for a graduate student in a group where graduate students were not so common. Thanks to Didi, for the knowledge, the advice, and the never-failing graciousness. You may have a “man in Gaarching” to do it for you, but I doubt he could do as good a job as you. Thanks to Chris Wood for all his help. Thanks to Quentin — I learned incredible amounts just talking to you. To Chris Myatt, for his unfailing good humour, and for being there for me in the lab towards the end. Finally, to Cass — who arrived late, but taught me how wonderful a scientific collaboration can be.

To David K.: Dave, you’re a smart guy. Take care of the group.

I’d like to acknowledge Eric Cornell for being my titular advisor. As well, I very much appreciate the willingness of Murray Holland and Carl Lineberger to serve on my committee.

On to my advisor: David Wineland. Dave, thank you. I simply wouldn’t have made it through graduate school had I not found you and the wonderful group you’ve created. You taught me so much, and have given me the opportunity to try and answer so many interesting questions. You’ve also taught me that you can be an exceptional physicist while still being a truly wonderful human being. Don’t ever think that you aren’t one in a million. I count myself lucky for having worked for and known you.

Finally, thank you to that Being Who has given me the opportunity to discover this world we live in — for the opportunity, and for making it such a wonderful, surprising, and counter-intuitive world in the first place.

# Contents

## Chapter

<b>1</b>	Introduction	1
<b>2</b>	Ion Trapping and Ion Traps	7
2.1	Ideal Quadrupole Paul Trap & the Secular Approximation . . . . .	8
2.2	Full Treatment: the Mathieu Equation . . . . .	12
2.3	Quantum Treatment of Ion Motion . . . . .	16
2.4	Real Paul Traps, Linear Traps, etc. . . . .	21
2.4.1	Elliptical Ion Trap . . . . .	21
2.4.2	Micromachined Linear Trap . . . . .	25
2.4.3	Vacuum System . . . . .	32
2.4.4	Ion Source . . . . .	35
<b>3</b>	Atomic Structure of ${}^9\text{Be}^+$ and Interaction with Lasers	37
3.1	Energy Levels of ${}^9\text{Be}^+$ and Single-Photon Transitions . . . . .	38
3.2	Coupling Spin and Motion . . . . .	41
3.3	Two-Photon, Stimulated-Raman Transitions . . . . .	48
3.4	Spin Diagnostics: the Ramsey Experiment . . . . .	52
3.5	Mapping Information From Motion to Spin . . . . .	53
<b>4</b>	Apparatus	56
4.1	Optics . . . . .	56

4.1.1	Resonant Beam Lines: the Doppler and Repumper Beams . . . .	58
4.1.2	The Raman Beam Line . . . . .	69
4.1.3	Revisions to the Laser Beam Lines . . . . .	73
4.1.4	Photon Detection . . . . .	74
4.2	Experiment Control and Data Acquisition . . . . .	77
4.2.1	Switching Logic . . . . .	79
4.2.2	Data Acquisition . . . . .	84
<b>5</b>	<b>Ground State Laser Cooling</b>	<b>91</b>
5.1	Doppler cooling . . . . .	92
5.2	Resolved Sideband, Stimulated-Raman Cooling . . . . .	94
5.3	Cooling the Collective Motion of Two Trapped Ions . . . . .	98
5.4	Cooling Three Trapped Ions . . . . .	102
5.5	Heating of the Modes of Motion . . . . .	102
<b>6</b>	<b>Quantum State Engineering of One and Two Ions</b>	<b>112</b>
6.1	Nonclassical States of Motion: One Ion . . . . .	112
6.1.1	Thermal States . . . . .	113
6.1.2	Fock States: Eigenstates of the Harmonic Oscillator . . . . .	113
6.1.3	Coherent States . . . . .	115
6.1.4	Squeezed States . . . . .	119
6.2	Entangling Spin and Motion: One Ion . . . . .	121
6.2.1	“Schrödinger’s Cat” . . . . .	121
6.3	Determining the Complete Motional State . . . . .	127
6.4	Quantum State Engineering of Two Ions . . . . .	133
6.4.1	Entangled States of Two Ions . . . . .	134
6.4.2	Creating Multi-Ion Entangled States . . . . .	141

<b>7</b>	Quantum Logic with Trapped Ions	144
7.1	Quantum Computation . . . . .	148
7.2	Errors and Error Correction . . . . .	155
7.3	Ion Trap Quantum Computers . . . . .	159
7.4	Quantum Logic on One Ion . . . . .	161
7.4.1	Simplified Controlled-NOT Gate . . . . .	164
7.5	Quantum Logic on Multiple Ions . . . . .	165
<b>8</b>	Reservoir Engineering	168
8.1	Reservoir Interactions and Decoherence . . . . .	169
8.1.1	Beyond the Master Equation . . . . .	174
8.2	Phase Reservoir . . . . .	177
8.3	Amplitude Reservoir . . . . .	183
8.3.1	Natural Amplitude Reservoir . . . . .	186
8.4	Engineered $T=0$ Reservoir . . . . .	187
8.5	Squeezed Reservoir . . . . .	193
<b>9</b>	SU(1,1) Berry's Phase with Trapped Ions	195
9.1	Berry's Phase . . . . .	196
9.2	An Example: a Spin-1/2 Particle in a Magnetic Field . . . . .	199
9.3	SU(1,1) Berry's Phase with Squeeze Operators . . . . .	208
9.4	Experimental Issues . . . . .	215
9.4.1	Differential Squeezing Using Polarization . . . . .	217
9.4.2	The Effect of Small Errors on Berry's Phase . . . . .	220
 <b>Appendix</b>		
<b>A</b>	Photon Statistics and "Peaking Up" the Experiment"	226

A.1	Peaking Up the Experiment With the Mean Photon Number . . . . .	226
A.2	Photon-Number Histograms . . . . .	228
A.2.1	Discrimination Limits: Off-Resonant Pumping . . . . .	229
A.2.2	Fine-Tuning the Resonant Beam Intensities . . . . .	235
<b>B</b>	<b>Matrix Elements</b>	<b>237</b>
<b>C</b>	<b>Mathematical Miscellany for SU(1,1) Berry's Phase</b>	<b>240</b>
C.1	Calculation of SU(1,1) Berry's Phase Integral . . . . .	240
<b>D</b>	<b>Glossary of Symbols</b>	<b>242</b>
	<b>Bibliography</b>	<b>249</b>

## Figures

### Figure

2.1	(a) Electrode structure for an rf (Paul) ion trap. (b) Motion of an ion trapped in an rf trap. . . . .	9
2.2	“Elliptical” rf ion trap electrode structure. . . . .	23
2.3	Quarter-wave coaxial resonator for producing high voltages at the ion trap electrodes. . . . .	25
2.4	“ $\pi$ -network” rf filters on the compensation-electrode feeds of the elliptical trap resonators. . . . .	26
2.5	(a) Electrode configuration for a linear rf ion trap. (b) Exploded view of micromachined linear ion trap. . . . .	28
2.6	“ $\pi$ -networks” on the linear trap static-potential electrodes. . . . .	30
2.7	(a) Simplified electrode structure for two-dimensional estimate of the static-potential trapping frequency. (b) The potential created by this electrode structure, plus that due to its mirror image, is equivalent to the potential produced by the electrode structure of (a). . . . .	30
2.8	Schematic of the vacuum system for the micromachined, linear ion trap.	33
2.9	Photograph of a portion of the coaxial resonator and quartz envelope. .	34
3.1	Simplified energy level diagram for ${}^9\text{Be}^+$ . . . . .	39
3.2	Photon number histograms for the cycling transition when the ion starts out in (a) $ \downarrow\rangle$ and (b) $ \uparrow\rangle$ . . . . .	41

3.3	Spectrum of a trapped beryllium ion, taken by sweeping the Raman beam frequency difference and monitoring the cycling transition fluorescence. . . . .	46
3.4	(a) “Rabi flopping curve” for the carrier transition. (b) “Rabi flopping curve” for the first upper (“blue”) motional sideband. . . . .	47
3.5	Ramsey fringes taken with an initial $ \downarrow\rangle$ state. . . . .	54
4.1	Laser beam geometry. . . . .	57
4.2	Schematic diagram of the resonant (Doppler and repumper) beam lines. . . . .	59
4.3	Schematic of the saturated absorption spectrometers used to lock the (a) Doppler and (b) repumper lasers to iodine. . . . .	61
4.4	(a) Portion of $I_2$ line # 961, as traced out by saturated absorption spectroscopy. (b) $I_2$ line # 954. . . . .	63
4.5	Resonant power build-up ring cavities for frequency doubling 626 nm to 313 nm. . . . .	65
4.6	Schematic of the Raman beam line. . . . .	71
4.7	Schematic of the Raman beam line, as modified to avoid fibre-induced, differential phase noise in the Red and Blue Raman beams. . . . .	75
4.8	Schematic of the imaging optics. . . . .	76
4.9	Timing diagram for a typical experiment. . . . .	80
4.10	(a) Schematic of the rf portion of the “rf switchbox” circuitry. (b) Schematic of the TTL circuitry inside the “rf switchbox.” . . . .	81
4.11	User interface for the LabView program which set up the HP 8175 pulse generator to run the experiment. . . . .	84
4.12	Schematic of counter/buffer box for data acquisition with HP 9826 computers. . . . .	86
4.13	(a) Schematic of PC-based data acquisition. (b) Timing diagram for PC-based data acquisition. . . . .	89

5.1	Laser cooling of a single ${}^9\text{Be}^+$ ion, as indicated by Raman probe spectrum.	95
5.2	Spectrum of sidebands due to two-ion $x$ -axis normal mode motion. . . .	101
5.3	Spectrum of sidebands due to three-ion $x$ -axis normal mode motion. . .	103
5.4	Summary of the heating rates in the various traps. . . . .	104
5.5	“Double trap” used for heating studies. . . . .	110
5.6	Heating rates for the small and large traps in the “double trap,” as a function of trap frequency. . . . .	111
6.1	Rabi flopping curve on the blue sideband for a thermal state of the ion’s motion. . . . .	114
6.2	Rabi flopping curve for a coherent state. . . . .	120
6.3	Rabi flopping curve for squeezed states. (a) In the Lamb-Dicke regime. (b) Outside the Lamb-Dicke regime. . . . .	122
6.4	Ratio of Rabi frequencies in $\downarrow$ and $\uparrow$ , as a function of the angle of the polarizer in the $\text{RR}_\perp$ beam line. . . . .	126
6.5	Measured and fit interference signals for a “Schrödinger cat” state as a function of the phase between coherent displacement and reversal. . . .	127
6.6	(a) Reconstructed Wigner function for an $ n = 1\rangle$ Fock state. (b) Recon- structed Wigner function for a coherent state $ \alpha\rangle$ . . . . .	130
6.7	Reconstructed density matrix amplitudes of an approximate $\frac{1}{\sqrt{2}}( n = 0\rangle - i n = 2\rangle)$ state. . . . .	132
6.8	Normalized carrier Rabi frequency of each of two ions as a function of center-of-mass displacement from the rf null. . . . .	136
6.9	Simplified level diagram showing four levels coupled by the lower (red) motional sideband, when the lasers illuminate two trapped ions. . . . .	138
6.10	Photon-number histograms for two trapped ions. . . . .	139
6.11	Carrier flopping curves for the state $ \psi_e(\phi)\rangle$ . (a) $\phi = \pi$ . (b) $\phi = 0$ . . . .	140

6.12	Schematic of the two-photon interaction proposed by Sørensen and Mølmer to produce maximally entangled states (two-ion case). . . . .	143
7.1	(a) Schematic representation of the Controlled-NOT gate. (b) Ramsey spectra of the Controlled-NOT (CN) gate. . . . .	163
7.2	“Interaction-free” laser beam profiler. . . . .	167
8.1	“Ramsey” fringe contrast as a function of coupling strength to phase reservoir. . . . .	184
8.2	“Ramsey” fringe contrast as a function of coupling strength to an amplitude reservoir. . . . .	187
8.3	“Ramsey” fringe contrast as a function of interaction time with the “natural” amplitude reservoir due to the background heating rate in the trap. . . . .	188
8.4	Populations of the motional levels $ 0\rangle$ , $ 1\rangle$ , and $ 2\rangle$ as a function of the reservoir interaction time, for an initial $ \downarrow, 2\rangle$ state. The solid lines are fits to data of the master equation solutions. . . . .	190
8.5	(a) Level scheme for realizing an engineered $T = 0$ amplitude reservoir. (b) Effective two-level system equivalent to the scheme in (a). . . . .	191
8.6	Evolution of the coherence $\rho_{02}$ for an initial $ \downarrow\rangle( 0\rangle +  2\rangle)/2^{1/2}$ state, as a function of the interaction time $t_{res}$ with an engineered $T = 0$ reservoir. . . . .	194
9.1	Rotations of a spin-1/2 particle in a magnetic field. . . . .	205
9.2	Unit hyperboloid in the vector space spanned by $\hat{J}_3$ , $\hat{K}_1$ , and $\hat{K}_2$ . . . . .	212
9.3	(a) Predicted phase shift for an initial $ n = 0\rangle$ state subject to a sequence of four squeezings constituting a closed path on the unit hyperboloid. . . . .	216
9.4	Dependence of the Rabi frequencies in $\downarrow$ and $\uparrow$ as a function of (a) the Raman detuning, (b) the quarter-wave plate angle, and (c) the half-wave plate angle. . . . .	219

9.5	Effect of small imperfections of the squeezing pulses on the measured geometric phase shift. . . . .	225
A.1	(a) Photon number histograms for $ \downarrow\rangle$ and $ \uparrow\rangle$ . (b) Carrier flopping curve with photon number histograms at select points. . . . .	230
A.2	(a) Relevant energy levels in ${}^9\text{Be}^+$ for discussing off-resonant pumping of $ \uparrow\rangle$ population into the cycling transition. (b) Simplified effective level diagram, showing the various rates of population transfer. . . . .	232
A.3	Photon number histograms versus power broadening. . . . .	234
A.4	Photon number histograms (a) without and (b) with the repumper laser aligned onto the ion. . . . .	236
B.1	(a) Matrix elements between the ground state, $F = 2$ hyperfine and $2p\ {}^2P_{1/2}$ levels. (b) Matrix elements between the ground state, $F = 1$ hyperfine and $2p\ {}^2P_{1/2}$ levels. . . . .	238
B.2	(a) Matrix elements between the ground state, $F = 2$ hyperfine and $2p\ {}^2P_{3/2}$ levels. (b) Matrix elements between the ground state, $F = 1$ hyperfine and $2p\ {}^2P_{3/2}$ levels. . . . .	239

## Tables

### Table

4.1	Optical characteristics of $\beta$ -barium borate (BBO) at 626 nm and room temperature. . . . .	66
4.2	Optical characteristics of rubidium dihydrogen phosphate (RDP) at 626 nm and room temperature. . . . .	69
5.1	Heating rates of the six normal modes of two trapped ions. . . . .	105
7.1	Effect of Controlled-NOT logic gate on the computational basis states. .	164

## Chapter 1

### Introduction

Quantum theory [1, 2] has been with us now for sixty-five years. It is, most physicists believe, the underlying description of all physical phenomena, and it certainly is unparalleled in the accuracy of its quantitative predictions [3] and in the breadth of its applicability. However, certain aspects of quantum theory are, as yet, poorly understood. For instance, the transition between quantum and classical mechanics is still elusive: in particular, the conflict between the classical phenomenon of chaos [4] and Heisenberg's Uncertainty Principle [2] is only beginning to be understood and resolved [5, 6]. And, in general, a better understanding of how the transition from a microscopic to a macroscopic description of matter and how "emergent properties" [7] arise, would be desirable.

Even the formulation of quantum mechanics seems paradoxical in certain respects. In general, quantum mechanics allows for the possibility of *superposition states*. A classic (though not classical!) example is the two-slit experiment [8], in which we consider light which passes through a solid screen with two slits cut in it and then is detected on a piece of photographic film (or some other such photo-detector). At high light intensities, the film shows the alternating bright and dark bands due to constructive and destructive interference from the two possible paths from the source to the film. However, if we turn down the intensity to low levels, then we detect single photons on the film. This implies that the photons must pass through the slits one at a time. The distribution

of these photons, however, still follows the pattern of bright and dark bands, indicating interference. This implies that a single photon must, in some sense, “pass” through *both* slits on its way to the film or, at least, that the probability of detecting the photon at a given location must depend on information from both paths. We say that the photon’s path from source to film is a superposition of both possible paths, even though, if we place a photo-detector at the location of the slits, we will only ever detect a photon at one slit *or* the other. Although any particular measurement of the photon’s location will find it at one and only one place, we see the “shadows” of superpositions reflected in the *probabilities* of detecting photons at a particular location.

Even these “shadows” of superposition properties disappear when we reach the realm of the macroscopic. And yet, if quantum mechanics is a complete theory of our universe, it ought to describe both microscopic and macroscopic objects. To highlight this paradox, Schrödinger proposed the *gedankenexperiment* involving his now-famous cat [9]. This *gedankenexperiment* involves a box containing a single radioactive nucleus, a bottle of cyanide with a trigger mechanism to release this material, and a hapless feline. If the nucleus decays, then the trigger is activated, and the cat is killed. However, quantum mechanically, after some period of time on the order of the half-life of the nucleus, the nucleus must be described as being in a *superposition* of undecayed and decayed. Since the state of the cat is correlated with the state of the nucleus, the *cat* must be described as being in a superposition of alive and dead. We have absolutely no evidence that cats are ever found in such a state!

Two of the main impediments to really understanding what quantum mechanics is trying to tell us about the universe, then, are understanding the apparent disappearance of superposition properties in the course of a single measurement and the apparently complete lack of superposition behaviour in macroscopic objects. In some sense, these issues may be the same: since we, who ultimately register the outcome of measurements in our state of being, are macroscopic objects, it may be this fact which

destroys superposition in measurement. But it is not entirely clear if, and how, this might happen.

Part of the conflict on the first point seems to arise from the fact that standard formulations of quantum mechanics interpret it as an inherently probabilistic theory, which makes only statistical predictions: on the other hand, we appear to only experience a *single* reality. Particularly when dealing with separate objects whose properties are correlated but which properties are prepared in a superposition state (so-called “entangled”) systems, this interpretation can seem paradoxical. This conflict has led some physicists (e.g. Einstein, Podolsky, and Rosen [10]) to propose that quantum mechanics is an incomplete theory. Others of the “founding fathers” [11] disputed this contention.

According to the standard, Copenhagen interpretation, time evolution in quantum mechanics falls into two categories. The first is unitary time evolution, described by the Schrodinger equation. The second, which describes the outcome of measurements (by classical-like apparatus), is the explicitly non-unitary “collapse of the wave function” to one and only one of the measurement eigenvalues [2] and the subsequent renormalization of the wave function.

However, the “classic” Copenhagen interpretation requires the existence of classical measuring devices, which are not described by quantum theory. Any attempt to dispense with these necessitates positing the physical reality of the collapse of the wave function. Quantum theory provides no explanation of how this occurs. It certainly seems difficult to explain this through the Schrodinger equation, which is unitary. Indeed, the “measurement paradox,” as it is called, has provoked much discussion (for a good, “plain English” review of what the problem is, and a description of several physicists’ approaches to resolving it, see Ref. [12]).

Physicists have proposed various ways to resolve the “measurement paradox.” Some proposals attempt to do so with only the mathematical apparatus prescribed by quantum theory: examples are the “many-worlds” interpretation [13, 14], the “de-

coherence approach” [15], and the “consistent histories” or “decoherent histories” approach [16, 17]. Others [18] posit the existence of new fundamental physical processes or even [19] [20](Ch. 22) a different, entirely non-quantum description of the universe. Many of these theories tie in the resolution of this paradox with the disappearance of superposition properties in “large” objects. The detailed mechanism by which the superposition properties disappear of course differs from theory to theory. For example, in some approaches [18] “large” refers to systems with large numbers of particles. In others [15], “large” refers to distinguishable quantum states of a system coupled to a larger system with many degrees of freedom.

It would be desirable, therefore, to be able to study quantum mechanics in a well-controlled environment. Perhaps, if we can simplify experiment down to the essentials, we can obtain a more precise understanding of what quantum mechanics means. Or, if we can control the quantum behaviour of a very simple quantum system, perhaps we can begin to build up “quantum complexity” in a controlled manner and see how emergent behaviours come about. In addition, experiment often demands description in very precise terms and this can sometimes lend clarity to the essentials of a theory.

This thesis will describe experiments involving a single  ${}^9\text{Be}^+$  ion confined in an rf (Paul) trap. These experiments realize two of the simplest quantum systems: the two-level system and the harmonic oscillator. The two-level system is comprised of two, ground-state hyperfine electronic levels. The trapping potential is harmonic, to a high degree of approximation, and so the ion’s motion is that of a three-dimensional harmonic oscillator. When we laser cool [21, 22, 23, 24] this motion to near its ground state [25], the quantum properties of the motion become significant.

By coupling the ion’s motional and electronic degrees of freedom with lasers, we can engineer entanglement between these quantum systems. Although these dynamics can be well-described theoretically [26, 27, 28, 29, 30], they still offer many surprises. Furthermore, if several ions are held in the trap, their Coulomb interaction causes

their motion to become a joint property of all the ions. Thus, we can create quantum entanglement between the ions' electronic and motional degrees of freedom, and between the electronic degrees of freedom of different, spatially separated ions. This allows us to begin building up “large” quantum systems (in either of the above senses) in a well-controlled way. We refer to this as “quantum state engineering.”

Being able to controllably engineer quantum states, and to isolate them from outside influences, allows us to investigate the new ideas of “quantum computation” [31, 32, 33, 34, 35, 36]. This field has grown out of the realization that “information is physical” [37], but really took off with the discovery in the early 1990's [38, 39] that a computer which utilizes quantum superposition can be exponentially more efficient at solving certain problems than any classical computer. The component parts of a quantum computer, called “qubits,” must be well- insulated from outside influences (which cause decoherence — the destruction of superposition) while interacting with each other strongly enough to allow conditional logic. Trapped ions addressed by laser beams [40] offer such a system. We are attempting to construct simple quantum information processors [41] with our system, and to study the scalability of trapped ions for quantum computing. Furthermore, since many aspects of wave function collapse seem to deal with the transfer of information between quantum systems, it may well be that the language of quantum information theory (quantum computation) will shed light on the issues discussed above [42, 43].

In this thesis, I will describe some of the experiments which we have performed in the NIST Time and Frequency Division Ion Storage Group. I will begin by describing in general how we confine charged atoms using time-varying electric fields (Ch. 2), and how the trapping potential modifies the atoms' interactions with laser radiation (Ch. 3). I will go on to describe the particular arrangement of apparatus actually used in our experiments (Ch. 4). From that point, I will describe laser cooling one [44] or more [45]

trapped ions to their ground state of motion. This puts the ion's motion into the quantum regime of behaviour, and is the starting point for quantum state engineering.

In the rest of the thesis (Chapters 6 through 9), I will describe creation of various non-classical states of motion [46, 47, 48] and entangled states [49] and the application of quantum state engineering to quantum logic [41]. The same techniques may be used to allow the ion's motion to interact with the "outside world." I will discuss experiments along these lines [50], and their implications for decoherence studies and quantum measurement theory in Ch. 8, and conclude by discussing a proposal for an experiment to measure a "surprising" quantum phase factor: Berry's phase.

## Chapter 2

### Ion Trapping and Ion Traps

Since their development in the late 1950's [51, 52, 53], ion traps have made increasing contributions to atomic physics. The ability to trap single to millions of atomic ions in good isolation from the outside world has led to improved spectroscopic measurements [54, 55], exquisite tests of QED [3], observations of quantum jumps [56, 57, 58], stimulating discussion of the “quantum Zeno effect” [59], and controllable engineering of quantum states of motion and the interaction of these states with the environment [50]. Laser cooling, which is the starting point for almost all modern atomic physics measurements, was first demonstrated in ion traps — in 1978 [60, 61]. Furthermore, the same properties of ion traps which make them attractive for high-precision spectroscopy also may make them an ideal candidate for implementing a simple quantum computer. At heart, these important properties are: (a) the ability to trap atoms for long periods of time (up to days [62]), which allows for long spectroscopic interrogation times and (b) the fact that, since the trapped atom is charged, it perforce finds the location in the trap such that  $\langle \mathbf{E} \rangle = 0$ , so that the atom's energy structure experiences only minor electric field perturbations.

There are different varieties of ion traps [63], but the most common use quadrupole fields [64]. These are the Penning trap, which uses static electric fields and a static magnetic field to confine the ions, and the rf, or ‘Paul’ trap, which uses radio frequency (rf) fields to do so. The work in this thesis was performed in Paul-type traps. This

chapter will describe the theory of operation of such traps, and describe the particular traps used for the research in this thesis.

## 2.1 Ideal Quadrupole Paul Trap & the Secular Approximation

Although Earnshaw’s Theorem [65] shows the impossibility of confining an isolated charge in free space using only static electric fields, it *is* possible to do so using time-dependent fields. To see how this occurs, consider applying an rf potential with frequency  $\Omega_T$  to the electrodes of the Paul trap shown in Fig. 2.1(a). These electrodes have the shape of hyperboloids of revolution. The central electrode is usually referred to as the “ring” electrode, and is connected to the rf source. The other two electrodes, referred to as “endcaps,” are held at rf ground. In the case where the electrodes are perfectly hyperbolic, the application of a sinusoidal rf signal results in the potential

$$V = V_0 \cos(\Omega_T t) \left( \frac{x^2 + y^2 - 2z^2}{d_0^2} \right), \quad (2.1)$$

between the electrodes of the trap. Here,  $d_0$  is a characteristic internal dimension of the trap: if the ring electrode has minimum radius  $r_0$  and the endcaps have smallest separations  $2z_0$ ,  $d_0 = \sqrt{r_0^2 + 2z_0^2}$ .

To gain insight into how this configuration can provide trapping for charged particles, consider the forces felt by a single such particle (with charge  $Q$ ) inside the electrode structure. At time  $t = 0$ , the center of the trap is a potential minimum in the  $x$ - and  $y$ -directions, but a local maximum in the  $z$ -direction. So, the ion is trapped in the  $x$ - and  $y$ -directions, but its  $z$ -motion is unstable (“anti-trapped”). Thus, the ion tends to be expelled from the trap in the  $z$ -direction. A half cycle later, however, the situation is reversed, so that the  $z$ -direction is confining while the  $x$ - and  $y$ -directions are not. The time-averaged result of this situation is that the charge is

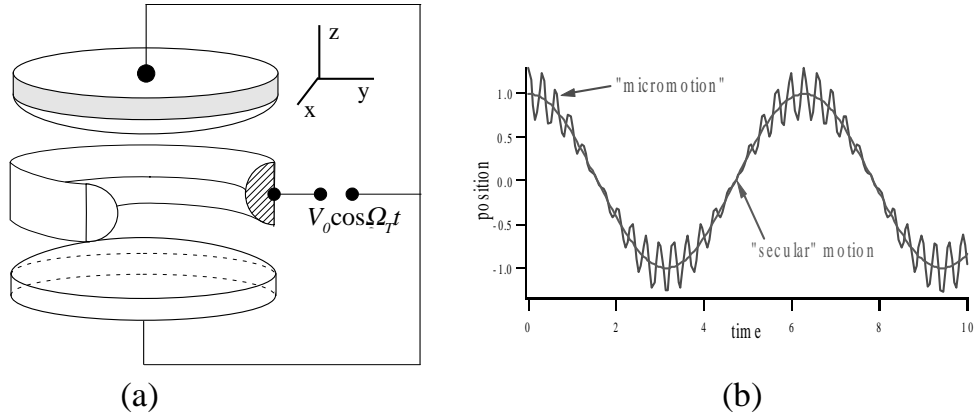


Figure 2.1: (a) Electrode structure for an rf (Paul) ion trap. The electrodes are hyperbolic in cross-section and, when an rf potential is applied to the electrodes as indicated, it gives rise to a potential of the form  $V = V_0 \cos(\Omega_T t) \left( \frac{x^2 + y^2 - 2z^2}{d_0^2} \right)$ . (b) The ion's motion in a Paul trap may be considered to be made up of two parts. The secular motion represents the ion's movement in a three-dimensional harmonic well of frequencies  $\omega_x = \omega_y = \omega_z/2 = \sqrt{2}QV_0/(md_0^2\Omega_T)$ . Here  $Q$  is the charge on the ion,  $m$  is its mass, and  $d_0$  is a characteristic internal dimension of the trap. The micromotion, which occurs at the drive frequency  $\Omega_T$ , is of small amplitude, vanishing at the null point of the rf field (in the center of the trap) .

trapped in a three-dimensional simple harmonic oscillator potential with “secular frequencies”  $\omega_x = \omega_y = \omega_z/2 \approx \sqrt{2}QV_0/(md_0^2\Omega_T)$ , where  $m$  is the ion's mass<sup>1</sup> .

At this point, the following mechanical analogy may help [66]. Consider a marble resting on a saddle-shaped surface (under the effect of gravity). The saddle is a stable potential in one direction, but is unstable in the other. Thus, under the influence of gravity, the marble tends to roll down the unstable “sides” of the saddle. However, if we rotate the saddle about the vertical at the proper frequency, we may create a stable trap for the marble: as the marble begins to roll downhill in some direction, the saddle rotates so that what was previously downhill now becomes uphill. With the proper rotation frequency (which depends upon the marble's mass and the curvature of the

<sup>1</sup> This result only holds in the so-called “pseudopotential approximation,” which I will discuss below.

saddle), the marble always “sees” an effectively uphill potential in any direction, and so is trapped.

The trapping of a charged particle with time-varying electric fields occurs in an analogous fashion. A simple mathematical approach to this trapping is the “secular” or “pseudopotential” approximation, originally considered by Kapitsa [67]. Using Eq. (2.1), we may write down the (separable) equations of motion for a charged particle in the trap. For example, in the  $z$ -direction, we have:

$$\ddot{z} = \left( \frac{4QV_0}{md_0^2} \cos(\Omega_T t) \right) z. \quad (2.2)$$

Similarly, for the radial motion, we have:

$$\ddot{r} = \left( \frac{2QV_0}{md_0^2} \cos(\Omega_T t) \right) r. \quad (2.3)$$

For the sake of explaining the pseudopotential approximation, let us consider only the  $z$  motion. We assume that the complete  $z$ -motion,  $z_{tot}$ , can be broken up into a large-amplitude slow motion  $z$  (the “secular motion”) and a small-amplitude high-frequency motion  $z_\mu$  (the “micromotion”), at the drive frequency  $\Omega_T$ . Thus,  $z_{tot} = z + z_\mu$  with  $z_\mu \ll z$ . We also assume that  $\dot{z}_\mu \gg \dot{z}$ . Then Eq. (2.2) becomes

$$\ddot{z} + \ddot{z}_\mu = \left( \frac{4QV_0}{md_0^2} \cos(\Omega_T t) \right) (z + z_\mu), \quad (2.4)$$

and, applying the two approximations given above, we obtain:

$$z_\mu(t) \approx - \left( \frac{4QV_0}{md_0^2 \Omega^2} \cos(\Omega_T t) \right) z. \quad (2.5)$$

This gives the functional form for the micromotion. Bearing in mind that the secular motion  $z$  occurs on a much slower time scale than this micromotion, we see that the micromotion is at frequency  $\Omega_T$ , and that its amplitude is proportional to the instantaneous amplitude of the secular motion. Plugging Eq. (2.5) back into Eq. (2.4), we have for the secular motion:

$$\ddot{z} = \left[ \frac{8QV_0}{md_0^2} \cos(\Omega_T t) \right] z - \left[ \frac{16Q^2 V_0^2}{m^2 d_0^4} \cos^2(\Omega_T t) \right] z. \quad (2.6)$$

Now, we average over one period of the rf. The cosine averages to zero and, of course the term  $\cos^2(\Omega_T t)$  averages to 1/2. Thus we have

$$\ddot{z} = -\left(\frac{8Q^2V_0^2}{m^2d_0^4\Omega^2}\right)z, \quad (2.7)$$

which is the equation of motion of a harmonic oscillator with frequency

$$\omega_z = \frac{2\sqrt{2}QV_0}{md_0^2\Omega_T}. \quad (2.8)$$

Thus, combining the secular motion with Eq. (2.5), we have:

$$z_{tot}(t) \propto \cos(\omega_z t) \left[ 1 - \frac{4QV_0}{md_0^2\Omega_T^2} \cos(\Omega_T t) \right] \quad (2.9)$$

A similar treatment shows that, for motion in the radial direction,  $\omega_r = \omega_z/2$ . Note that, in general,  $\omega_x + \omega_y - \omega_z = 0$ , due to Poisson's equation.

To recap, we may, in the pseudopotential approximation, break the ion's motion into two parts: the secular motion and the micromotion. The secular motion occurs on a timescale longer than the period of the rf drive signal, and is the motion of a particle trapped in a harmonic oscillator (the ‘‘pseudopotential’’) with trap frequency  $\omega_z = \frac{2\sqrt{2}QV_0}{md_0^2\Omega}$ . The micromotion occurs at the same frequency as the rf drive signal, and its amplitude is proportional to the instantaneous displacement of the particle from the rf null in the trap. However, comparing Eq. (2.5) and Eq. (2.8), we see that the constant of proportionality is  $\frac{\omega_z}{\sqrt{2}\Omega_T} \ll 1$ , so that the micromotion amplitude is, indeed, much smaller than that of the secular motion. It is shown in [68] that ‘‘potential energy’’ of the particle in the pseudopotential is, in fact, just the kinetic energy associated with the micromotion.

The well depth of the pseudopotential is given by  $\overline{D}_z \approx \frac{m\omega_z^2 d_0^2}{8Q} = \frac{QV_0^2}{md_0^2\Omega_T^2}$ , where  $QD_z$  is the maximum pseudopotential energy the particle can have without running into the trap electrodes. For 10 MHz secular frequencies and a singly charged  ${}^9\text{Be}^+$  ion in a trap with  $d_0 = 400 \mu\text{m}$  (typical for the experiments described in this thesis), this corresponds to a well depth of about 10 eV, with a corresponding temperature of

about  $10^5$  K! This implies that elastic collisions with (room-temperature) background gas atoms and molecules will not eject the ion from the trap. In practice, the lifetime of trapped ions is dominated by inelastic collisions with background gas.

## 2.2 Full Treatment: the Mathieu Equation

The *complete* motion of a trapped ion may be written down without recourse to the secular approximation. For the sake of completeness, I will sketch the technique here, again for the  $z$  direction. For more details, see Ghosh [64] or Walker [69]. The method is also nicely sketched out by Cirac, *et al.* [70] and by Bardroff, *et al.* [71].

To be more general, I will allow for the possibility of a static voltage  $U_0$  being applied to the ring electrode in addition to the rf potential, so that Eq. (2.1) becomes:

$$V = (U_0 + V_0 \cos(\Omega_T t)) \left( \frac{x^2 + y^2 - 2z^2}{d_0^2} \right). \quad (2.10)$$

Then the equation of motion for the  $z$  direction becomes:

$$\ddot{z} - \left( \frac{4Q}{md_0^2} \right) (U_0 - V_0 \cos(\Omega_T t)) z = 0. \quad (2.11)$$

With the substitutions  $\zeta = \Omega_T t/2$ ,  $a_z = \frac{-16QU_0}{md_0^2\Omega_T^2}$ , and  $q_z = \frac{-8QV_0}{md_0^2\Omega_T^2}$ , we can put Eq. (2.11) into the canonical form:

$$\frac{d^2 z}{d\zeta^2} + (a_z - 2q_z \cos(2\zeta)) z = 0. \quad (2.12)$$

(Note that, if we instead treat the radial direction, we have  $a_r = \frac{8QU_0}{md_0^2\Omega_T^2}$ , and  $q_z = \frac{4QV_0}{md_0^2\Omega_T^2}$ ). This equation is called the Mathieu equation, and its solutions are known (see, for example, Abramowitz and Stegun [72]). What we seek are stable solutions of this equation, i.e. solutions for which the particle trajectory remains bounded (trapped).

Given that the coefficients in the differential equation are periodic, we may express the solution in terms of the two, independent ‘‘Floquet solutions’’

$$u_1(\zeta) = e^{\mu\zeta} \phi_1(\zeta), \quad (2.13)$$

$$u_2(\zeta) = e^{-\mu\zeta}\phi_2(\zeta), \quad (2.14)$$

where  $\phi_1(\zeta)$  and  $\phi_2(\zeta) \equiv \phi_1(-\zeta)$  are periodic functions of  $\zeta$  with the same period as the coefficient in the Mathieu equation: that is, since the Mathieu equation contains the term  $\cos(2\zeta)$ ,  $\phi_i$  is of period  $\pi$ . Since we are looking for bounded solutions of the Mathieu equation,  $\mu \equiv \alpha + i\beta$  must be purely imaginary, i.e.  $\alpha = 0$ . (Note, then, that if  $\beta$  gives a possible solution, then so does  $-\beta$ ). If we use this fact and make a Fourier expansion of  $\phi_1$  and  $\phi_2$ , we may express the most general (bounded) solution of the Mathieu equation as

$$z(\zeta) = A \sum_{n=-\infty}^{\infty} C_{2n} e^{i(2n+\beta)\zeta} + B \sum_{n=-\infty}^{\infty} C_{2n} e^{-i(2n+\beta)\zeta} \quad (2.15)$$

where  $A$  and  $B$  are integration constants which depend on the initial conditions, and the  $C_{2n}$  are the Fourier coefficients in the expansion of  $\phi_i$ . Using Euler's Theorem, we may write this alternatively as

$$z(\zeta) = A' \sum_{n=-\infty}^{\infty} C_{2n} \cos[(2n + \beta)\zeta] + iB' \sum_{n=-\infty}^{\infty} C_{2n} \sin[(2n + \beta)\zeta], \quad (2.16)$$

where  $A' = A + B$  and  $B' = A - B$ . Looking at the above equations, we can immediately see that the lowest-frequency motion, that for which  $n = 0$ , is given by  $\omega_z \doteq \frac{1}{2}\beta\Omega_T$ . (The next-highest frequencies in the motion are at  $\omega_z \mp \Omega_T$ .) The question, then, is to determine the characteristic frequency  $\beta$ .

In order to do this, we plug (2.16) back into the Mathieu equation (2.12) and compare, for example, the coefficients of the cosine terms, to obtain

$$\begin{aligned} & -A' \sum_{n=-\infty}^{\infty} C_{2n} (2n + b)^2 \cos[(2n + \beta)\zeta] \\ & \quad + a_z A' \sum_{n=-\infty}^{\infty} C_{2n} \cos[(2n + \beta)\zeta] \\ & - 2q_z A' \sum_{n=-\infty}^{\infty} C_{2n} \cos[(2n + \beta)\zeta] \cos[2\zeta] = 0, \end{aligned} \quad (2.17)$$

which we may re-write as

$$\sum_{n=-\infty}^{\infty} \left( -C_{2n}[(2n + \beta)^2 - a_z] \cos[(2n + \beta)\zeta] - q_z C_{2n} \cos[(2n + \beta + 2)\zeta] - q_z C_{2n} \cos[(2n + \beta - 2)\zeta] \right) = 0. \quad (2.18)$$

Finally, we may write

$$\sum_{n=-\infty}^{\infty} \left( C_{2n}[a_z - (2n + \beta)^2] - q_z C_{2n-2} - q_z C_{2n+2} \right) \cos[(2n + \beta)\zeta] = 0. \quad (2.19)$$

If we define  $D_{2n} \equiv \frac{a_z - (2n + \beta)^2}{q_z}$ , then 2.19 gives us the three-term recursion relation

$$-D_{2n}C_{2n} + C_{2n-2} + C_{2n+2} = 0, \quad (2.20)$$

which we can use to determine  $\beta$ . To determine  $\beta$ , we will use Eq. (2.20) in three ways.

First, writing the equation with  $n = 0$ , we obtain:

$$D_0 C_0 \equiv \frac{a_z - \beta^2}{q_z} C_0 = C_{-2} + C_2, \quad (2.21)$$

which we will, in the end, solve for  $\beta$ . We may also use Eq. (2.20) to write, in general,

$$D_{2n} = \frac{C_{2n-2} + C_{2n+2}}{C_{2n}}. \quad (2.22)$$

After some re-writing, we finally obtain

$$\frac{C_{2n}}{C_{2n-2}} = \frac{1}{D_{2n} - \frac{C_{2n+2}}{C_{2n}}} \quad (2.23)$$

or, applying (2.23) recursively, we obtain the continued fraction:

$$\frac{C_{2n}}{C_{2n-2}} = \frac{1}{D_{2n} - \frac{1}{D_{2n+2} - \frac{1}{\dots}}}. \quad (2.24)$$

Similarly, we can also write

$$\frac{C_{-2n}}{C_{-2n-2}} = \frac{1}{D_{-2n-2} - \frac{1}{D_{-2n-4} - \frac{1}{\dots}}}. \quad (2.25)$$

Plugging these formulae back into Eq. (2.21), and expressing the  $D_{2n}$  as  $D_{2n} = \frac{a_z - (2n + \beta)^2}{q_z}$ ,

we can solve to any desired order in  $a_z$  and  $q_z$  for  $\beta$ .

To lowest order, we have

$$\beta = \sqrt{a_z + \frac{q_z^2}{2}}. \quad (2.26)$$

If the static potential  $U_0 = 0$  so that  $a_z = 0$ , we have  $\beta = \frac{q_z}{\sqrt{2}}$ . Plugging into the formula of the lowest-frequency motion,  $\omega_z = \frac{\beta\Omega_T}{2}$ , we finally have:

$$\omega_z = \frac{2\sqrt{2}QV_0}{md_0^2\Omega_T}. \quad (2.27)$$

This agrees with Eq. (2.8), the expression for the frequency of secular motion in the pseudopotential approximation of the previous Section. Indeed, rigorously speaking, the condition  $a_z, q_z \ll 1$  defines the pseudopotential approximation. To next-highest order in  $q_z$ ,

$$\beta = \sqrt{\frac{a_z + q_z^2 \left( \frac{1}{2} + \frac{a_z}{8} \right) + \frac{q_z^4}{128}}{1 - q_z^2 \left( \frac{3}{8} + \frac{5a_z}{16} \right)}}. \quad (2.28)$$

The ion motion in the exact treatment, then, has frequency components at  $(2n \pm \beta)\Omega_T/2$ . The lowest frequency motion, which we identify with the secular frequency  $\omega_z$ , occurs at a frequency lower than the drive frequency  $\Omega_T$ . The other motions occur at around the drive frequency or higher. But note that there is *no* component of the ion's motion *at*  $\Omega_T$ . Thus, in particular, although the fields at  $\Omega_T$  trap the charged particle, they do not couple energy into the particle's secular motion. If, however, there are fields at frequency  $\Omega_T \pm \omega_z$  (due, for example, to noise from the rf source producing the trapping potential), then this *can* produce heating of the secular motion [54, 73]. As the spectral purity of typical rf sources is very high, this is rarely a problem. Higher-order couplings of the secular motion to the trapping field can be produced by, for example, deviations of the trapping potential from pure quadrupole [73] but, in practice, this is not frequently an issue.

The treatment thus far has only treated a single ion in an ion trap. However, the situation for several ions is not much different. The ions interact through their Coulomb repulsion; but, as with the case of a single ion, the ions arrange themselves so

that, for each ion,  $\langle \mathbf{E} \rangle = 0$ . Nonetheless, in such a situation the ions cannot all occupy the null point of the rf drive field. Thus the amplitude of the ions' micromotion can be substantial (recall from Eq. (2.5) that the amplitude of the micromotion is given by  $z_\mu(t) \approx -\left(\frac{4QV_0}{md_0^2\Omega^2} \cos(\Omega_T t)\right)z$ , where  $z$  is the displacement of the ion from the rf null). The micromotion, together with the ions' nonlinear Coulomb interaction, can lead to "rf heating" of the secular motion for cases in which more than perhaps a few ions are simultaneously confined [74, 75]. Roughly speaking, the nonlinear nature of the Coulomb interaction can, when the ions are not at zero temperature, produce chaotic motion of the ions with its concomitant continuous power spectrum. This continuous power spectrum allows the ions to absorb energy from the trapping field, and they can be driven out of the trap. Rf heating may also be caused by resonances due to trap anharmonicities [76].

### 2.3 Quantum Treatment of Ion Motion

The simplest approach to treating the quantum mechanics of a single trapped ion is to directly quantize the harmonic oscillator which describes the ion's secular motion along a principle direction of the trap, for example  $\mathbf{z}$ . Thus one introduces the usual harmonic oscillator raising and lowering operators  $\hat{a} = \sqrt{\frac{m\omega_z}{2\hbar}}\left(\hat{z} + \frac{i}{m\omega_z}\hat{p}\right)$  and  $\hat{a}^\dagger$ . Inverting these relationships, we have that

$$\hat{z} = z_0(\hat{a} + \hat{a}^\dagger) \quad (2.29)$$

and

$$\hat{p} = p_0(\hat{a} - \hat{a}^\dagger), \quad (2.30)$$

with  $z_0 = \sqrt{\frac{\hbar}{2m\omega_z}}$  and  $p_0 = im\omega_z z_0$ . Thus, one ends up with the usual Hamiltonian operator for a quantized harmonic oscillator:

$$\hat{H}_{HO} = \left(\hat{n} + \frac{1}{2}\right)\hbar\omega_z, \quad (2.31)$$

where  $\hat{n} = \hat{a}^\dagger \hat{a}$  is the number operator<sup>2</sup>.

However, the question arises whether this procedure is appropriate, since the secular approximation is, in the end, only an approximation. This question was first examined in Ref. [78], and has been generalized by others [79, 70, 71]. The short answer is that the procedure is, indeed, appropriate. I will outline some of the results, closely following Glauber.

In the case  $U_0 = 0$ , the equation of motion for (say) the  $z$ -coordinate is of the form:

$$\ddot{z} = P(t)z = 0, \quad (2.32)$$

where  $P(t)$  is a  $c$ -number. This equation holds true in *both* the classical case and (in the Heisenberg picture [2]) the quantum case. Eq. (2.32) is a  $2^{nd}$ -order ODE, possessing two linearly-independent solutions. A general property of such a differential equation is that, if  $u_1(t)$  and  $u_2(t)$  are *any* two solutions to the equation, then the following Wronskian identity holds:

$$u_1(t)\dot{u}_2(t) - \dot{u}_1(t)u_2(t) = \text{const.} \quad (2.33)$$

We can use (2.33) to determine the quantum motion of the trapped atom. In order to do this, we define a “standard”  $\mathcal{C}$ -number solution to Eq. (2.32)  $u(t)$ , with the constraints (initial conditions)

$$\begin{aligned} u(0) &= 1 \\ \dot{u}(0) &= i\omega_{ref}, \end{aligned} \quad (2.34)$$

where  $\omega_{ref}$  is an arbitrary parameter which we will choose later to simplify the math. Note that we can solve for  $u(t)$  using the techniques discussed above for solving the Mathieu equation. Again, Eq. (2.33) holds for *any* two solutions to the differential

---

<sup>2</sup> The quantum version of the secular approximation was examined in Ref. [77].

equation: even if one solution is a  $\mathcal{C}$ -number solution and the second is an operator-valued solution (in the Heisenberg picture). So, for example:

$$u(t)\dot{\hat{z}}(t) - \dot{u}(t)\hat{z}(t) = \text{const.} \quad (2.35)$$

It follows immediately that the operator

$$\hat{C}(t) \equiv \frac{i}{\sqrt{2m\hbar\omega_{ref}}} [u(t)\hat{p}(t) - m\dot{u}(t)\hat{z}(t)] \quad (2.36)$$

is constant in time:

$$\hat{C}(t) = \hat{C}(0) = \frac{i}{\sqrt{2m\hbar\omega_{ref}}} [\hat{p} - im\omega_{ref}\hat{z}]. \quad (2.37)$$

Here,  $\hat{z}$  and  $\hat{p}$  are shorthand for the values of these operators at time  $t = 0$ . An alternative way of visualizing the situation is to view  $\hat{z}$  and  $\hat{p}$  as *Schrödinger* picture, time-independent operators. We then recognize the time-independent operator  $\hat{C}$  as the annihilation operator familiar from the quantized harmonic oscillator:

$$\hat{a} = \frac{i}{\sqrt{2m\hbar\omega_{ref}}} [\hat{p} - im\omega_{ref}\hat{z}]. \quad (2.38)$$

So  $\hat{a}$  is associated with a static-field harmonic oscillator of frequency  $\omega_{ref}$ . We can construct the eigenstates, operators, etc., for this oscillator as usual, and the basis states of this oscillator will be a convenient set of basis states upon which to expand the motional state of the trapped atom. For example, we have for the ground state,  $\hat{a}|n=0\rangle_{w_{ref}} = 0$  which, through the constancy of the operator  $\hat{C}$ , implies that

$$\hat{C}(t)|n=0\rangle_{w_{ref}} = 0. \quad (2.39)$$

In order to obtain the ground-state wave function of this “reference” oscillator (and hence, in the usual manner, the other eigenfunctions), we go over to the Schrödinger picture, by applying the unitary time-evolution operator  $\hat{U}(t)$  to in the usual manner:

$$\hat{C}(t) = \hat{U}^{-1}(t)\hat{C}_S(t)\hat{U}(t) \quad (2.40)$$

to obtain the Schrödinger-picture operator  $\hat{C}_S(t)$ . (We obtain  $\hat{U}(t)$  by solving the Schrödinger equation — but it turns out that we can take a “short cut” to solving for the oscillator wave functions.) Applying  $\hat{U}(t)$  to the left-hand side of Eq. (2.39), we obtain

$$\hat{C}_S(t)\hat{U}(t)|n=0\rangle_{\omega_{ref}} \equiv \hat{C}_S(t)|n=0\rangle_t = 0, \quad (2.41)$$

where  $|n=0\rangle_t$  is the Schrödinger-picture state of the oscillator which evolves under the trapping potential from the ground state of the reference harmonic oscillator. We can rewrite Eq. (2.41) in terms of the position and momentum operators:

$$[u(t)\hat{p} - m\dot{u}(t)q]|n=0\rangle_t = 0 \quad (2.42)$$

In the position representation, we have:

$$\left[u(t)(\hbar/i)\frac{\partial}{\partial z} - m\dot{u}(t)z\right]\psi_0(z) = 0. \quad (2.43)$$

Finally, this first-order differential equation may be solved to obtain the time-dependent wave function of the state which evolves from the ground state of the reference harmonic oscillator:

$$\psi_0(z) = \left(\frac{m\omega_{ref}}{\pi\hbar}\right)^{1/4} \frac{1}{\sqrt{u(t)}} \exp\left[\frac{im\dot{u}(t)z^2}{2\hbar u(t)}\right]. \quad (2.44)$$

We can determine the states which evolve from the other eigenstates of the reference harmonic oscillator by applying raising operators, and so forth [79]. These states all have the form of the usual harmonic oscillator wave functions, with the exception that, as with the ground state shown above, the size of the wave functions changes with time because of the factor  $\dot{u}(t)/u(t)$ . The time dependence is parametric only, and this treatment justifies the simple-minded approach taken at the beginning of this section.

This treatment is not yet complete, however — we have yet to determine a value for the frequency  $\omega_{ref}$  of the reference oscillator. To clarify, what we do have is the expansion of our system upon a basis set of states in Hilbert space. In general, for any quantum mechanical problem, we can expand the state vector in terms of *any*

set of basis functions of the Hilbert space. However, *some* sets of basis functions are more convenient than others. For example, given a regular, static harmonic oscillator of frequency  $\omega$ , we could expand in the basis of a harmonic oscillator of *different* frequency. However, this would only complicate the math and obscure the issue — that is why, in practice, we expand in the natural set of basis functions: those associated with an harmonic oscillator of the *given* frequency,  $\omega$ .

The question, then, is: can we find a “natural” choice of  $\omega_{ref}$  which will simplify solution of the quantum Mathieu equation and which will give us a clear picture of the underlying physics. The answer (of course!) is yes. To get at this picture, recall from Sect. 2.2 that our “standard” solution  $u(t)$  may be written in terms of the Floquet solutions 2.13 and 2.14 as:

$$u(t) = Ae^{i\beta\Omega_T t/2}\phi(\Omega_T t/2) + Be^{-i\beta\Omega_T t/2}\phi(-\Omega_T t/2), \quad (2.45)$$

where  $A$  and  $B$  are constants. In general, this is a very complicated time dependence. But, by judicious choice of initial conditions for our “standard” solution, we will be able to simplify this dependence considerably. Recalling Eqs. (2.34) and choosing to normalize the Floquet solutions such that  $\phi(0) = 1$ , we have that

$$u(0) = 1 = A + B \quad (2.46)$$

and

$$\dot{u}(0) = i\omega_{ref} = (A - B)i\beta\Omega_T/2 + \dot{\phi}(0). \quad (2.47)$$

Now then, if we *choose*  $\omega_{ref}$  such that

$$i\omega_{ref} = i\beta\Omega_T/2 + \dot{\phi}(0) \quad (2.48)$$

then we obtain  $A = 1$ ,  $B = 0$ , and

$$u(t) = e^{i\beta\Omega_T t/2}\phi(t) \quad (2.49)$$

where we have investigated the behaviour of  $\phi(t)$  in Sec. 2.2. From Eq. (2.48) we see that, to lowest order, the frequency of the reference harmonic oscillator is that of the secular motion; that the only effect of the rf drive is to produce a “breathing” motion of the usual harmonic oscillator wave packets.

To sum up, then: for both the classical and the quantum cases, we may, to high accuracy, picture an ion trapped in a Paul trap as moving in a harmonic oscillator potential of frequency  $\omega$ . The micromotion (at  $\Omega_t \pm \omega$ ) does not directly affect this harmonic oscillator motion.<sup>3</sup>

## 2.4 Real Paul Traps, Linear Traps, etc.

The experiments described in this thesis were performed in three different ion traps: two elliptical microtraps and a micro-machined linear trap. I will describe this latter trap in Sec. 2.4.2 and, for now, will focus on the microtraps, which behave very much like the ideal quadrupole trap.

### 2.4.1 Elliptical Ion Trap

Consider Fig. 2.1 for a moment. If the geometry in the  $x - y$  plane is stretched so that the ring and endcaps are elliptical, rather than circular, when looking down the  $z$ -axis, then the potential remains quadratic but the degeneracy between the  $x$ - and  $y$ -axes is broken [80, 81, 82, 83]. This has several advantages. First, there are now three, non-degenerate secular modes of motion with which to perform quantum state engineering. Second, non-degenerate trap frequencies facilitate ground state laser cooling in three dimensions (see Ch. 3). Finally, if several ions are held in the trap, they will preferentially line up along the weakest axis of the trap (given a sufficient anisotropy). Thus they will be easily addressable by laser beams.

---

<sup>3</sup> Note, however, that the micromotion could lead to excitations of the ion’s motion, were we to drive the ion at  $\Omega_T \pm \omega$ .

For experiments in quantum state engineering, it is advantageous to work with high trap frequencies. This facilitates resolved-sideband laser cooling to the ground state of motion and the Lamb-Dicke regime [81, 84], simplifies the interaction of the ions with the lasers (see Ch. 3), and reduces the deleterious effects of background heating on the harmonic oscillator occupation number,  $n$ . From Eq. (2.8), it is apparent that high secular frequencies can be achieved with small traps (i.e. small  $d_0$ ) and/or high rf drive voltages  $V_0$ .

Fig. 2.2 shows a schematic of the small traps used for many of the experiments described in this thesis. Two such traps were used. In order to achieve high secular frequencies, the electrode spacing of these traps was about  $200 \mu\text{m}$ . With such small electrode sizes, it becomes very difficult to machine hyperboloidal electrode surfaces, which is why a somewhat simpler approach was taken: the “ring” electrode was an elliptical hole drilled in a metal sheet, and the “endcap” electrodes were formed from a second metal sheet with a slot cut into it.

One of the elliptical traps (which I will refer to from here on as Trap I) [81] was constructed of  $130 \mu\text{m}$ -thick molybdenum. For this trap,  $r_0 \approx 170 \mu\text{m}$  and  $z_0 \approx 130 \mu\text{m}$ , and the combination of the ellipticity and the asymmetry of the endcap fork electrode gave  $(\omega_x : \omega_y : \omega_z) \approx (0.38 : 0.61 : 1)$ . The trap was typically operated with  $\Omega_T/2\pi \approx 230 \text{ MHz}$ ,  $V_0 \approx 600 \text{ V}$ , and  $U_0 = 0 \text{ V}$  (the trap construction precluded adding a static voltage). These operating parameters gave  $\omega_x/2\pi \approx 11.2 \text{ MHz}$ . This was the trap used for ground-state laser cooling, the Controlled-NOT quantum logic gate, the Schrödinger cat experiment, and much of the quantum state engineering and reconstruction work.

The second trap (which will be referred to as Trap II) was constructed from beryllium metal sheets  $125 \mu\text{m}$  thick, and had a pronounced ellipticity. This trap had  $z_0 \approx 125 \mu\text{m}$ . The semi-major axis of the elliptical ring electrode was  $\approx 210 \mu\text{m}$  long, and the ellipse had an aspect ratio of approximately  $3 : 2$ . With  $\Omega_T/2\pi \approx 240 \text{ MHz}$ ,  $V_0 \approx 520 \text{ V}$ , and  $U_0 = 0 \text{ V}$ ,  $(\omega_x, \omega_y, \omega_z)/2\pi \approx (4.6, 12.7, 17.0) \text{ MHz}$ . With this trap, we

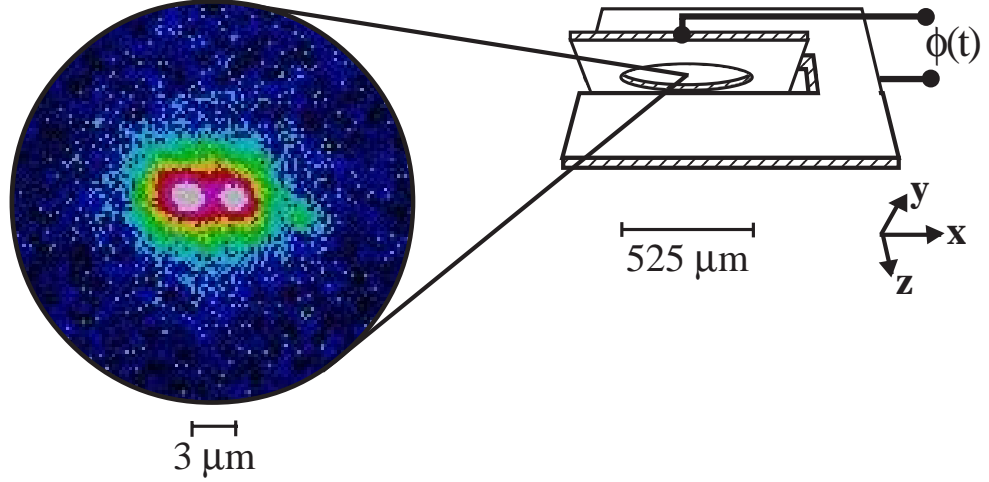


Figure 2.2: Typical “elliptical” ion trap electrode structure for the work described in this thesis, with inset showing two trapped  ${}^9\text{Be}^+$  ions, held in “Trap II.” The ring electrode is formed by the elliptical hole in the one metal plate. The endcaps are formed by the slot in the other plate. The plates are either molybdenum or beryllium, and are  $\approx 130 \mu\text{m}$  thick. The applied potential  $\phi(t) = V_0 \cos \Omega_t t + U_0$ , with  $U_0$  giving rise to a static electric field. With an  $x$ -axis secular frequency of  $\omega_x/2\pi = 4.6 \text{ MHz}$ , the ion-ion spacing is approximately  $3 \mu\text{m}$ .

were able to apply a static voltage  $U_0$  to the ring electrode, in addition to the rf potential. Recalling that the secular frequency is given by Eq. (2.27) as  $w_m = \frac{\Omega_t}{2} \sqrt{a_m + \frac{q_m^2}{2}}$  (where  $m \in \{x, y, z\}$ ) and, from Eq. (2.12), that  $a_z \propto -U_0$  while  $a_r \propto +U_0$ , we see that  $U_0 > 0$  increases  $\omega_x$  and  $\omega_y$  at the cost of lowering  $\omega_z$ . For example, with  $U_0 = 18.2 \text{ V}$  (typical operating conditions),  $(\omega_x, \omega_y, \omega_z) \rightarrow (8.6, 17.6, 9.3) \text{ MHz}$ .

In the previous sections, I discussed a Paul trap with ideal electrodes (as shown in Fig. 2.1a). The electrode geometries of the microtraps was very far from ideal. However, for trapping small numbers of cold ions, where the extent of the ions’ motions is much less than  $d_0$ , the restrictions on the electrode configuration are not stringent. Traps I and II, though far from having the “ideal” geometry, still produced a harmonic trapping potential in the region where the ions were held [81]. Even for non-ideal electrode

geometries, the lowest term in the expansion of the trapping potential is harmonic and, near the trap centre, this term dominates. A relevant expansion parameter is the amplitude of the ion’s motion divided by the size of the electrodes, a factor of  $< 10^{-4}$  for the work in this thesis. If the trap exhibits reflection symmetry about the  $z$ -axis<sup>4</sup>, then next-highest term in the potential expansion is of order  $(d/d_0)^2 \approx 10^{-8}$ . For this reason, the elliptical microtraps were easily “harmonic enough” for our experiments<sup>5</sup>.

In operation, each of these traps was mounted at the high-voltage point of a quarter-wave, coaxial resonator [81]. This resonator was designed to produce large values of  $V_0$ , again for the purpose of having high secular frequencies. A schematic such a resonator is shown in Fig. 2.3. Constructed of OFHC copper, the resonator was vacuum compatible, with a (loaded)  $Q$  on the order of 700<sup>6</sup>. Optical access was through several holes cut in the outer conductor of the resonator. The resonator was excited by the loop antenna at its base, whose area was carefully adjusted so that, on resonance, the antenna/resonator assembly presented a nominal 50  $\Omega$  load to the generator. This design was meant to circumvent the problem of passing high-voltage rf through vacuum feedthroughs (both in terms of the capacitive loading and impedance mismatch introduced by the feedthrough and in terms of high-voltage breakdown at the feedthrough) and thus to allow high  $V_0$  with the concomitant high secular frequencies. In practice, the voltage which could be applied to the trap was limited to  $\approx 1$  kV, due vacuum rf discharges<sup>7</sup>.

The resonator assembly also held four “compensation” electrodes, which were formed from bent pieces of metal rod ( $\approx 2$  mm diameter). By applying voltage to these

---

<sup>4</sup> Of course, care was still taken to align the trap electrodes as well as possible, to minimize the contributions from the higher order terms in the potential

<sup>5</sup> The one price to be paid for using a non-ideal geometry is that the strength of the pseudopotential is reduced with respect to that of an ideal trap of the same physical dimensions. For our traps, the reduction was approximately 10%.

<sup>6</sup> This agrees well with a theoretical estimate based on the resonator geometry and the conductivity of copper.

<sup>7</sup> Vacuum rf discharges are thought to be initiated at field- emission points on the rf system. The high field at these emitters creates a plasma, wherein the material of the system (the electrode surfaces plus any gas adsorbed onto them) provides the material which makes up the plasma.

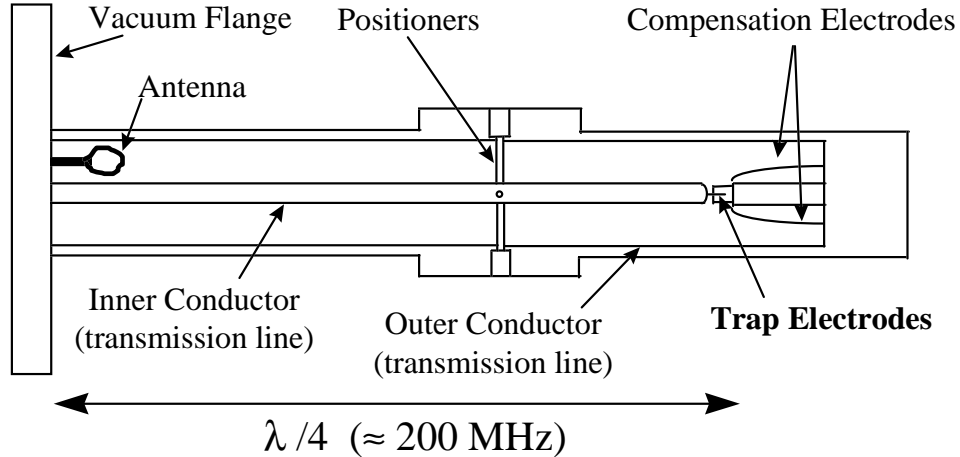


Figure 2.3: Quarter-wave coaxial resonator for producing high voltages  $V_0$  at the ion trap electrodes. As indicated, the ion trap ring electrode is mounted at the antinode of the rf standing wave. The endcap (or fork) electrode is attached to rf ground. The positioners allow for alignment of the two trap electrodes with respect to each other to, e.g., ensure reflection symmetry of the trap about the  $x - y$  plane.

electrodes, we were able to compensate for stray electric fields due to patch fields on the trap electrodes. Such fields are undesirable since they displace a trapped ion from the rf null position and hence increase the amplitude of the micromotion. Rudimentary rf filters (a “ $\pi$ -network” with a roll-off frequency of approximately a half MegaHertz), consisting of hand-made metal-mylar-metal capacitors and wire inductors provided rf isolation of the compensation electrodes from the outside world (see Fig. 2.4).

#### 2.4.2 Micromachined Linear Trap

When several ions are held in a Paul trap (either ideal or non-ideal), they cannot all occupy the position where the rf field is zero. As mentioned in Sec. 2.2, this results in enhanced micromotion for most of the trapped ions. For small numbers of ions, this is not an issue, but as the number increases, rf heating becomes more and more likely. Although the elliptical geometry does reduce the micromotion with respect to a spher-

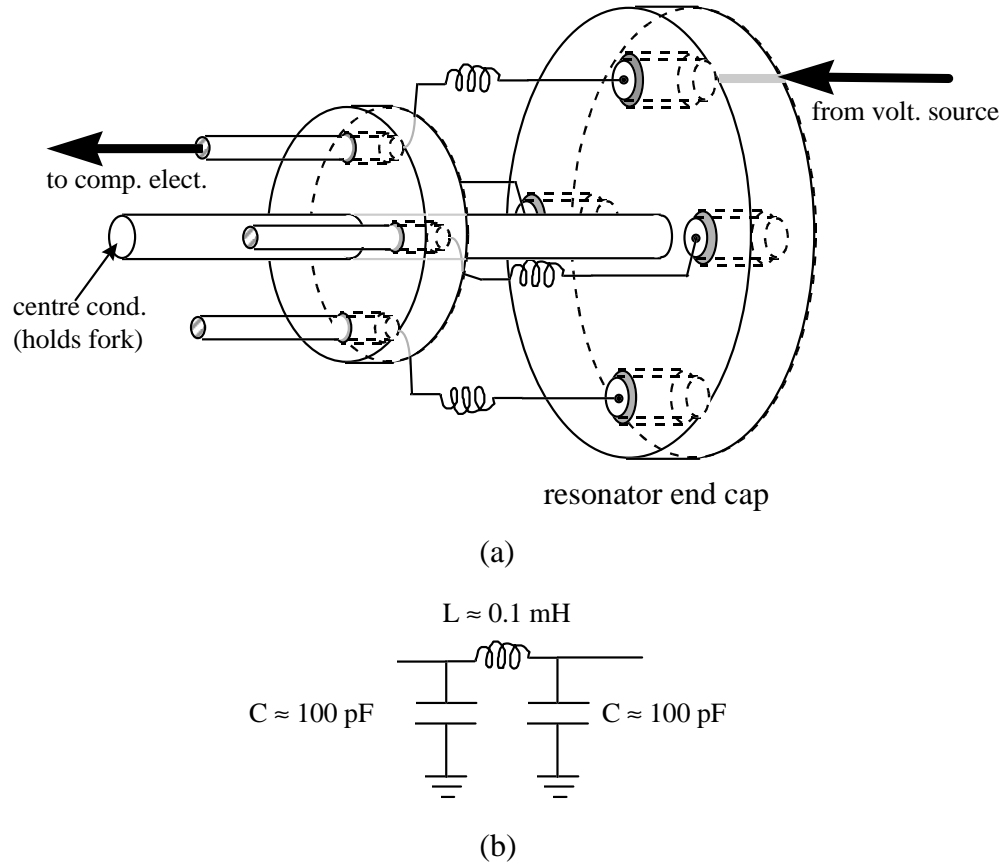


Figure 2.4: (a) Schematic of the “ $\pi$ -network” rf filters on the compensation electrode feeds of the elliptical trap resonators. The rods were insulated from the rf-grounded metal discs (part of the resonator’s outer conductor structure) with mylar: these assemblies formed the capacitor in the “ $\pi$ -network.” The inductors consisted of a few turns ( $\approx 8$ ) of wire hand-wound around the rods. (b) The equivalent “ $\pi$ -network” formed by this assembly.

ical quadrupole trap [82, 83], and the micromotion can be reduced along a particular direction by the addition of a static potential  $U_0$  [82], the micromotion becomes more of an issue as the number of ions grows. For this reason, ion trappers have turned to “linear ion traps” [85, 86].

A linear ion trap confines ions in a two-dimensional Paul trap (which, really is just a Paul-type mass spectrometer [66]), and uses a static potential to contain them in the third direction. A typical electrode configuration is shown in Fig. 2.5(a). Two

of the four rods are held at rf high, and the other two at rf ground. This produces an effectively two-dimensional rf field with a nodal line along the line of symmetry (the  $z$ -axis). Trapping along the rf nodal line is accomplished by applying positive static potentials to the outermost segments of the segmented electrodes. Note that the static electric fields, although they provide trapping in the axial direction, *reduce* the trap strength in two other (“radial”) directions, by Poisson’s theorem. That is, the effective radial trapping strength is lower than it would be were the static fields absent, since these fields counteract the confinement produced by the radio-frequency fields. Thus, there is a trade-off between the trap strength in the three directions. If the  $z$ -direction (static-field trapping) is much weaker than the other two directions, then multiple ions will be confined along the rf nodal line [86, 87]. Since the rf field is zero along this line, they will not experience significant micromotion (when cold). Note that, in the  $z$ -direction, the trapping potential is (near the centre of the trap) purely harmonic: since the trapping potential along this direction is produced by static fields, there is no pseudopotential approximation necessary (see Sec. 2.1).

Although linear traps offer advantages for spectroscopy [88, 85, 86], they offer significant manufacturing challenges when their dimensions are small. Thus, in order to produce a linear-type trap with characteristic dimensions on the order of our elliptical microtraps ( $200\ \mu\text{m}$ ), we turned to micro-machining techniques. Fig. 2.5(b) shows the geometry of such a trap, and indicates the relationship between its electrodes and that of a more traditional linear trap.

The trap consisted of two alumina wafers, 1.5 cm long by 1.0 cm wide by  $125\ \mu\text{m}$  thick. These wafers were held  $200\ \mu\text{m}$  apart by two, gold-coated spacer wafers — one at each end. The spacer wafers were  $175\ \mu\text{m}$  thick, with the remaining  $25\ \mu\text{m}$  consisting of the silver paint used as cement. The trapping region consisted of a series of laser-machined slots in the two wafers: the slots in one wafer were the reflection about the  $z$ -axis of the slots in the other. The main slot in each wafer, which separated

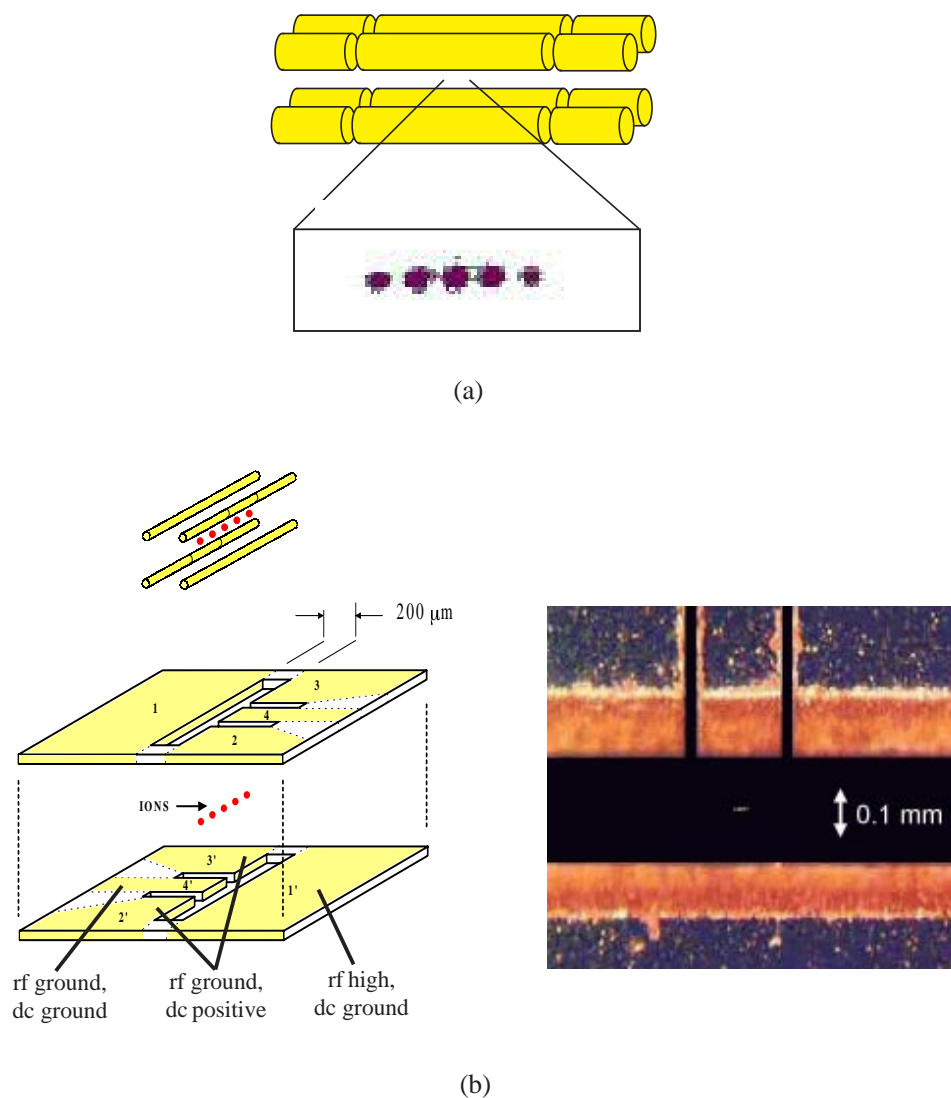


Figure 2.5: (a) Electrode configuration for a linear rf ion trap, with an inset showing several trapped ions. Ion-ion spacing is on the order of ten micrometers for these pictures. (b) Exploded view of the micromachined linear ion trap, with a linear ion trap shown above it for comparison. The rf and static potentials are indicated on the bottom plate. The potentials on the top electrodes 1 through 4 are the same as on the corresponding (unprimed) electrodes on the bottom plate. The right-hand side is a composite image showing a close-up photograph of the electrodes and an image of five trapped beryllium ions.

the continuous rf electrode on one side from the segmented static voltage electrodes (rf ground) on the other, was 2 mm long and 200  $\mu\text{m}$  wide. The two slots in the static voltage electrodes were each 20  $\mu\text{m}$  wide, and were separated by 200  $\mu\text{m}$ . The edges of the main slots were bevelled at a  $45^\circ$  angle sloping away from the trapping region. This created a geometry somewhat closer to the ideal of infinitely thin wire electrodes than if the edges were not bevelled. However, the main reason why the slots were bevelled was for optical access.

The alumina wafers were coated with gold to form conducting electrodes and to allow electrical connections to the “outside” world. A ceramic chip capacitor was spot-welded between ground and each static-potential electrode. These capacitors, along with 1 k $\Omega$  resistors, formed RC filters (see Fig. 2.6) which provided rf-grounding and electrical isolation between these electrodes and the outside world. The rest of the filters were placed on two additional alumina wafers which were attached to the sandwich structure with silver paint and glass-and-gold frit. Each of the two filter stages (Fig. 2.6) had a nominal roll-off frequency of  $\approx 200$  kHz.

It is relatively straightforward to estimate the strength of the  $z$ - direction (static) trapping field. To do this, consider the simplified geometry in Fig. 2.7(a). (This is a two-dimensional structure, rather than the true, three-dimensional sandwich structure of the trap, but will allow an estimate of the trap strength, nonetheless.) The potential due to this structure, in turn, is equivalent to the superposition of the potential due to the electrodes in Fig. 2.7(b) with that of its mirror image (up to the definition of zero potential). It is relatively straightforward [89] to write down the potential as:

$$\Phi(x, z) = \sum_{n=1}^{\infty} A_n \sinh\left[\frac{n\pi}{2L}(y + a/2)\right] \cos\left[\frac{n\pi z}{2L}\right] \quad (2.50)$$

Applying the boundary conditions indicated in Fig. 2.7(b), we find that

$$A_n = -\frac{4 U_0 \sin\left(\frac{n\pi d}{2L}\right)}{\pi \sinh\left(\frac{n\pi a}{L}\right)} \quad (2.51)$$

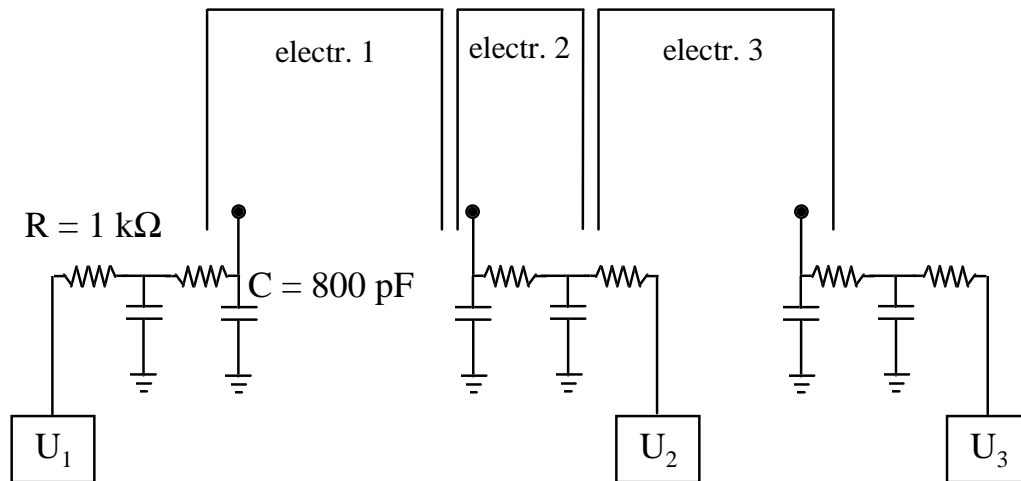


Figure 2.6: Connections of the DC voltages to the linear trap's static-potential electrodes (only three of the six electrodes are shown). The RC filters provided filtering of the DC lines as seen by the trap, while also shorting the electrodes to ground at radio frequencies. All the resistors were  $1\text{ k}\Omega$ , and all the capacitors were  $800\text{ pF}$ . The filters rolled off around  $200\text{ kHz}$ .  $U_1$ ,  $U_2$ , and  $U_3$  represent the voltage supplies for the electrodes.

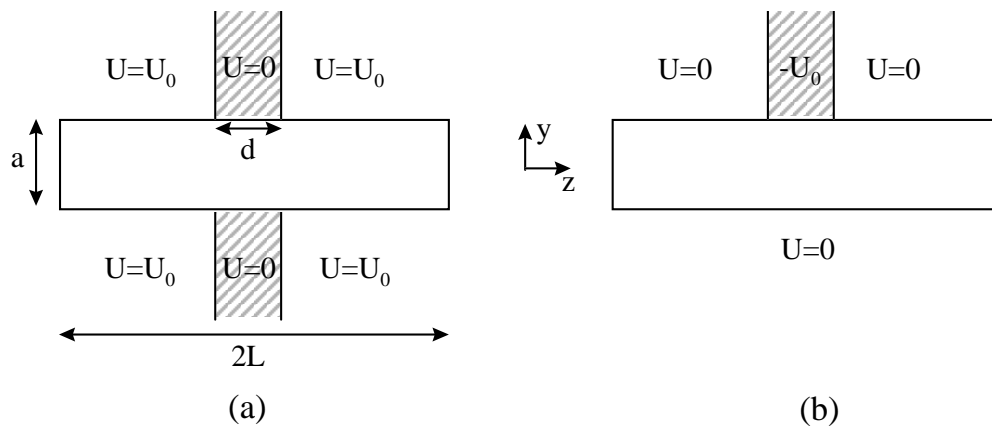


Figure 2.7: (a) Simplified electrode structure for two-dimensional estimate of the static-potential trapping frequency. (b) The potential created by this electrode structure, plus that due to its mirror image, is equivalent to the potential produced by the electrode structure of (a).

In particular, along the  $z$ -axis, we end up with

$$\Phi(0, z) = \sum_{n=1}^{\infty} \frac{4 U_0 \sin(\frac{n\pi d}{2L}) \sinh(\frac{n\pi a}{4L})}{\pi \sinh(\frac{n\pi a}{L})} \cos(\frac{n\pi z}{L}). \quad (2.52)$$

We get an extra factor of two from the contribution of the other “tongue.” Expanding the cosine term, we identify the quadratic term:

$$\Phi^{(2)}(0, z) = \sum_{n=1}^{\infty} \frac{U_0 \sin(\frac{n\pi d}{2L}) \sinh(\frac{n\pi a}{4L})}{\pi \sinh(\frac{n\pi a}{L})} \frac{4n^2 \pi^2}{L^2} x^2. \quad (2.53)$$

Taking into account the charge  $Q$  of the ion, and identifying with the harmonic oscillator potential  $\Phi(z) = -\frac{1}{2}m\omega^2 x^2$ , we see that

$$\left(\frac{\omega_z}{2\pi}\right)^2 = \frac{8U_0 Q}{mL^2} \sum_{n=1}^{\infty} \sin\left[\frac{n\pi d}{2L}\right] \frac{\sinh\left[\frac{n\pi a}{4L}\right]}{\sinh\left[\frac{n\pi a}{L}\right]} n^2. \quad (2.54)$$

The trigonometric and hyperbolic functions make it difficult to sum the series analytically, or even to check convergence. However, evaluating the expression numerically, we see that we would expect  $\frac{\omega_z}{2\pi} \approx 60$  MHz for  $U_0 = 30$  V, the usual operating voltage.

In the actual trap, a static voltage of 30 V gave a  $z$ -axis trap frequency of  $\frac{\omega_z}{2\pi} \approx 11.3$  MHz. This difference from the predictions of Eq. (2.54) was due to the differences between the actual trap geometry and the one assumed in deriving Eq. (2.54).

In operation, the micromachined linear trap was, as with the elliptical microtraps, placed at the antinode of a quarter-wave coaxial resonator (of essentially the same design as indicated above). A difference between the linear trap’s resonator structure and that of the other traps was that an alumina plug was placed inside the resonator during a rebuild of the vacuum system. This was done in order to lower the resonance frequency  $\Omega_T$  of the resonator, and thus raise the secular frequency (see Eq. (2.8)). Although stability requirements in the Paul trap require that  $\omega_m < \Omega_T/2$ , the secular frequency was limited by  $V_0$  due to vacuum rf discharge, and so this stability requirement was not a limiting factor. In this case, it made sense to *lower* the drive frequency, and thus the resonance frequency of the coaxial resonator had to be lowered with the dielectric filler.

Unfortunately, the quality factor of the resonator degraded during the re-processing of the system, and our rf amplifier was unable to put out enough power to compensate for this degradation. For this reason, no real net gain in secular frequencies was realized.

### 2.4.3 Vacuum System

In operation, the rf resonator structures, with the ion traps at their high-voltage end, were enclosed in quartz envelopes, which had (UV-transparent) optical-quality quartz windows fritted onto them (see Fig. 2.8). The vacuum assembly primarily consisted of standard 2 3/4" UHV conflat fittings, with some 3 3/8" fittings as well. Pumping was provided by a Varian StarCell ion pump, which had a 22 L/s pumping speed. Additional pumping (particularly for hydrogen gas) was provided by a titanium sublimation pump. The pump filament was housed in a 3 3/8" jacket. A photograph of a portion of the glass envelope, showing the trapping region of the coaxial resonator, is shown in Fig. 2.9.

The vacuum chamber, resonator, trap, and associated hardware were prepared for use with a "bake-out" to drive water vapour and hydrogen gas off of the various surfaces. In order to accomplish this bake, the entire assembly was enclosed in a custom-built oven (constructed from insulating bricks and heater filaments). After preliminary pumping with a turbo pump, the system was pumped into an external ion pump for several days, while the vacuum assembly was maintained at a temperature of approximately 350°C. During this time, the titanium sublimation pump was also fired off to clean its electrodes. The valve leading to the external ion pump was then closed, and the assembly was pumped with its internal ion pump for another few days at the same temperature. During the course of the trap's lifetime the titanium sublimation pump was turned on every few days to few weeks, in order to deposit a fresh layer of titanium on the vacuum sleeve.

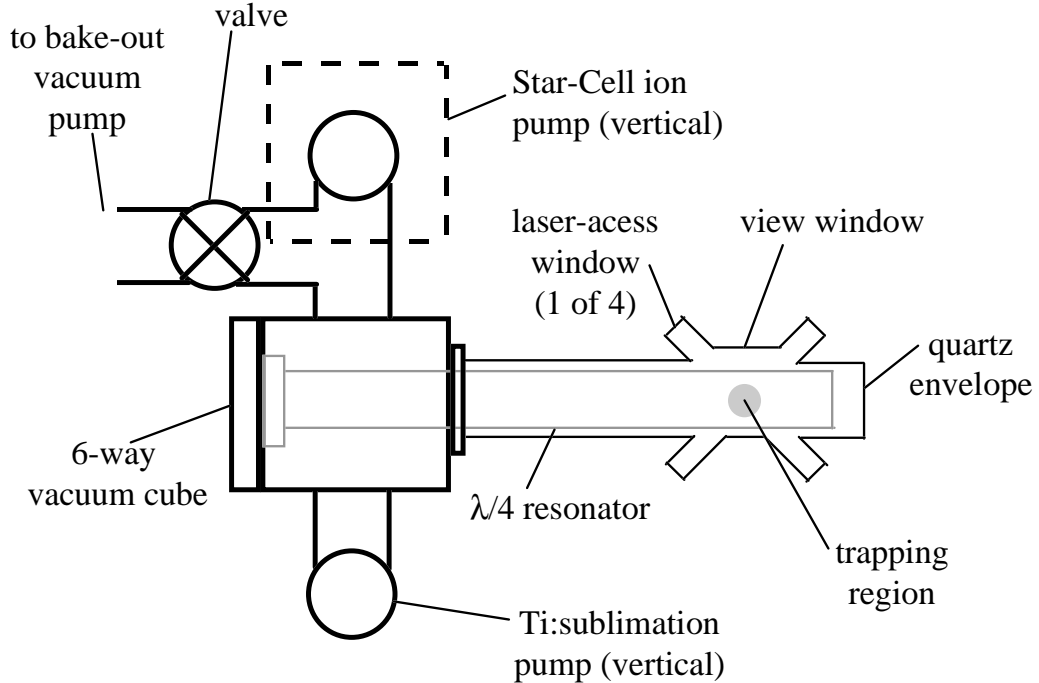


Figure 2.8: Schematic of the vacuum system enclosing the micromachined linear ion trap and its quarter-wave, coaxial resonator. The resonator was mounted to a vacuum blank which was mounted at the back of a six-way vacuum cube (all tubing and fittings were standard, 2 3/4" or 3 3/8" vacuum components). The quartz envelope was attached to a quartz-to-metal seal, which was fastened to the front of the vacuum cube. This design minimized the footprint of vacuum system. The titanium sublimation pump and the ion pump were mounted vertically for the same reason. The valve allowed the vacuum system to be hooked up to external roughing and ion pumps for use while baking the system out.

With Trap II and the micro-machined linear ion trap, the pressure was monitored with a Granville-Phillips ion gauge: the vacuum inside the envelope assembly was approximately 4 nPa.<sup>8</sup>

At these pressures, the collisions between the ion and background gas particles were infrequent. To obtain an upper limit on the collision rate, we may estimate the Langevin rate: this is the rate at which background neutral atoms penetrate the angular momentum barrier and spiral into a permanent or temporary orbit about the

<sup>8</sup> 1 Pa  $\approx$  7.5  $\times$  10<sup>-3</sup> torr. Thus, the background pressure was  $\approx$  3  $\times$  10<sup>-11</sup> torr

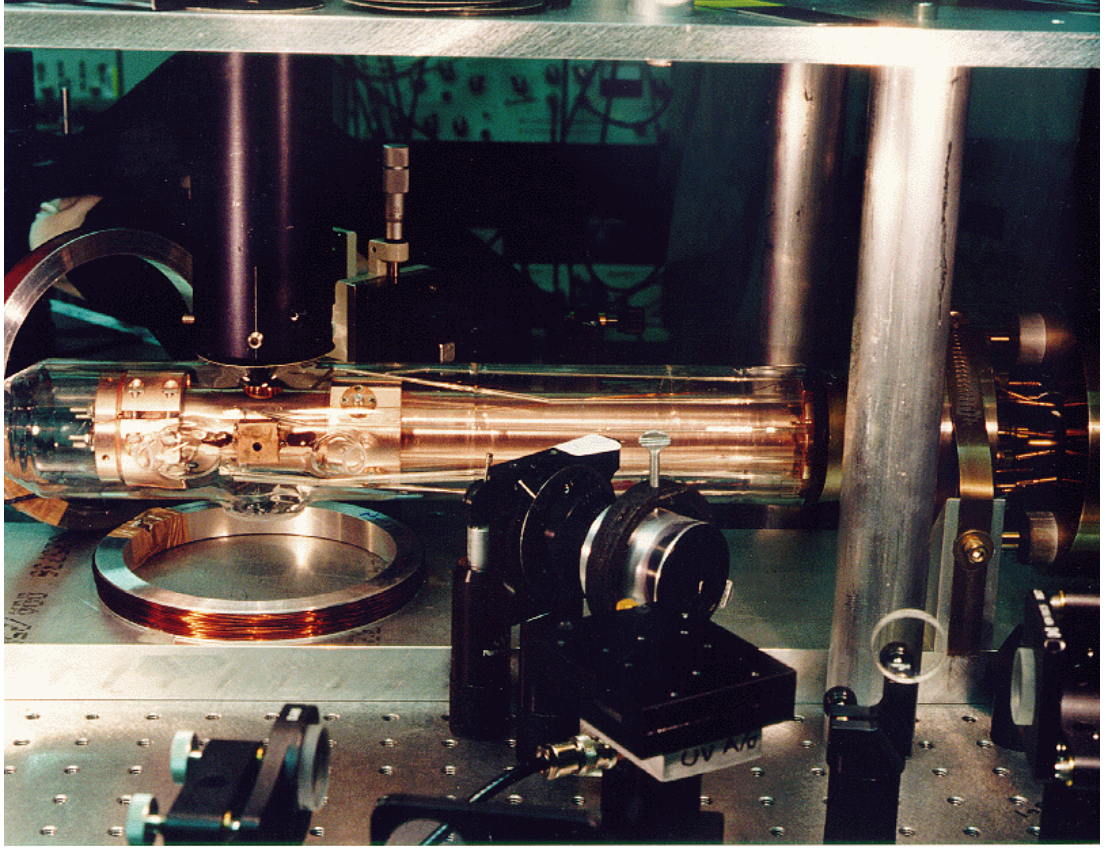


Figure 2.9: A photograph of a portion of the coaxial resonator and quartz envelope of Trap I, showing the trapping region. Several lens mounts are visible outside the quartz envelope.

ion [90]. In cases in which the ion's charge polarizes the electron cloud of the incoming neutral, the interaction potential is given by  $U(r) = -\alpha Q^2 / (8\pi\epsilon_0 r^4)$  (where  $\alpha$  is the atomic polarizability). Spiralling collisions result if the impact parameter,  $b$ , is less than some critical value:  $b_{crit} = (\alpha Q^2 / \pi\epsilon_0 \mu_{red} \nu^2)^{1/4}$ . Here,  $\mu_{red}$  is the reduced mass of the ion/neutral system, and  $\nu$  is the relative speed of the two particles (which, since the ion is laser-cooled, is just the speed of the room-temperature, background gas particle). The velocity-independent Langevin rate constant  $k_{Langevin} \equiv \sigma\nu = \pi b_{crit}^2 \nu$  leads to an overall reaction rate

$$\gamma_{Langevin} = \rho k_{Langevin} = \rho Q \sqrt{\frac{\pi\alpha}{\epsilon_0 \mu_{red}}}, \quad (2.55)$$

where  $\rho$  is the density of the background gas. In a metal/glass vacuum envelope such as those described herein, the dominant background gas constituent is usually  $\text{H}_2$ , for which  $k_{\text{Langevin}} = 1.64 \times 10^{-15} \text{ m}^3/\text{s}$  at room temperature. At a pressure of 5 nPa and a temperature of 300 K, this gives  $\gamma_{\text{Langevin}} \approx 0.002/\text{s}$ , or about one collision every ten minutes.

A more careful calculation, takes into account energy transfer during an “elastic” collision (i.e. one which does not change the electronic state of the ion or neutral). A conservative estimate for the heating rate may be derived using the total collision cross section. This is given by [73, 91]

$$\sigma_{el} = \pi \Gamma\left(\frac{1}{3}\right) \left[ \frac{\alpha Q^2}{16\epsilon_0 \hbar \nu} \right]^{2/3} \quad (2.56)$$

(where  $\Gamma$  is the gamma function). Averaging over a room-temperature thermal distribution of background  $\text{H}_2$  velocities [73], we obtain  $\gamma_{el} \approx 0.015/\text{s}$ , or approximately one collision per minute. This is much longer than the time required for a single experiment ( $\approx 1 \text{ ms}$ ), so that “elastic” heating collisions were negligible.

For inelastic collisions, the above rate must be multiplied by the probability of a chemical reaction occurring: this probability is much less than one. From our experience in the lab, such collisions occurred approximately once every ten hours: such inelastic collisions were the limiting factor in the trapped ions’ lifetime. For example, with  ${}^9\text{Be}^+$ , collisions with background hydrogen gas produced<sup>9</sup>  $\text{BeH}^+$ , which resulted in the effective loss of the ion. Thus, the ultra-high vacuum was a prerequisite for our experiments.

#### 2.4.4 Ion Source

Ions were created in the trapping region by producing a non-collimated “beam” of neutral beryllium atoms with an oven, and ionizing these atoms in the trapping region

---

<sup>9</sup> We could determine the identity of the molecule by the spectral shift of the normal modes of two trapped ions in the case in which one of them had undergone a chemical reaction

with an electron beam. The oven consisted of a coil of 25  $\mu\text{m}$  tungsten wire, with 12  $\mu\text{m}$  beryllium wire wrapped around it. The beryllium was wound so that it entirely covered the tungsten: this prevented the problem of the beryllium melting and flowing to some inconveniently located “hot spot” on the tungsten. The use of a heat gun while winding the beryllium wire made the beryllium more malleable and facilitated the process. Passing current through the tungsten wire heated it up and so heated up the beryllium, producing an effusive source. In practice, approximately 1 A of current was typically passed through the oven filament.

The electron beam was produced from a filament formed by either a coil of thoriated tungsten wire or a strip of thin tantalum ribbon. The filament was biased at -100 V, and the electrons were accelerated into the trapping region by passing through a hole in a grounded metal plate. Typically, 4 A of current were passed through the electron filament during loading. With this electron filament current and the above oven current, we loaded single ions a majority of the time.

The oven and the electron gun were mounted on the resonator structure, approximately 2.5 cm from the trapping region. Baffles were installed on the resonator structure to prevent the optical windows from being plated with beryllium. With the linear trap, a copper plate was placed between the ovens and the trap structure. Attached directly above the alumina wafers, this plate had a hole drilled in it to allow atoms to pass into the trapping region, and for optical access. The purpose of the plate was to prevent beryllium metal from the ovens from short-circuiting the trap structure.

## Chapter 3

### Atomic Structure of ${}^9\text{Be}^+$ and Interaction with Lasers

If the Paul trap (spherical or elliptical) is the stage for our experiments, then it is the interaction of the ion(s) with light which sets the action in motion. Of course, atoms interacting with radiation are nothing new, but what is different with the experiments described herein is the well-controlled coupling between the ion's electronic degree of freedom and its motional degrees of freedom. This interaction is mediated by the field gradients inherent in the laser beams.

In this chapter, I will discuss the atomic structure of the  ${}^9\text{Be}^+$  ion in sufficient detail to understand our experiments. I will then go on to describe the interaction of the trapped ion with laser beams, and explain how this interaction couples the ion's electronic and motional degrees of freedom. In particular, I will focus in on two particular electronic levels, which I will describe in detail below. Note that the formalism used herein to describe the electronic degree of freedom relies heavily on the formal equivalence of a two-level system to a spin-1/2 particle. Indeed, I will use the terms "electronic degree of freedom" and "spin" interchangeably. For more on this topic, the reader is referred to Ref. [2].

The idea, then, is that our system presents us with two, basic quantum systems: the two-level system (formally equivalent to a spin-1/2 particle), and the quantum harmonic oscillator. Although these are two of the best-understood quantum systems, the coupling between them provides a wealth of interesting behaviour. A similar coupling,

and a similar wealth of behaviour, is found in cavity-QED systems [92], although there are differences between that system and the one described in this thesis.

### 3.1 Energy Levels of ${}^9\text{Be}^+$ and Single-Photon Transitions

Fig. 3.1 shows a simplified energy-level diagram for  ${}^9\text{Be}^+$ . The two-level system which is of interest to us is formed by two ground-state hyperfine levels: the  $2s\ {}^2S_{1/2}|F = 2, m_F = -2\rangle$  and  $2s\ {}^2S_{1/2}|F = 1, m_F = -1\rangle$  states, abbreviated by  $|\downarrow\rangle$  and  $|\uparrow\rangle$ , respectively.<sup>1</sup> These levels are separated by their hyperfine splitting. While running the experiment, we added a magnetic field of  $\approx 8$  Gauss, which further split the different  $m_F$  sub-levels of the  $F = 2$  and  $F = 1$  hyperfine levels, by  $\Delta E = g_F m_F \mu_B B$ . (Here,  $\mu_B \approx 1.4$  MHz/Gauss is the Bohr magneton,  $g_1 = -\frac{1}{2}$  and  $g_2 = +\frac{1}{2}$  are the Landé  $g$ -factors, and  $B$  is the magnitude of the magnetic field. The quantization axis determined by this magnetic field lay in the direction<sup>2</sup>  $-\frac{1}{\sqrt{2}}\mathbf{e}_x + \frac{1}{2}(\mathbf{e}_y - \mathbf{e}_z)$ . (Ambient magnetic fields such as that due to the Earth were nulled out using shim coils.) If we denote the total splitting of  $|\uparrow\rangle$  and  $|\downarrow\rangle$  by  $\omega_0$  then, in the course of the experiments, we had  $\omega_0/2\pi \approx 1.26$  GHz.

The  $2p\ {}^2P_{1/2}$  and  $2p\ {}^2P_{3/2}$  excited states are separated from the  $2s$  ground state by 313 nm. The fine-structure splitting between the  $2p$  levels is  $\approx 197$  GHz. The  ${}^2P_{1/2}$  hyperfine splitting is  $\approx 237$  MHz, and the  ${}^2P_{3/2}$  hyperfine splitting is less than 1 MHz. The natural linewidth of these states is  $\approx 19.4$  MHz.

When the ion is trapped in a strong harmonic potential, such as produced (in the pseudopotential approximation) by the ion trap, each of the electronic states is “dressed” with an associated “ladder” of motional eigenstates. In the diagram, I have only shown these motional states for  $|\downarrow\rangle$  and  $|\uparrow\rangle$ . In addition, for clarity and simplicity, I have

<sup>1</sup> Upon occasion, we used the  $2s\ {}^2S_{1/2}|F = 2, m_F = 2\rangle$  and  $|F = 1, m_F = 1\rangle$  states for the two level system. Aside from a slightly different energy separation between  $|\downarrow\rangle$  and  $|\uparrow\rangle$ , this had no significant effect upon the physics

<sup>2</sup> Note that, in this Chapter, I shall use the coordinate convention that the  $z$ -axis lies along the axis of symmetry of the coaxial resonator. The  $x$ - and  $y$ -axes lie along the other two principal directions of the trap. This is the convention used with the micromachined linear trap.

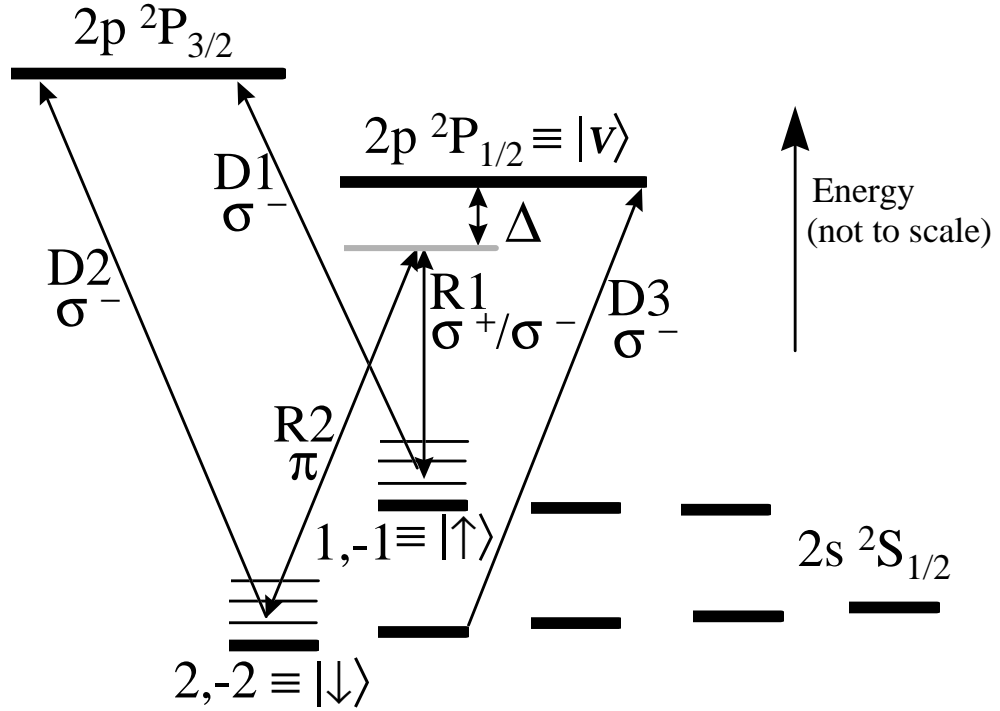


Figure 3.1: Simplified energy level diagram for  ${}^9\text{Be}^+$ , with energy increasing towards the top of the diagram (not to scale). The two levels of interest are the  $|F = 2, m_F = -2\rangle$  and  $|F = 1, m_F = -1\rangle$  hyperfine sub-levels (denoted  $|\downarrow\rangle$  and  $|\uparrow\rangle$ ) of the  $2s\ {}^2S_{1/2}$  ground state. The motional energy levels, spaced by  $\approx 10$  MHz, are indicated for these two states but are omitted for clarity in the other states. Single-photon transitions are driven by beams D1 and D2 to the  $2p\ {}^2P_{3/2}$  level (radiative linewidth  $\gamma/2\pi \approx 19.4$  MHz), and  $|\downarrow\rangle$  and  $|\uparrow\rangle$  are coupled through the  $2p\ {}^2P_{1/2}$  level using two-photon, stimulated Raman transitions driven by beams R1 and R2 ( $\Delta/2\pi \approx 40$  GHz). Beam D3 clears population out of the  $2s\ {}^2S_{1/2}|F = 2, m_F = -1\rangle$  level. These optical transitions correspond to a laser wavelength of 313 nm. For further details, see Ch. 3. The  ${}^2S_{1/2}$  hyperfine splitting is  $\omega_0/2\pi \approx 1.25$  GHz, the  ${}^2P$  fine-structure splitting is  $\approx 197$  GHz, the  ${}^2P_{1/2}$  hyperfine splitting is  $\approx 237$  MHz, and the  ${}^2P_{3/2}$  hyperfine structure ( $< 1$  MHz) is unresolved. The Zeeman splitting between adjacent  $m_F$  levels is  $\approx 0.7$  MHz/Gauss. Under typical operating conditions, the Zeeman contribution to the  $|\downarrow\rangle - |\uparrow\rangle$  splitting was about 12 MHz.

indicated only the motional eigenstates associated with a single direction  $m$  ( $m = x, y,$  or  $z$ ). These states are spaced by energy  $\hbar\omega_m$ .

One may use an ultraviolet laser beam with  $\lambda \approx 313$  nm to couple either  $|\uparrow\rangle$  or  $|\downarrow\rangle$  to the  $2p^2P_{3/2}$  excited electronic state. In particular, the transition  $|\downarrow\rangle \rightarrow |2p^2P_{1/2}, F = 3, m_F = -3\rangle$  is a cycling transition (driven by laser beam D2). Thus, if the atom is in  $|\downarrow\rangle$  and the laser light is polarized  $\sigma^+$ , then the atom repeatedly cycles between this state and the excited state  $|F = 3, m_F = -3\rangle$ , spontaneously emitting a photon each time. It repeats this cycle until slight imperfections in the laser polarization cause transitions to a different excited state, from which the atom can decay to a different ground-state level where the laser is off-resonant. Thus, this transition allows determination of whether the ion is in the state  $|\downarrow\rangle$  (and, by inference,  $|\uparrow\rangle$ ) with almost unit quantum efficiency [56, 57, 58].

On the other hand, the transition  $|\uparrow\rangle \rightarrow |2p^2P_{1/2}, F = 3, m_F = -2\rangle$ , which is driven by beam D1, is not a cycling transition. From the excited state, the atom can decay back to  $|\uparrow\rangle$ , to  $|\downarrow\rangle$ , or to the  $|2s^2S_{1/2}, F = 2, m_F = -1\rangle$  state. In the latter case, we have to re-pump the atom back into the two-level system. In practice, we did this with laser beam D3, resonant with the  $|2s^2S_{1/2}, F = 2, m_F = -1\rangle \rightarrow |2p^2P_{1/2}, F = 2, m_F = -2\rangle$  transition, which optically pumped the ion back into the  $|\uparrow\rangle/|\downarrow\rangle$  manifold. When D2 and D3 were turned on together, the ion was optically pumped into  $|\downarrow\rangle$ . This optical pumping was used to initialize the spin state of the ion at the beginning of each experiment.

Returning to state detection with the cycling transition, Fig. 3.2 shows histograms of the number of photon counts measured per experiment with the ion in  $|\downarrow\rangle$  and in  $|\uparrow\rangle$ .<sup>3</sup> In practice, several factors limited the quantum efficiency of spin detection. Since the hyperfine splitting in the  $2p^2P_{3/2}$  level is negligible, the efficiency of the cycling transition is, in part, determined by the degree to which beam D2 is pure  $\sigma^+$ .

---

<sup>3</sup>  $|\uparrow\rangle$  is prepared from  $|\downarrow\rangle$  using a  $\pi$ -pulse Raman transition (see next Section)

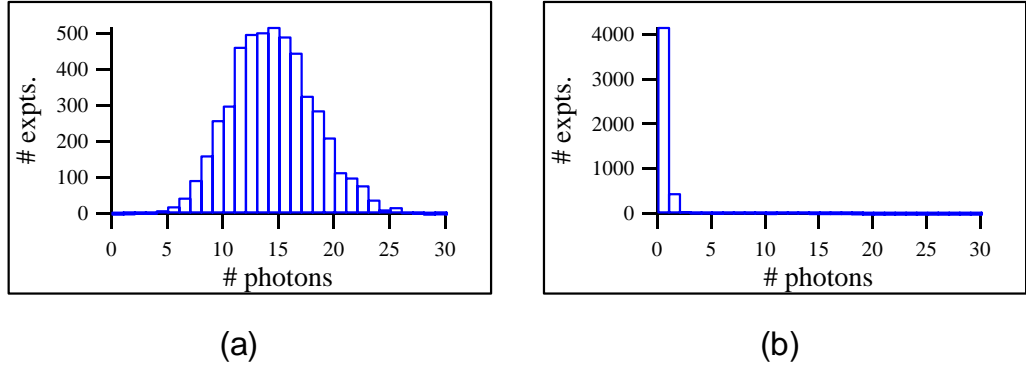


Figure 3.2: (a) Photon number histogram on the cycling transition when the ion starts out in the state  $|\downarrow\rangle$ . (b) Photon number histogram for the state  $|\uparrow\rangle$ . The counts in channels one and two are due to background and to off-resonant pumping out of  $|\uparrow\rangle$  by the cycling transition beam (see Appendix A).

The quantum efficiency of the  $|\uparrow\rangle/|\downarrow\rangle$  determination is also fundamentally limited by the atomic physics of  ${}^9\text{Be}^+$ : since the ground-state hyperfine splitting is only about 60 times the excited state linewidth, spontaneous emission after off-resonant transitions from  $|\uparrow\rangle$  to the excited state can transfer population from  $|\uparrow\rangle$  into the cycling transition. For a given effective quantum efficiency of the photodetection system (solid angle and photodetection quantum efficiency), this places a limit on the quantum efficiency of  $|\uparrow\rangle/|\downarrow\rangle$  discrimination. For our typical operating conditions, this discrimination quantum efficiency was 96-98%. For a more complete discussion of this effect, and a discussion of other uses of the photon number histograms, see Appendix A.

### 3.2 Coupling Spin and Motion

Single-photon transitions are thus useful for optical pumping and for detecting which of the states ( $|\downarrow\rangle$  or  $|\uparrow\rangle$ ) the atom is in. However, we still need a way to couple the ion's electronic levels *coherently* to its motion if we wish to produce quantum entanglement between the spin and motion, or to use entangle the spins of separate ions using their collective motion as an intermediary. Such a coupling must be spectrally

narrow enough to resolve different states of ionic motion. Furthermore, in order to couple the ion's electronic state with its motion, we require strong field gradients.

To see how this coupling occurs, first consider the Hamiltonian of a single, trapped ion interacting with an applied electric field in the case when two of its levels (which I will denote  $\downarrow$  and  $\uparrow$ ) have an allowed electric dipole transition between them:<sup>4</sup>

$$\hat{H} = \hat{H}_{\uparrow\downarrow} + \hat{H}_{HO} + \hat{H}_{int}. \quad (3.1)$$

Here,  $\hat{H}_{\uparrow\downarrow} = \frac{1}{2}\hbar\omega_0\hat{\sigma}_3$  is the free Hamiltonian for the two-level system  $\{|\uparrow\rangle, |\downarrow\rangle\}$  and, in the usual spin- $\frac{1}{2}$  formalism,  $\hat{\sigma}_3$  is the Pauli spin operator.<sup>5</sup>  $\hat{H}_{HO} = \hbar\hat{\mathbf{n}} \cdot \boldsymbol{\omega}$  is the Hamiltonian for motion along the  $x$ -direction, with  $\hat{\mathbf{n}} = (\hat{n}_x, \hat{n}_y, \hat{n}_z)$ , ( $\hat{n}_m$  being the number operator for direction  $m$ ),  $\boldsymbol{\omega} = (\omega_x, \omega_y, \omega_z)$ , and the zero-point energy suppressed.

Finally,

$$\hat{H}_{int} = -\hat{\boldsymbol{\mu}} \cdot \mathbf{E}(\hat{\mathbf{x}}, t) \quad (3.2)$$

expresses the interaction between the ion and the laser beams, in the electric-dipole approximation [93]. In Eq. 3.2,  $\hat{\boldsymbol{\mu}} = e\mathbf{r}_{el}$  is the electric dipole moment of the atom (with  $\mathbf{r}_{el}$  the electron-nucleus relative position operator) and  $\hat{\mathbf{x}}$  is the position operator for the ion's centre- of-mass. This dependence of  $\hat{H}_{int}$  on the ion's position gives the desired coupling between the ion's motional and spin degrees of freedom. For example, suppose that  $\mathbf{E} = E(\hat{z}, t)\mathbf{e}_x$  (where  $\mathbf{e}_x$  is the unit vector in the  $x$ -direction). If we expand the electric field in a power series, we have that

$$\hat{H}_{int} = -\hat{\mu}_x \left[ E(z=0, t) + \frac{\partial E}{\partial z} \Big|_{z=0} \hat{z} + \frac{\partial^2 E}{\partial z^2} \Big|_{z=0} \hat{z}^2 + \dots \right]. \quad (3.3)$$

The key term in Eq. (3.3) is the gradient term. Suppose, for instance, that the electric field were constant in time, but spatially non-uniform. Since the ion is oscillating in

<sup>4</sup> The  ${}^9\text{Be}^+$  ground state hyperfine levels which I identified as  $\downarrow$  and  $\uparrow$  above do not have such a transition. However, they may be coupled by two-photon, stimulated Raman transitions, which I will discuss in Sec. 3.3.

<sup>5</sup> Another notation for the Pauli operators uses  $\hat{\sigma}_x \equiv \hat{\sigma}_1$ ,  $\hat{\sigma}_y \equiv \hat{\sigma}_2$ , and  $\hat{\sigma}_z \equiv \hat{\sigma}_3$ . However, to avoid confusion with the motional operators, I will use the present notation. The Pauli operators act in the Hilbert space of the ion's spin degree of freedom.

the  $z$ -direction, it experiences a modulation of  $\mathbf{E}$  at the ion's oscillation frequency (in the rest frame of the ion). So, if the oscillation frequency were equal to the atomic transition frequency  $\omega_0$ , the static field could still cause transitions between electronic levels.

In practice, time-dependent fields are used to drive transitions. However, the idea remains the same: field gradients couple the spin and motion and drive transitions. To flesh this out a bit, consider the one-dimensional case of a single ion constrained to move only in the  $z$ -direction, interacting with an electric field  $\mathbf{E}(z, t) = E_0 \mathbf{e}_x \cos(kz - \omega_L t + \phi)$ . For the following derivation, I shall assume that the laser linewidth is much less than the motional frequency, so that the different motional sidebands are spectrally resolved. This is the so-called “resolved-sideband” regime.

The interaction Hamiltonian for such a situation is given by

$$\hat{H}_{int} = \hbar\Omega(\hat{S}_+ + \hat{S}_-)(e^{i(k\hat{z} - \omega_L t + \phi)} + e^{-i(k\hat{z} - \omega_L t + \phi)}), \quad (3.4)$$

where  $\hat{\Omega} \doteq -\hat{\mu}E_0/2$  is the Rabi frequency, giving the interaction strength between the ion and the field, and  $\hat{S}_\pm = \hbar(\hat{\sigma}_1 \pm i\hat{\sigma}_2)/2$  are the atomic raising and lowering operators which indicate the effect of the interaction on the atomic levels  $|\downarrow\rangle$  and  $|\uparrow\rangle$ . Now let us go into an interaction picture defined by  $\hat{H}_0 = \hat{H}_{\uparrow\downarrow} + \hat{H}_{HO}$  and  $\hat{V}_{interaction} = \hat{H}_{int}$ . Then

$$\begin{aligned} \hat{H}'_{int} &= \hbar\Omega(\hat{S}_+ e^{i\omega_0 t} + \hat{S}_- e^{-i\omega_0 t}) \left[ \exp(i[\eta(\hat{a}e^{-i\omega_z t} + \hat{a}^\dagger e^{i\omega_z t})]) e^{-i(\omega_L t + \phi)} \right. \\ &\quad \left. + \exp(-i[\eta(\hat{a}e^{-i\omega_z t} + \hat{a}^\dagger e^{i\omega_z t})]) e^{i(\omega_L t - \phi)} \right]. \end{aligned} \quad (3.5)$$

In this last equation, I have expressed  $\hat{z} = z_0(\hat{a} + \hat{a}^\dagger)$ , where  $z_0 = \sqrt{\frac{\hbar}{2m\omega_z}}$  is the spread of the ground state harmonic oscillator wave function ( $\psi_0(z) = (\frac{m\omega_z}{\pi\hbar})^{1/4} \exp[-m\omega_z z^2/2\hbar]$ ), and then defined the Lamb-Dicke parameter:  $\eta \doteq k_z z_0$ .

Now, I will make the “rotating wave” approximation: assuming that  $\omega_L \approx \omega_0$ , I will drop terms which have an exponent oscillating at optical frequencies. The idea

behind this is that such terms will average to zero on the long (compared to optical time scales) time scales of interest to us.<sup>6</sup> Defining the detuning  $\delta = \omega_L - \omega_0$  of the laser from resonance, we have:

$$\hat{H}'_{int} = \hbar\Omega \left[ S_+ \exp \left( i\eta (a_z^\dagger e^{i\omega_z t} + a_z e^{-i\omega_z t}) - i\delta t + i\phi \right) \right] + H.C. \quad (3.6)$$

We may expand the first term in the exponential in Eq. 3.6 in a power series in  $\eta$  to obtain

$$\hat{H}'_{int} = \hbar\Omega \left[ S_+ \sum_{k=0}^{\infty} \frac{(i\eta)^k (a_z^\dagger e^{i\omega_z t} + a_z e^{-i\omega_z t})^k}{k!} \right] e^{-i(\delta t - \phi)} + H.C. \quad (3.7)$$

At this point, if we make one final rotating-wave approximation, it may be apparent that the detuning  $\delta$  picks out different powers of  $a$ ,  $a^\dagger$ : that is, depending on  $\delta$ , different motional levels are coupled together.

Going back to the general expression, Eq. (3.7), we can put  $\hat{H}'_{int}$  into the Schrödinger equation for the interaction-picture state vector. Since I will assume that we are close to one of the resonances implicit in Eq. (3.6), let  $\delta = (n - m)\omega_z + \epsilon$ , where  $|\epsilon| \ll \omega_z, \Omega$  and  $n, m$  are the indices of the motional levels coupled by the resonance. Representing  $|\Psi\rangle = \sum_{\{j=\uparrow, \downarrow\}} \sum_n C'_{j,n}(t) |j, n\rangle$ , we obtain:

$$\dot{C}'_{\uparrow, n} = -i^{(1+|n-m|)} e^{-i(\epsilon t - \phi)} \Omega_{n,m} C'_{\downarrow, m} \quad (3.8)$$

$$\dot{C}'_{\downarrow, m} = -i^{(1-|n-m|)} e^{i(\epsilon t - \phi)} \Omega_{n,m} C'_{\uparrow, n}. \quad (3.9)$$

In these equations,

$$\Omega_{n,m} = \Omega \langle n | e^{i\eta(\hat{a}_z + \hat{a}_z^\dagger)} | m \rangle \quad (3.10)$$

is the Rabi frequency for the coupling between levels  $|\uparrow, n\rangle$  and  $|\downarrow, m\rangle$ . Another way to express  $\Omega_{n,m}$  is:

$$\Omega_{n,m} = \Omega \langle n | \hat{D}(i\eta) | m \rangle, \quad (3.11)$$

---

<sup>6</sup> Note that these terms have very large energy denominators in a perturbative expansion and, thus, are indeed negligible

where  $\hat{D}(\alpha) = e^{\alpha\hat{a}^\dagger - \alpha^*\hat{a}}$  is the displacement operator [94]. We may evaluate the expectation value in Eq. (3.27) to obtain:

$$\Omega_{n,m} = \Omega e^{-\eta^2/2} \sqrt{\frac{n_{<}!}{n_{>}!}} \eta^{|m-n|} L_{n_{<}}^{|m-n|}(\eta^2), \quad (3.12)$$

where  $L_n^m$  is an associated Laguerre polynomial [72, 94]. In the Lamb-Dicke limit,  $\eta \ll 1$ , this expression simplifies considerably and, for example, we have that  $\Omega_{n,n-1} = \eta\Omega\sqrt{n}$ , and that  $\Omega_{n,n+1} = \eta\Omega\sqrt{n+1}$ .

The dynamics described by Eq. (3.9) exhibit Rabi oscillations between  $|\uparrow, n\rangle$  and  $|\downarrow, m\rangle$ . In particular, if we express  $|\Psi\rangle$  as a column vector,  $|\Psi\rangle \equiv \begin{bmatrix} C_{\uparrow,n} \\ C_{\downarrow,m} \end{bmatrix}$ , then we have

$$\begin{aligned} |\Psi(t)\rangle = & \\ & \begin{bmatrix} e^{-i\epsilon t/2} [\cos(\frac{X_{n,m}t}{2}) + i\frac{\epsilon}{X_{n,m}} \sin(\frac{X_{n,m}t}{2})] & -2i\frac{\Omega_{n,m}}{X_{n,m}} e^{-i(\epsilon t - 2\phi - \pi|m-n|)/2} \sin(\frac{X_{n,m}t}{2}) \\ -2i\frac{\Omega_{n,m}}{X_{n,m}} e^{i(\epsilon t - 2\phi - \pi|m-n|)/2} \sin(\frac{X_{n,m}t}{2}) & e^{i\epsilon t/2} [\cos(\frac{X_{n,m}t}{2}) - i\frac{\epsilon}{X_{n,m}} \sin(\frac{X_{n,m}t}{2})] \end{bmatrix} \\ & \times |\Psi(0)\rangle, \end{aligned} \quad (3.13)$$

where  $X_{n,m} = \sqrt{\epsilon^2 + 4\Omega_{n,m}^2}$ . On resonance,  $\epsilon = 0$ , Eq. (3.13) simplifies to:

$$|\Psi(t)\rangle = \begin{bmatrix} \cos(\Omega_{n,m}t) & -ie^{i(\phi+\pi|m-n|/2)} \sin(\Omega_{n,m}t) \\ -ie^{-i(\phi+\pi|m-n|/2)} \sin(\Omega_{n,m}t) & \cos(\Omega_{n,m}t) \end{bmatrix} |\Psi(0)\rangle, \quad (3.14)$$

which indicates sinusoidal oscillations between  $|\downarrow, n\rangle$  and  $|\uparrow, m\rangle$ .

To put all this on a more physical footing, suppose that we prepare the atom in  $|\downarrow\rangle$  through optical pumping and turn on the laser interaction for some time  $t_{pr}$ , then measure the occupation of the state  $|\downarrow\rangle$  through the cycling transition. If we repeat this process for various relative detunings  $\delta$  of the laser, we build up a spectrum of the form shown in Fig. 3.3.

The central feature in Fig. 3.3 is the so-called ‘‘carrier’’ transition at  $\delta = 0$ . This transition couples the levels  $|\downarrow, n\rangle \leftrightarrow |\uparrow, n\rangle$ ; that is, it flips the spin but leaves the ion’s motional state unaffected. If we sit on resonance,  $\delta = 0$ , and apply the interaction for time  $t_{pr}$ , then the probability  $P_{\downarrow}$  is (in the Lamb-Dicke limit) given by

$$P_{\downarrow}(t_{pr}) = \cos^2(\Omega t_{pr}). \quad (3.15)$$

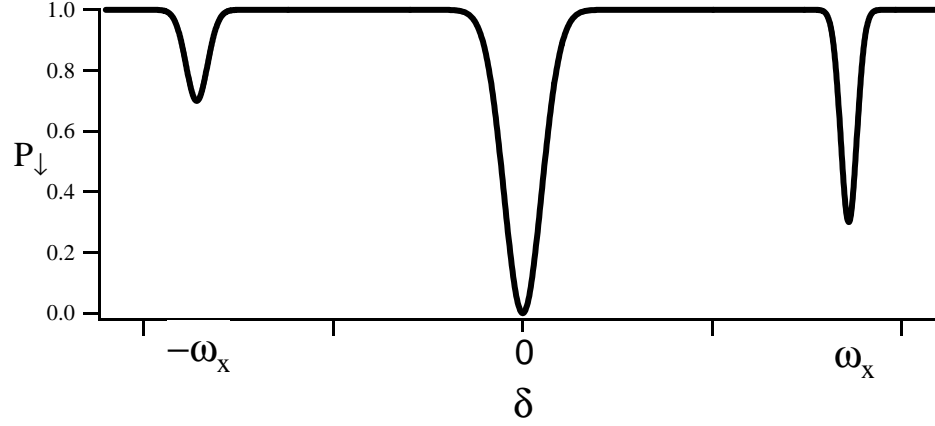


Figure 3.3: Representation of the spectrum swept out when the Raman laser beam difference frequency  $\delta + \omega_0$  is swept, holding the length of the probe pulse constant ( $\Omega t_{pr} = \pi/2$ ). The signal we measure is proportional to the probability that the ion remains in  $|\downarrow\rangle$  after the probe pulse. The feature at  $\delta = 0$  is the carrier, which flips the ion spin but does not affect the motion. The upper motional (or “blue”) sideband, at  $\delta = +\omega_x$  couples the levels  $|\downarrow, n\rangle \leftrightarrow |\uparrow, n+1\rangle$ . The lower (or “red”) sideband, at  $\delta = -\omega_x$  couples  $|\downarrow, n\rangle \leftrightarrow |\uparrow, n-1\rangle$ , and vanishes if the ion starts out in  $|\downarrow, n=0\rangle$ .

This sort of behaviour is indicated by the “Rabi flopping curve” in Fig. 3.4(a). In the usual nomenclature, a pulse for which  $\Omega t_{pr} = \pi/2$ , and thus for which the population is inverted (since  $P_{\downarrow}$  oscillates at  $2\Omega$ ) is referred to as a “ $\pi$  pulse.” One for which  $\Omega t_{pr} = \pi$  is referred to as a “ $2\pi$  pulse,” and so on.

The feature at  $\delta = +\omega_x$  in Fig. 3.3 is the first upper motional (or “blue”) sideband, which couples the levels  $|\downarrow, n\rangle \leftrightarrow |\uparrow, n+1\rangle$ . In this case, the ion undergoes Rabi flopping between these two levels with Rabi frequency  $\Omega_{n,n+1}$ . In the Lamb-Dicke regime  $\Omega_{n,n+1} = \eta\Omega\sqrt{n+1}$ . However, outside the Lamb-Dicke regime contributions to the Rabi frequency from higher-order terms in the sum of Eq. (3.7) with equal powers of  $a$  and  $a^\dagger$  also contribute to the Rabi frequency, and we must use the general expression,

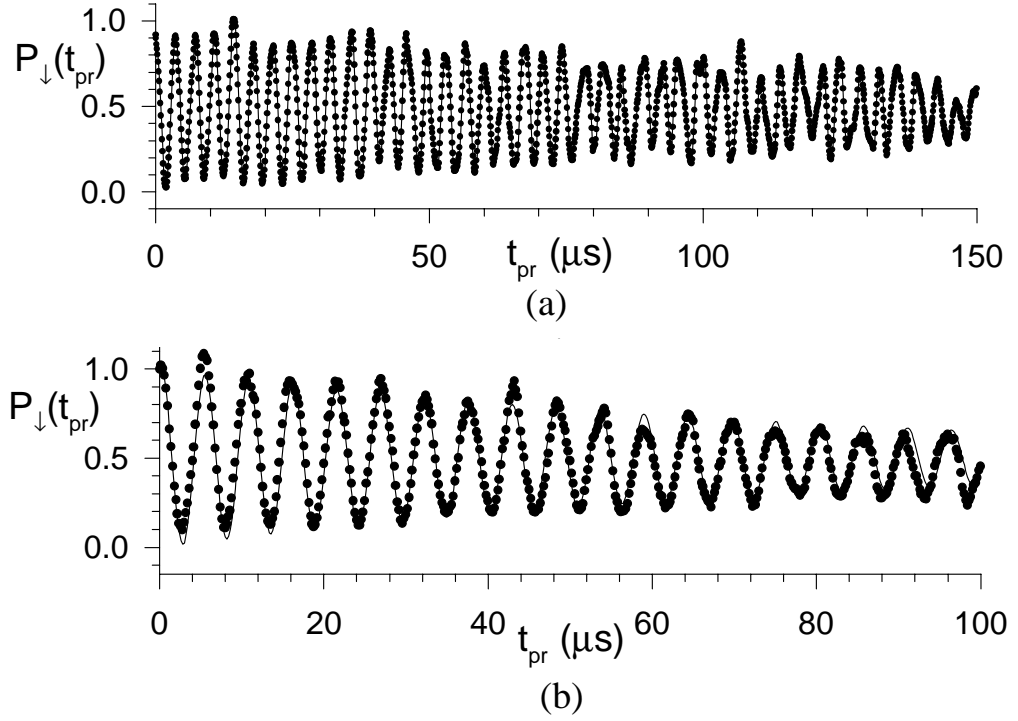


Figure 3.4: (a) “Rabi flopping curve” showing the ground-state occupation probability  $P_{\downarrow}(t_{pr})$  for the carrier transition:  $\delta = 0$  (see Eq. 3.15). Each point represents an average of  $\approx 4000$  measurements, or 1 s of integration. The slow decay of the envelope is mostly due to technical noise, with small contributions due to background heating of the ion’s motion (which affects the single-photon carrier Rabi frequency at order  $\eta^2$ ). (b) Ground state occupation probability  $P_{\downarrow}(t_{pr})$  for the first upper (“blue”) sideband:  $\delta = +\omega_x$ , starting in the ground state. The envelope decay is due to both technical noise and some background heating of the ion’s motion.

Eq. (3.12). A typical upper (“blue”) sideband Rabi flopping curve for a harmonic-oscillator motional eigenstate is shown in Fig. 3.4(b).

Finally, the feature at  $\delta = -\omega_z$  in Fig. 3.3 is the first lower (or “red”) sideband, coupling  $|\downarrow, n\rangle \leftrightarrow |\uparrow, n-1\rangle$ . Thus, if the ion starts out in the motional state  $|\downarrow, n=0\rangle$ , this feature vanishes (since there is no lower vibrational state with which to couple). The Rabi frequency on the lower sideband is  $\Omega_{n,n-1} = \Omega\eta\sqrt{\frac{1}{n}}e^{-\eta^2/2}L_{n-1}^1(\eta^2)$  (or  $\Omega_{n,n-1} = 0$  if the ion is in its ground state), which, in the Lamb-Dicke regime, reduces to  $\Omega_{n,n-1} =$

$\eta\sqrt{n}\Omega$ . In this regime, the interaction Hamiltonian for the trapped ion interacting with the laser beam is formally equivalent to the Hamiltonian of Cavity-QED [92].

It is worth noting that one can treat the interaction between the lasers and the ion's complete motion (including the micromotion) in a completely quantum-mechanical manner [70]. However, such a treatment does not alter any of the results significantly. Although this treatment does show that one can perform, for example, laser cooling on rf-sidebands (i.e. sidebands induced by the ion's micromotion), we shall see in Sec. 6.4.1, we can predict much of the relevant behaviour by treating the micromotion as classical, as indicated in Ch. 2.

### 3.3 Two-Photon, Stimulated-Raman Transitions

Rather than use single-photon transitions to couple  $|\downarrow\rangle$  ( $|F = 2, m_F = -2\rangle$ ) and  $|\uparrow\rangle$  ( $|F = 1, m_F = -1\rangle$ ) in our experiment, we use two-photon, stimulated Raman transitions. That is, we apply two laser beams with  $\Delta\omega_L = \omega_{L1} - \omega_{L2} = \omega_0 + \delta$  and  $\Delta\mathbf{k} = \mathbf{k}_1 - \mathbf{k}_2$ . Each laser beam is detuned by  $\Delta_R$  from resonance with the  $2p^2P_{1/2}$  level. The result is that transitions are driven from  $|\downarrow\rangle$  to  $|\uparrow\rangle$ , with the  $2p^2P_{1/2}$  level serving as a “virtual level” (which I will refer to as  $|v\rangle$ ). The difference frequency between the two Raman beams is determined by a radio frequency, with its associated low level of frequency jitter. At the same time, by choosing  $\Delta\mathbf{k}$  judiciously, we have the high field gradients (e.g.  $\frac{\partial\mathbf{E}}{\partial z} \propto k_z\mathbf{E}$ ) associated with optical wavelengths. Using Raman transitions also allows us to be selective in coupling the spin and the motion. In general, these transitions are sensitive to motion in all three principal trap directions. But, for example, if  $\Delta\mathbf{k} \parallel \mathbf{e}_z$ , we are only sensitive to motion in the  $z$ -direction, and if  $\Delta\mathbf{k} \approx 0$ , we are highly insensitive to motion.

To quantify the situation, let  $\mathbf{E}_1(\mathbf{x}, t) = \epsilon_1 E_1 \cos(\mathbf{k}_1 \cdot \mathbf{r} - \omega_{L1}t + \phi_1)$  and  $\mathbf{E}_2(\mathbf{x}, t) = \epsilon_2 E_2 \cos(\mathbf{k}_2 \cdot \mathbf{r} - \omega_{L2}t + \phi_2)$  (where  $\epsilon_j$  gives the polarization of the  $j^{\text{th}}$  laser). Then the

interaction Hamiltonian may be written as:

$$H_{int} = -\hbar \left[ \hat{g}_1^\dagger e^{i\mathbf{k}_1 \cdot \hat{\mathbf{x}}} e^{i\omega_{L1}t} + \hat{g}_2^\dagger e^{i\mathbf{k}_2 \cdot \hat{\mathbf{x}}} e^{i\omega_{L2}t} + H.C. \right], \quad (3.16)$$

where  $\hat{g}_i = E_i e^{-i\phi_i} \boldsymbol{\epsilon}_i \cdot \hat{\mathbf{x}} / 2\hbar$  ( $i = 1, 2$ ) and  $e$  is the charge of the electron.

Let  $C_{j,\mathbf{n}} = \langle j, \mathbf{n} | \psi \rangle$ , where  $j \in \{\uparrow, \downarrow, v\}$  and  $|\psi\rangle$  is the state of the system. If we go into an interaction picture defined by  $\hat{H}_0 = \hat{H}_{elec} + \hat{H}_{HO}$  (where  $\hat{H}_{elec}$  includes contributions from  $H_{\uparrow\downarrow}$  and the energy of the level  $|v\rangle$ ), and  $\hat{V}_{interaction} = \hat{H}_{int}$ , then we find that

$$\dot{C}'_{\downarrow,\mathbf{n}} = ig_1^* \sum_{\mathbf{n}'} \langle \mathbf{n} | e^{-i\mathbf{k}_1 \cdot \hat{\mathbf{x}}} | \mathbf{n}' \rangle e^{i[\boldsymbol{\omega} \cdot (\mathbf{n} - \mathbf{n}') - \Delta_R]t} C'_{v,\mathbf{n}'} \quad (3.17)$$

$$\dot{C}'_{\uparrow,\mathbf{n}} = ig_2^* \sum_{\mathbf{n}'} \langle \mathbf{n} | e^{-i\mathbf{k}_2 \cdot \hat{\mathbf{x}}} | \mathbf{n}' \rangle e^{i[\boldsymbol{\omega} \cdot (\mathbf{n} - \mathbf{n}') - \Delta_R - \delta]t} C'_{v,\mathbf{n}'} \quad (3.18)$$

$$\begin{aligned} \dot{C}'_{v,\mathbf{n}} &= ig_1 \sum_{\mathbf{n}'} \langle \mathbf{n} | e^{i\mathbf{k}_1 \cdot \hat{\mathbf{x}}} | \mathbf{n}' \rangle e^{i[\boldsymbol{\omega} \cdot (\mathbf{n} - \mathbf{n}') + \Delta_R]t} C'_{\downarrow,\mathbf{n}'} + \\ &ig_2 \sum_{\mathbf{n}'} \langle \mathbf{n} | e^{i\mathbf{k}_2 \cdot \hat{\mathbf{x}}} | \mathbf{n}' \rangle e^{i[\boldsymbol{\omega} \cdot (\mathbf{n} - \mathbf{n}') + \Delta_R + \delta]t} C'_{\uparrow,\mathbf{n}'}. \end{aligned} \quad (3.19)$$

Here,  $g_1 \doteq \langle \downarrow | \hat{g}_1 | v \rangle$ ,  $g_2 \doteq \langle \uparrow | \hat{g}_2 | v \rangle$ , and the  $C'_{i,\mathbf{n}}$  are the coefficients of the interaction-picture state vectors. In writing these three equations, I have made the ‘‘rotating wave approximation:’’ that is, I have neglected terms with time-dependences at optical frequencies. If we now make the substitution  $\tilde{C}_{v,\mathbf{n}} \doteq C_{v,\mathbf{n}} e^{-i\Delta_R t}$  (corresponding to a transformation to a new interaction picture), we obtain:

$$\dot{\tilde{C}}'_{\downarrow,\mathbf{n}} = ig_1^* \sum_{\mathbf{m}} \langle \mathbf{n} | e^{-i\mathbf{k}_1 \cdot \hat{\mathbf{x}}} | \mathbf{m} \rangle e^{i[\boldsymbol{\omega} \cdot (\mathbf{n} - \mathbf{m})]t} \tilde{C}'_{v,\mathbf{m}} \quad (3.20)$$

$$\dot{\tilde{C}}'_{\uparrow,\mathbf{n}} = ig_2^* \sum_{\mathbf{m}} \langle \mathbf{n} | e^{-i\mathbf{k}_2 \cdot \hat{\mathbf{x}}} | \mathbf{m} \rangle e^{i[\boldsymbol{\omega} \cdot (\mathbf{n} - \mathbf{m}) - \delta]t} \tilde{C}'_{v,\mathbf{m}} \quad (3.21)$$

$$\begin{aligned} \dot{\tilde{C}}'_{v,\mathbf{n}} + i\Delta \tilde{C}'_{v,\mathbf{n}} &= ig_1 \sum_{\mathbf{m}} \langle \mathbf{n} | e^{i\mathbf{k}_1 \cdot \hat{\mathbf{x}}} | \mathbf{m} \rangle e^{i[\boldsymbol{\omega} \cdot (\mathbf{n} - \mathbf{m})]t} C'_{\downarrow,\mathbf{m}} + \\ &ig_2 \sum_{\mathbf{m}} \langle \mathbf{n} | e^{i\mathbf{k}_2 \cdot \hat{\mathbf{x}}} | \mathbf{m} \rangle e^{i[\boldsymbol{\omega} \cdot (\mathbf{n} - \mathbf{m}) + \delta]t} C'_{\uparrow,\mathbf{m}}. \end{aligned} \quad (3.22)$$

At this point, we perform an adiabatic elimination of the excited state  $|v\rangle$ : we assume  $\dot{\tilde{C}}'_{v,\mathbf{n}} \ll i\Delta \tilde{C}'_{v,\mathbf{n}}$  and solve the last of the three equations above for  $\tilde{C}'_{3,\mathbf{n}}$ . Plugging this into the first two equations, we obtain:

$$\dot{C}'_{\downarrow,\mathbf{n}} = i \frac{|g_1|^2}{\Delta_R} C'_{\downarrow,\mathbf{n}} + i \frac{g_1^* g_2}{\Delta_R} \sum_{\mathbf{m}} \langle \mathbf{n} | e^{-i\boldsymbol{\Delta} \mathbf{k} \cdot \hat{\mathbf{x}}} | \mathbf{m} \rangle e^{i[\boldsymbol{\omega} \cdot (\mathbf{n} - \mathbf{m}) + \delta]t} C'_{\uparrow,\mathbf{m}} \quad (3.23)$$

$$\dot{C}'_{\uparrow, \mathbf{n}} = i \frac{|g_2|^2}{\Delta} C'_{\uparrow, \mathbf{n}} + i \frac{g_2^* g_1}{\Delta_R} \sum_{\mathbf{m}} \langle \mathbf{n} | e^{i \Delta \mathbf{k} \cdot \hat{\mathbf{x}}} | \mathbf{m} \rangle e^{i[\boldsymbol{\omega} \cdot (\mathbf{n} - \mathbf{m}) - \delta]t} C'_{\downarrow, \mathbf{m}}. \quad (3.24)$$

with  $\Delta \mathbf{k} = \mathbf{k}_1 - \mathbf{k}_2$ . The first terms in these equations,  $i|g_j|^2/\Delta_R$ , represent AC Stark shifts of  $|\uparrow\rangle$  and  $|\downarrow\rangle$ . These can be eliminated from our discussion by redefining the energies of  $|\uparrow\rangle$  and  $|\downarrow\rangle$  to include them, or by transforming to yet another interaction picture. The interesting dynamics are induced by the second terms in the equations.

The expressions  $\langle \mathbf{n} | e^{i \Delta \mathbf{k} \cdot \hat{\mathbf{x}}} | \mathbf{m} \rangle$  determine the strength of the coupling between the different motional levels. For example, if  $\Delta \mathbf{k} = \mathbf{0}$ , then only levels for which  $\mathbf{m} = \mathbf{n}$  are coupled; that is, the interaction with the lasers changes the spin state but *not* the motional state, as claimed above. Moreover, in contrast to Eq. (3.12), the  $|\downarrow\rangle \leftrightarrow |\uparrow\rangle$  carrier Rabi frequency is independent of the motional state. If  $\Delta \mathbf{k} \parallel \mathbf{e}_z$ , then the coupling is sensitive to motion only in the  $z$ -direction, and only different  $z$ -motional states are coupled; in this case, the sums collapse down to one-dimensional ones (i.e. sums over  $n_z$ ).

The detuning  $\delta$  picks out particular terms in the sums. For example, assume, that  $\Delta \mathbf{k} \parallel \mathbf{e}_z$  so that  $\Delta \mathbf{k} = k_z \hat{z}$ , and assume that  $\delta \approx \omega_z(n_z - m_z)$  for some particular  $n_z - m_z$ . Then this term will be slowly-varying with respect to all the other terms in the sum, and another rotating-wave approximation allows us to drop all these other terms (which average to zero). Then Eqs. (3.24) become:

$$\dot{C}'_{\downarrow, n_z} = -i \Omega_{n, m}^* e^{i\delta t} C'_{\uparrow, m} \quad (3.25)$$

$$\dot{C}'_{\uparrow, n_z} = -i \Omega_{n, m} e^{-i\delta t} C'_{\downarrow, m}. \quad (3.26)$$

Here,  $m$  is the natural number closest to  $n - \frac{\delta}{\omega_z}$ , and I have defined:

$$\begin{aligned} \Omega_{n, m} &= -\frac{g_2^* g_1}{\Delta_R} \langle n | e^{i \Delta k_z \hat{z}} | m \rangle \\ &= -\frac{g_2^* g_1}{\Delta_R} \langle n | e^{i \eta (\hat{a}_z + \hat{a}_z^\dagger)} | m \rangle, \end{aligned} \quad (3.27)$$

where  $\eta_z \doteq \Delta k_z z_0$  is the Lamb-Dicke parameter for the two-photon transition and  $z_0 = \sqrt{\frac{\hbar}{2m\omega_z}}$  is the spread of the ground state harmonic oscillator wave function in  $z$ .

In general  $\eta_m = \Delta \mathbf{k} \cdot \hat{\mathbf{e}}_m m_0$  ( $m \in \{x, y, z\}$ ), where  $m_0$  is the spread of the ground state harmonic oscillator wave function in direction  $m$ .

Thus, according to Eq. (3.26), the dynamics induced by the two-photon, stimulated Raman transitions are qualitatively the same as those described in the last Section for a single laser beam, with the exceptions that  $\mathbf{k} \rightarrow \Delta \mathbf{k}$  and  $\omega_L \rightarrow \omega_1 - \omega_2$ . The advantage is that, for transitions between atomic levels separated by radio frequencies, we retain the frequency and phase control associated with rf, but at the same time achieve the high field gradients associated with optical transitions. We also achieve the benefit of being able to arrange  $\Delta \mathbf{k}$  so that we are sensitive to all directions of the ion's motion, only one direction of ion motion, or such that we are entirely insensitive to the ion's motion.

One possible issue with stimulated Raman transitions is that there will be some population in the “virtual” level  $|v\rangle$ , which decays with a time constant of 8 ns. We may make an estimate of the probability that the virtual level is populated in, for example, a  $\pi$ -pulse operation, by solving Eq. (3.22) for  $\tilde{C}_{3,\mathbf{n}}$ . Roughly speaking,  $|\tilde{C}_{3,\mathbf{n}}| \sim |\frac{g}{\Delta_R}|$ , where  $g$  is on the order of the single-photon coupling strengths  $g_1$  and  $g_2$ . However, from Eq. (3.27), we also have that the carrier Rabi frequency is roughly given by  $\Omega = \frac{g^2}{\Delta_R}$ , so that  $g \approx \sqrt{\Omega \Delta_R}$ . Thus,

$$\tilde{C}_{3,\mathbf{n}} \approx \sqrt{\frac{\Omega}{\Delta_R}} \quad (3.28)$$

$$P_v = |\tilde{C}_{3,\mathbf{n}}|^2 \approx \frac{\Omega}{\Delta_R}. \quad (3.29)$$

For typical operating conditions,  $\Omega/2\pi \approx 1$  MHz and  $\Delta_R/2\pi \approx 10$  GHz, so that  $P_v \approx 10^{-4}$  in a  $\pi$ -pulse operation. Decay from the virtual level is thus a small effect<sup>7</sup>.

---

<sup>7</sup> In principle, we would like to increase  $\Delta_R$  as much as possible in order to minimize the effects of decay from the virtual level. However, if  $\Delta_R$  is bigger than the  $2p \ ^2P$  fine-structure splitting ( $\approx 197$  GHz), destructive interference between the  $^2P_{1/2}$  and  $^2P_{3/2}$  virtual levels makes the stimulated-Raman coupling between  $|\downarrow\rangle$  and  $|\uparrow\rangle$  ineffective.

### 3.4 Spin Diagnostics: the Ramsey Experiment

One experiment which will appear in different forms throughout this thesis is the “Ramsey experiment” [95], which is typically used for high-precision spectroscopy. In the Ramsey method, a  $\frac{\pi}{2}$  pulse is applied to an atom or sample of atoms which previously has been prepared in some pure state. The state is then allowed to evolve without perturbation by applied fields for a time  $T_R$ , after which time a second  $\frac{\pi}{2}$  pulse is applied and the probability that the atom(s) remains in its initial state is probed. In the usual nomenclature, the first and second  $\pi/2$ -pulses are referred to as the first and second “Ramsey zones.” If the applied radiation is on resonance and the Ramsey zones have the same laser phase, then the probability of the atom remaining in the initial state is zero; for a general detuning from resonance, a series of narrow fringes is found as a function of the detuning. The Ramsey method offers an approximate factor of two improvement in resolution over the (optimum) Rabi flopping in spectroscopy, as well as offering practical advantages for atomic beam standards (in particular, for microwave spectroscopy) [95].

In our experiments, we typically build up spectra by keeping  $T_R$  fixed while sweeping the frequencies  $\nu_{pr}$  of the  $\pi/2$ -pulses. In order to determine  $P_{\downarrow}(\nu_{pr})$ , we may multiply the matrices corresponding to on-resonance  $\pi/2$ -pulses from Eq. (3.13), with a matrix  $\mathcal{M}_{fe}$  sandwiched in between to account for the effects of the free evolution during the time  $T_R$  between the  $\pi/2$ -pulses:

$$\mathcal{M}_{fe} = \begin{bmatrix} e^{-i\delta t/2} & 0 \\ 0 & e^{i\delta t/2} \end{bmatrix}. \quad (3.30)$$

This procedure is straightforward, but the expressions are complicated enough to obscure the underlying physics.

To obtain a clearer picture of the Ramsey experiment, consider instead the case in which the laser is on resonance with the  $|\downarrow\rangle \leftrightarrow |\uparrow\rangle$  transition, but where we sweep

the phase  $\phi$  of the second  $\pi/2$ -pulse. In this case, Eq. (3.13) becomes:

$$\begin{bmatrix} \frac{1}{\sqrt{2}} & \frac{-i}{\sqrt{2}}e^{i\phi_j} \\ \frac{-i}{\sqrt{2}}e^{-i\phi_j} & \frac{1}{\sqrt{2}} \end{bmatrix}, \quad (3.31)$$

where  $\phi_j$  ( $j = 1, 2$ ) is the phase of the  $j^{\text{th}}$  laser pulse. Taking  $\phi_1 = 0$  and  $\phi_2 = \phi$ , and multiplying the matrices together, we have <sup>8</sup> :

$$\frac{1}{2} \begin{bmatrix} 1 - e^{i\phi} & -i(1 + e^{-i\phi}) \\ -i(1 + e^{i\phi}) & 1 - ie^{-i\phi} \end{bmatrix}. \quad (3.32)$$

Thus, if we start out in the state  $|\downarrow\rangle$  and perform the experiment, the probability  $P_{\downarrow}(\phi)$  of finding the atom in  $|\downarrow\rangle$  at the completion of the second Ramsey zone is given by:

$$P_{\downarrow}(\phi) = \frac{1}{2}(1 - 2 \cos \phi) = \sin^2 \phi. \quad (3.33)$$

This describes sinusoidal oscillations in  $P_{\downarrow}$  as a function of the phase difference between the  $\pi/2$ -pulses. For small detunings of the laser from resonance, the predominant effect is due to the free evolution matrix, Eq. (3.30), which results in a net phase difference between the first and second Ramsey zones. Thus, Eq. (3.33) also applies to such cases.<sup>9</sup>

Fig. 3.5 shows typical Ramsey fringes, from an experiment in which the Ramsey zone pulse frequencies were varied near resonance.

### 3.5 Mapping Information From Motion to Spin

The interactions between the ion and the lasers couple the ion's spin and motional degrees of motion, through the field gradients of the laser. We may use this coupling to engineer the ion's quantum state of motion, as will be discussed in Ch. 6. Alternately,

---

<sup>8</sup> This equation is the same as that obtained in the case where the phase is held constant, but the detuning is changed — in the case that the detuning is small enough to ignore during the  $\pi/2$ -pulses, but where  $T_R$  is large enough that the detuning plays a large effect during the free evolution. This is easy enough to verify by using Eq. (3.31) for the  $\pi/2$ -pulses and Eq. (3.30) for the free evolution, and comparing the result to Eq. (3.32). Aside from an irrelevant overall phase factor, the two results are identical.

<sup>9</sup> For larger detunings, the complete result also exhibits an envelope which is given by the same line shape which would result from Rabi spectroscopy

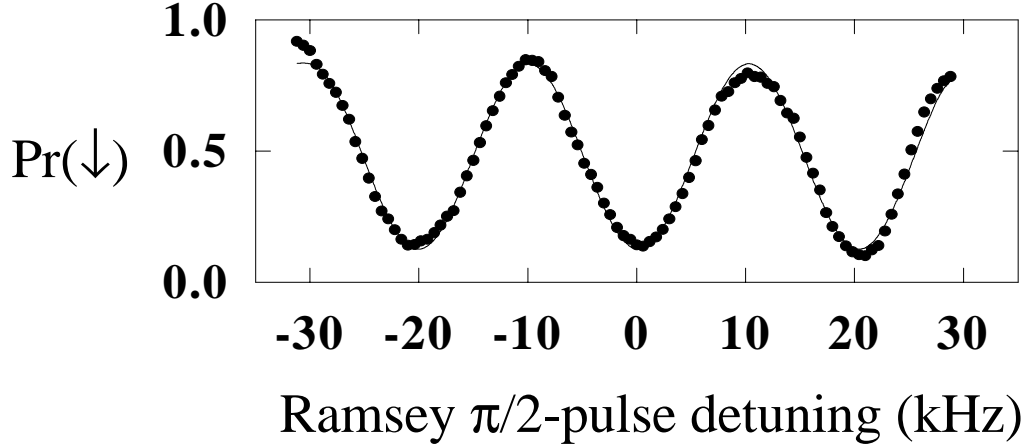


Figure 3.5: Ramsey fringes taken with an initial  $|\downarrow\rangle$  state. For these data, the frequencies of the Ramsey zones ( $\pi/2$ -pulses) were varied near the  $|\downarrow\rangle \leftrightarrow |\uparrow\rangle$  resonance frequency. For small detunings, the Ramsey fringes are well-fit by the sinusoidal form of Eq. (3.33).

we may use the coupling to map information about the ion’s motion onto its spin degree of freedom. This is necessary because we do not have the ability to measure the motional state occupation numbers directly. To do perform the mapping, we start with the ion in spin down and in some “unknown” (but reproducible) motional state:  $|\psi\rangle = |\downarrow\rangle \sum C_n |n\rangle$ . We then turn on the Raman beams, tuned to some particular motional sideband; in practice we choose to tune to the blue sideband.

If we leave the interaction on for a time  $t_{pr}$ , then measure the probability  $P_{\downarrow}$  that the ion is in  $|\downarrow\rangle$ , we find that

$$P_{\downarrow}(t_{pr}) = \sum P_n \cos^2(\Omega_{n,m} t_{pr}) = \frac{1}{2} \sum P_n (1 + \cos(2\Omega_{n,m} t_{pr})) \quad (3.34)$$

as discussed in Sec. 3.2 and indicated for a Fock state in Fig. 3.4(b). In Eq. (3.34),  $P_n = |C_n|^2$ . By performing a Fourier decomposition of the Rabi flopping curve, we can extract the  $P_n$ ’s. Furthermore, we can do this with *unit* quantum efficiency as long as the different Rabi frequencies  $\Omega_{n,m}$  are well-resolved. On the blue sideband, in

the Lamb-Dicke regime,  $\Omega_{n,n+1} = \eta\Omega\sqrt{n+1}$ , and so it is easy to resolve the different Fourier components.

In the experiment, background heating of the ion’s motion and technical noise (laser beam intensity fluctuations, fluctuating background magnetic fields, etc.) wash out the Rabi flopping curves, as is evident in Fig. 3.4(b). To approximate these effects, we may write:

$$P_{\downarrow}(t_{pr}) = \frac{1}{2} \sum P_n (1 + \cos(2\Omega_{n,m}t_{pr})e^{-\gamma_n t_{pr}}) + \mathcal{B} \quad (3.35)$$

where  $\mathcal{B}$  is due to background counts and the  $\gamma_n$  are  $n$ -dependent decay coefficients.<sup>10</sup>

The data analysis proceeds as before except that a singular-valued decomposition analysis with decaying sinusoids as basis functions is used instead of Fourier analysis [96]. The frequencies of the various (decaying) sinusoidal basis functions are calculated from a base Rabi frequency (either the carrier or the  $|\downarrow, n=0\rangle \leftrightarrow |\uparrow, n=1\rangle$  transitions) using Eq. (3.12).

In summary, then, the interaction between the ion and the motion provides us with the “handle” we use to manipulate the ion’s motion and also with the “camera” we use to analyze this motion.

---

<sup>10</sup> For example, if the decay is due to slow laser intensity fluctuations, then different Fock state flopping curves decay in the same number of flops and so, in a different absolute time.

## Chapter 4

### Apparatus

In this chapter, I will describe the apparatus used to realize the interactions discussed in the last Chapter (the ion trapping apparatus was discussed in Ch. 2). First, I will discuss the laser and optical systems used to cool and manipulate the ion's motional state. Then I will describe the digital logic and rf control used to switch the laser beams on and off and control their frequency. The experiment was a fluid object, constantly changing and evolving. In order to describe it, I have had to choose one particular configuration. However, this setup was generically the same as any of the other incarnations of the laser systems.

#### 4.1 Optics

The optical setup of the experiment was divided into three sets of beam lines: (i) the beams used for optical pumping, Doppler cooling and driving the cycling transition, (ii) the “repumper,” used to clean out the  $2s\ 2^S_{1/2}F = 2, m_F = -1$  level, and (iii) the Raman beams. The orientation of these beam lines with respect to the vacuum envelope of the trap is shown in Fig. 4.1. For each of these beam lines, the wavelength of the light at the ion was  $\approx 313$  nm. This light was created by frequency-doubling light from a 626 nm dye laser (the dye was Kiton Red), pumped by green light from an argon-ion laser. The argon-ion laser was a Spectra Physics Model 2030, which was usually run

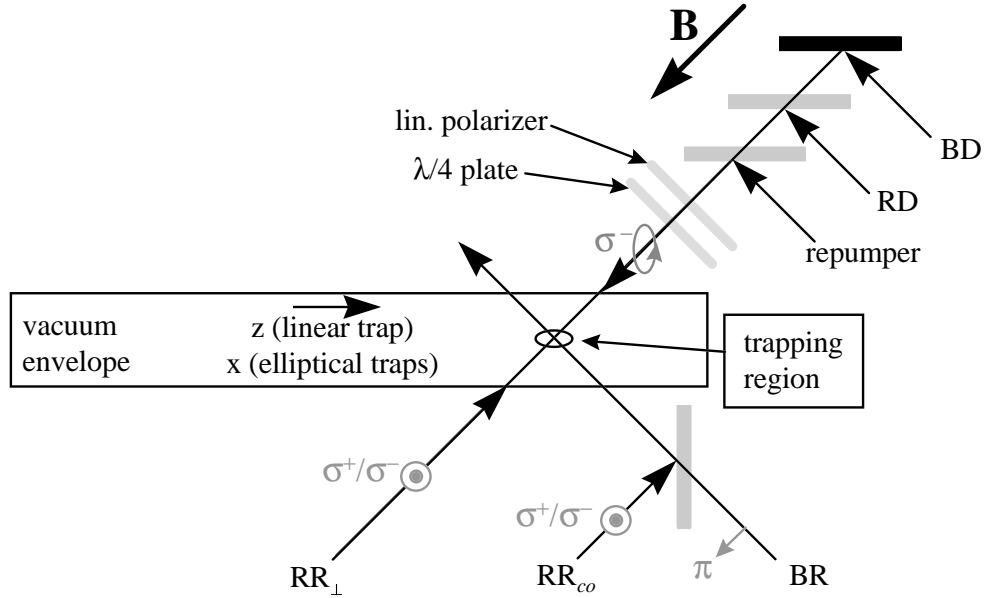


Figure 4.1: Laser beam geometry. The long axis of the vacuum envelope was parallel to the  $x$ -axis for the elliptical microtraps, and parallel to the  $z$ -axis for the micromachined linear ion trap. The Blue Doppler, Red Doppler and repumper beams entered the trap through the same window. The Red Raman  $\perp$  beam entered through the opposite window. The Blue Raman beam and the Red Raman  $co$  beam entered at  $90^\circ$  to the Red Raman  $\perp$  beam. The resonant beams were polarized  $\sigma^-$ , Blue Raman was  $\pi$ -polarized,  $RR_{co}$  was polarized  $(\sigma^+ + \sigma^-)/2^{1/2}$ , and  $RR_{\perp}$ 's polarization was selected as discussed in Ch. 6.2.1: usually, its polarization was  $(\sigma^+ + \sigma^-)/2^{1/2}$  as well.

with an output power of  $\approx 16.8$  W. This light was then split three ways by optical beam splitters: roughly 5.6 W was sent to each of the dye lasers.

The argon-ion laser and all the 626 nm optics associated with the dye lasers and their locking systems were on one optical table (the “red table”). The frequency doubling, the 313 nm optics and optical switches, and the ion trap were on a second optical table (the “UV table”). The 626 nm light was passed to this table through fibre optics.

#### 4.1.1 Resonant Beam Lines: the Doppler and Repumper Beams

A schematic diagram of the resonant beam lines (the Doppler and repumper lines) is shown in Fig. 4.2. There were two “Doppler” beams: the Blue and Red Doppler. The names arose from the frequencies of the two beams: since the Blue Doppler connected  $|\downarrow\rangle$  with the  $2p\ ^2P_{3/2}$  level, it was of higher frequency than the Red Doppler, which connected  $|\uparrow\rangle$  with the same state. Blue Doppler drove the cycling transition used for state detection (see Sec. 3.1), and provided laser cooling. Red Doppler was also turned on during laser cooling and, in conjunction with the repumper laser, provided optical pumping.

The Doppler beams were produced by a Coherent 699 dye laser circulating Kiton Red (at a pressure of 40-55 psi). The conversion efficiency from the green pump light to 626 nm output was approximately 10% (depending on the age of the dye and the state of the laser cavity). So, with 5.6 W of green pump light, the laser produced up to 600 mW of output light. The 699 has an internal cavity assembly consisting of a thin and thick etalon, and a Brewster-angle plate used to scan the laser over large frequency ranges (in principle, up to tens of GigaHertz). The laser was modulation-locked to the maximum of the thick etalon transmission. Frequency stability was provided by locking to an external, stable reference cavity (a “side-lock” to the side of the external cavity’s transmission). The error signal derived from the reference cavity was fed back to the Brewster-angle plate and to a piezo-electric transducer which supported one of the laser cavity mirrors. By tuning the laser to the side of the transmission curve of an external cavity, we could determine that the 699 typically exhibited a linewidth of 1-4 MHz when locked up.

A portion of the 699’s output light was split off by a beam splitter and sent to diagnostics. These diagnostics consisted of a Burleigh Model #SA-PLUS-200-B1 spectrum analyzer (2 GHz free spectral range), a travelling-cart wavemeter [97, 98], and

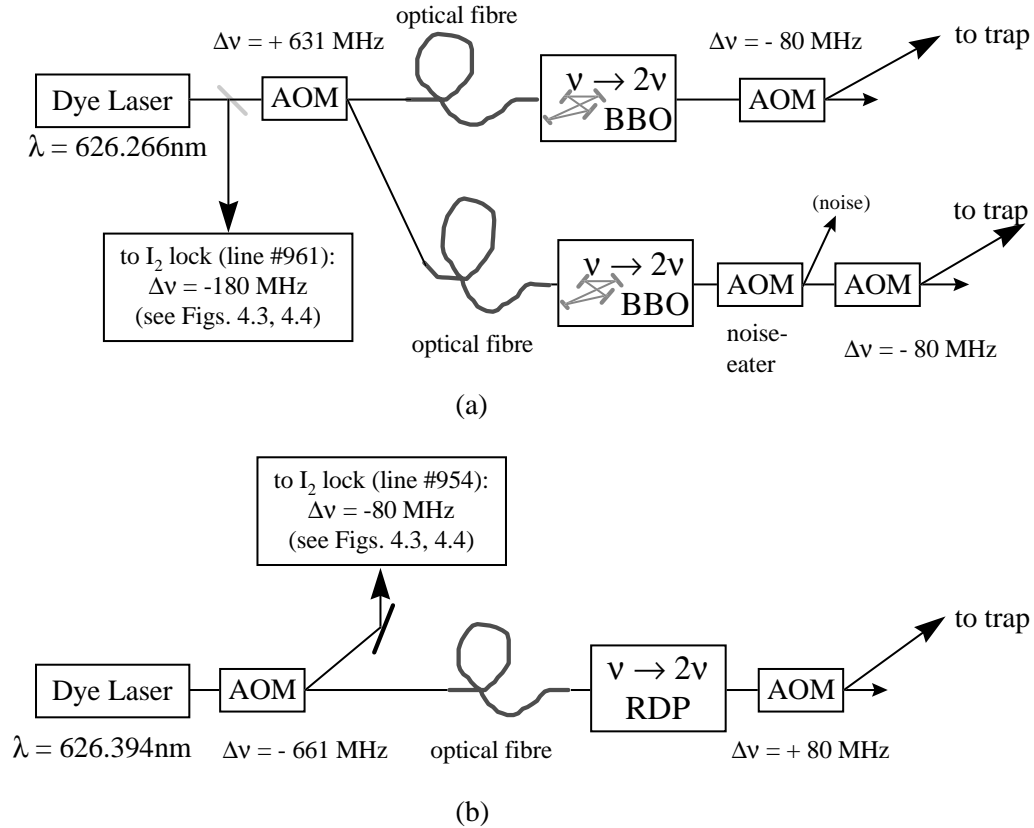


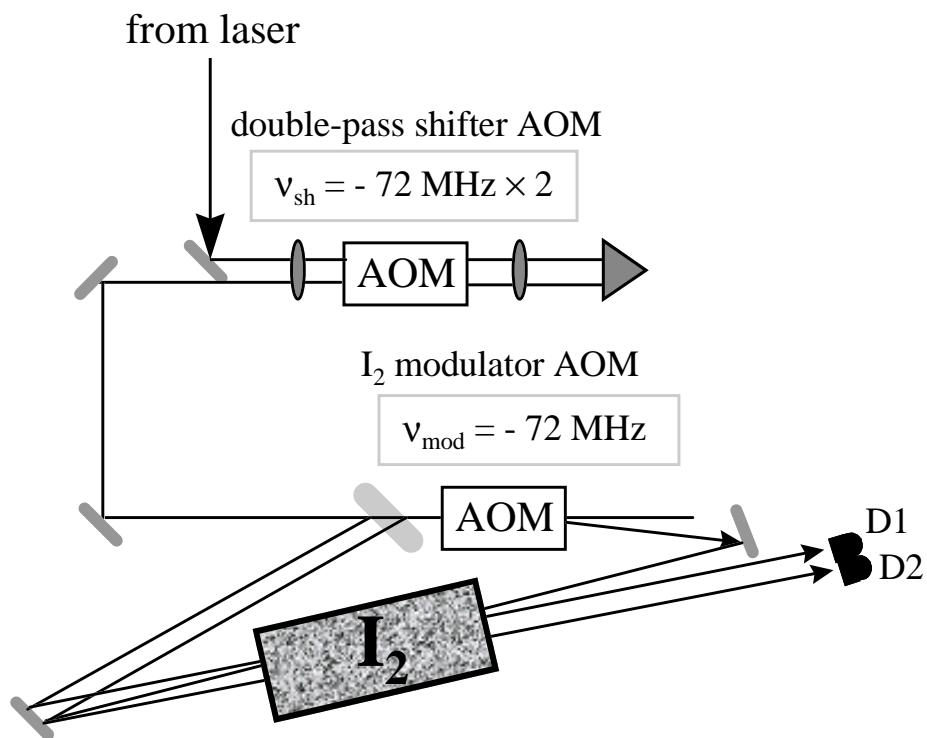
Figure 4.2: Resonant beam lines: Doppler (a) and repumper (b). The Doppler beams were derived from a Coherent 699 dye laser. The 1.26 GHz hyperfine and Zeeman splitting between Red and Blue Doppler was achieved with a 631 MHz AOM in the red (i.e. at 626 nm). The frequencies of the beams were doubled in a BBO ( $\beta$ -barium borate) crystal inside a double-ring optical resonator structure. In the UV (at 313 nm), the frequency difference between the two beams became 1.26 GHz. The beams were turned on and off with two more “switch” AOMs. The BBO rings and the UV optics were on a separate optical table from the dye laser, its Ar-ion pump laser, and the laser diagnostics. Light at 626 nm passed between the two tables through a single-mode optical fibre. The repumper beam was derived from a home-built dye laser. This beam line was generically equivalent to the Doppler beam lines, except that the frequency doubling was performed by single-passing the red light through a cooled RDP crystal.

an  $I_2$  saturated absorption spectrometer [99]. The spectral features of the iodine provided a stable reference to which to lock the laser at long times. Details of the setup are shown in figure 4.3(a). The laser light first passed through a double-pass AOM, where it picked up a frequency offset (from the laser output) of  $\Delta\nu = -2 \times 72 \text{ MHz} = -144 \text{ MHz}$ . This double-pass configuration allowed us to change the frequency offset between the laser light and the iodine lock without causing appreciable beam steering. From there, the light passed through a thick beam splitter (approximately 4% reflectance per face), which produced the weak probe and reference beams for the saturated spectroscopy. The transmitted beam passed through another AOM: this AOM produced a frequency shift of  $\Delta\nu = -72 \text{ MHz}$  in the pump beam. The frequency of the rf driving this AOM was modulated at  $\approx 3 \text{ kHz}$  in order to allow lock-in detection of the iodine fluorescence.<sup>1</sup> The modulation depth was on the order of the linewidth of the iodine features ( $\approx 5 - 10 \text{ MHz}$ ).

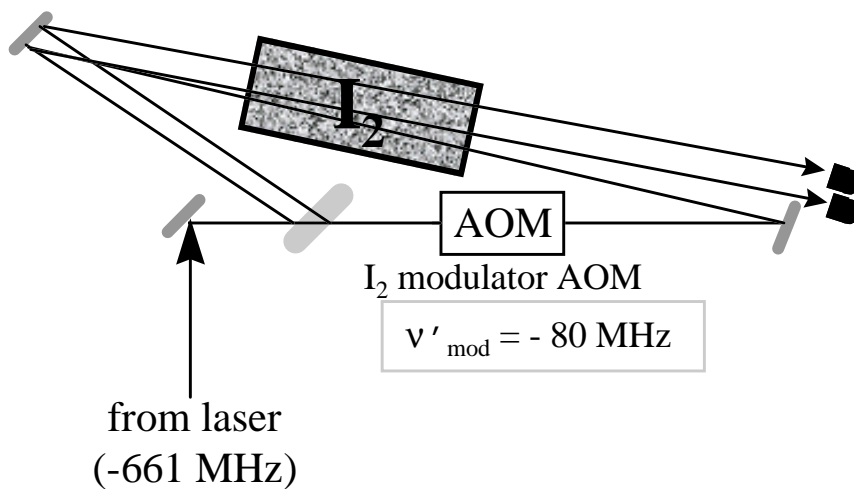
As usual in saturated absorption spectroscopy [99], the strong pump beam saturated the  $I_2$  population with which it was resonant. This depleted the absorption signal of the weak (counter-propagating) probe beam in the velocity class of  $I_2$  which was simultaneously in resonance with the pump and probe beams. Subtraction of the reference beam signal from the probe beam signal removed the background absorption profile of the probe beam (and also reduced the effects of laser intensity fluctuations), leaving only the narrow, Doppler-free, saturated-absorption dip. The pump beam was frequency-modulated at 30 kHz to move the saturated-absorption signal away from DC, using standard phase-sensitive detection techniques [100]. The probe and reference beams were detected and subtracted in a New-Focus Nirvana auto-balanced photodiode-pair detector, and the output was sent to a lock-in amplifier, which fed back into the 699 control box lock circuitry.

---

<sup>1</sup> Note that, if the beam had been modulated *before* the beam splitter, then the reference beam would have had 30 kHz FM on it. If the amplitude of this beam fluctuated, the fluctuations then would have passed through the phase-sensitive detection to the lock signal.



(a)



(b)

Figure 4.3: Schematic of the saturated absorption spectrometers used to lock the Doppler (a) and repumper (b) lasers to iodine. The frequencies driving the various AOMs are indicated. Note that the “modulation” AOM frequency shift was effectively half the frequency driving the AOM. The beam which went to the iodine lock from the repumper laser was first down-shifted by 661 MHz.

The 699 was locked to hyperfine feature (a) of line # 961 of the “Iodine atlas” [101]. See Fig. 4.4(a) for a spectrum of this iodine line. Feature a lies at the blue-most edge of line # 961: thus, if the laser (on resonance with the  ${}^9\text{Be}^+, |\downarrow\rangle \rightarrow |2p\ ^2P_{3/2}\rangle$ ) transition jumped out of lock, it would not re-lock to the blue of resonance (which would cause heating). There was no lock point to the blue of Feature (a).

From Figs. 4.2 and 4.3(a), we can determine the relationship between the frequency  $\nu_{I_2}$  of Feature a of line # 961 of  $\text{I}_2$  and the  $|\uparrow\rangle \rightarrow |2p\ ^2P_{3/2}\rangle$  resonance <sup>2</sup> frequency  $\nu_{Be}$  of the ion. First note that, in order for both the pump and probe beams to be in resonance with the same velocity class of the  $\text{I}_2$  sample, we must have

$$\begin{array}{ccc} \text{probe beam} & & \text{pump beam} \\ \nu_L - 2\nu_{sh} - \nu_D & = & \nu_L - 2\nu_{sh} - \nu_{mod} + \nu_D. \end{array} \quad (4.1)$$

Here,  $\nu_L$  is the frequency of the laser’s output,  $\nu_{sh} = 72$  MHz is the frequency driving the double-pass AOM,  $\nu_{mod} = 72$  MHz is the frequency driving the pump-beam modulation AOM, and  $\nu_D$  is the magnitude of the Doppler shift of the selected velocity class. Equation (4.1) implies that

$$\nu_D = \frac{1}{2}\nu_{mod}. \quad (4.2)$$

Finally, we have

$$\begin{aligned} \nu_{Be} &= 2(\nu_{I_2} + 2\nu_{sh} + \nu_{mod} + \nu_D) - 80 \text{ MHz} \\ &= 2\left(\nu_{I_2} + 2\nu_{sh} + \frac{1}{2}\nu_{mod}\right) - 80 \text{ MHz} \\ &= 2\nu_{I_2} + 280 \text{ MHz} . \end{aligned} \quad (4.3)$$

The main part of the Doppler laser’s power passed through a high-frequency AOM which was driven at 631 MHz (half the  ${}^9\text{Be}^+$  hyperfine splitting, plus Zeeman shifts). The undeflected beam produced the Red Doppler beam when doubled, while

---

<sup>2</sup> Recall that  $|\uparrow\rangle \equiv |2s\ ^2S_{1/2}, F = 1, m_F = -1\rangle$ .

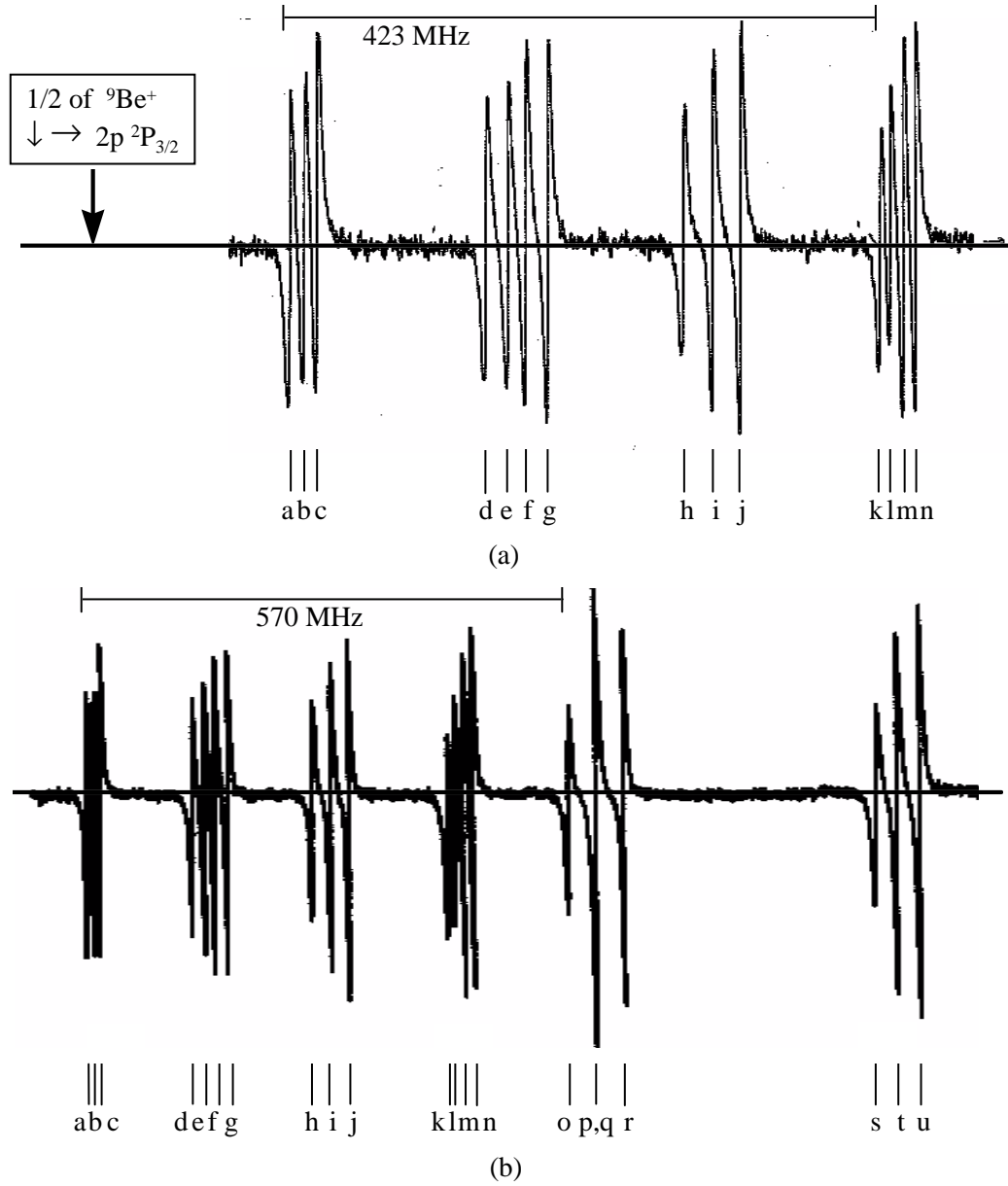


Figure 4.4: (a) Portion of I<sub>2</sub> line # 961, as traced out by saturated absorption spectroscopy. The line is the result of the phase-sensitive detection signal of the photodiode current difference between the probe and reference beams, as described in the text. The Doppler laser was locked to Feature (a). Features (o) through (u) are not shown on this trace: they lie to the right of Feature (n), which is towards lower frequencies. The relative position of the <sup>9</sup>Be<sup>+</sup>, |↑⟩ → |2p <sup>2</sup>P<sub>3/2</sub>⟩ resonance (after frequency doubling) is indicated by the arrow. From the text, the 626 nm light which was doubled to be on resonance with this transition lay 140 MHz to the blue of Feature (a). (b) Complete trace of I<sub>2</sub> line # 954. The repumper laser was locked to Feature (a) of this line. The 626 nm light which, when frequency doubled, drove the |F = 2, m<sub>F</sub> = -1⟩ → |2p <sup>2</sup>P<sub>1/2</sub>⟩ transition, was 681 MHz to the blue of this feature.

the (positive) first-order diffracted beam produced the Blue Doppler. These two beams were then coupled from the “red” table to the “UV” table through single-mode fibres. The fibres were a convenient way to pass the light from one table to the other, since they allowed us to change the alignment of the “red” optics without affecting the doubling ring or UV optics alignment.<sup>3</sup>

Frequency doubling of the 626 nm Doppler-line light occurred in a BBO crystal which was enclosed in a double-ring cavity (see Fig. 4.5). The two rings shared three of the four mirrors which comprised their respective cavities, as well as the BBO crystal in which the frequency-doubling took place, and the UV output-coupler. The mirrors which the two rings did not share were mounted on piezo-electric transducers, which allowed feedback of an error signal to lock the cavity. Sharing one BBO crystal between the two beams was a convenient way to maximize the use of the BBO crystal.

As Fig. 4.5 indicates, each ring was in a bow-tie configuration. The long side of the bow-tie was 15 cm in length, whereas the short side was 10.6 cm long. The other relevant dimensions are shown in Fig. 4.5. Two of the mirrors were high-reflectance ( $R > 99.9\%$ ), 10 cm radius of curvature mirrors. The piezo-mounted mirror was a high-reflectance ( $R > 99.9\%$ ) flat. The final mirror, which served as the input coupler, was a 98.5% reflectance flat. Coupling into the cavity was achieved through two telescopes, each of which consisted of two, 10 cm lenses. The polarization of the 626 nm light inside the cavity was in the plane of the ring (horizontal). The cavity had a finesse of  $\approx 200$  and a free spectral range of approximately 0.5 GHz. The power build-up factor was measured to be  $\approx 75$ . The cavities were locked on resonance by monitoring the polarization of the 626 nm light reflected off the input coupler, according to the scheme of Hänsch and Couillaud [102], and feeding the resultant error signal back to the piezo-mounted cavity mirrors.

---

<sup>3</sup> Of course, changing the red alignment necessitated realignment of the fibres’ input couplers.

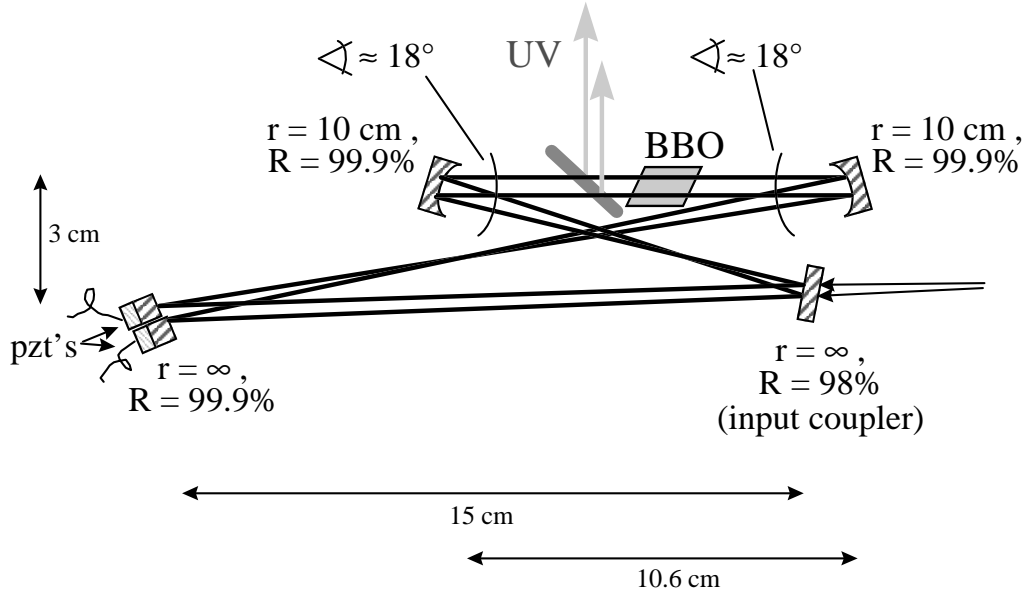


Figure 4.5: Resonant power build-up ring cavities for frequency doubling 626 nm to 313 nm. With 220 mW of 626 nm light coupled into one of the cavities, approximately 15-20 mW of 313 nm light was produced. Type II phase matching was used.

The BBO crystal was approximately 6 mm (length) by 4 mm by 4 mm. It lay in the short section of the cavity bow-tie, and its front and rear facets were cut at Brewster's angle with respect to the horizontally polarized, 626 nm light. The two fundamental beams (for Blue and Red Doppler) passed through the BBO crystal parallel. Second-harmonic generation was achieved through angle-tuned, Type II phase matching, and the crystal was cut so as to satisfy the phase-matching condition. The relevant BBO optical properties at 626 nm are listed in Table 4.1. From the nonlinear coefficient  $d_{20}$  and the beam characteristics, we would expect a conversion efficiency [103]  $\eta_{nl} = \frac{P^{2\omega}}{[P^\omega]^2} \approx 1 \times 10^{-4}/\text{W}$  (where the powers are measured in Watts). In practice, with 200 mW of power entering the cavity, 10 mW of UV was produced (corresponding to an inter-cavity doubling efficiency of  $\eta \approx 5 \times 10^{-5}/\text{W}$ ). The UV was coupled out of the cavity with a dichroic beam splitter, which reflected the 313 nm light out of the ring while presenting little loss ( $< 0.5\%$ ) to the 626 nm light.

Table 4.1: Optical characteristics of  $\beta$ -barium borate (BBO) at 626 nm and room temperature [104]. The second-harmonic generation scheme uses 626 nm (ordinary ray) + 626 nm (extraordinary ray) = 313.0 nm (extraordinary ray).

property	value
refractive index (o,e)	1.66747, 1.61568
$d_{eff}$	1.77 pm/V
Phase matching angle	38.4°
Walk off (o,e)	0.00 mrad, 72.89 mrad

The UV light (at 313 nm) passed from the cavity to an AOM (Intra-Action Model #ASM-802B8.<sup>4</sup> The negative first order diffracted spot (with a frequency shift  $\Delta\nu = -80$  MHz) was then sent to the trap. Thus, by turning the rf which drove the AOM on and off, we could turn on and off the UV at the trap. Details of the rf switching will be discussed in Sec. 4.2.1. The conversion efficiency of this switch AOM was  $\approx 80\%$  when driven with  $\approx 2$  W of rf.

Since the Blue Doppler beam drove the cycling transition, which was our only observable in the experiment, it was imperative that this beam have stable intensity. For this reason, the Blue Doppler beam passed through a “noise-eater” AOM before the switch AOM. Blue Doppler’s intensity was monitored by fast photodiodes after the frequency-doubling ring, and the results were accumulated on a fast integrator, which derived an error signal. This error signal was mixed with the rf driving the noise-eater AOM in order to control the light intensity: intensity fluctuations were shunted into the AOMs first-order deflected beam. The undeflected beam thus exhibited reduced amplitude fluctuations (up to  $\approx 100$  kHz), and this beam was passed on to the Blue Doppler switch AOM. The noise-eater circuitry did not have a sample-and-hold capability, and so had to be placed before of the switching AOM.

From the switch AOMs, the light passed through a linear polarizer and then through a quarter-wave plate. This produced pure circularly polarized light so that the

---

<sup>4</sup> This was the same model as all the other UV AOMs.

ion could be illuminated by pure  $\sigma^-$  light.<sup>5</sup> The quantization axis for the ion was set with a magnetic field coil whose axis of symmetry was roughly coincident with the laser beam propagation direction. The coil was outside the vacuum envelope, about 15 cm in diameter, and about 7.5 cm from the ion trap, producing a field of about eight Gauss at the location of the ion with several Amperes of current passing through the coil. Fine adjustments of the quantization direction and nulling out of external fields (such as that due to the Earth's magnetic field) were accomplished with two similar coil coils at right angles to the first and an equal distance from the trap.

The UV was focussed onto the ion with a 10 cm focal length, UV lens, which was external to the glass vacuum envelope. This lens was mounted on an XYZ-translator. As indicated in Fig. 4.1, the Blue Doppler beam was combined with the Red Doppler on a 50-50 beam splitter. These two beams were then combined with the repumper (the weakest of the resonant beams) on another 50-50 beam splitter before passing through the polarizer, quarter-wave plate, the lens, the vacuum window, and into the trapping region.

The repumper beam line was quite similar in its features to the Doppler beam line. The main differences were in the dye laser and in the crystal used for frequency doubling. The dye laser used to produce 626 nm light for the repumper beam was a Jim Bergquist-designed, "home-built" ring laser. The ring cavity had a free spectral range of 100 MHz. Single direction lasing was ensured by an optical diode in the ring cavity, and frequency selectivity was achieved by a manually-tuned birefringent filter (200 GHz free spectral range),<sup>6</sup> a galvanometer-driven thin etalon (20 GHz free spectral range) and a thick etalon assembly (1.6 GHz free spectral range).<sup>7</sup> Fine tuning was accomplished with a piezo-mounted mirror which was one of the ring cavity mirrors. The laser was

---

<sup>5</sup> A method for peaking up the polarization of the light is discussed in Appendix A.

<sup>6</sup> This birefringent filter assembly was purchased from Coherent Radiation, Inc., and was the assembly used in their 699

<sup>7</sup> Again, this thick etalon assembly was the same as used in Coherent's Model 699

kept on-mode with a dither-lock feeding back to the thick etalon — this kept the laser at maximum output intensity. Short-term frequency stability was ensured by locking the laser to an external Invar cavity (750 MHz free spectral range) using a Hänsch-Couillaud scheme to feed back to one of the ring-cavity mirrors. (This is in contrast to the Coherent 699, which uses a side-lock technique.) Unlike the 699 laser, the home-built laser did not have a Brewster-angle plate; however, it was still possible to scan the laser frequency by approximately 2 GHz. With 5.6 W of pump light, the laser typically put out between 650 and 750 mW, depending on the age of the dye and the day-to-day condition of the laser cavity. With the described locking scheme, the linewidth of the laser varied between 50 and 200 kHz, again depending on the day-to-day condition of the laser cavity.

As with the Doppler laser, a small portion of the output of this laser was split off with a beam splitter, and sent to the spectrum analyzer and travelling-cart wavemeter. The rest of the light passed through a high-frequency AOM: the undeflected beam was coupled through a single-mode optical fibre to the UV table, whereas approximately 30 mW in the negative first-order diffracted beam was sent off to a saturated-absorption iodine spectrometer.

This iodine setup, which is shown in Fig. 4.3(b), was used for long-term frequency stability of the repumper. The apparatus was very similar to that described above for the  $I_2$  lock of the 699 dye laser, except that the double-pass AOM was absent in the repumper beam line. The error signal from the lock-in amplifier was fed back to the piezo-mounted cavity mirror of the laser ring cavity. The high-frequency splitter AOM which deflected the beam into the  $I_2$  set up was driven with 661 MHz rf, the modulating AOM shifted the pump beam by  $\Delta\nu = -80 \text{ MHz} = \nu'_{mod}$ , and, as Fig. 4.2 shows, the UV switch AOM added a frequency shift of  $\Delta\nu = +80 \text{ MHz}$  to the UV (instead of the -80 MHz in the Doppler beams). The laser was locked to Feature (a) of Line # 954 of iodine [101], which is shown in Fig. 4.4(b). Thus, the complete frequency offset between

Table 4.2: Optical characteristics of rubidium dihydrogen phosphate (RDP) at 626 nm and room temperature [104]. The second-harmonic generation scheme uses Type I phase-matching: 626 nm (ordinary ray) + 626 nm (extraordinary ray) = 313.0 nm (extraordinary ray).

property	value
refractive index (o,e)	1.51, 1.49
$d_{eff}$	0.379 pm/V
walk off angle (o,o,e)	0 mrad, 0 mrad, 3.02 mrad

the iodine frequency  $\nu_{I_2}$  and the frequency  $\nu_r$  of the repumper light at the ion satisfied

$$\begin{aligned}
 \nu_r &= 2\nu_{I_2} + 2 \times 661 \text{ MHz} + 2 \times \frac{1}{2}\nu'_{mod} + 80 \text{ MHz} \\
 &= 2\nu_{I_2} + 1362 \text{ MHz}.
 \end{aligned}
 \tag{4.4}$$

The 626 nm light in the repumper beam line was doubled by single-passing it through an rubidium dihydrogen phosphate (RDP) crystal. The relevant optical characteristics of RDP are at 626 nm are shown in Table 4.2. The crystal was 5 cm long, and was cooled (using a thermoelectric cooler) to  $-1.86^\circ\text{C}$  for  $90^\circ$  (non-critical) Type I phase matching. The red light was focussed into the crystal with a 10 cm focal length lens. With 200 mW of power at 626 nm, the crystal produced  $\approx 17 \mu\text{W}$  of 313 nm UV light, which corresponds to  $\eta_{nl} \approx 3.5 \times 10^{-4}/\text{W}$ . As indicated in Fig. 4.2, the UV passed through a +80 MHz switch AOM, before being combined with the Red and Blue Doppler beams on a 50-50 beam splitter and passing into the trap.

#### 4.1.2 The Raman Beam Line

The Raman beams were produced by another home-built ring dye laser, of the same design as that which produced the repumper light. This laser was locked to an external Invar cavity similar to that in the repumper setup, which provided frequency stability. Since stimulated-Raman transitions were used to couple the ion's spin and motion (see Ch. 3), the overall laser frequency stability was not as important as that

of the frequency difference of the two Raman beams. This difference frequency was set by a high-frequency AOM (driven at 550 MHz) through which the Raman light passed before being coupled into two single-mode fibres and over to the UV table (see Fig. 4.6). Drifts in the overall Raman laser frequency produced only higher-order effects in the laser coupling to the ion: from Eq. (3.27),

$$\begin{aligned}\delta\Omega &= \frac{g_2^* g_1}{\Delta_R^2} \delta\Delta_R \\ \Rightarrow \frac{\delta\Omega}{\Omega} &= \frac{\delta\Delta_R}{\Delta_R},\end{aligned}\tag{4.5}$$

where  $\delta\Delta_R$  is the fluctuation in the Raman laser detuning. For this reason, it was not necessary to stabilize the laser to a narrower linewidth than the 50–100 kHz it exhibited when locked to the external Invar cavity. Nor was it necessary to lock the Raman laser to an iodine feature for long-term stability.<sup>8</sup>

Once the 626 nm light passed through the optical fibres to the UV table, it was coupled into a two-ring buildup cavity of the same design as that in the Doppler beam lines. The 626 nm light was doubled in BBO. The design parameters and the doubling efficiency of this setup were the same as with the Doppler beam rings.

From the doubling ring, the Blue Raman (which was detuned by  $\Delta_R$  from the  $|\downarrow\rangle \leftrightarrow |v\rangle$  transition) beam passed through a noise-eater detector and AOM setup identical to that in the Blue Doppler beam line. The undeflected beam from the noise-eater AOM (which had reduced amplitude fluctuations) then passed through a switch AOM driven at 80 MHz: the negative first-order beam was selected for use in the experiment. This beam was combined with the Red Raman (detuned by  $\Delta_R$  from the  $|\uparrow\rangle \leftrightarrow |v\rangle$  transition) co-propagating beam on a polarizing beamsplitting cube, and then focussed onto the ion by a 10 cm focal length lens, which was mounted on an XYZ-translation stage.

---

<sup>8</sup> The Raman laser typically exhibited a drift rate of  $\approx 200$  MHz/h.

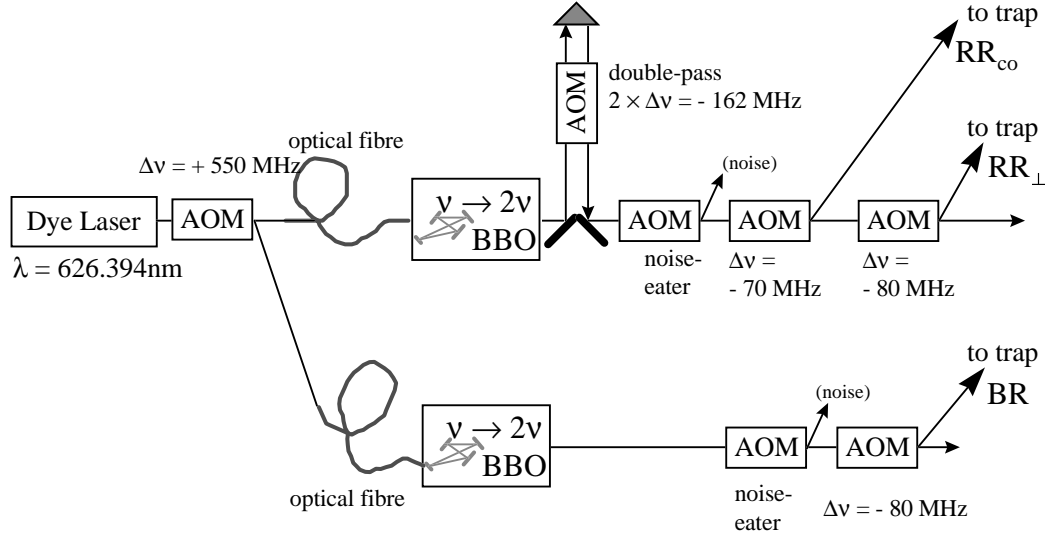


Figure 4.6: Raman beam line. The Red and Blue Raman beams were split in the red, then sent to the UV table through optical fibres. Blue Raman was detuned by  $\Delta_R$  from the  $|\downarrow\rangle \leftrightarrow |v\rangle$  transition, while Red Raman was detuned from the  $|\uparrow\rangle \leftrightarrow |v\rangle$  transition. Since we used Raman transitions to couple spin and motion, frequency fluctuations of the laser were not significant to first order. For this reason, no  $I_2$  lock was needed. The double-pass AOM in the Red Raman beam line determined the overall frequency separation of the Red and Blue beams: the double-pass configuration allowed us to scan the frequency over a large (30 MHz) range without introducing appreciable beam steering.

The Red Raman UV beam line was somewhat more complicated. This beam had the frequency-control elements in it. It was also split into two, independent beam lines: the co-propagating<sup>9</sup> ( $RR_{co}$ ) and the perpendicular ( $RR_{\perp}$ ) beams. From the doubling ring, the Red Raman UV beam went to a double-pass AOM which set the overall difference frequency between the Blue and Red Raman beam lines. The rf which drove this AOM came from a switchable rf multiplexer, which could switch one of many different rf sources to the AOMs rf input. By selecting the frequencies of these rf sources appropriately, we could drive any of the interesting ion-laser couplings (see Ch. 3): carrier, blue sideband, red sideband, etc. Usually, a frequency of approximately 80 MHz

<sup>9</sup> This beam, in conjunction with the Blue Raman beam, drove transitions for which  $\Delta\mathbf{k} \approx 0$ , which were insensitive to the ion's motion (see Sec. 3.3).

sent to the double-pass AOM drove the carrier transition (90° configuration): this frequency corrected for Zeeman shifts of the atomic levels due to the applied quantization magnetic field (see above). The details of the rf switching will be discussed in Sec. 4.2.1. The double-pass configuration of the AOM allowed us to change the frequency of the Red Raman beam by a large amount (up to 30 MHz) without appreciable beam steering.

After the double-pass AOM, the beam passed through a noise-eater AOM setup similar to those in the Blue Doppler and Blue Raman beam lines. Since the noise-eater was downstream of the double-pass AOM, it could correct for imbalances in the rf levels of the various synthesizers which drove the double-pass.

Having passed through the noise-eater AOM, the Red Raman beam continued on through an AOM which split the perpendicular and co-propagating Red Raman beams. This AOM was driven with 80 MHz rf, and the negative, first-order deflected beam was combined on a polarizing beamsplitting cube with the Blue Raman beam (see above). This beam constituted the co-propagating (“...with the Blue Raman”) beam, and could be switched off by turning off the rf driving the “splitter” AOM. The undeflected beam from the splitter AOM passed into a final AOM (the “Red Raman switch”) driven with 80 MHz rf, and the negative, first-order deflected beam passed through a 10 cm focal-length lens (mounted on an XYZ-translation stage) and into the trap.

From Fig. 4.6, we may determine the frequency differences between the  $RR_{co}$  and  $BR$  beams, and between the  $RR_{co}$  and  $RR_{\perp}$  beams at the ion. These are:

$$\begin{aligned} \Delta\nu_{BR,RR} &= 2 \times 550 \text{ MHz} - 80 \text{ MHz} + 2\nu_{dp} + 80 \text{ MHz} \\ &\approx 1100 \text{ MHz} - 80 \text{ MHz} + 2 \times 81 \text{ MHz} + 80 \text{ MHz} \\ &= 1262 \text{ MHz} , \end{aligned} \tag{4.6}$$

$$\Delta\nu_{co,\perp} = -80 \text{ MHz} + \nu_{splt} . \tag{4.7}$$

In Eq. (4.6),  $\nu_{dp}$  is the frequency driving the double-pass AOM: for the last equality, I have assumed that this frequency was set to drive the carrier transition. In Eq. (4.7),

$\nu_{splt}$  is the frequency driving the splitter AOM: had this frequency been set to 80 MHz, then the two carrier transitions (perpendicular and co-propagating) would have been at the same double-pass frequency. In practice, the frequency was usually set to  $80 \text{ MHz} - \omega_m/2\pi$  so as to allow coherent-state generation (see Sec. 6.1.3), so that the two carrier transitions did not correspond to the same double-pass AOM frequency.

#### 4.1.3 Revisions to the Laser Beam Lines

The optical setup described above held for many of the experiments described in this thesis. However, two major changes were made to this setup in the spring of 1998. One involved the resonant beams, and the other involved the Raman beams.

The Coherent 699 laser used to produce the Doppler beams frequently exhibited a linewidth of  $\approx 4 \text{ MHz}$  at 626 nm. This translated into a spectral width of  $\approx 8 \text{ MHz}$  in the UV — a substantial fraction of the  ${}^9\text{Be}^+$  excited-state linewidth. The laser noise produced a widening of the normally Poissonian photon distributions of the cycling transitions (see Sec. 3.1). Since the homemade lasers had much narrower linewidths, we decided to use what had formerly been the repumper dye laser to drive the cycling transition, and the 699 as a repumper. However, we continued to use the 699 to produce the Red Doppler beam. This necessitated changing the Red Doppler transition from being resonant with the  $|\uparrow\rangle \rightarrow |2p^2P_{3/2}\rangle$  transition to being resonant with the  $|\uparrow\rangle \rightarrow |2p^2P_{1/2}\rangle$  transition. However, this was a minor change. This switch in laser roles had the desired effect on the photon statistics.

A second major change was prompted by the discovery that the single-mode fibres used to translate the Red and Blue Raman beams from the red table to the UV table introduced significant phase noise between the two beams. This problem was resolved by the purchase of several 250 MHz UV AOMS, which enabled the  $\approx 1.25 \text{ GHz}$  hyperfine splitting between the Red and Blue Raman beams to be achieved in the UV. In the new scheme, the 626 nm light was transported to the UV table with a single fibre, and then

doubled. The double-pass AOM frequency was changed slightly, but the Red Raman splitter and the Red Raman switch frequencies were kept the same. A high-frequency AOM was placed upstream of the double-pass AOM and driven at 257 MHz. Its positive, first-order diffracted beam was then passed through three other AOMs, all driven at 257 MHz. In each case, the positive, first-order beam was passed on to the next AOM, and the resulting beam was taken as the Blue Raman, with the last high-frequency AOM being used as the new Blue Raman switch.<sup>10</sup> The total frequency separation of the Red and Blue Raman beams at the trap was thus given by

$$\begin{aligned}
 \Delta\nu_{tot} &= 4 \times 257 \text{ MHz} + 2 \times \nu_{dp} + 80 \text{ MHz} \\
 &\approx (1028 + 2 \times 77 + 80) \text{ MHz} \\
 &= 1262 \text{ MHz} = \omega_0/2\pi .
 \end{aligned}
 \tag{4.8}$$

A schematic of the modified Raman beam line is shown in Fig. 4.7.

#### 4.1.4 Photon Detection

Fluorescence from the ion was collected by an  $f/1$  optical system, the details of which are shown in Fig. 4.8. This system consisted of two lenses, with an aperture between the two.

The first lens was a six-element compound lens (designed by Howard Smith and assembled by Coastal Optics), with a working distance of 40 mm. A 600  $\mu\text{m}$  diameter aperture was located at the position of the primary focus. After passing through this aperture, the collected fluorescence was focussed by a second lens (a 2.5 cm focal length, Newport UV doublet consisting of two, 5 cm lenses) onto either one of two photon counting devices (see below). The magnification of the first lens assembly was 5 and that of the second was 25, for an overall magnification of 125.

---

<sup>10</sup> The higher frequency operation had the added benefit of increasing the angular separation of the different diffracted orders, making it easier to separate the desired order from the others and reducing stray light

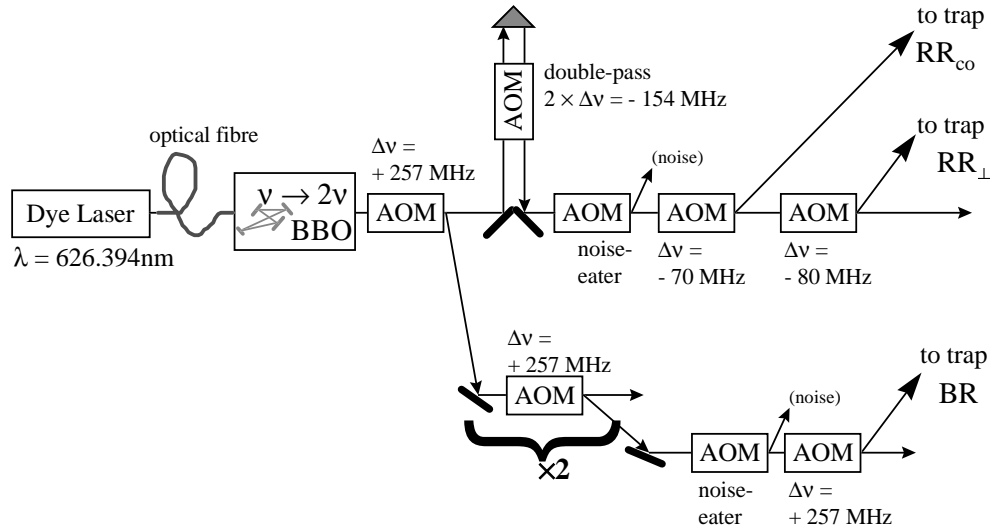


Figure 4.7: Raman beam line as modified to avoid fibre-induced, differential phase noise in the Red and Blue Raman beams. The 626 nm light now passed to the UV table through a single fibre, and was frequency doubled to 313 nm before being split. The Red Raman beam line was identical to before (see Fig. 4.6). The Blue Raman beam passed through four, 257 MHz AOMs in order to pick up a frequency shift with respect to Red Raman equal to the hyperfine splitting plus Zeeman shifts.

The fluorescence was either imaged onto a micro-channel plate imaging tube or a photomultiplier tube (PMT). The former was convenient for forming an image of the trapped ion and its environs, but had lower quantum efficiency than the photomultiplier tube. For this reason, the imager was used for loading the trap, but the PMT was usually used for taking data.

Two imager tube systems were used in the experiments described in this thesis. The first was manufactured by Quantar Technologies. It had a quantum efficiency of  $\approx 5\%$ . The second was produced by Photek, and had roughly the same quantum efficiency. Both tubes produced voltage outputs proportional to the  $x - y$  position of the detected photons: these outputs could be displayed on an oscilloscope, producing a real time image of the fluorescing ion. In addition, both tubes had digital outputs which allowed an integrated picture to be displayed on a computer. The inset of Fig. 2.2 shows

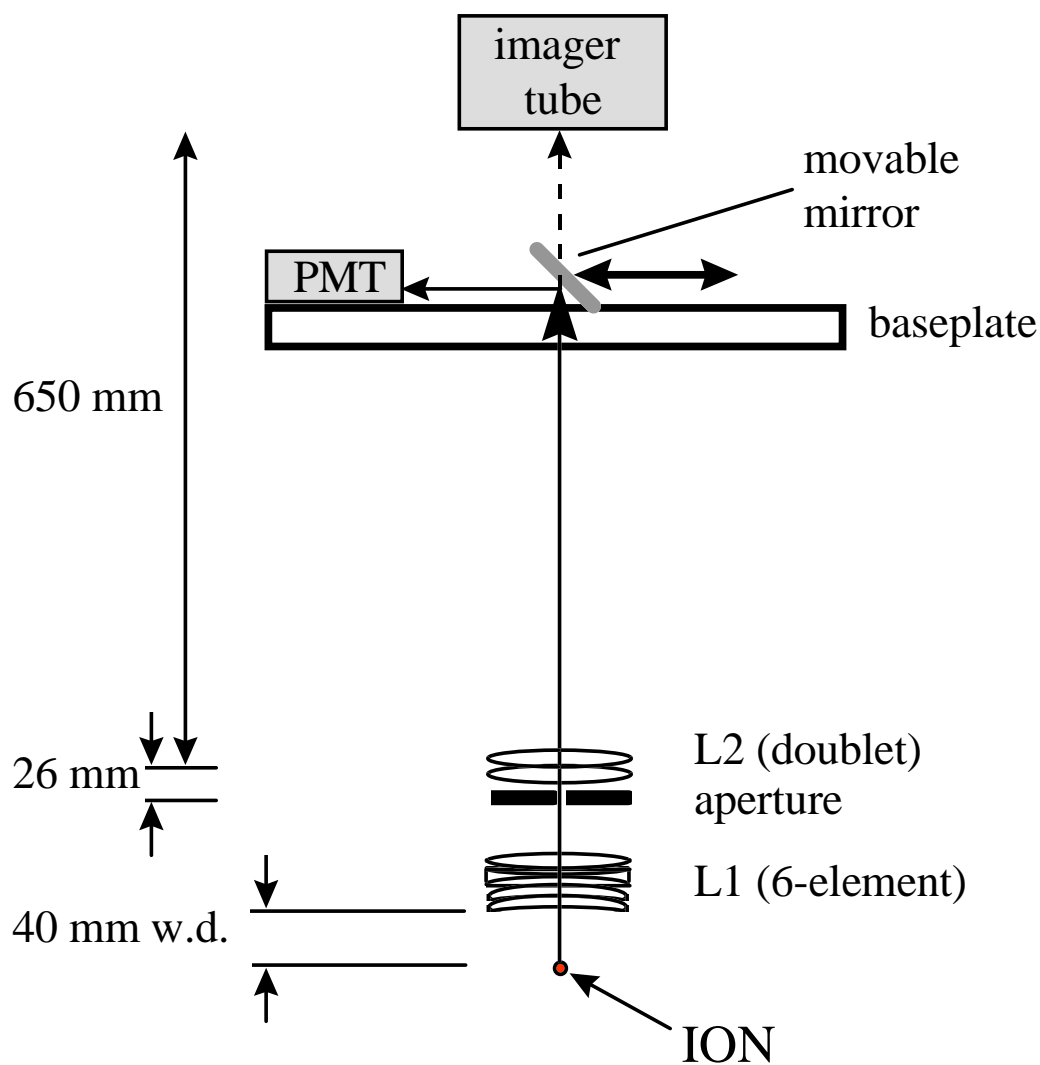


Figure 4.8: Schematic of the imaging optics. The first lens was a custom-made (Howard Smith, design/Coastal Optics, assembly) six-element lens with a working distance of 40 mm. The second was a 2.5 cm focal length Newport UV doublet. The overall magnification of the system was 125, and its  $f/\#$  was equal to one.

an image of two trapped ions held in the beryllium-electrode elliptical microtrap. These data were taken with the Photek imager. Finally, both imaging tubes output a TTL-compatible pulse for every photon they detected. These pulses could then be counted by the data-acquisition system (see Sec. 4.2.2), or converted to an average count rate. The photomultiplier tube was a Hamamatsu Model #H6240-01 “side-on” PMT. Its quantum efficiency was  $\approx 20\%$ . This unit takes +5 V in and puts out a TTL-compatible pulse for every photon it detects.

The imager tube (whichever one was in use) and the photomultiplier tube were mounted on the base plate (see Fig. 4.8). The imager was mounted facing the ion and the PMT at right angles. The fluorescence was usually focussed directly onto the imager photo-anode. However, by putting a  $45^\circ$  mirror into the path of the fluorescence, the light could instead be diverted onto the PMT’s window. This mirror was mounted on a motorized stage, and the whole assembly was made light-tight.

When counting photons with the photomultiplier tube, the overall detection efficiency of the system was calculated from the measured ion fluorescence to be  $\approx 8 \times 10^{-3}$ , when it was used with the linear trap. The detection efficiency includes effects due to the ion’s dipole radiation pattern, the solid angle of the detection system, losses in the optics, and the quantum efficiency of the PMT. Due to said dipole radiation pattern, the detection efficiency with the elliptical traps was two-thirds this value (since these traps were viewed at  $90^\circ$  to the plane of the laser beams).

## 4.2 Experiment Control and Data Acquisition

Before delving into the details of the control logic for the experiment, or into the details of the photon-counting, it will be worthwhile to provide an overview of how the experiment ran. Each single experiment generically consisted of four parts: (1) laser cooling (Ch. 5) and optical pumping to  $|\downarrow, n=0\rangle$ , (2) quantum state engineering (Chs. 6 through 9), (3) mapping motional information onto the spin (Sec. 3.5), and (4)

measuring fluorescence on the cycling transition (Sec. 3.1 and Appendix A). Of course, sometimes certain of these parts were absent, or mingled together: as an example, in creating Schrödinger cat states (see Sec. 6.2.1), the state engineering was actually sandwiched between two parts of the motion/spin mapping.

In taking data, the experiment was usually repeated many times while some parameter was changed. To be more concrete, let us assume that the particular experiment at hand consists of creating some motional state and then taking a Rabi flopping curve (Sec. 3.2) on the blue sideband. To acquire such a curve, we would change the parameter  $t_{pr}$ : the length of the blue sideband “probe” pulse. At each value of  $t_{pr}$ , we would, in principle, repeat the experiment enough times to obtain good signal-to-noise on the probability  $P_{\downarrow}$  that the atom is in  $|\downarrow\rangle$  after the probe pulse. In actuality, the dwell time was chosen to make the settling time of the pulse-producing instrument negligible with respect to the dwell time. Typically, about one hundred experiments were taken at each value of  $t_{pr}$ . By repeating this procedure for  $t_{pr}$  ranging from zero to  $t_{max}$ , we would obtain a curve such as Fig. 3.4(b).

A typical experiment took about one millisecond to execute, so that each data point took about one-tenth of a second. Thus, for example, the entire Rabi flopping curves of Fig. 3.4 took about 20 s to obtain.

The experiment thus consisted of two time scales: a fast time scale on which, in the course of a single shot, the various laser beam combinations needed for cooling, state creation, and mapping were turned on and off, and a slower time scale on which (every ten to one thousand repetitions of the single shots), parameters such as the length or frequency of the probe pulses were changed. This latter time scale was the time scale on which the data acquisition took place. I shall describe this in Sec. 4.2.2. First, however, I shall discuss the laser beam switching.

### 4.2.1 Switching Logic

A diagram showing the control aspects of a single experiment is shown in Fig. 4.9. As this diagram indicates, it was necessary not only to switch laser beams on and off in various combinations, but also to change the frequency of the Red Raman beam within the course of a single experiment. This change in frequency was accomplished by changing the frequency of the rf sent to the Red Raman double-pass AOM. The on/off switching for all the beams was accomplished by switching on and off the rf driving the various “switch” AOMs. Typical pulse lengths ranged from sub-microsecond (for a carrier transition) to hundreds of microseconds (for driving the cycling transition).<sup>11</sup>

The rf control (both on/off and frequency) was accomplished through a large rf “switchbox.” The heart of this box were the Mini-Circuits ZYSWA and GSWA, TTL-controlled rf switches. The ZYSWA switch has two rf inputs and one rf output (although the switch could also equally well work in reverse configuration with one input and two outputs). A TTL input controlled which of the two rf inputs was connected to the output. If only one rf input was connected to an rf source, the switch functioned as a TTL-controlled on/off switch. If both inputs were connected to rf sources, the switch acted as a multiplexer. The TTL inputs floated high (logic 1). The GSWA is a four input version of the ZYSWA and, for our use, four of these were wired up as a 16- input multiplexer, controlled by four TTL lines.

The rf portion of the rf switchbox contained the 4-bit, 16-input multiplexer, two 2-bit, 4-input multiplexers, and seven (one-input) on/off switches. The box also contained some TTL logic, which I will discuss below. A schematic of these parts of the rf switchbox is shown in Fig. 4.10(a).

---

<sup>11</sup> Of course, these values are meant to be representative. The actual pulse lengths were determined by the relevant Rabi frequencies, which depended on the laser power, beam waist at the ion, Raman laser detuning from the  $2p \ ^2P_{1/2}$  level, etc. These factors varied from day to day and from week to week. However, this variation was rarely more than a factor of two.

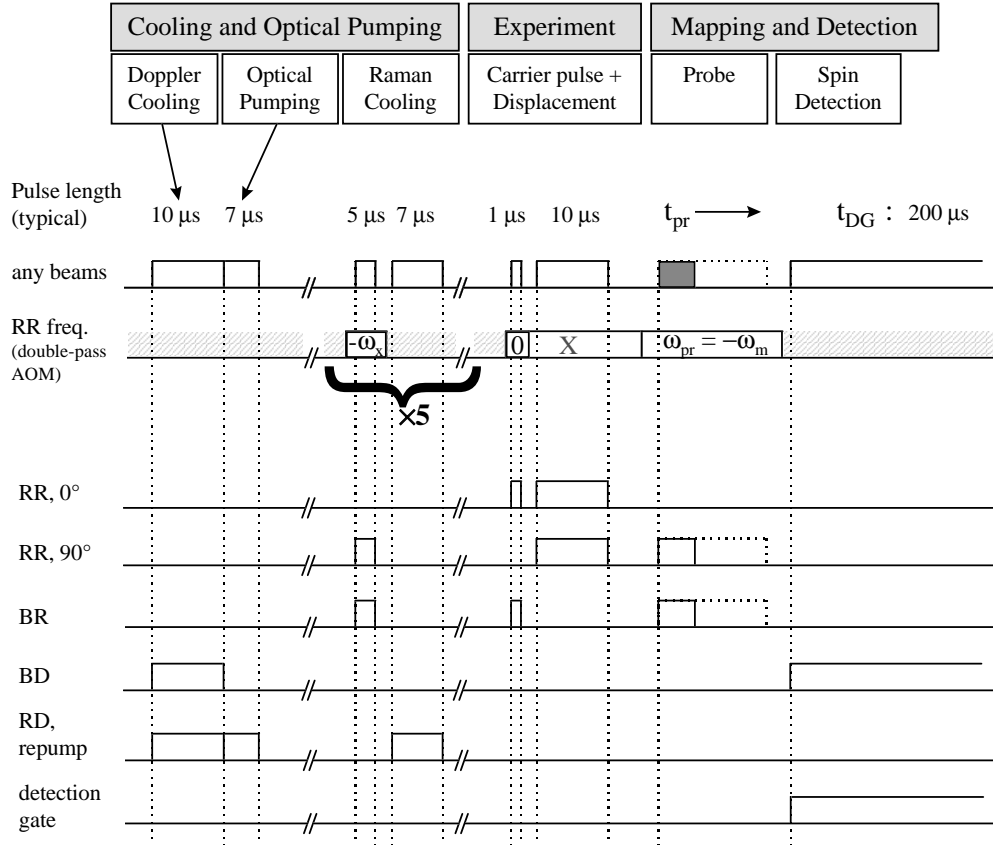


Figure 4.9: Timing diagram for a typical experiment. In this experiment, a coherent state (Sec. 6.1.3) is created in  $\uparrow$ , then a Rabi flopping curve is taken on the red sideband. The experiment consists of (1) Doppler cooling (2) optical pumping to  $|\downarrow\rangle$  by Red Doppler and the repumper (3) Raman cooling (4) a  $\pi$ -pulse on the co-propagating carrier to flip the spin (5) a  $10 \mu$ s coherent displacement pulse on the two Red Raman beams (“walking standing wave”) (6) a probe pulse on the red sideband for variable time  $t_{pr}$  (7) detection of  $P_{\downarrow}(t_{pr})$  by driving the cycling transition with Blue Doppler. The indicated pulse lengths are typical values.

The 16 input multiplexer controlled the rf signal source which was sent to the Red Raman double-pass AOM. Each frequency of interest (i.e. corresponding to the blue sideband, the red sideband, the co-propagating or perpendicular carrier, etc.) was derived from a separate rf synthesizer, and this rf source was selected at the appropriate point in the experiment. We typically used either Fluke Model #6160B or HP Model #3335A synthesizers. The “probe” frequency, however, had to be swept when we

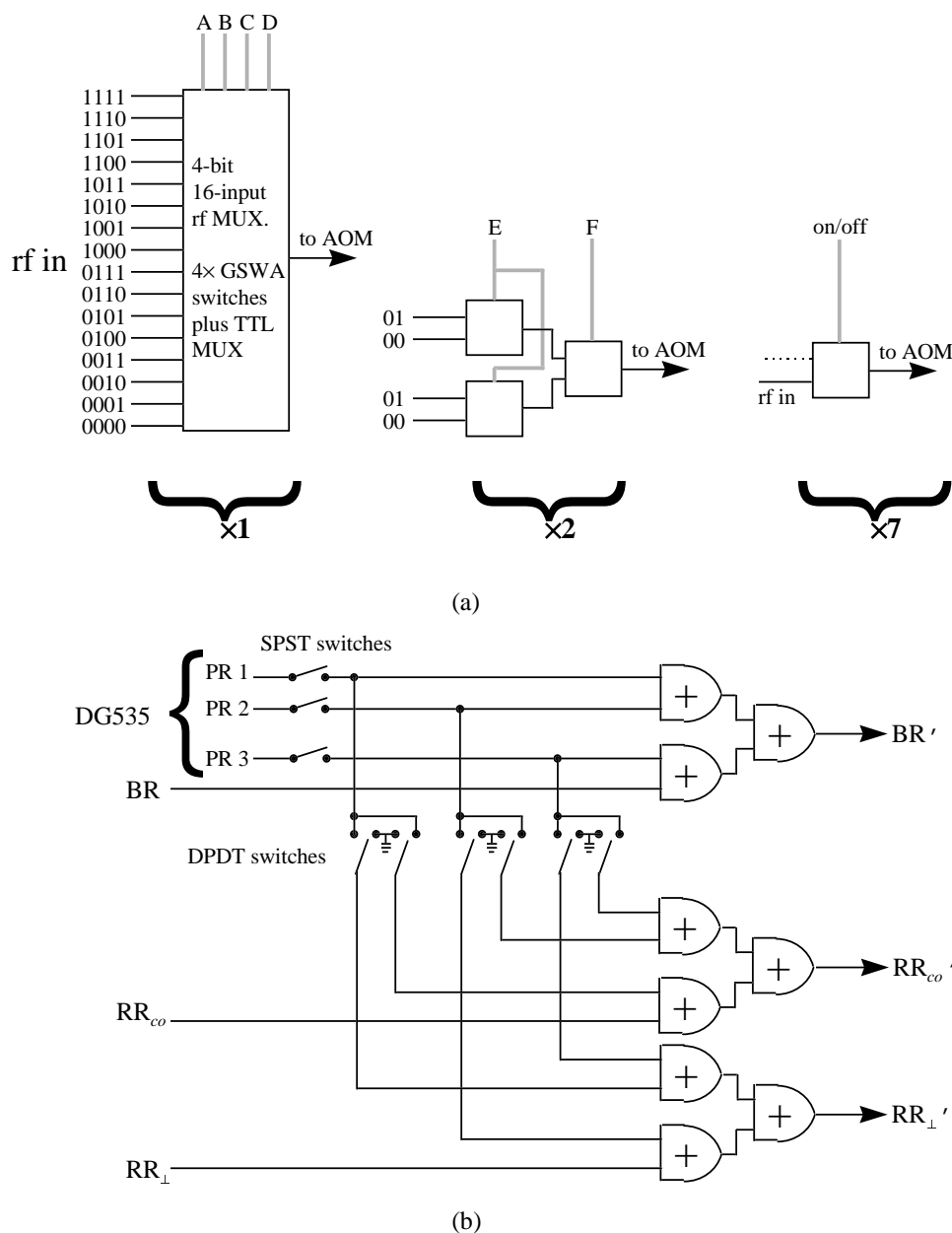


Figure 4.10: (a) Schematic of the rf portion of the "rf switchbox" circuitry. The individual rf switches were Mini-Circuits ZYSWA, TTL-controlled rf switches. These either operated as on/off switches, or were cascaded together to make rf multiplexers. The box contained one 4-bit, 16-input multiplexer, two 2-bit, 4-input multiplexers, and seven rf on/off switches. (b) Schematic of the TTL circuitry inside the "rf switchbox." This circuitry performed a logical OR operation between the BR, RR, and/or Co outputs of the HP 8175 and the output of the Stanford Research DG535 "probe" pulse generator.

wished to take spectra. The rf source for this pulse was a GPIB-controlled HP Model #8660D. The GPIB interface was fast enough to allow the frequency to change in a few milliseconds, as will be discussed in Sec. 4.2.2. All the rf synthesizers driving the UV AOMs were phase-locked together.

One of the two 4-input multiplexers was used to switch in different rf sources to the Red Raman splitter AOM, which separated the co-propagating from the perpendicular Red Raman beams. These two beams were turned on simultaneously to create coherent or squeezed states using the “walking standing wave” technique (see Sec. 6.1.3), and the multiplexer allowed us to switch rf of different phases to the splitter AOM, thus putting different relative phase shifts between the co-propagating and perpendicular Red Raman beams. Note that the rf could also be turned off by not connecting one of the inputs to an rf source, and selecting that vacant input when the co-propagating Red Raman beam was wished to be off.

The other 4-input multiplexer was usually left unused. It was, however, used for creating coherent states (Sec. 6.1.3) by driving the trap electrodes with electric fields (oscillating at the trap frequency) — again, the multiplexer allowed us to switch in rf of different phases. It was also used in trying the Sørensen and Mølmer scheme for creating maximally entangled states (Sec. 6.4.2).

The TTL control pulses which turned the rf switches on and off and selected the rf multiplexer inputs were produced by an HP Model #8175 digital pulse generator. This instrument has up to 24 TTL output channels. By setting the appropriate control bits, any combination of the outputs can be set to logic 0 or 1 (0 or  $\approx 5$  V). The 8175 scans through its memory one 24-bit word at a time, and sets the appropriate TTL values on its outputs. The length of time spent at each 24-bit word is programmable: it may be any length of time from 20 ns to one second. This allows one to efficiently output a pulse sequence even if it contains pulses of widely varying lengths (for example, a carrier  $\pi$ -pulse versus driving the cycling transition). The repetition rate at which the HP 8175

repeated its scan through its memory was set by a Stanford Research Model #DG535 digital pulse generator: each pulse from the DG535 triggered one scan through the HP 8175's memory. The frequency of the pulses from the DG535 was set to be the inverse of the sum total of the pulse lengths in a single shot of the experiment.<sup>12</sup>

The HP 8175 output the four control bits for the 16-input multiplexer and the four control bits for the two 4-input multiplexers. It also output the on/off signals for the Red Doppler (RD) (which also controlled the repumper switch), Blue Doppler (BD), the Blue Raman (BR), Red Raman perpendicular (RR), and Red Raman co-propagating (Co) beams. However, the HP 8175 output for these latter beams was logically OR-ed with the output of a second Stanford DG535 pulse generator, as will be discussed below. The HP 8175 also put out the TTL-logic Detection Gate (DG) pulse, which determined when photons detected by the imager tube or the photomultiplier tube were counted by the data acquisition systems. Finally, it put out trigger signals for the "probe" DG535 and trigger signals which could be used to change the trap voltages (to change the trap frequency or to move ions around in the trap).

In the course of taking data, it was desirable to be able to quickly change the length of the probe pulse. This probe pulse consisted of either Blue and Red Raman, or Blue Raman and the co-propagating Red Raman beam. As discussed in the introduction to this section, this probe length had to be changed every ten to hundred milliseconds. The GPIB interface for the HP 8175 was far too slow to allow this. For this reason, and to allow differing configurations of the probe pulse, the probe pulse was created by the second DG535 pulse generator, which was triggered by the HP 8175 at the appropriate point in each experiment. This pulse was then logically OR-ed with the Blue Raman (BR) 8175 output and either the Red Raman (RR) or co-propagating Red Raman (Co) output. The circuitry to do this was housed inside the rf switchbox, and is shown

---

<sup>12</sup> with some extra time added in for a margin of error

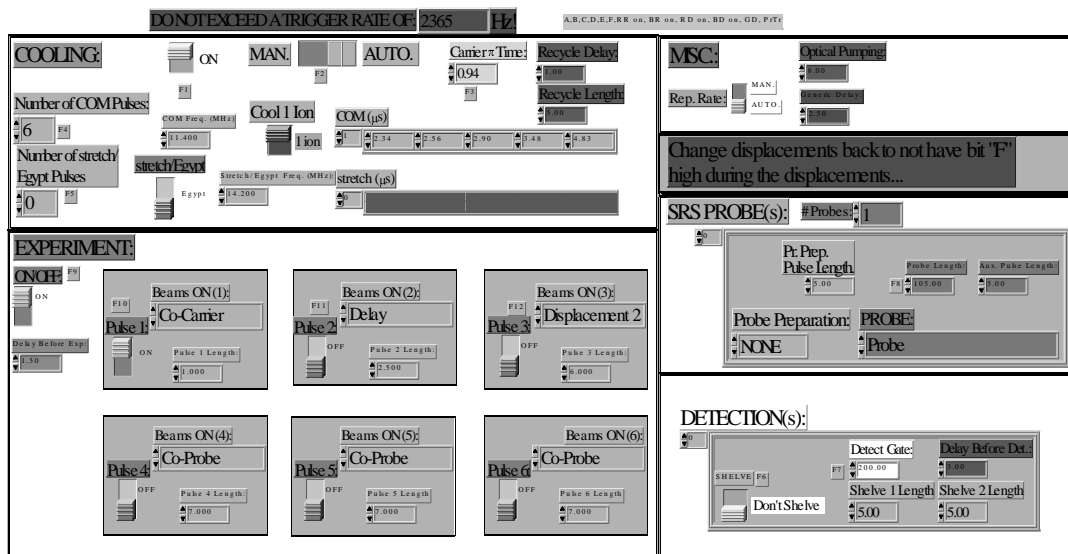


Figure 4.11: User interface for the LabView program which set up the HP 8175 pulse generator to run the experiment. This program offered the user a convenient, menu-like means of selecting which laser beams to turn on, then converted this information to ASCII arrays of “which beams” and pulse length information, then downloaded these arrays to the HP 8175.

in Fig. 4.10(b). The length of the probe pulse was controlled by the data acquisition programs (see Sec. 4.2.2).

The GPIB control of the HP 8175 was accomplished through a LabView program running on a PC. This program offered a convenient user interface, which allowed us to select pulse combinations and pulse lengths in a menu-like format. The user interface to the program is shown in Fig. 4.11. Once the desired sequence of pulses was selected, the program produced an array of pulse lengths and a corresponding array of “which beam is on” information, and transmitted these arrays in ASCII format to the HP 8175 according to the IEEE 488.2 (GPIB) interface standard.

#### 4.2.2 Data Acquisition

As mentioned in the introduction to this section, the data acquisition occurred on a slower time scale than that of a single experiment. Nonetheless, the data acquisition

equipment had to take in photon counts every experiment — that is to say, every millisecond — and change the probe pulse length, phase, or frequency every ten to hundred experiments. These timing requirements were too stringent to allow control by, say, a PC, and less straightforward methods were required.

Much of the data were taken on HP Model #9826 computers. These computers, which dated from the early 1980's, were old, but dated from a time when the microprocessors were “weighted down” by far fewer interrupts than those in modern PC's. When running the FORTH operating system/programming language, they were able to identify and service an experiment-generated flag in as little as tens of nanoseconds. Thus, they were more than adequate for our needs. The programs for these computers were written and maintained by Wayne Itano.

In their data-taking role, these computers worked with a home-built counter/buffer box. This box took in photon counts (which were logically AND-ed with the Detection Gate pulse from the HP 8175), and stored them in a buffer until the computer could process the data. A schematic of this counter/buffer box is shown in Fig. 4.12. The computer processed the data and updated the probe time, phase, or frequency by communicating with the appropriate device — Stanford Research DG535, HP 3335A, or HP 8660D, respectively — over the GPIB bus.

The programs used to take much of the data actually ran *asynchronously* with the experiment.<sup>13</sup> A separate clock set the rate at which the counter/buffer box accepted counts and passed them onto the computer, and also the rate at which the computer updated the instruments over the GPIB bus. The clock rate was set by hand to be roughly ten times (for spectra) or one hundred times (for flopping curves)<sup>14</sup> the experiment repetition rate. Although this meant that the exact number of experiments

---

<sup>13</sup> Synchronous versions of these programs were created, but the desire for familiarity led to continued use of the original program versions.

<sup>14</sup> The HP 8660D executed GPIB updates much more quickly than the DG535, and settled to its new parameter values faster. For this reason, the spectrum program could spend less time at each data point than the flopping program, as there was a smaller time period during which the parameter values were ambiguous.

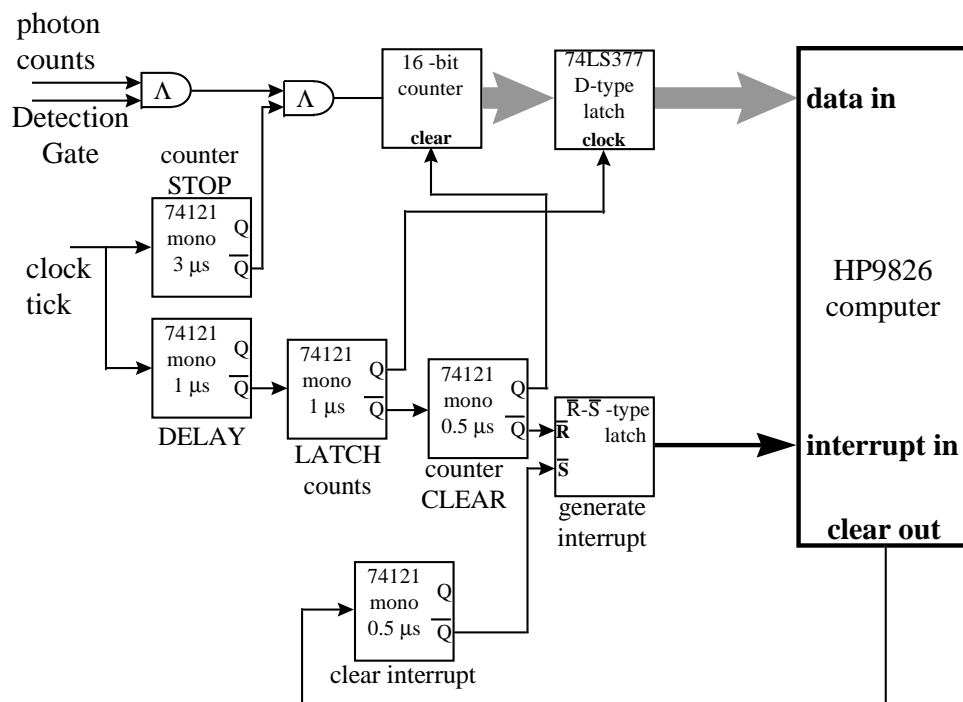


Figure 4.12: Schematic of counter/buffer box for data acquisition with HP 9826 computers. Upon receiving a clock tick, the “counter STOP” one-shot outputs a logic “low” which stops the counting. The value of the counter is then latched into the data latch, after which, the counter is cleared, and an interrupt for the HP 9826 is generated. The HP 9826 then reads the latched data, processes it, then clears the interrupt. The photon counts are “ANDed” with Detection Gate before passing on to the counter.

per data point differed at different data points (by perhaps one experiment), this was not significant. The same could be said for the settling time of the instruments after the GPIB update command received: this effect merely amounted to a smoothing of the data. In any case, the programs were carefully evaluated, and these effects were not found to be appreciable.

As alluded to above, there were three main types of programs run on the HP 9826 computers. The first was a spectrum-taking program, which changed the frequency of the probe HP 8660D synthesizer. Typically, each data bin was 10 ms long when using this program (although this was changeable), so that each data point consisted of about

ten experiments. The second type of program used was one which changed the length of the pulse put out by the probe DG535 pulse generator in order to take Rabi flopping curves. For this program, the dwell time was usually 100 ms per data point, or on the order of a hundred experiments. Finally, we used a third type of program to sweep the phase of the rf put out by one of the HP 3335AA synthesizers driving the Red Raman splitter AOM. This program was useful for taking Ramsey spectra, but was mostly used in the Schödinger cat experiments (see Sec. 6.2.1) and for density-matrix reconstruction (see Sec. 6.3). The dwell time with this program was also 100 ms per data point.

Various varieties of these programs were used at different times. Most of these were minor variations on the basic programs. However, it is worthwhile as an example to single out the program used to perform density-matrix reconstruction of the ion's motional state. As will be discussed in Sec. 6.3, this required us to displace the motional wave packet in various directions in the  $z-p$  plane. This was done by applying different rf phases to the Red Raman splitter AOM. For each phase, the probabilities  $P_n$  that the ion was in the motional Fock state  $|n\rangle$  had to be determined from blue sideband Rabi flopping curves. The data acquisition program for this experiment thus had two control loops. The inner loop changed the probe DG535 pulse length to obtain a Rabi flopping curve at each phase of the HP 3335A. Once a flopping curve was completed, the outer control loop then changed the phase of the HP 3335A.

As discussed at the beginning of this section, it was not straightforward to implement similar programs on a PC. Due to calls by different interrupts at different times, a PC cannot be trusted to execute data-acquisition code at sub-millisecond to millisecond timescales in a deterministic fashion. Nonetheless, it was possible to create programs which used plug-in data acquisition cards. These programs could not acquire data at the sub-millisecond level (as the HP 9826's could), but could reliably acquire data with only a few (2 to 5) milliseconds dead time in between acquiring one data point's data and being ready to receive the next point. The programs were thus suitable for our

experiments, and performed with no noticeable increase in experiment dead time. The programs were written in LabView.

The heart of these programs was a National Instruments PCI-MIO16E multi-function data acquisition board. This board featured two available “DAQ-STC” counter/timer chips, which allowed buffered counting. The photon counts from the imager tube or PMT were logically AND-ed with the Detection Gate pulse from the HP 8175, and sent to the input of one of the counters. Detection Gate also served as a clock to synchronize the counter’s acquisition of counts. These programs, therefore, were run *synchronously* with the experiment. The counters stored the number of photon counts at each Detection Gate “clock tick” into a different buffer location. Every few experiments, the PC was triggered to send a GPIB update to the appropriate instrument. The data at one instrument setting constituted one data point, as it had on the HP 9826 programs. Details of this set up are shown in Fig. 4.13.

On a longer timescale (usually two to four data points), the PC was triggered to read out the buffer, bin the data into the respective data points, average the data with corresponding previous data points, and update a graph with the new, averaged data.<sup>15</sup> Unfortunately, the AT-MIO-16E board could not generate a hardware interrupt from the counter chips. It was not possible, therefore, to simply count the number of Detection Gates received and send an interrupt to the PC after the appropriate number of experiments. However, the board did allow its analog input functions to generate interrupts upon completion of a channel scan. By using Detection Gate as the update clock of a “dummy” analog input scan, it was possible to achieve the desired effect.<sup>16</sup>

Each Detection Gate triggered the measurement of the voltage on an input of the D/A converter. At the end of one scan of the input channels, the D/A chip set a

---

<sup>15</sup> The graph update was the major bottleneck in the program. Unfortunately, it was not possible to run the graph update separately from the rest of the data acquisition program, due to LabView and Windows 95 OS constraints

<sup>16</sup> It was also possible to achieve the same end using an analog output scan — this could be convenient for experiments in which a trap electrode voltage is changed in the middle of an experiment

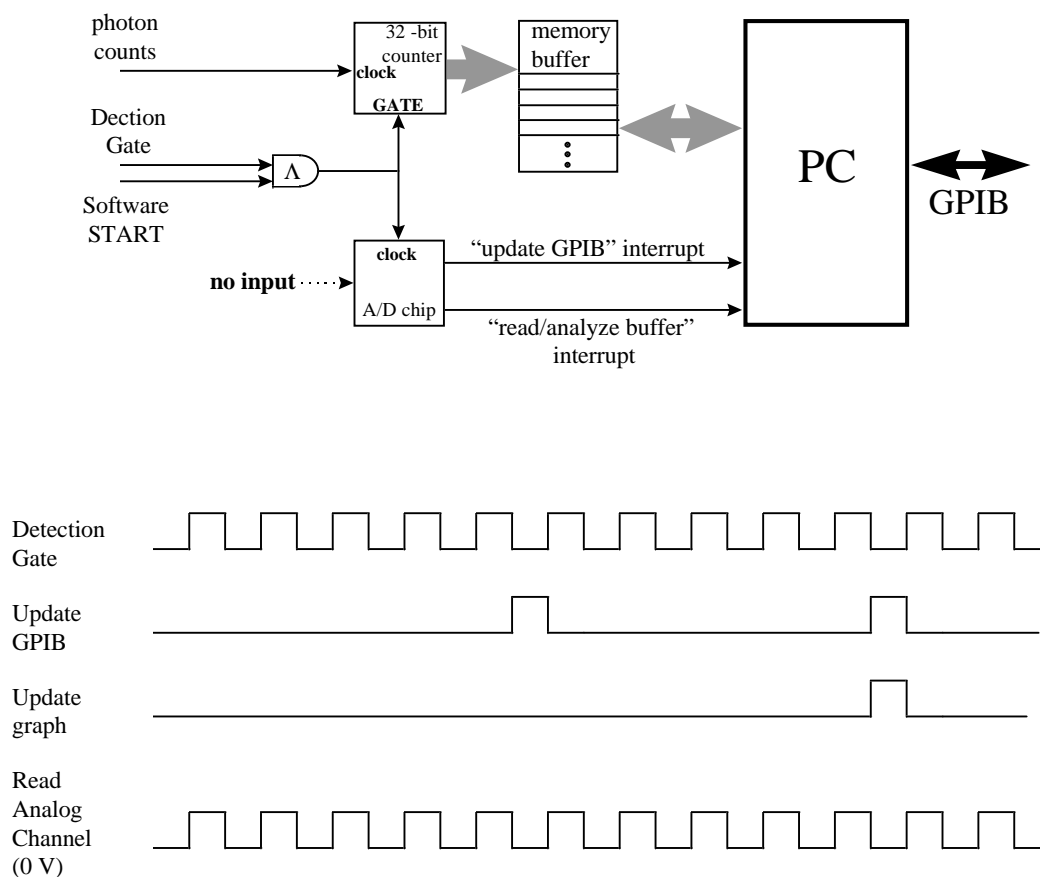


Figure 4.13: (a) Schematic of PC-based data acquisition system. Detection Gate serves both to gate the photon counts *and* as a data-acquisition clock. The counter latches its count value into memory every time its GATE (Detection Gate) goes low. In order to keep track of how many experiments have occurred, Detection Gate is used as the scan clock of a “dummy” analog input scan. This scan generated interrupts to tell the PC to update the probe instrument (DG535, HP 8660D, or HP 3335A) over the GPIB bus. On a longer time scale, the scan generated interrupts which caused the computer to read counts out from the counter’s memory buffer, analyze the data, and update its graphs. (b) Timing diagram for PC-based data acquisition. Detection Gate enables photon counting and serves as the scan clock for the “dummy” analog input scan. For this example, the probe instrument is updated every five experiments, and the data buffer is read and analyzed every ten experiments. In a typical experiment with a repetition rate of  $\approx 1.5$  kHz, the probe instrument was updated every 500 experiments, while the data buffer was read in every 1000 experiments.

hardware/software interrupt, which flagged the data acquisition software to change the probe instrument (DG 535, HP 8660D, or HP 3335A) settings over the GPIB bus. After several (usually two) such scans, another interrupt (similarly generated) triggered the buffer read out, etc. Details are shown in Fig. 4.13.

Programs were created on the PC which reproduced the HP 9826's spectrum, flopping, and phase programs with an efficiency appropriate for our data acquisition rates. In addition, a histogram-creating program was written which calculated and displayed a histogram of the number of photons received per experiment (typically, 1000 experiments were binned together for a single histogram update). As is discussed in Appendix A, this program was very convenient for peaking up the experiment.<sup>17</sup>

---

<sup>17</sup> Another diagnostic useful for peaking up the cycling transition was stand-alone Ortec Turbo MCS multi-channel analyzer. This instrument binned the photon counts according to their arrival time from the start of the Detection Gate.

## Chapter 5

### Ground State Laser Cooling

Cooling the ion's motion to its ground state is the prerequisite for most of our experiments. An ion at room temperature is in a highly classical thermal state of motion. Cooling takes the ion into the quantum regime, with its interesting dynamics. In this chapter, I will briefly discuss Doppler cooling, and then go on to describe resolved-sideband cooling (using stimulated-Raman transitions) for a single ion and for multiple ions. Finally, I will discuss the observed heating of the ion out of the ground state and possible sources for this heating.

There are different possible diagnostics of the ion's temperature. In practice, we determined the ion's temperature through its interaction with the lasers. Recall from Ch. 3, Eq. (3.12) that, in the Lamb-Dicke regime, the Rabi frequency on the red sideband (first lower motional sideband) is  $\Omega_{n,n-1} = \eta\Omega\sqrt{n}$  (where  $\Omega$  is the carrier Rabi frequency). So if the ion is in its motional ground state, the red sideband vanishes. On the other hand (in the Lamb-Dicke limit)  $\Omega_{n,n+1} = \eta\Omega\sqrt{n+1}$ , so even if the ion is in its ground state the blue sideband doesn't vanish. Indeed, the ratio  $r$  of the red to the blue sideband can tell us the average excitation number  $\bar{n}$  of the ion's motion.

If an ion is in a thermal state with density matrix  $\rho_{n,n} = \sum P_n |n\rangle\langle n|$  with average occupation number  $\bar{n}$ , then the  $P_n$  are given by [105]:

$$P_n = \frac{\bar{n}^n}{(1 + \bar{n})^{n+1}}. \quad (5.1)$$

If we have a single trapped ion in  $|\downarrow\rangle$ , and turn on the Probe for a time  $t_{pr}$  on resonance with the blue sideband, then measure  $P_{\downarrow}$  with the cycling transition, we find that

$$\begin{aligned} P_{\downarrow,BSb}(t_{pr}) &= \sum_{n=0}^{\infty} \frac{1}{2} P_n \cos^2(\Omega_{n,n+1} t_{pr}) \\ &= \sum_{n=0}^{\infty} \frac{1}{2} \frac{\bar{n}^n}{(1+\bar{n})^{n+1}} \cos^2(\Omega_{n,n+1} t_{pr}) . \end{aligned} \quad (5.2)$$

On the other hand, if we drive on the red sideband, we find:

$$\begin{aligned} P_{\downarrow,RSb}(t_{pr}) &= \sum_{n=0}^{\infty} \frac{1}{2} P_n \cos^2(\Omega_{n,n-1} t_{pr}) \\ &= \sum_{n=0}^{\infty} \frac{1}{2} \frac{\bar{n}^n}{(1+\bar{n})^{n+1}} \cos^2(\Omega_{n,n-1} t_{pr}) \\ &= 0 + \sum_{n=1}^{\infty} \frac{1}{2} \frac{\bar{n}^n}{(1+\bar{n})^{n+1}} \cos^2(\Omega_{n,n-1} t_{pr}) \\ &= \sum_{n=0}^{\infty} \frac{1}{2} \frac{\bar{n}^{n+1}}{(1+\bar{n})^{n+2}} \cos^2(\Omega_{n+1,n} t_{pr}) \\ &= \frac{\bar{n}}{1+\bar{n}} P_{\downarrow,BSb}(t_{pr}) . \end{aligned} \quad (5.3)$$

It follows that the ratio of the red sideband signal to the blue sideband signal is

$$r = \frac{P_{\downarrow,RSb}(t_{pr})}{P_{\downarrow,BSb}(t_{pr})} = \frac{\bar{n}}{1+\bar{n}}, \quad (5.4)$$

which gives:

$$\bar{n} = \frac{r}{1-r}. \quad (5.5)$$

Thus the ratio of the red to the blue sideband signal strengths gives a measure of the effectiveness of laser cooling.

## 5.1 Doppler cooling

Laser cooling of atoms was first proposed in 1975 [106, 107], and the first demonstration occurred three years later [61, 60]. In these first experiments, the linewidth  $\gamma$  of the cooling transition was greater than the ions' motional frequency. This is the so-called weak-binding, or Doppler limit:  $\omega_m \ll \gamma$ . In this case (c.f. [26]), the scattering

of a photon takes place in a time much shorter than that required for one oscillation of the ion in its binding potential, and the ion essentially may be treated as if it were free during the scattering. If the laser is tuned *below* resonance, then the ion is more likely to absorb a photon when it is travelling *towards* the direction in which the laser beam is propagating, since in that case the ion is Doppler shifted closer to resonance. Upon absorbing a photon, the ion receives a momentum “kick” which, being in the opposite direction to the ion’s motion, slows the ion down. Of course, when the ion re-emits, it receives another momentum kick from the emitted photon (the so-called “recoil momentum,”  $p_r = \hbar k = h/\lambda$ ). However, since the emission occurs symmetrically, this kick averages to zero over the course of many scattering events. The overall effect is that the ion’s motional energy is reduced. If the ion were free, it would eventually turn around and start moving in the opposite direction. For this reason, effective cooling of all three motional degrees of freedom requires at least four laser beams for a free atom. For a bound atom, the situation is different. In this case, a single laser beam, directed obliquely to the trap’s principal axes, generally suffices. (However, if the trap frequencies along different axes are degenerate, then there is always a mode of motion which is uncoupled to the modes being laser cooled [26], and this mode heats due to recoil. This was not the case for any of the traps discussed in this thesis.)

The limiting kinetic energy for Doppler cooling is  $\langle E_{min,D} \rangle = \hbar\gamma/4$  (when  $p_r/(2m_{atom}) \ll \hbar\gamma$ ). This limit is due to the random times of the photon absorption and the random direction of the spontaneous emission. Even though the average momentum kick due to spontaneous emission averages to zero, for example, its random nature results in a non-zero root-mean-square momentum for the ion. One may think of this as a random walk in momentum space — the random walk about zero mean momentum produces a lower limit to the temperature attainable.

In order to perform Doppler cooling, we turn on Blue Doppler, Red Doppler, and the Repumper for typically  $10\mu s$  (enough time for hundreds of absorption/emission

cycles). We then turn off the Blue Doppler to optically pump the ion to  $|\downarrow\rangle$ , whereupon we turn on the Probe beam long enough to drive a nominal  $\pi$ -pulse ( $\approx 1 \mu\text{s}$ ), on the motional sidebands, mapping the motional information onto the spin degree of freedom. We then measure  $P_{\downarrow}$  by turning on the cycling transition<sup>1</sup>.

A typical spectrum taken after Doppler cooling is shown with solid points in Fig. 5.1. These data, taken in the molybdenum elliptical microtrap, show cooling of the  $x$  degree of freedom, with  $\omega_x/2\pi = 11.2$  MHz. For these curves, the usual probe pulse was preceded by a  $\pi$ -pulse on the carrier transition, which flipped the spin from  $|\downarrow\rangle$  to  $|\uparrow\rangle$ <sup>2</sup>. This served to reduce the noise in the background due to photon shot noise. From the ratio of red to blue sidebands, we determined that  $\bar{n} \approx 0.47(5)$ . Thus, Doppler cooling put us in the Lamb-Dicke regime ( $\eta\sqrt{\bar{n}} \approx 0.1 \ll 1$ ). However, the non-vanishing red sideband for the solid points shows that Doppler cooling alone was not enough to cool the ion to its ground state of motion. In order to do that, we must employ resolved-sideband laser cooling (hollow points), which I will now discuss.

## 5.2 Resolved Sideband, Stimulated-Raman Cooling

The Doppler cooling limit occurs in the weak-binding regime for two-level atoms. Much progress has been made in circumventing this limit in this regime for multi-level atoms [22, 23, 24]. However, in the strong-binding case, the cooling limit is already sub-Doppler [26]. For strongly bound atoms,  $\omega_m \gg \gamma$ , and the ion's absorption spectrum consists of well-resolved sidebands.

Resolved-sideband cooling occurs in a trapped, two-level atom if laser radiation tuned to a lower motional sideband irradiates the atom. Consider, for example, the situation when the laser is tuned to the first lower motional (Red) sideband. In this

---

<sup>1</sup> Note that, since Blue Doppler is detuned red of resonance, the cycling transition actually provides some laser cooling. However, this does not affect the temperature measurement, since the motional information has already been mapped onto the spin degree of freedom before the cycling transition is turned on.

<sup>2</sup> The probe pulse was then chosen to drive the Red, rather than blue, sideband

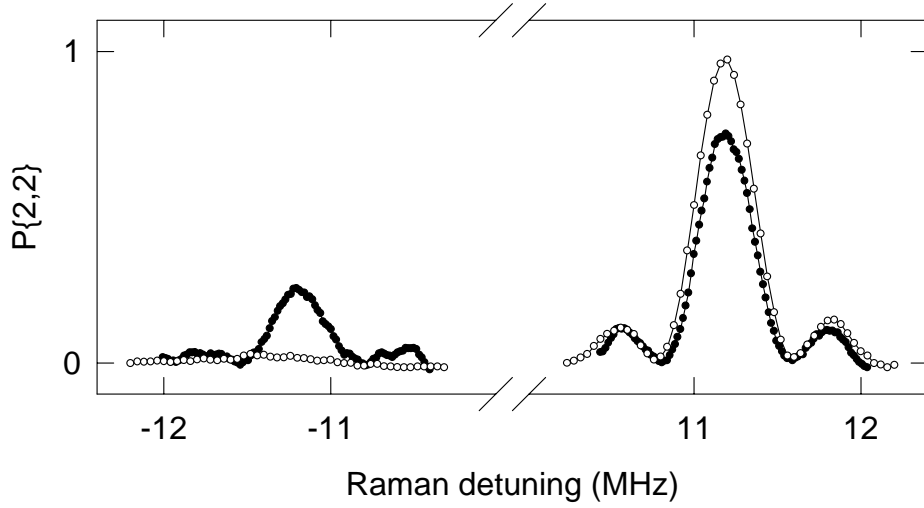


Figure 5.1: Laser cooling of a single  ${}^9\text{Be}^+$  ion. The spectra show the fluorescence rate on the cycling transition as the probe frequency was swept near the first upper (right) and lower (left) motional sidebands. The probe pulse was preceded by a  $\pi$ -pulse on the carrier, in order to reduce the photon shot noise on the background. The count rate is normalized to the probability  $P\{|2, -2\rangle\}$  of the ion being in the state  $|\downarrow\rangle = |2, -2\rangle$ . The solid points indicate the result of Doppler cooling alone. In this case,  $\bar{n} \approx 0.47(5)$ . The addition of five cycles of Raman cooling reduces  $\bar{n}$  to  $\approx 0.014(10)$ , as evidenced by the vanishing lower motional sideband (hollow points). The widths of the features are consistent with the  $2.5 \mu\text{s}$  Raman probe time. Each point represents an average of 400 measurements. The lines are meant only as guides to the eye.

case, photons of energy  $\hbar(\omega_0 - \omega_m)$  are absorbed and (neglecting the recoil energy,  $E_r \ll \omega_m$ ) spontaneously emitted photons of average energy  $\hbar\omega_0$  return the atom to its initial internal state<sup>3</sup>. In one such cycle, the atom's motional energy is reduced by  $\hbar\omega_m$ , on average. This cooling process continues until the ion reaches the motional state  $|n = 0\rangle$ , which is a dark state for the red sideband interaction (see Ch. 3).

For this type of cooling process, the cooling limit is  $\bar{n}_{min} \approx (\gamma/2\omega_m)^2$  [26]. This limit reflects the probability that, once the ion reaches  $|n = 0\rangle$  it may absorb an off-resonant photon on the carrier or higher motional sidebands. Note that, since  $\gamma \ll \omega_m$ , the resolved-sideband cooling limit is much smaller than the Doppler cooling limit.

<sup>3</sup> The spontaneous emission is the dissipative process which allows cooling

Resolved sideband cooling in 2D was achieved in  $^{199}\text{Hg}^+$  using a narrow, single-photon, optical quadrupole transition [108].

In the case of  $^9\text{Be}^+$ ,  $\gamma/2\pi = 19.4$  MHz, whereas  $\omega_m/2\pi \approx 10$  MHz for our typical operating conditions. Thus, single-photon transitions do not put us in the resolved-sideband regime. We can circumvent this limitation by using two-photon, stimulated Raman transitions instead of single-photon ones. To perform ‘‘Raman cooling,’’ we apply the Raman interaction on the red sideband (starting in spin down) to drive  $|\downarrow, n\rangle \rightarrow |\uparrow, n-1\rangle$ . In order to dissipatively recycle the ion to its original internal state, we then turn on the Red Doppler to drive the atom from  $|\uparrow\rangle$  to  $|2p^2P_{3/2}\rangle$ , from where it spontaneously decays back to  $|\downarrow\rangle$ . As in the single-photon case, the spontaneous emission increases the ion’s motional energy by  $E_r$ , on average, whereas the red sideband drive reduces the ion’s motional energy by  $\hbar\omega_m \gg E_r$ : thus the ion is cooled in nearly every cycle of Raman cooling.

Because the ion sometimes ends up in the  $|2s^2S_{1/2}, F=2, m_F=-1\rangle$  state during the Red Doppler recycling, we also turn on the Repumper laser during the recycling pulses. If the ion ends up in the  $|2, -1\rangle$  state, the Repumper promotes it to the  $|2p^2P_{1/2}, F=2, m_F=-2\rangle$  state. From Fig. B.1(a) and (b), the ion has a  $1/3$  probability of ending up in the desired state ( $|\downarrow\rangle$ ) from this level. Thus, if the ion ends up in the  $|2s^2S_{1/2}, F=2, m_F=-1\rangle$  state, it requires an average of  $\sum_{k=1}^{\infty} k p_k = \sum_{k=1}^{\infty} \frac{k}{3} (\frac{2}{3})^{k-1} = 3$  photons to reach  $|\downarrow\rangle$  (here,  $p_k$  represents the probability that the ion ends up in  $|\downarrow\rangle$  after  $k$  scattering events of the repumper).

With Raman cooling, the effective linewidth of the transition is usually insignificant (see Ch. 3), and the effective linewidth of the transition is Fourier-limited. Thus,  $\bar{n}_{min} \approx (\Omega/\omega_m)^2$ , due to off-resonant transitions. In addition, spontaneous emission from the (small) population of the  $2p^2P_{1/2}$  level during the Raman transitions also can limit the cooling:  $\bar{n}_{min,sp.em.} \approx (\gamma\eta^2/\Delta_R)$ .

In order to perform Raman cooling, we typically apply five pulses on the red sideband, with each pulse followed by a recycling pulse (Red Doppler and Recycler beams). If  $M$  is the number of red sideband pulses, then we choose the length of the first red sideband to drive a  $\pi$ -pulse on the transition  $|\downarrow, M\rangle \rightarrow |\uparrow, M-1\rangle$ , the length of the second pulse to be a  $\pi$ -pulse on  $|\downarrow, M\rangle \rightarrow |\uparrow, M-1\rangle$ , and so on. Thus, the last pulse is a  $\pi$ -pulse on  $|\downarrow, 1\rangle \rightarrow |\uparrow, 0\rangle$ . In this manner, the motional levels are sequentially “cleared out.” The recycling pulses are typically  $\approx 7 \mu\text{s}$  long. This is more than enough time for the ion to scatter the  $\approx 3$  photons needed on average to return to  $|\downarrow\rangle$ .

Fig. 5.1 indicates the effects of five pulses of Raman cooling on the  $x$ -mode of motion, showing the further reduction in the red sideband amplitude (hollow points) over the Doppler cooling case (solid points). In this case, the five pulses were all on the  $x$  red sideband. By alternating pulses on the  $x, y$ , and  $z$  red sidebands, we could sequentially cool all three modes of ion motion.<sup>4</sup> By analyzing the ratio of red to blue sidebands on the probe transition, we determined that  $\{\bar{n}_x, \bar{n}_y, \bar{n}_z\} \approx \{0.033, 0.022, 0.029\}$  when simultaneous Raman cooling was performed on these three modes of motion. When we varied  $t_{pr}$ , the ratio of sidebands did not vary, which indicated that the vibration number distribution was thermal.

From the theoretical estimates of  $\bar{n}_{min}$ , one would expect  $\bar{n}_{min} \approx 10^{-3}$ , which is considerably lower than the data indicate. We believe this to be due to heating of the ion’s motion by fluctuating stray electric fields, whose origin we are still investigating. I will discuss this heating in more detail in Sec. 5.5.

We have also performed “continuous” cooling of the  $z$ -mode of motion of a single ion trapped in the micromachined linear trap. In this case, the red sideband interaction was turned on simultaneously with the Red Doppler and Repumper beams. This interaction was left on for  $10 - 20 \mu\text{s}$ , and the subsequent  $\bar{n}$  was measured in the usual

---

<sup>4</sup> Since the weakest trap direction is most likely to heat due to photon recoil, it is advantageous to cool the modes with alternating pulses, with the weakest mode last: in our case, we therefore cooled first  $z$  (strongest), then  $y$ , and finally  $x$  (weakest).

fashion. The continuous mode of cooling worked with approximately the same efficiency as the pulsed cooling.

### 5.3 Cooling the Collective Motion of Two Trapped Ions

When two (or more) cold ions are held in the trap and undergo small oscillations about their equilibrium positions, we may solve the equations of motion using normal mode coordinates [109]. For two ions lying along the  $x$ -axis there are two modes involving motion along this axis: the center-of-mass (COM) mode (in which the ions move together with frequency  $\omega_{\text{COM}} = \omega_x$ ) and the stretch mode (wherein the ions move out of phase, with frequency  $\omega_{\text{str}} = \sqrt{3}\omega_{\text{COM}}$ ). The other motional frequencies are  $\omega_y$  ( $y$  center-of-mass),  $\omega_z$  ( $z$  center-of-mass),  $\sqrt{\omega_y^2 - \omega_x^2}$  ( $xy$  rocking), and  $\sqrt{\omega_z^2 - \omega_x^2}$  ( $xz$  rocking) [45].

In the case of two ions driven on the *carrier* transition, each ion independently undergoes Rabi oscillations between  $|\downarrow\rangle$  and  $|\uparrow\rangle$  with Rabi frequency  $\Omega$ . In our experiments, the laser beam waists ( $\approx 20\ \mu\text{m}$ ) were much larger than the ion-ion separation ( $\approx 2\ \mu\text{m}$ ), and so the ions were equally illuminated, and had equal Rabi frequencies<sup>5</sup>.

Since the sideband transitions affect the motional state, which is a shared property of both ions, such transitions produce entanglement between the ions' spins and their collective motion [110]. The system can no longer be treated as two, independent, two-level systems and the measured fluorescence following a Raman probe is a complicated function of the probe pulse duration  $t_{pr}$ . For example, in the Lamb-Dicke regime, given an initial state  $|\downarrow, \downarrow, n\rangle$  (where  $n$  is the vibrational level of the COM or stretch motion along the  $x$ -axis) driven on the corresponding lower sideband for a time  $t_{pr}$ , the wave

---

<sup>5</sup> However, had the micromotion of the two ions been different, then the reduction of the carrier (and sideband) transition strengths due to the micromotion would have given a different Rabi frequency for each ion. This will be discussed in Sec. 6.4.1.

function evolves as [45]

$$\begin{aligned}
|\psi_n(t_{pr})\rangle &= \left\{ 1 - \frac{n}{2n-1} [1 - \cos(G_n t_{pr})] \right\} |\downarrow, \downarrow, n\rangle \\
&\quad - i e^{i(\theta-\phi)/2} \sqrt{\frac{n}{2n-1}} \sin(G_n t_{pr}) \frac{(|\downarrow, \uparrow\rangle \pm e^{i\phi} |\uparrow, \downarrow\rangle) |n-1\rangle}{\sqrt{2}} \\
&\quad \mp e^{i\theta} \frac{\sqrt{n^2-n}}{2n-1} [1 - \cos(G_n t_{pr})] |\uparrow, \uparrow, n-2\rangle,
\end{aligned} \tag{5.6}$$

where  $G_n = \sqrt{2(2n-1)} \Omega \eta_{x,m}$  and  $\theta, \phi$  are the sum and difference of the Raman beam phases at the ions. On the COM sideband (top sign in Eq. (5.6)),  $\eta_{x,m} = \eta_{x,\text{COM}} = \eta_x/\sqrt{2}$  (down by a factor of  $\sqrt{2}$  from the single-ion case due to the extra mass of the two-ion string), whereas on the stretch sideband (lower sign),  $\eta_{x,m} = \eta_{x,\text{str}} = \eta_x/\sqrt{2\sqrt{3}}$ . The expressions for transitions on the upper motional sidebands are similar. If, before the Raman probe pulse, the ions have probability  $P_n$  of being in the motional state  $|n\rangle$ , the subsequently-measured average fluorescence from the cycling transition is

$$S(t_{pr}) \propto \sum_n P_n \left( 2 |\langle \downarrow, \downarrow, n | \psi_n(t_{pr}) \rangle|^2 + |\langle \downarrow, \uparrow, n-1 | \psi_n(t_{pr}) \rangle|^2 + |\langle \uparrow, \downarrow, n-1 | \psi_n(t_{pr}) \rangle|^2 \right). \tag{5.7}$$

This signal is proportional to the expectation value of the number of atoms in the state  $|\downarrow\rangle$ .

It is not as straightforward to extract  $\bar{n}$  from experimental data as in the one-ion case. In particular, the more complicated time dependence of the wave function when the ion is driven on the motional sidebands Eq. (5.6) means that  $\bar{n}$  can no longer be expressed as a simple ratio of the red to blue sideband amplitudes. Indeed, this ratio is no longer even time-independent. However, it is still possible to extract  $\bar{n}$  from the data.

To see how this can be done, plug Eq. (5.6) into Eq. (5.7). After some algebra, we obtain:

$$S(t_{pr}) \propto 2 \left( P_0 + \sum_n P_n \left[ 1 - \frac{n[4n-3 + \cos(G_n t_{pr})][1 - \cos(G_n t_{pr})]}{2(2n-1)^2} \right] \right). \tag{5.8}$$

Since the population of  $|n = 0\rangle$  is dark to the red sideband interaction, the fluorescence due to  $P_0$  remains constant; the fluorescence due to higher  $P_n$ 's oscillates in time due. If we substitute a thermal distribution (Eq. (5.1)) for the  $P_n$ 's and allow for some signal  $\mathcal{B}$  due to background counts, we have that

$$\begin{aligned}
S(t_{pr}) &= (S_0 - \mathcal{B}) \left( \frac{1}{1 + \bar{n}} \right. \\
&\quad \left. + \sum_{n=1}^{\infty} \frac{\bar{n}^n}{(1 + \bar{n})^{n+1}} \left[ 1 - \frac{n[4n - 3 + \cos(G_n t_{pr})][1 - \cos(G_n t_{pr})]}{2(2n - 1)^2} \right] \right) + \mathcal{B},
\end{aligned} \tag{5.9}$$

where  $S_0$  is the ion count rate at  $t_{pr} = 0$  (or off-resonance). Now, the location of the first minimum of the fluorescence rate is almost entirely determined by  $P_1$ , so we can make the simplifying assumption that  $t_{pr,min} \approx \frac{\pi}{2G_1} = \frac{\pi}{2\sqrt{2}\Omega\eta_{x,m}}$ . Then Eq. (5.9) becomes

$$\begin{aligned}
S_{min} &= (S_0 - \mathcal{B}) \left( \frac{1}{1 + \bar{n}} \right. \\
&\quad \left. + \sum_n \frac{\bar{n}^n}{(1 + \bar{n})^{n+1}} \left[ 1 - \frac{n[4n - 3 + \cos(\sqrt{2n - 1}\pi/2)][1 - \cos(\sqrt{2n - 1}\pi/2)]}{2(2n - 1)^2} \right] \right) \\
&\quad + \mathcal{B}.
\end{aligned} \tag{5.10}$$

Thus, in principle, given  $S_{min}$ ,  $S_0$ , and  $\mathcal{B}$ , we must invert this equation to determine  $\bar{n}$ : in practice, higher terms in the sum decrease in magnitude, so that the sum can be truncated and the equation solved numerically. For cold ions, this procedure is robust with respect to small changes in the measured background and overall count rate.

Fig. 5.2 shows laser cooling of the COM and stretch modes of motion of two trapped  ${}^9\text{Be}^+$  ions. The lower traces, taken with  $\delta\mathbf{k} \parallel \hat{\mathbf{e}}_x$ , show an  $x$ -axis normal mode spectrum after Doppler cooling. The stretch mode is colder than the COM because its motional frequency is higher. Results for the  $y$ - and  $z$ -modes were very similar. We took the data with the following steps: first we Doppler cooled the ions to the Lamb-Dicke regime. Next, we optically pumped both ions to the  $|\downarrow\rangle$  state. We then performed a Raman probe pulse for time  $t_{pr}$ , with relative detuning  $\omega_0 + \delta_{pr}$ . Finally, we drove the cycling transition and measured the ions' fluorescence. We repeated the experiment at

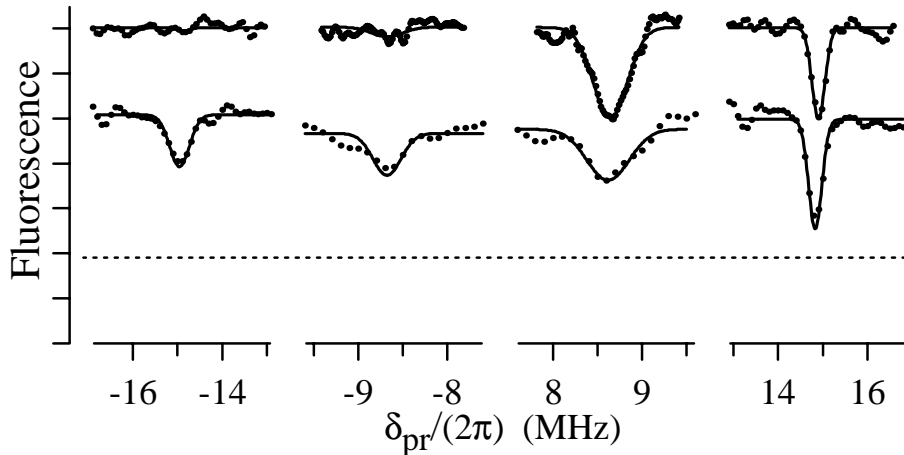


Figure 5.2: Spectrum of sidebands due to two-ion  $x$ -axis normal mode motion: (from left to right) lower stretch, lower COM, upper COM, and upper stretch. The ordinate is the detuning of the Raman probe beam difference frequency from the carrier transition. The abscissa shows the ion fluorescence (proportional to the expectation value of the number of atoms in the state  $|\downarrow\rangle$ ), plus a constant background (whose approximate level for the lower curves is indicated by the dashed line). The solid lines, meant as guides to the eye, are fits to Gaussians. The lower traces show the effects of Doppler cooling. The upper traces, offset vertically for clarity, show the effects of several pulses of Raman cooling on the mode which is displayed. Vanishing lower motional sidebands indicate cooling to the ground state of motion. The peak widths are consistent with the Raman probe pulse lengths ( $\approx 3 \mu\text{s}$ ).

a rate of a few kilohertz while slowly sweeping  $\delta_{pr}$ . If the probe Raman beam difference frequency was resonant with a transition, then an ion was driven from  $|\downarrow\rangle \rightarrow |\uparrow\rangle$  and the fluorescence rate on the cycling transition dropped, as discussed above. For these data,  $t_{pr} \approx 3 \mu\text{s}$  was chosen to maximize the sideband features.

The upper traces in Fig. 5.2 show the effects of adding several cycles of Raman cooling [44] on one particular  $x$ -mode after the Doppler cooling but before the probe pulse. The reduction in the mean vibrational number  $\bar{n}$  is indicated by the reduction in size of the lower sideband, which vanishes in the limit  $\bar{n} \rightarrow 0$ . Analysis of the data according to the technique outlined above showed that the data were consistent with a thermal state of  $\bar{n}_{\text{COM}} = 0.11^{+0.17}_{-0.03}$  or  $\bar{n}_{\text{str}} = 0.01^{+0.08}_{-0.01}$ . This implies that the COM and

stretch modes are in their ground states  $90_{-12}^{+3}\%$  and  $99_{-7}^{+1}\%$  of the time, respectively. We believe that the cooling limits are again due to anomalous heating of the ions out of the ground state between the last red sideband pulse and the probe pulse (see Sec. 5.5).

We have also *simultaneously* cooled the COM and stretch modes along  $x$ , to comparable values of  $\langle n \rangle$  (and have separately cooled the other four motional modes— $y$  and  $z$  COM,  $xy$  rocking, and  $xz$  rocking)—to near their ground states.

#### 5.4 Cooling Three Trapped Ions

For the sake of completeness, I will present here data indicating cooling of the collective modes of motion of three trapped ions. In this case, only Doppler cooling was performed. Fig. 5.3 shows spectra for the three normal modes along the weak trap direction: the COM, the stretch, and the “Egyptian” mode (in which the outer two ions move  $180^\circ$  out of phase with the central one). Again, the mode with the highest motional frequency had the lowest  $\bar{n}$ : since the ratio of the COM:stretch:Egyptian mode frequencies is  $1 : \sqrt{3} : \sqrt{\frac{29}{5}}$ , this meant that the “Egyptian” mode had the lowest  $\bar{n}$ .

#### 5.5 Heating of the Modes of Motion

In all the traps used for quantum state engineering and quantum logic experiments (i.e. both the elliptical traps and the linear trap), heating of the ions’ motional degrees of freedom was observed. The heating rate was much higher than one would expect from, for example, thermal noise. Fig. 5.4 shows a summary of the heating rates measured in the various traps at different trap frequencies and at different times. These heating rates were measured by putting a varying delay  $\tau_d$  between the last cooling pulse and the probe  $\pi$ -pulse. The heating rate is continuous: that is, the ion is heated uniformly from  $|n = 0\rangle$  to  $|n = 1\rangle$  and so on,<sup>6</sup> rather than making a discontinuous jump from

---

<sup>6</sup> This was determined by taking a flopping trace on the blue sideband instead of varying the frequency of the probe pulse. The distribution over the Fock states determined from the flopping traces indicated a thermal distribution, with  $\bar{n}$  consistent with continuous heating

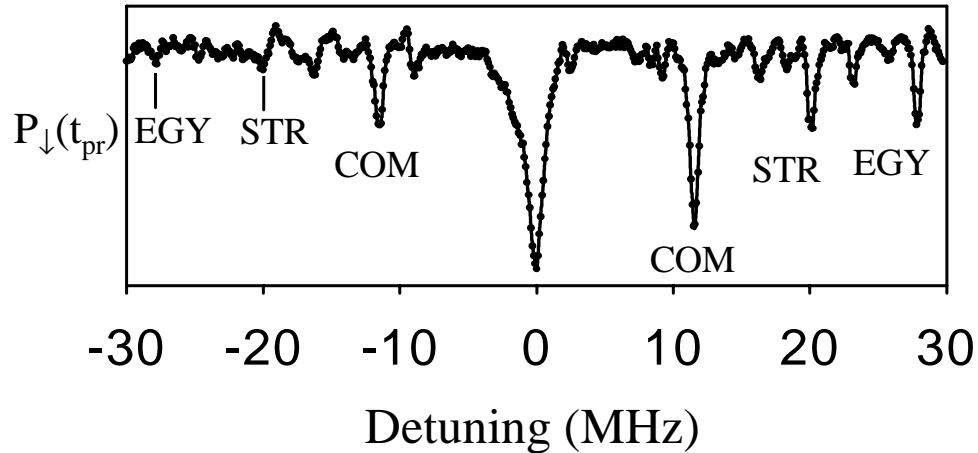


Figure 5.3: Spectrum of sidebands due to three-ion  $x$ -axis normal mode motion: (from left to right) lower “Egyptian,” lower stretch, lower COM, carrier upper COM, upper stretch, and upper “Egyptian.” The ordinate is the detuning of the Raman probe beam difference frequency from the carrier transition. The abscissa shows the ion fluorescence, plus a constant background. The ratio of the COM:stretch:Egyptian mode frequencies is  $1 : \sqrt{3} : \sqrt{\frac{29}{5}}$ .

a low  $\bar{n} \approx 0$  to a high  $\bar{n}$ . The exact source of the heating is still not well-understood although, as I will explain below, it might be caused by fluctuating patch fields on the electrodes.

By looking at the heating rates of the COM, stretch, and rocking modes of motion for two trapped ions, we have determined that the heating is due to fields rather than field gradients. Table 5.5 shows heating rate data for the normal modes: note that the COM modes heat at a rate of about one quantum per hundred microseconds, whereas the stretch and rocking mode heating is unmeasurable out to a millisecond. Now, since these latter modes involve differential motion of the ions, they *cannot* be heated by a uniform field, which affects both ions in the same manner. Therefore, the stretch and rocking modes can *only* be heated by field gradients, or higher-order terms in an expansion of the field. This is not the case for the COM modes, in which both ions

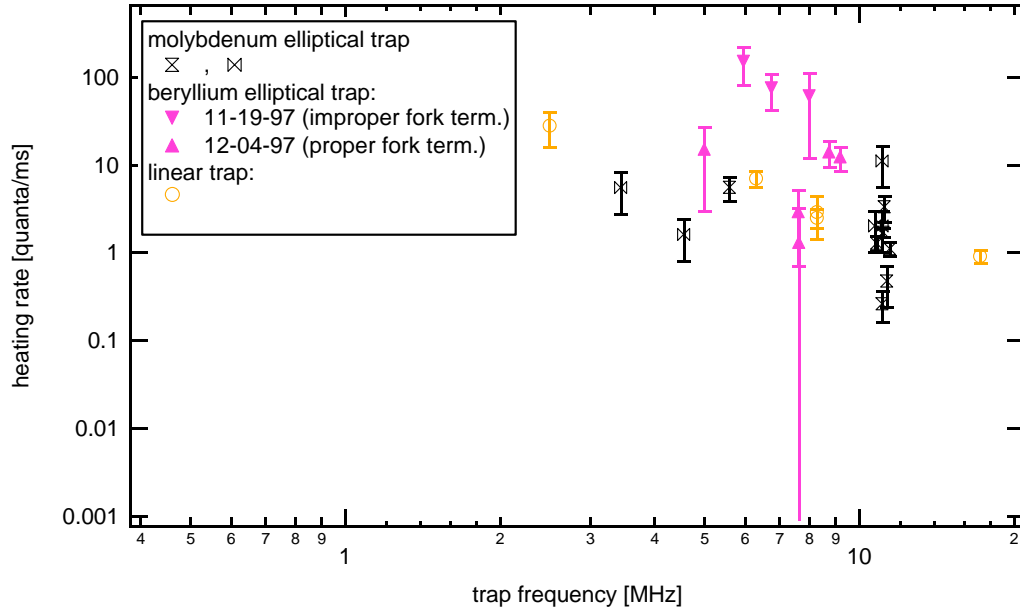


Figure 5.4: Summary of the heating rates in the various traps. The data set for the beryllium-electrode, elliptical microtrap labelled “improper fork term.” was taken when the fork electrode was connected to a cable of such length that the fork was no longer held at rf ground. The other data set for this trap was taken with the fork connection properly terminated. The heating rate ranged between 1 and 10 quanta/ms at the typical secular frequencies.

move together. If the fluctuating field at the ion is  $E(t)$ , than an estimate of the field gradient is  $E(t)/d_0$ . For Gaussian-distributed stochastic sources, the heating rate of the COM mode scales as  $\langle E^2(t) \rangle$ , so that the stretch mode heating rate scales as  $\langle E^2(t) \frac{\Delta x}{d_0} \rangle$ , where  $\Delta x \approx 2 \mu\text{m}$  is the ion separation and  $d_0 \approx 200 \mu\text{m}$  the electrode size [45, 73, 111]. Thus, for example, one would expect the heating rate of the stretch mode to be down from that of the COM mode by at least a factor of  $\approx (\frac{\Delta x}{d_0})^2$ , a factor of  $\approx 10^4$  for the Be-electrode trap in which the data were taken. That the stretch mode heating was observed to be at least several orders of magnitude lower than that of the COM mode is a strong indication that field gradients do not play a significant role in the heating process.

mode	$\omega_m/2\pi$ (MHz)	$\delta\langle n \rangle/\delta t$ ( $\text{ms}^{-1}$ )
$x_{\text{COM}}$	8.6	$19^{+40}_{-13}$
$y_{\text{COM}}$	17.6	$> 10$
$z_{\text{COM}}$	9.3	$> 20$
$x_{\text{str}}$	14.9	$< 0.18$
$xy_{\text{rocking}}$	15.4	$< 1$
$xz_{\text{rocking}}$	3.6	$< 0.5$

Table 5.1: Heating rates of the six normal modes of two trapped ions. The Raman beams were counter-propagating for the  $y$ - and  $z$ - axis data, making the Raman probe sensitive to motion in all three dimensions. Note that the COM modes are heated at a much higher rate than the non-COM modes (see text). (The precision with which the heating rates are given for the last five modes is limited by measurement noise.)

Various possible heating mechanisms can be ruled out, either from measurements or from theoretical estimates of the heating rate they would produce. For example, one may make a simple estimate (see Sec. 2.4.3) to show that elastic or inelastic collisions of the ions are infrequent at the operating pressures ( $< 5$  nPa). Furthermore, we observed no change in the measured heating rates upon turning off the ion pump in the vacuum envelope. Finally, since the Langevin critical impact parameter is much less than the ion-ion separation (see Sec. 2.4.3), collisions should couple to the stretch as well as the COM mode: this is inconsistent with the COM vs. stretch/rocking mode heating measurements. The low stretch/rocking mode heating rate also rules out mode cross-coupling as a heating mechanism, since this, too, would have required field gradients.

We were able to rule out other heating mechanisms by changing the trap frequency (i.e. by lowering the rf voltage  $V_0$  providing the secular trapping potential). The fact that the heating was broadband ruled out “heating resonances” [73], such as those wherein the rf drive couples secular modes in two trapping directions. As Fig. 5.4 indicates, the heating rate (in quanta per millisecond) scales roughly as  $1/\omega_m$ , consistent with a constant rate of change of energy. This behaviour also argues against field emission, which is expected to exhibit an exponential dependence on the voltage (which determines  $\omega_m$ ).

A general approach to discussing heating from noisy electric fields (whatever their origin) follows the work of Savard, O'hara, Thomas, and Gehn [112, 113, 73, 111]. Although they considered heating mechanisms in neutral atom dipole traps, their approach is applicable in a more general context. It indicates that the rate  $\Gamma_0$  at which the ground motional state is vacated due to noisy electric fields is given by:

$$\Gamma_0 = \frac{Q^2}{4m\hbar\omega_m} S_E(\omega_m). \quad (5.11)$$

Here,  $S_E(\omega_m)$  is the electric field noise spectral density in  $(\text{V/m})^2/\text{Hz}$ . In actuality, this equation is complete only for static-field trapping (i.e. the  $z$ -direction in the linear trap). For a Paul trap, it is also possible for electric field noise at  $\Omega_T \pm \omega_m$  to couple into the secular motion. A field of amplitude  $E_0$  at this frequency behaves as a resonant electric field at  $\omega_m$  with effective amplitude [114, 73]  $\frac{E_0\omega_m}{\sqrt{2}\Omega_T}$ , so a noisy electric field at this frequency results in an effective noise spectral density of

$$\frac{\omega_m^2}{2\Omega_T^2} S_E(\Omega_T \pm \omega_m), \quad (5.12)$$

In this case, Eq. (5.11) may be generalized to [111]:

$$\Gamma_0 = \frac{Q^2}{4m\hbar\omega_m} \left[ S_E(\omega_m) + \frac{\omega_m^2}{2\Omega_T^2} S_E(\Omega_T \pm \omega_m) \right]. \quad (5.13)$$

We may use Eq. (5.13) to estimate the effects of various noise sources on the ions. Consider, for example, the effects of noise on the rf or static field drives which produce the trapping fields. Such noise cannot directly cause heating of the ion, since the noise voltage is applied symmetrically to the trap electrodes. Thus it can only heat the ion's motion through field gradients, which the two-ion heating data rule out.

However, if patch fields exist on the electrodes, they can displace the ion from the nominal trap centre. In the case of static field confinement (e.g. the axial confinement a linear trap), the amount of displacement depends on the trap strength: that is, on the static potential  $U_0$ . Thus, if  $U_0$  is varying in time, with average  $\langle U_0 \rangle$ , then the trap centre is randomly displaced with time, allowing excitation of the ion's axial motion. Let

us write the electric field at the ion due to patch potentials as  $E_{static} \approx \phi/d_0$ , where  $\phi$  is the effective axial potential difference between the electrodes and  $d_0$  their separation. Then  $S_E(\omega) \approx (E_{static}/\langle U_0 \rangle)^2 S_{U_0}(\omega) \approx \phi^2/(\langle U_0 \rangle d_0)^2 S_{U_0}(\omega)$ , where  $S_{U_0}$  is the noise density of the static voltage  $U_0$  at the trap electrodes. Thus, Eq. (5.13) gives [73]:

$$\Gamma_0 = \frac{Q^2}{4m\hbar\omega_z d_0^2} F^2 \left( \frac{\phi}{\langle U_0 \rangle} \right)^2 S_{U_0}(\omega_z). \quad (5.14)$$

Let us take  $\phi \approx 1$  V,  $U_0 \approx 30$  V,  $d_0 \approx 200$   $\mu\text{m}$ , and  $\omega_z \approx 10$  MHz. If the static voltage power supply has an rms noise of 0.1 mV uniformly distributed across a 20 MHz bandwidth, then the filter network on the trap structure will reduce this noise voltage by a factor  $F \approx 10^{-4}$ , yielding  $\Gamma_0 \approx 1 \times 10^{-5}$ /s. for the assumed parameters. This is obviously too small to explain the observed heating.

Similarly, such patch fields could displace the ion from the rf null, converting noise on the trapping potentials into noisy fields at the ion's location. In general, the rf at the ion trap is produced using step-up transformer, which can be characterized by its characteristic impedance  $Z_0$  and its quality factor  $Q$ . Given the resonant nature of the step-up transformer, we may neglect the first term in Eq. (5.13) entirely. The filtering provided by the transformer/trap circuit will be at least the  $F \approx 10^{-4}$  assumed in the static case. The rf voltage will be a factor of approximately 100 times greater than the static voltage but, even if the noise voltage scales by this amount, the second term in Eq. (5.13) is smaller than the first term by a factor of  $(\omega_m/2\Omega_T)^2 \approx 10^{-4}$ , so that noise on the rf drive is no more significant than that on the static voltage supplies.

One may also use Eq. (5.13) to estimate the effects of blackbody radiation on the ion [73, 111]. Since the frequencies of interest are relatively low (MHz), the effect of the "cavity" formed by the trap electrodes is significant. However, these low frequencies also mean that such effects may be treated in the long-wavelength limit, which is to say that we may consider the electromagnetic field in terms of lumped circuit elements [115, 116]. In this case, the blackbody radiation is manifested as Johnson noise in the resistive part

of the equivalent resistance  $R$  through which currents induced by ion motion flow. Since the voltage noise spectral density from a resistor  $R$  at temperature  $T$  is given by  $4k_B T R$  (where  $k_B$  is Boltzmann's constant) [117], we have that  $S_E(\omega) \approx 4k_B T R(\omega)/d^2$ . Thus, for static-field trapping, we have

$$\Gamma_{0,s} \approx \frac{Q^2 k_B T R(\omega_z)}{m \hbar \omega_z d^2} \quad (5.15)$$

and for rf trapping,

$$\Gamma_{0,rf} \approx \frac{Q^2 k_B T}{m \hbar \omega_z d^2} \left( R(\omega_m) + \frac{\omega_m^2}{2\Omega_T^2} R(\Omega_T \pm \omega_m) \right). \quad (5.16)$$

In the case of the elliptical microtraps, we may consider two resistive paths which would most likely have produced the largest resistances [73, 111]: one around the perimeter of the slot which formed the endcap electrodes, and the other through the step-up transformer used to produce the rf voltages at the trap electrodes, from the ring to the endcaps. For the path from one endcap to the other, around the slot, we may estimate the resistance as  $R(\omega) \approx \rho l/A(\omega)$ . Here,  $\rho$  is the resistivity of the electrode material (molybdenum or beryllium) and  $A(\omega)$  is the effective cross-sectional area of the resistive path, which is proportional to the skin depth. If we are conservative, we estimate  $R(\omega_x) \approx 0.04 \Omega$  at 11 MHz for the molybdenum trap and, with  $\Omega_T/2\pi = 241$  MHz,  $R(\Omega_T \pm \omega_x) \approx 0.20 \Omega$ . This leads to  $\Gamma_{0,rf} \approx 0.7$  s — much smaller than the observed heating rate. Similar results are obtained for  $\Gamma_{0,s}$ .

If we consider the other possible resistive path, between the ring and endcaps through the step-up transformer (in our case, a quarter-wave, coaxial resonator) we find that the impedance between ring and endcaps is given by [73]

$$Z(\omega) = Z_0 \tanh \left[ \frac{\pi}{4Q} \sqrt{\frac{\omega}{\Omega_T}} + i \frac{\pi}{2\Omega_T} \right], \quad (5.17)$$

where  $Z_0$  is the characteristic impedance of the coaxial resonator (nominally,  $96 \Omega$ ). Taking the real part of Eq. (5.17), we find that  $R(\omega_m) \approx \frac{\pi Z_0}{4Q} \sqrt{\omega_m/\Omega_T} \approx 0.01 \Omega$  with

$\omega_m \approx 10$  MHz, and  $R(\Omega_T \pm \omega_m) \approx \frac{Z_0}{\pi Q}(\Omega_T/\omega_m)^2 \approx 9 \Omega$ . I have taken  $Z_0 = 96 \Omega$ ,  $Q \approx 700$  and  $\Omega_T \approx 200$  MHz. Plugging into Eq. (5.13), this gives  $\Gamma_0 \approx 1.2/\text{s}$ , with approximately equal contributions from each term.

From these estimates, it is clear that thermal noise/blackbody radiation cannot quantitatively explain the heating rates measured in any of the traps. There is another reason why thermal fields are an unsatisfactory explanation. Fig. 5.5 shows a trap which we have just recently “commissioned.” This molybdenum trap is similar in construction to the first two elliptical microtraps (see Ch. 2), save that there are *two* ring electrodes cut into the molybdenum sheet. (The endcaps for both trapping regions are again formed by a slot in the other metal sheet — this slot is tapered to preserve the ring/endcap aspect ratio.) In the first trap, the radius of the ring electrode is  $r_0 \approx 180 \mu\text{m}$ , and the endcap separation is  $2z_0 \approx 2 \times 152 \mu\text{m}$ . The second trap has  $r_0 \approx 395 \mu\text{m}$  and  $2z_0 \approx 2 \times 350 \mu\text{m}$ .  $\Omega_T/2\pi \approx 150$  MHz. This trap was designed for quick vacuum processing and so, to minimize the volume of the vacuum system, the resonator was external to the vacuum can.

Fig. 5.6 shows the relative heating rates in the small and larger traps as a function of trap frequency. These rates were measured in the usual manner. The rates scale as a strong function of the trap size (i.e.  $> d_0^5$ ) whereas Eq. (5.15) and Eq. (5.16) show that thermal fields from external sources produce a  $d_0^2$  scaling.

The outstanding question, then, is what causes the observed heating of the ion’s motion? One possibility is that the heating is caused by fluctuating patch fields on the trap electrodes [73]. Although most investigations into patch fields have been done on time-independent or slowly varying ( $< 500$  Hz) fields [118], there have been some studies at higher frequencies [119, 120]. These studies found different behaviour at times less than a surface diffusion time constant, but at higher frequencies, they both predict a spectral density  $S(\Phi_n, \omega)$  of rms potential fluctuations  $\Phi_n$  which scales as  $\omega^{-\chi}$ , with

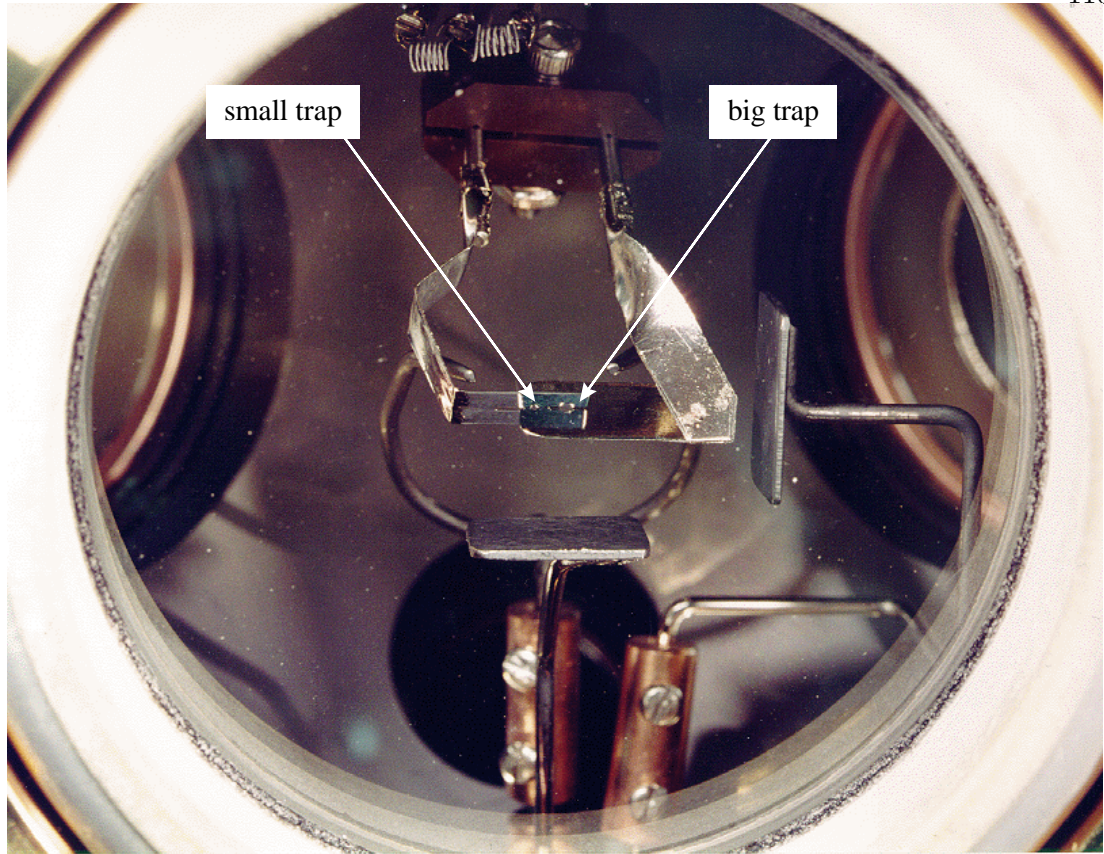


Figure 5.5: “Double trap” used for heating studies. It was constructed from molybdenum sheets. One sheet had two holes drilled in it, forming two ring electrode trapping regions. The endcaps were formed by an slot in the second sheet, cut to preserve the aspect ratio between the two traps. One trap, had  $r_0 \approx 180 \mu\text{m}$  and  $z_0 \approx 152 \mu\text{m}$  ( $z$  is one-half the endcap spacing), which produced a trap frequency of  $\omega_x/2\pi \approx 8 \text{ MHz}$  with  $\approx 250 \text{ V}$  of rf applied to the ring electrodes at  $\Omega_T \approx 150 \text{ MHz}$ . The other trap had  $r_0 \approx 395 \mu\text{m}$  and  $z_0 \approx 350 \mu\text{m}$ , which yielded  $\omega_x/2\pi \approx 2 \text{ MHz}$  with the same applied rf.

$\chi \approx 3/2$ . The high-frequency fluctuations appear to be caused by surface diffusion, rather than adsorption/desorption [120].

The field from one such patch potential may be estimated by assuming a circular patch is on the surface of a sphere of radius  $R$ . The sphere is assumed to be held at ground, except for the patch, which is at potential  $V$ . (This estimates the effect of the electrodes.) At the centre of the sphere, the field produced by the patch is [89]  $E_p \approx \frac{3V}{4R} \sin^2 \theta \approx \frac{3Vr_p^2}{4R^3}$  in a direction pointing away from the patch. Here,  $\theta = \arcsin r_p/R \approx (r_p/R)$  is the angle subtended by the patch’s radius  $r_p$ , as viewed from the centre of the

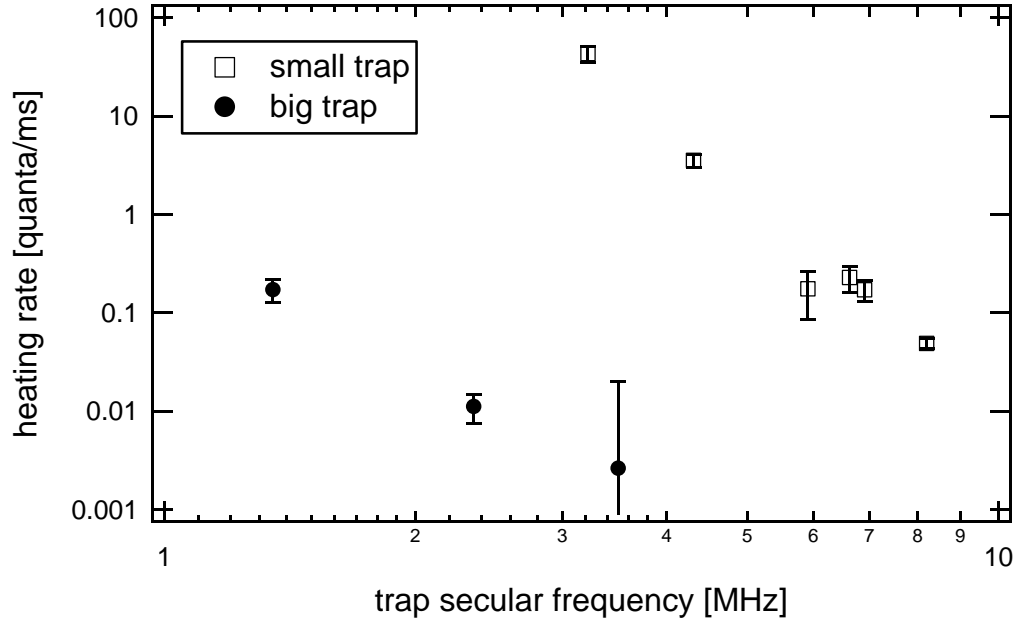


Figure 5.6: Heating rates for the small and large traps in the “double trap,” as a function of trap frequency. The heating rate was a strong function of the trap electrode size. A fluctuating patch field model of trap heating scales approximately as  $r_0^4$ , or higher.

sphere. If  $N$  patches cover the surface of the sphere, with randomly distributed voltages  $V_i$ , then  $\langle E_{tot}^2 \rangle = N \frac{9\langle V^2 \rangle r_p^4}{32R^6}$  in any given direction. Using the fact that  $N = \mathcal{C} \frac{4\pi R^2}{\pi r_p^2}$  (where the coverage  $\mathcal{C} \ll 1$ ), we obtain:

$$\langle E_{tot}^2 \rangle = \mathcal{C} \frac{3\langle V^2 \rangle r_p^2}{4R^4} \propto \frac{1}{R^4}. \quad (5.18)$$

Since  $\langle E_{tot}^2 \rangle = \int S_E(\omega) d\omega$ , this tells us that, for randomly distributed patches,  $S_E(\omega) \propto R^{-4}$ . Although this is a very approximate model, it shows that patch potentials can produce a electric field power noise spectral density which scales strongly with the characteristic size of the trap.

In conclusion, then, it seems desirable to characterize the scaling of the trap heating rate as a function of trap size. This would allow one to optimize trap strength versus heating rate, and construct a trap which allows the minimum heating-induced decoherence.

## Chapter 6

### Quantum State Engineering of One and Two Ions

Thus far, we have discussed the ion trap and other apparatus necessary for performing quantum state engineering, investigated the interaction between the ion's spin and motional degrees of freedom, as mediated by the laser, and examined laser cooling, which gets us into the “quantum regime.” We are now ready to examine some of the ways in which these tools enable us to control the quantum state of our trapped ion(s). In this chapter, I shall discuss ways to control the motional and electronic degrees of freedom of the ion and create entanglement between them. I shall then discuss ways to characterize the complete quantum motional state. Finally, I shall discuss the creation of entanglement between two trapped ions.

#### 6.1 Nonclassical States of Motion: One Ion

Of course, the ability to engineer various quantum states of the ion's motion does us no good whatsoever if we have no way to *verify* that we have successfully created said state. Although I will discuss methods of completely characterizing the motional state in Sec. 6.3, often it suffices to determine the  $P_n$  for the motional state: the probability that a measurement in the Fock state basis will project the state of the system onto a particular Fock state.

In other systems similar to ours (such as molecules or Rydberg atoms), the binding potential is anharmonic, so that the populations in the various potential eigenstates can

be resolved spectroscopically. However, since our system is a harmonic oscillator, it is patently *not* anharmonic, and we cannot use this technique to determine the  $P_n$ . Instead, we use the blue sideband to map motional information onto the spin state and then use the cycling transition to measure  $P_{\downarrow}$  and  $P_{\uparrow}$ , as discussed in Sec. 3.5.

### 6.1.1 Thermal States

There is nothing particularly nonclassical about an ion whose motion is in a thermal state. However, it is the “natural state” of a trapped ion, which normally is in thermal equilibrium with its surroundings. It is also the state in which we find the ion after optimum Doppler laser cooling, with  $\bar{n} + \frac{1}{2} \approx \gamma/(4\omega)$  and  $\bar{n}$  the average vibrational quantum number. Finally, we have found that the heating discussed in Sec. 5.5 leaves the ion’s motion in a thermal state.

We may choose to express the thermal state in terms of the number state basis: from Eq. (5.1) the probability that the ion is in the motional state  $|n\rangle$  is

$$P_n = \frac{\bar{n}^n}{(1 + \bar{n})^{n+1}}, \quad (6.1)$$

with  $\bar{n} = (e^{\hbar\omega_m/k_B T} - 1)^{-1}$ . Figure 6.1 shows the Rabi flopping curve on the upper motional sideband for a thermal state with  $\bar{n} = 1.3 \pm 0.1$  [46], corresponding to a temperature of  $T = 940\mu\text{K}$ . The inset shows the results of a singular-valued decomposition (SVD) of the flopping curve, which extracts the various  $P_n$ . As one would expect, the distribution falls off exponentially in the Fock state number. The solid curve is a fit to the thermal distribution of Eq. (6.1), from which  $\bar{n}$  is extracted.<sup>1</sup>

### 6.1.2 Fock States: Eigenstates of the Harmonic Oscillator

The Fock states  $|n\rangle$  are the eigenstates of the harmonic oscillator Hamiltonian. (In the context of the formal equivalence between our system and cavity QED, the Fock

---

<sup>1</sup> Note that, as  $n$  increases, the Rabi frequencies of the different Fock state components grow closer to each other, and the error bars on the  $P_n$  grow [46]

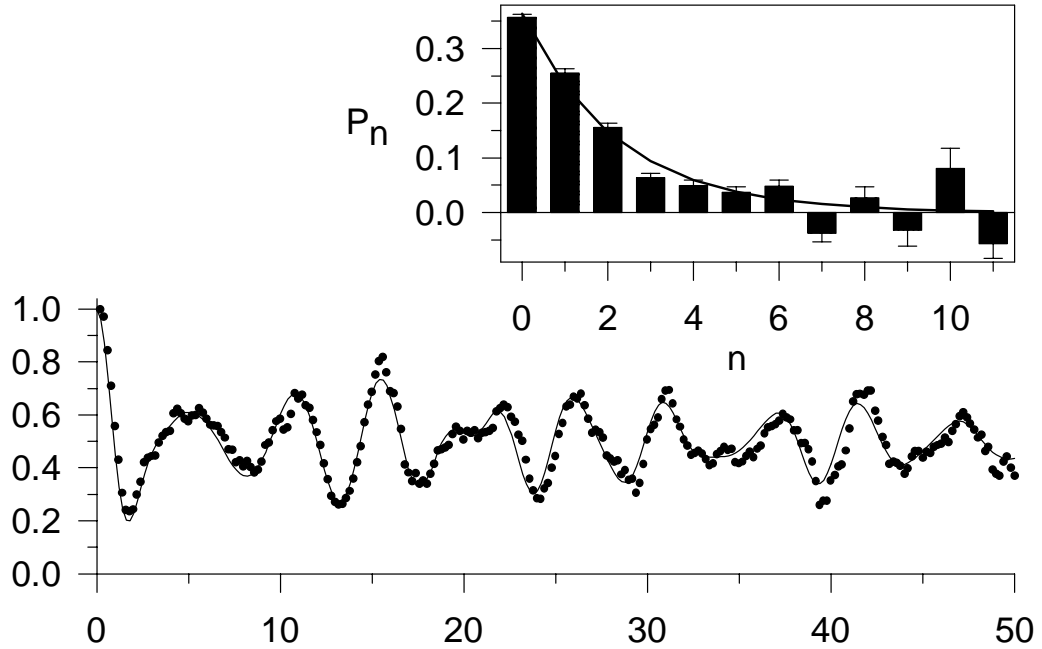


Figure 6.1: Rabi flopping curve on the blue sideband for a thermal state of the ion's motion. Different Fock state components flop sinusoidally with different Rabi frequencies (see Ch. 3), leading to the complicated dependence on the length  $t_{pr}$  of the probe pulse. The inset shows a singular-valued decomposition (SVD) of the Rabi flopping curve (see Sec. 3.5), showing the exponential distribution over the Fock states that one would expect for a thermal distribution. The solid line is a fit to a thermal distribution, yielding  $\bar{n} = 1.3 \pm 0.1$ .

states in the latter case give the number of photons in the cavity mode.) The Fock states are nonclassical: they are delocalized, with wave functions spread out between the corresponding classical turning points. In the position representation, the wave function of the Fock state  $|n\rangle$  is given by:

$$\psi_n(z) = \left(\frac{m\omega_z}{\pi\hbar}\right)^{1/4} \frac{1}{\sqrt{2^n n!}} e^{-m\omega_z z^2/2\hbar} H_n\left(\sqrt{\frac{m\omega_z}{\hbar}} z\right). \quad (6.2)$$

The  $H_n$ 's are the Hermite polynomials [72].

The ground state of the motional mode is obtained through Raman cooling (Sec. 5.2). Starting in the ground state of motion, we can prepare  $|n = 1\rangle$  by applying a  $\pi$  pulse on the upper motional sideband to drive  $|\downarrow, n\rangle$  to  $|\uparrow, n+1\rangle$ . The pulse

length is required  $t = \pi/(2\Omega_{0,1})$ . Indeed, the minima of the curve in Fig. 3.4(b) simply correspond to interaction times such that the ion ends up in  $|\uparrow, n = 1\rangle$  from  $|\downarrow, n = 0\rangle$ .

In order to produce higher- $n$  Fock states, we simply use the carrier transition to return the ion to  $|\downarrow\rangle$  and then apply another pulse on the upper sideband, alternating these steps until we reach the desired value of  $n$ . Alternatively, we can return the ion to  $|\downarrow\rangle$  using the *lower* sideband which, if we start out in  $|\uparrow\rangle$ , adds another quantum of motion to the system (since the lower sideband interaction couples  $|\downarrow, n\rangle \leftrightarrow |\uparrow, n - 1\rangle$ ). In this manner, we have created Fock states up to  $|n = 16\rangle$  [46].

Similar techniques may be used to engineer superpositions of Fock states. For example, we may create the state  $\frac{1}{\sqrt{2}}(|\downarrow, 0\rangle + |\downarrow, 2\rangle)$  by applying a  $\pi/2$  pulse on the blue sideband followed by a  $\pi$  pulse on the red sideband. Such states are useful in interferometers to probe certain kinds of decoherence (see Sec. 8.2). Indeed, by applying a sequence of pulses of appropriate lengths on the carrier and motional sidebands we can, in principle, create any desired superposition of Fock states, i.e., any motional state [121]. However, for certain classes of motional states, other techniques of production exist. In the next few sections, we shall examine some of these.

### 6.1.3 Coherent States

A coherent state of motion  $|\alpha\rangle$  [2, 94] corresponds to a displaced ground state wave packet [Eq. (6.2)] oscillating back and forth in the harmonic potential. A coherent state has the same position-momentum uncertainty product as the ground state:  $\Delta\hat{z}\Delta\hat{p} = \hbar/2$ . As this is the minimum value possible for this product, a coherent state is an example of a so-called “minimum uncertainty state.” For large amplitudes  $|\alpha|$  of oscillation, the zero-point width is much smaller than the amplitude of motion, and the coherent state approximates a point object moving in a harmonic well; for this reason, coherent states are also called “quasi-classical states” [2], and provide a means to draw a correspondence between the quantum and classical behaviour of a particle in a har-

monic well. They are also of interest because they represent the quantized harmonic oscillator of one mode of the electromagnetic field as produced by a laser [2].

Mathematically, coherent states are those for which the ensemble averages  $\langle \hat{z} \rangle$  and  $\langle \hat{p} \rangle$  of the position and momentum operators follow the same equations of motion as the classical position and momentum, and for which the expectation value of the energy is equal to that of the corresponding classical particle. This is mathematically equivalent (see Ref. [2], §G<sub>V</sub>) to the statement that  $|\alpha\rangle$  are eigenstates of the operator  $\hat{a}$ :  $\hat{a}|\alpha\rangle = \alpha|\alpha\rangle$ . This leads to the expression

$$|\alpha\rangle = e^{-|\alpha|^2/2} \sum_{n=0}^{\infty} \frac{\alpha^n}{\sqrt{n!}} |n\rangle. \quad (6.3)$$

Note that this is a Poisson distribution over the Fock states. Physically,  $\alpha$  gives the “size” of the coherent state: for example,  $\langle z \rangle = 2z_0 \text{Re}(\alpha)$ .

From a theoretical standpoint, coherent states are produced from the harmonic oscillator ground state through the action of the unitary displacement operator  $\hat{D}(\alpha) = \exp(\alpha\hat{a}^\dagger - \alpha^*\hat{a})$ . It is straightforward to use the Baker-Hausdorff formula to prove that  $\hat{D}(\alpha)|0\rangle = |\alpha\rangle$ . This is the origin of the displacement operator’s name:  $\hat{D}(\alpha)$  “displaces” the ground state wave packet from the origin of the  $\{z, ip\}$  plane by  $\alpha$ . Physically, we may realize the displacement operator by applying an electric field to the ion which is oscillating at the trap frequency. If we write the field as  $E = \mathbf{e}_z E_z \sin(\omega t - \phi)$ , then the interaction Hamiltonian between the field and the ion’s charge is given in the interaction picture by

$$\hat{H}_I(t) = -QE_z z_0 (\hat{a}e^{-i\omega_z t} + \hat{a}^\dagger e^{i\omega_z t}) \sin(\omega t - \phi). \quad (6.4)$$

If we express the sin function in exponential form, make a rotating wave approximation and set  $\omega = \omega_z$ , we obtain the time evolution operator:

$$\hat{U}(t) = e^{(\Omega_d t)\hat{a}^\dagger - (\Omega_d t)^*\hat{a}} = \hat{D}(\Omega_d t), \quad (6.5)$$

where I have defined  $\Omega_d \doteq -QE_z z_0 e^{i\phi}/(2\hbar)$ .

We may also effectively realize the displacement operator by applying a “walking standing wave” of light which resonantly drives the ion’s motion through the optical dipole force. In order to do this, we turn on the Raman beams such that their difference frequency is equal to  $\omega_z$  (rather than  $\omega_0 \pm \omega_z$ , as is usually the case). The light field polarizes the ion’s electron cloud, and the beat note between the two beams then drives the ion’s motion through the interaction with the induced dipole moment. One may analyze the interaction in the same manner as in Sec. 3.3. For example, if we consider the interaction between  $|\downarrow\rangle$  and  $|v\rangle$  induced by the Raman lasers (with  $\Delta\mathbf{k}\parallel\mathbf{z}$ ), and adiabatically eliminate  $|v\rangle$ , we obtain [73]:

$$\begin{aligned} \dot{C}'_{\downarrow,n} &= i \frac{|g_1|^2 + |g_2|^2}{\Delta_R} C'_{\downarrow,n} \\ &- \sum_m \langle n | \left[ \Omega^* \exp\left(i\eta(\hat{a}e^{-i\omega_z t} + \hat{a}^\dagger e^{i\omega_z t})\right) e^{-i\delta t} + H.C. \right] | m \rangle C'_{\downarrow,m}. \end{aligned} \quad (6.6)$$

As in Eq. (3.24), the first term represents an overall Stark shift of  $|\downarrow\rangle$ . If we absorb this into the definition of the ground state energy, then the dynamics of the  $C'_{\downarrow,n}$  are the same as those obtained in the interaction picture with the Hamiltonian

$$\hat{H}_I = \hbar\Omega^* \exp\left(i \left[ \eta(\hat{a}e^{-i\omega_z t} + \hat{a}^\dagger e^{i\omega_z t} - \delta t) \right]\right) + H.C. \quad (6.7)$$

If we make a rotating wave approximation, expand the exponentials of the operators  $\hat{a}$  and  $\hat{a}^\dagger$ , and assume we are in the Lamb-Dicke limit, this gives the time evolution operator

$$\hat{U}(t) = e^{(\eta\Omega^*t)\hat{a}^\dagger - (\eta\Omega t)\hat{a}} = \hat{D}(\eta\Omega^*t). \quad (6.8)$$

The above derivation is somewhat mathematical, and it is easy to lose sight of the fundamental physics in the situation. To try and identify this physics, we must remember that the two Raman beams are far-detuned from the virtual level  $|v\rangle$ , so that they do not drive much of the atomic population from  $|\downarrow\rangle$  to  $|v\rangle$ . Instead, their primary effect on the atom is to produce an energy shift of the atomic levels through the AC Stark effect. In order to examine this shift, we may use time-dependent perturbation

theory to calculate the energy of the part of the state vector left in  $|\downarrow\rangle$  (the eigenstate of the free Hamiltonian of the atom's spin degree of freedom). This is given by

$$\begin{aligned} \langle \downarrow | \hat{H}_{int} | \psi(t) \rangle &\approx \langle \downarrow | \hat{H}_{int} | \psi^{(1)}(t) \rangle \\ &\approx \langle \downarrow | \hat{H}_{int} [ |\downarrow\rangle + c_v^{(1)}(t) |v\rangle ], \end{aligned} \quad (6.9)$$

where the superscripts refer to first-order expansion perturbation theory solutions.

Now, assuming that the ion is illuminated equally by two plane waves travelling in the  $z$ -direction, the total electric field experienced by the ion is given by:

$$\begin{aligned} \mathbf{E} &= \mathbf{e}_x E (\cos(k_1 z - \omega_{L1} t + \phi_1) + \cos(k_2 z - \omega_{L2} t + \phi_2)) \\ &= \mathbf{e}_x 2E \cos(k_{avg} z - \omega_{avg} t + \phi_{avg}) \cos\left[\frac{1}{2}(\Delta k z - \delta t + \delta\phi)\right]. \end{aligned} \quad (6.10)$$

In the first cosine term, the *avg* subscripts refer to the averages of the laser wave-vectors, frequencies, and phases. This term is very rapidly varying. The second cosine term, however, is slowly-varying. Thus, we may express  $H_{int}$  as:

$$H_{int} = -2g(t) \left[ e^{i(k_{avg} z - \omega_{avg} t + \phi_{avg})} + e^{-i(k_{avg} z - \omega_{avg} t + \phi_{avg})} \right], \quad (6.11)$$

where

$$g(t) \doteq \langle \downarrow | \mathbf{e}_x \cdot \mathbf{r}_{el} \frac{eE}{2\hbar} \cos\left[\frac{1}{2}(\Delta k z - \delta t + \delta\phi)\right] | v \rangle \quad (6.12)$$

is a coupling strength which varies slowly in time. Substituting this interaction Hamiltonian into the usual time-dependent perturbation theory expansion, we find that (Schrödinger picture):

$$C_v^{(1)}(t) = \frac{-2g^*(t)e^{ik_{avg}z}}{\omega_{avg} - \omega_{v,\downarrow}} \left( e^{-i\omega_{avg}t} - e^{i\omega_{v,\downarrow}t} \right). \quad (6.13)$$

Finally, if we plug this into Eq. (6.9) and make a rotating wave approximation, we obtain:

$$\langle \downarrow | \hat{H}_{int} | \psi(t) \rangle = \frac{4|g(t)|^2\hbar}{\omega_{v,\downarrow} - \omega_{avg}} \left[ e^{-i(\omega_{v,\downarrow} - \omega_{avg})t} - 1 \right], \quad (6.14)$$

where  $\epsilon_{\downarrow}$  is the unperturbed energy of  $|\downarrow\rangle$ . Now,  $\omega_{v,\downarrow} - \omega_{avg} = \Delta_R - \frac{1}{2}\delta \approx \Delta_R$ . Thus, averaging over the fast time scale  $1/\Delta_R$ , we have

$$\langle \downarrow | \hat{H}_{int} | \psi(t) \rangle \approx -\frac{4\hbar |g(t)|^2}{\Delta_R}. \quad (6.15)$$

So the effect of the “standing walking wave” is to create a time-dependent Stark shift of the level  $|\downarrow\rangle$ . The time dependence occurs in the term  $|g(t)|^2$  and thus, at the frequency  $\delta \approx \omega_z$ . This time-dependent Stark shift leads to a time-dependent force on the ion which, in the Lamb-Dicke limit, acts like a displacement operator upon the ion. Although the effects on  $|\downarrow\rangle$  have been treated here,  $|\uparrow\rangle$  is affected in a similar way.

The “walking standing wave” technique has the following advantage: the force produced by this interaction depends on the polarization of the lasers and the matrix elements of the atomic levels. So, for example, if the Raman beams are polarized  $\sigma^-$  then, since there is no  $|F = 2, m_F = -(2 + 1)\rangle$  virtual state in the  $2p \ ^2P_{1/2}$  level to which  $|\downarrow\rangle$  may couple, only the  $|\uparrow\rangle$  state is affected by the Raman beams. This allows us to create a coherent state *only* in the component of the ion’s state vector which is in  $|\uparrow\rangle$ , which is useful for interferometry or for producing “Schrödinger cat” states. I shall discuss these issues in greater detail in Sec. 6.2.1.

Fig. 6.2(a) shows the Rabi flopping curve on the upper sideband for a coherent state with  $|\alpha| = 3.1 \pm 0.1$  [46]. Notice the so-called “collapse” and “revival” in  $P_1$ : the Rabi flopping collapses to almost a straight (50%) line around time  $t = 8\mu s$ , but then coherent features reappear (“revive”) at around  $t_{pr} = 15\mu s$ . These features are characteristic of coherent states [122, 123], and are a result of the strongly peaked Poisson distribution of Fock states which make up a coherent state.

#### 6.1.4 Squeezed States

A coherent state is one example of a “minimum-uncertainty state.” For this state,  $\Delta\hat{z} = \sqrt{\frac{\hbar}{2m\omega_z}}$  and  $\Delta\hat{p} = \sqrt{\frac{m\hbar\omega_z}{2}}$ , so that  $\Delta\hat{z}\Delta\hat{p} = \hbar/2$ . However, it is possible to create

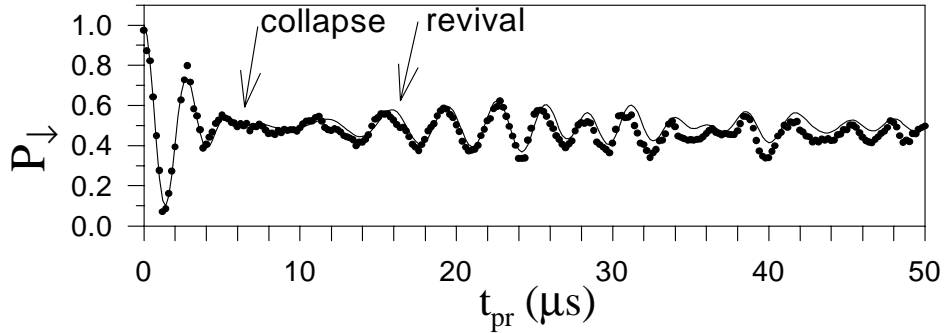


Figure 6.2: Rabi flopping curve for a coherent state, with  $|\alpha| = 3.1 \pm 0.1$ . The “collapse” and “revival” characteristic of such a state are evident. The solid curve is a fit to a coherent state population distribution (yielding  $|\alpha| = 3.1 \pm 0.1$  for the fit).

states such that  $\Delta \hat{z} < \sqrt{\frac{\hbar}{2m\omega_z}}$  at the expense of increasing  $\Delta \hat{p}$  commensurately, or vice versa. Such states are called “squeezed states” [124]. If we picture the ion’s wave packet in the  $\{z, p\}$  plane then, roughly speaking, a coherent state forms a circular disk (of finite “radius” to satisfy Heisenberg) a distance  $|\alpha|$  from the origin. A squeezed state is an ellipse — a squeezed circle, if you will.

Mathematically, squeezed states are produced from the ground state of motion through the action of the unitary “squeeze operator”<sup>2</sup>  $\hat{S}(\epsilon) = \exp[\frac{1}{2}(\epsilon^* \hat{a}^2 - \epsilon (\hat{a}^\dagger)^2)]$  where, in the traditional nomenclature,  $\epsilon$  is expressed as  $\epsilon = R e^{2i\phi}$ . One can show [105] that  $\hat{S}^\dagger(\epsilon)(\tilde{z} + i\tilde{p})\hat{S}(\epsilon) = \hat{y}_1 e^{-R} + i\hat{y}_2 e^R$ , where  $\hat{y}_1 + i\hat{y}_2 = (z + ip)e^{-i\phi}$ . Thus, the squeeze operator causes a rotation in the  $\{z, p\}$  plane by angle  $\phi$ , then attenuates one component of the motion as it amplifies the other. This leads to  $\Delta \hat{y}_1 = e^{-R}$  and  $\Delta \hat{y}_2 = e^R$ , so that indeed, the squeezed state features reduced uncertainty in one quadrature at the expense of increased uncertainty in the other.

<sup>2</sup> Actually, in full generality, a squeezed state is produced by  $\hat{D}(\alpha)\hat{S}(\epsilon)$  acting on the vacuum, rather than only  $\hat{S}(\epsilon)$ . This is a squeezed state which is displaced from the origin of the  $z - p$  plane. What I am referring to as “squeezed states” are, to be more accurate, actually called “squeezed vacuum states.”

We can create squeezed states by modulating the strength of the trap at twice the trap frequency. This produces a parametric resonance (much like the parametric resonance one uses to get oneself going when one is sitting on a swing!), which produces a squeezed state of motion [125]. However, this technique is not practical with our apparatus: since we would like to modulate the strength of the trap, we require strong field gradients at frequency  $2\omega_z$  (see Ch. 2), but frequency components at  $2\omega_z$  are heavily attenuated by the filters on the trap.

Instead, we use the same “walking standing wave” technique used to produce coherent states. This time, we set the detuning  $\delta$  of the laser beams to be equal to  $2\omega_z$ . Now in Eq. (6.7),  $\delta = 2\omega_z$ , and if we are in the Lamb-Dicke limit and make a rotating wave approximation (neglecting off-resonant terms), the result is that

$$\hat{H}_I = \frac{\hbar\eta^2}{2} \left[ \Omega^* \hat{a}^2 + \Omega (\hat{a}^\dagger)^2 \right], \quad (6.16)$$

leading to

$$\hat{U}(t) = e^{\frac{1}{2}[(i\eta^2\Omega)^* \hat{a}^2 - (i\eta^2\Omega)(\hat{a}^\dagger)^2]t} = \hat{S}(i\eta^2\Omega t) \quad (6.17)$$

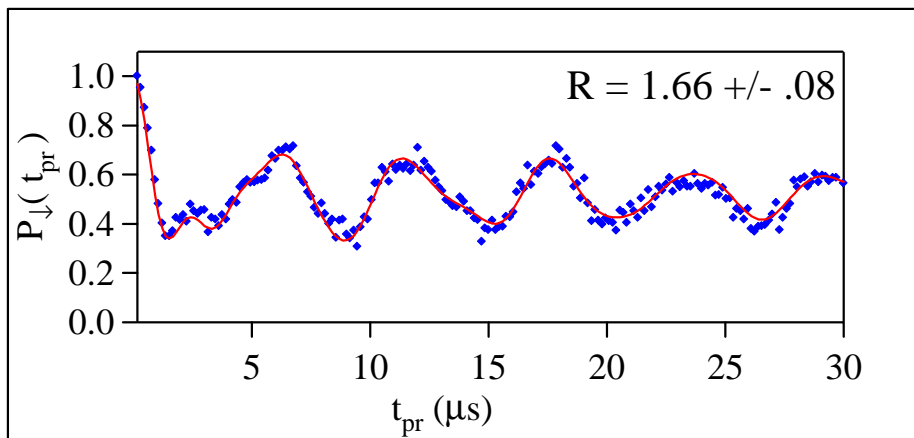
(where the laser phase is included in  $\Omega$ ).

Figure 6.3(a) shows the Rabi flopping curve on the blue sideband for a squeezed state with  $R \approx 1.5$ . Figure 6.3(b) shows the result of leaving the lasers on for a longer period of time. In this latter case, the ion is driven out of the Lamb-Dicke regime, and the higher-order terms in Eq. (3.7) come into play. The resulting state is no longer a pure squeezed state, but suffers additional rotation and shearing in the  $\{z, p\}$  plane.

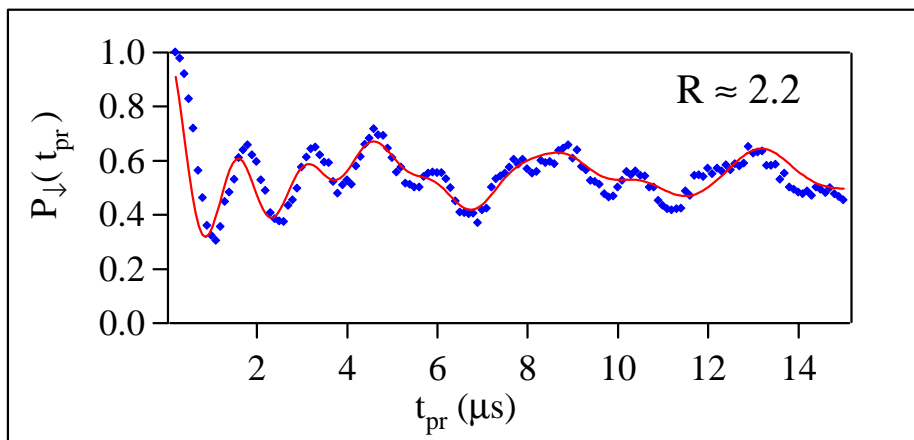
## 6.2 Entangling Spin and Motion: One Ion

### 6.2.1 “Schrödinger’s Cat”

The phrase “Schrödinger’s cat” refers to a paradoxical *Gedankenexperiment* [9] in which Schrödinger envisioned correlating the state of a macroscopic object with that of a microscopic one (which obeys quantum mechanics). In particular, he imagined a



(a)



(b)

Figure 6.3: (a) Rabi flopping curve for a squeezed state, with  $R = 1.5 \pm .2$ . (b) Rabi flopping curve for a state in which the parametric, “walking standing wave” interaction is left on long enough for nonlinearities to enter the expressions for the Rabi frequencies. The solid curves are fits to the squeezed state population distribution.

cat to be confined inside a box with a radioactive nucleus, a bottle of cyanide, and a trigger device which would break the bottle if the nucleus decayed — thus killing the cat. The paradox arises in the case when the nucleus is in a superposition of decayed and undecayed. Although we are used to considering such a situation, in this case it poses a problem. For, if we consider the system as a whole quantum mechanically then, since the cat’s state is correlated with that of the nucleus, we are left with a situation in which, according to the standard interpretation of quantum mechanics, we must consider the cat to be in a superposition of being alive *and* dead. This is not a state in which cats are normally found!

This paradox was meant to highlight some of the difficulties with the traditional Copenhagen interpretation, which drew an (arbitrarily placed) dividing line between the microscopic world of quantum mechanics and the macroscopic world which we experience. Much discussion has ensued on the subject of Schrödinger’s hapless feline, but the *Gedankenexperiment* illustrates the general lack of agreement on exactly how the transition from quantum mechanical to classical behaviour occurs.

In the context of quantum optics, the phrase “Schrödinger’s cat” was appropriated to describe a situation in which a microscopic degree of freedom is entangled with a mesoscopic one. We use the term in the same vein in the context of our trapped-ion system, to describe the situation in which the atom’s spin is entangled with two mesoscopically distinct motional states. In particular, such states provide a controlled environment for studying quantum decoherence, which may shed light on the issue of “wave function collapse” [15] and also is of interest to us in our examination of quantum computation (see Sec. 7.1).

In particular, we can create the state [47]

$$|\Psi\rangle = \frac{1}{\sqrt{2}}(|\downarrow, \alpha_1\rangle + |\uparrow, \alpha_1\rangle), \quad (6.18)$$

where  $|\alpha_j\rangle$  is a coherent state of motion. If, for example,  $|\alpha_\uparrow\rangle = |-\alpha_\downarrow\rangle$ , then we have a situation when, at the extremum of the ion's motion, it is (in some sense) *simultaneously* in the state  $|\downarrow\rangle$  and at one side of the trap and in the state  $|\uparrow\rangle$  and at the *opposite* side of the trap! We have created such a state where the two coherent state wave packets were separated by 80 nm, about ten times the width of the wave packet.

In order to create such a state, we take advantage of the “walking standing wave” method of generating coherent states. As mentioned in Sec. 6.1.3, the interaction between the laser beams and the ion depends on the ion's electronic state (different electronic states have different matrix elements — see Appendix B). So, for example, if the light is polarized  $\sigma^-$  then, since there is no  $2p\ ^2P_{1/2}, m_F = -3$  level with which  $|\downarrow\rangle$  can interact, the lasers only affect  $|\uparrow\rangle$  (at least, if we ignore off-resonant transitions through the  $2p\ ^2P_{3/2}$  level). To create the state  $\frac{1}{\sqrt{2}}(|\downarrow\rangle + |\uparrow\rangle)$ , we could turn on the “walking standing wave”, exchange  $|\uparrow\rangle$  and  $|\downarrow\rangle$ , and repeat the process. This was the technique used in Ref. [47].

However, there is a simpler technique for producing states of the form  $|\Psi\rangle$ . If we arrange the polarizations of the two laser beams correctly, then we can drive both  $|\downarrow\rangle$  and  $|\uparrow\rangle$  at the same time. In practice, the  $RR_{co}$  beam must have the polarization  $\frac{1}{\sqrt{2}}(\sigma^+ + \sigma^-)$ , since it is put into the trap with a polarizing beamsplitter cube. Let the  $RR_\perp$  beam have the polarization  $\Lambda\sigma^- + \Upsilon\sigma^+$ . Assume that  $g_1 = g_2 = g$ . Then, including the matrix elements between  $|\downarrow\rangle$ ,  $|\uparrow\rangle$ , and the  $2p\ ^2P_{3/2,1/2}$  states explicitly (see Appendix B), the effective Rabi frequencies when we turn on the displacement beams are

$$\Omega_\downarrow = \frac{g^2}{\Delta_R + \omega_0} \frac{2\Upsilon}{3} + \frac{g^2}{\Delta_R + \delta_{FS} + \omega_0} \left( \Lambda + \frac{\Upsilon}{3} \right) \quad (6.19)$$

$$\Omega_\uparrow = \frac{g^2}{\Delta_R} \left( \frac{\Lambda}{2} + \frac{\Upsilon}{6} \right) + \frac{g^2}{\Delta_R + \delta_{FS}} \left( \frac{\Lambda}{2} + \frac{5\Upsilon}{6} \right). \quad (6.20)$$

In these equations,  $\delta_{FS}$  is the fine-structure splitting of the  $2p\ ^2P$  levels ( $\approx 197$  GHz). It is convenient to set  $|\Lambda| = |\Upsilon|$  when running the experiment, for then the Stark shifts

of the two levels ( $|\downarrow\rangle$  and  $|\uparrow\rangle$ ) are the same (up to order  $\delta_{HF}/\Delta_R$ ). To get a rough idea of the effects of the two beams on the different atomic levels, assume that we are tuned near the  $2p\ ^2P_{1/2}$  level, so that we may neglect the second terms in Eqs. (6.19) and (6.20). Let us also neglect  $\omega_0$  with respect to  $\Delta_R$ . If we assume that  $\Lambda$  is purely real, then we may write  $\Upsilon = \Lambda e^{2i\chi}$ . (For example, we may alter the polarization of the  $RR_\perp$  beam with a half-wave plate. In this case,  $\chi$  is the angle of said wave plate from the vertical, which is  $90^\circ$  from the plane of the Blue Raman polarization.) Making these substitutions, we find that:

$$\frac{\Omega_\downarrow}{\Omega_\uparrow} \approx \frac{4}{1 + 3e^{-2i\chi}}. \quad (6.21)$$

Since  $\alpha$  is proportional to  $\Omega_j$ , we can vary  $\alpha_\downarrow/\alpha_\uparrow$  by varying the laser beam polarization. Fig. 6.4 shows  $\Omega_\downarrow/\Omega_\uparrow$  as a function of the angle of the aforementioned polarizer. In practice, we usually chose to have  $\alpha_\downarrow = -2\alpha_\uparrow$ .

Thus, in order to create a state of the form  $\Psi$ , we apply a  $\pi/2$ -pulse on the co-propagating carrier, to create  $\frac{1}{\sqrt{2}}(|\downarrow\rangle + |\uparrow\rangle)$ , then turn on the displacement laser beams, creating  $\Psi$  with only one displacement pulse. If  $|\alpha|$  were large enough, we could, in principle, spatially resolve the two wave packets and correlate the atom's position with its electronic state [126]. However, this is not possible for the size of cats which we produced (which really, given their size, were more like kittens than cats).

Instead, we interfere the motional wave packets in  $|\uparrow\rangle$  and  $|\downarrow\rangle$ , to produce interference fringes. In order to do this, we reverse the original carrier and displacement pulses to reverse the state creation. However, we put a variable phase between the first displacement pulse and the reversal pulse (by putting a phase shift on the rf driving the splitter AOM). As this phase is swept, a pattern of fringes appears in  $P_\downarrow$ . Thus, the complete experiment is really a form of Ramsey-type interferometer (see Sec. 3.4 or Ref. [95]). The first carrier and displacement pulses create a superposition state, playing the role of the first Ramsey zone. Similarly, the reversal pulses, which have a

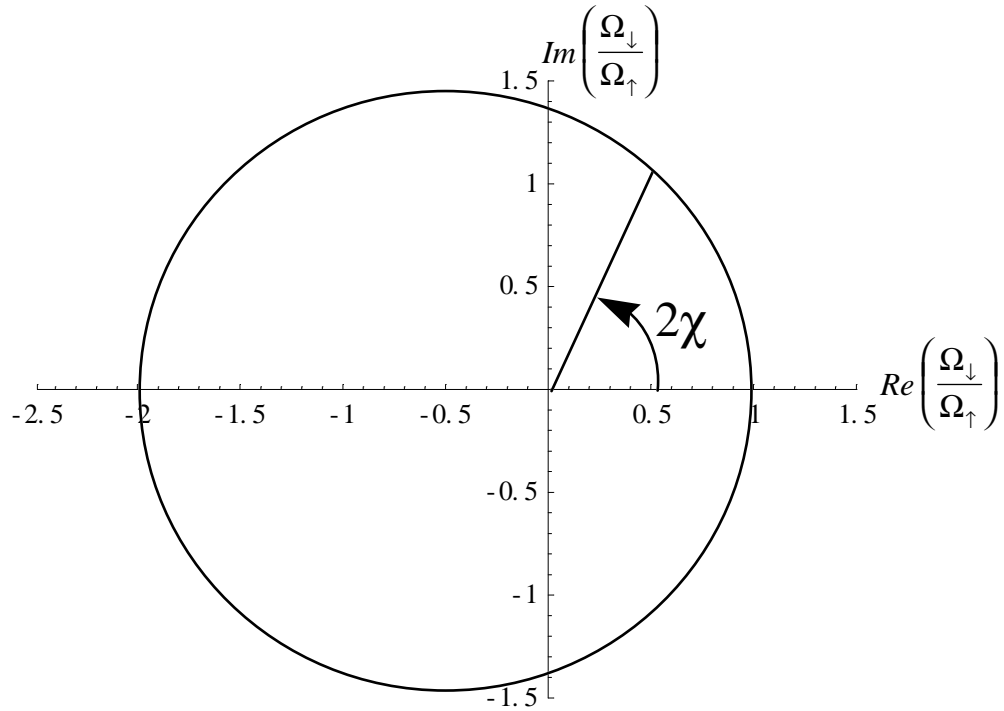


Figure 6.4:  $\frac{\Omega_{\downarrow}}{\Omega_{\uparrow}}$  as a function of the angle of the polarizer in the  $RR_{\perp}$  beam line from the vertical. This assumes that  $\alpha_{\uparrow} = 1$ , that  $|\Upsilon| = |\Lambda|$ , and neglects the ground-state hyperfine splitting. By varying the polarizer angle, we can vary the relative displacements of  $|\downarrow\rangle$  and  $|\uparrow\rangle$  produced by the “walking standing wave” interaction, and produce “Schrödinger cat” states.

different effective phase than the first pulses, play the role of the second Ramsey zone.

We shall return to this idea in Ch. 8.

As a function of the phase  $\phi$  between the state creation and reversal (and assuming equal Rabi frequencies on the creation and reversal pulses),  $P_{\downarrow}$  is given by:

$$P_{\downarrow}(\phi) = \frac{1}{2} \left( 1 + e^{-|\alpha_{\downarrow} - \alpha_{\uparrow}|^2 (1 + \cos \phi)} \times \cos \left[ \vartheta + 2(1 + \cos \phi) \text{Im}\{\alpha_{\downarrow}^* \alpha_{\uparrow}\} + \sin \phi (|\alpha_{\downarrow}|^2 - |\alpha_{\uparrow}|^2) \right] \right), \quad (6.22)$$

where  $\alpha_{\downarrow}$  and  $\alpha_{\uparrow}$  are the coherent state amplitudes in  $|\downarrow\rangle$  and  $|\uparrow\rangle$  produced by the state creation, and  $\vartheta$  allows for the possibility of a phase between the two carrier  $\pi/2$

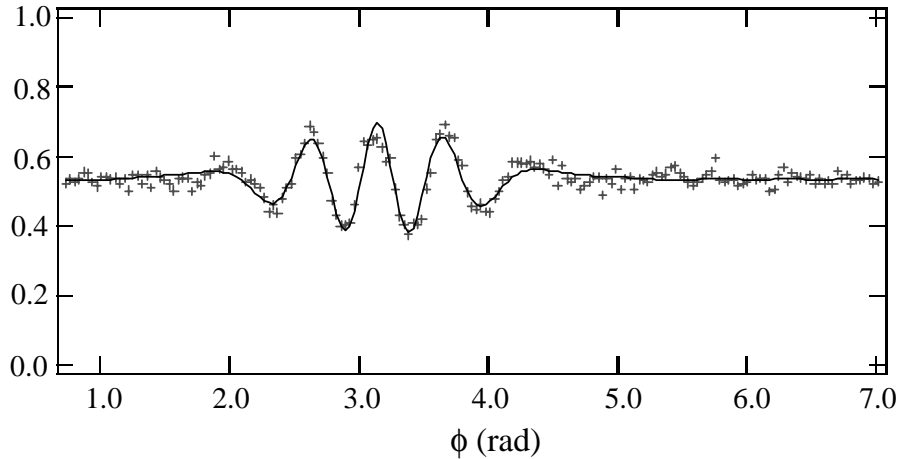


Figure 6.5: Measured and fit interference signals  $P_{\downarrow}(\phi)$  for a “Schrödinger cat” state [see Eq. (6.18)], as a function of the phase  $\phi$  between coherent state creation and reversal. For this data, one of the spin states was displaced while the other was not. The solid line is a fit to theory.

pulses. Characteristic interference patterns are shown in Fig. 6.5 — they indicate the correlations and coherence inherent in the state.<sup>3</sup>

The creation of Schrödinger cat states with trapped ions is paralleled in systems such as atom [127, 128, 129, 130], electron [131], or neutron [132] interferometers or in Rydberg states in atoms [133, 134, 135]. However, in our case, there is no dispersion of the wave packet with time, since the confining potential is harmonic. This provides a well controlled system with which to study, for example, decoherence. I shall return to this in Ch. 8.

### 6.3 Determining the Complete Motional State

One of the more significant changes in our concept of the physical universe wrought by quantum mechanics is the lack of distinction between measurement and

---

<sup>3</sup> The data in Ref. [47] were taken in a slightly different manner: only one displacement pulse was used, and the phase of the second  $\pi/2$  pulse was swept.

state preparation. In our case, for example, the same Raman interactions that we use to create motional states are also used to map information about the motional-level populations onto the ion’s spin, which is our observable. The fact that the Rabi frequency on the motional sidebands depends on the motional level allows us to discriminate different Fock state components with unit efficiency (by, for example, a singular-value decomposition [96] of the frequency components of the Rabi flopping curve), as discussed in Sec. 3.5.

This technique allows us to determine the  $n$ -state populations (or probabilities), but does not give us phase information; therefore, it does not provide us with a *complete* description of the motional states. However, by using a coherent state generation interaction — which is equivalent to a displacement in phase space — in conjunction with the Rabi flopping curves, we can reconstruct the Wigner function or the density matrix of the motional state [136]. The techniques we use are similar to those of quantum state tomography [48].

Like the density matrix, the Wigner function [137] provides a complete description of a quantum state. It is a description formulated in phase space — the same phase space familiar from classical mechanics. However, the Heisenberg Uncertainty Principle prohibits us from simultaneously specifying both position and momentum, so we must make some modifications to our classical picture of phase space and phase space probability distributions. The Wigner function  $W(z, ip) \equiv W(\alpha)$  (where  $\alpha = z + ip$ ) is the “best possible phase space distribution” [138]:

$$W(\alpha) \equiv W(z, ip) = \frac{1}{2\pi} \int_{-\infty}^{+\infty} e^{ipq} \left\langle z - \frac{q}{2} \left| \rho \right| z + \frac{q}{2} \right\rangle dq. \quad (6.23)$$

(Here  $\rho$  is the motional state density matrix.) However, the “weirdness” of quantum mechanics gives it some unusual properties for a probability distribution: it can, for example, be negative! For this reason, it is usually referred to as a “quasiprobability distribution.” Nonetheless, for a given state, the Wigner function does give the correct

marginal distributions for  $z$  and  $p$  (as we would calculate from  $\langle z \rangle$  or  $\langle p \rangle$ ). For example:

$$\langle z | \rho | z \rangle = \int_{-\infty}^{+\infty} W(z, ip) dp > 0. \quad (6.24)$$

The basic idea for determining the density matrix  $\rho$  or the Wigner function  $W(\alpha)$  is to measure the overlap of the motional state with some known set of basis functions — in our case, the Fock states. If we displace the motional states by different amounts and in different directions in phase space, we can measure how the overlap with the Fock states changes with the (phase-dependent) displacement and thus extract phase, as well as amplitude, information.

If we represent the initial motional state as  $|\psi\rangle = \sum_{n=0}^{\infty} C_n |n\rangle$ , then the first step in determining the Wigner function is to displace this state using a resonant electric field at the motional frequency (see Sec. 6.1.3). After the displacement, the motional state  $|\psi_d\rangle$  is now given by  $|\psi_d\rangle = \sum_{n=0}^{\infty} C_n(\alpha) |n\rangle$ , where the expansion coefficients  $C_n(\alpha)$  explicitly depend on the displacement. If a Raman probe pulse on the upper motional sideband is then applied, the signal is given by (see Eq. (3.34)):

$$P_{\downarrow}(t_{pr}, \alpha) = \sum_{n=0}^{\infty} |C_n(\alpha)|^2 \cos^2(\Omega_{n,n+1} t_{pr}). \quad (6.25)$$

From this, the coefficients  $|C_n(\alpha)|^2$  (which are simply the  $P_n$ 's of the displaced motional state) can be determined by performing a singular-valued decomposition. The Wigner function at the point  $\alpha = z + ip$  in phase space is then given by the simple formula [139, 140, 141, 142]:

$$W(\alpha) = \frac{2}{\pi} \sum_{n=0}^{\infty} (-1)^n |C_n(\alpha)|^2. \quad (6.26)$$

In practice, we truncate the sum at some  $n_{max}$ . Fig. 6.6(a) shows the reconstructed Wigner function for an approximate  $|n = 1\rangle$  Fock state; the negative values near the origin indicate the highly nonclassical nature of the state. Fig. 6.6(b) shows the reconstructed Wigner function of a coherent state. The theoretically predicted Wigner function is a two-dimensional Gaussian, and the reconstructed Wigner function, indeed, appears Gaussian.

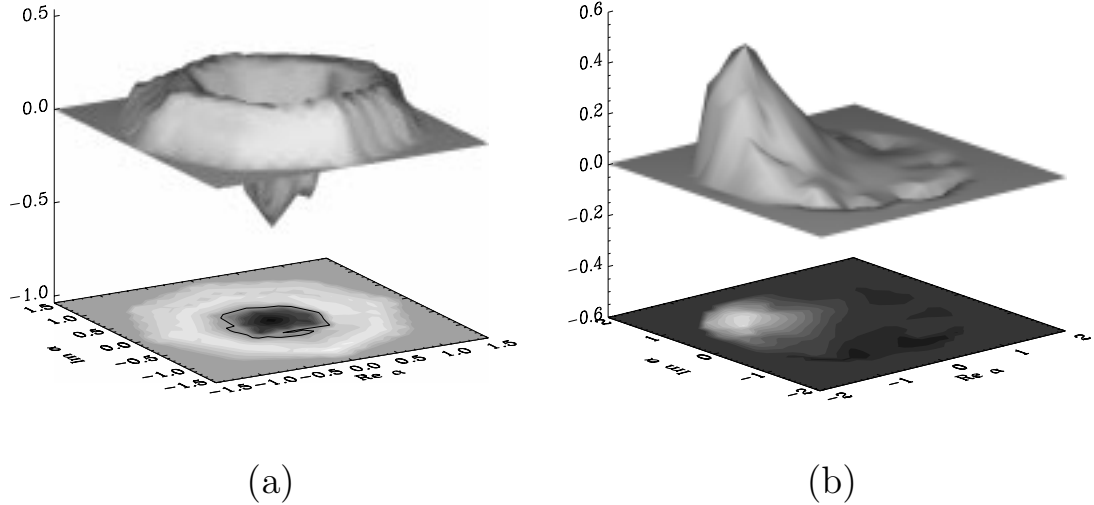


Figure 6.6: (a) Reconstructed Wigner function for an  $|n = 1\rangle$  Fock state. The plotted points are the result of fitting a linear interpolation between the actual data points to a 0.1 by 0.1 grid. The octagonal shape is an artifact of the eight measured phases per radius (ten radii were measured). The white contour represents the line  $W(\alpha) = 0$ . The negative values around the origin highlight the nonclassical nature of this state. (b) Reconstructed Wigner function for a coherent state  $|\alpha\rangle$ . The points are the fit of a linear interpolation of the data points to a 0.13 by 0.13 grid. The approximately Gaussian minimum-uncertainty wave packet is centred around an amplitude of 1.5 (from the origin). The half-width at half maximum is  $\approx 0.6$ , in accordance with the minimum uncertainty half width of  $\approx 0.59$ . To suppress artifacts in the Wigner function summation, data with  $n_{max} = 5, 6$  have been averaged together (as suggested by M. Collett, *private comm.*).

This technique gives the Wigner function at a particular point in phase space: in order to map out the motional state with a given precision, a suitably large number of measurements is required. It is also possible to make  $2N$  measurements and completely reconstruct the density matrix elements  $\rho_{nm}$  with respect to the Fock states up to  $n = m = M - 1$ . To do this, we displace the state to be measured to  $2M$  different locations in phase space equally spaced along a circle of radius  $|\alpha|$ , each time measuring the Rabi flopping curve. This allows us to invert the relationship

$$|\mathcal{C}_n(\alpha)|^2 = \langle n | \hat{D}^\dagger(\alpha) \hat{\rho} \hat{D}(\alpha) | n \rangle, \quad (6.27)$$

where  $\hat{D}(\alpha)$  is the unitary operator representing the displacement interaction. (In practice, since the data over-constrained the relationship, we used a fitting procedure instead of an inversion.) Note that  $|\mathcal{C}_0(\alpha)|^2/\pi$  is the  $Q$ -function [105]. The details are described in Refs. [136, 48] and a similar technique is described in Ref. [143]. However, I shall briefly outline the idea of the technique here. Write  $|\mathcal{C}_n(\alpha)|^2 = Q_n(\alpha)$ . Then, using the fact that  $\hat{a}^n e^{-\alpha\hat{a}^\dagger} = \hat{a}^{n-1} e^{-\alpha\hat{a}^\dagger} (\hat{a} - \alpha)$ , and applying the properties of  $\hat{a}$  and  $\hat{a}^\dagger$ , we can rewrite Eq. (6.27) as

$$Q_n(\alpha) = \frac{e^{-|\alpha|^2} |\alpha|^{2n}}{n!} \sum_{l,m=0}^{\infty} \sum_{j,j'=0}^n \frac{(\alpha^*)^{l-j} \alpha^{m-j'}}{l!m!} (-1)^{-j-j'} \\ \times \binom{n}{j} \binom{n}{j'} \sqrt{(m+j)!(l+j)!} \rho_{l+j',m+j}. \quad (6.28)$$

Now, suppose that we measure  $Q_n(\alpha)$  with  $\alpha$  equally spaced on a circle:  $\alpha_p = a e^{i(\pi/M)p}$ , with  $p \in \{-M, \dots, M-1\}$ . Then, Eq. (6.28) becomes

$$Q_n(p) = \frac{e^{-a^2} a^{2n}}{n!} \sum_{l,m=0}^{\infty} \sum_{j,j'=0}^n \frac{a^{l+m-j-j'}}{l!m!} (-1)^{-j-j'} \\ \times \binom{n}{j} \binom{n}{j'} \sqrt{(m+j)!(l+j)!} \rho_{l+j',m+j} e^{ip(\pi/M)(j+m-l-j')}. \quad (6.29)$$

One can then determine  $\rho_{n,m}$  by use of the following orthonormality relationship:

$$\frac{1}{2M} \sum_{p=-M}^{M-1} e^{ip(\pi/M)r} e^{-ip(\pi/M)s} = \delta_{r,s}. \quad (6.30)$$

So, if we multiply Eq. (6.29) by  $\frac{1}{2M} e^{-ip(\pi/M)s}$  and sum over the data from  $p = -M, \dots, M-1$ , we obtain (after some reworking of the indices):

$$Q_n^{(s)} \doteq \frac{1}{2M} \sum_{p=-M}^{M-1} Q_n(p) e^{-ip(\pi/M)s} \\ = \sum_{k=\max\{0,-s\}}^{\infty} \mathcal{M}_{nk}^{(s)} \rho_{k,k+s} \quad (6.31)$$

with matrix elements

$$\mathcal{M}_{nk}^{(s)} = \frac{e^{-a^2} |\alpha|^{2n}}{n!} \sum_{j=0}^{\min\{n,k\}} \sum_{j'=0}^{\min\{n,s+l\}} |\alpha|^{2(l-j-j')+s} (-1)^{-j-j'} \\ \times \binom{n}{j} \binom{n}{j'} \frac{\sqrt{(s+n)!n!}}{(s+n-j)!(n-j)!}. \quad (6.32)$$

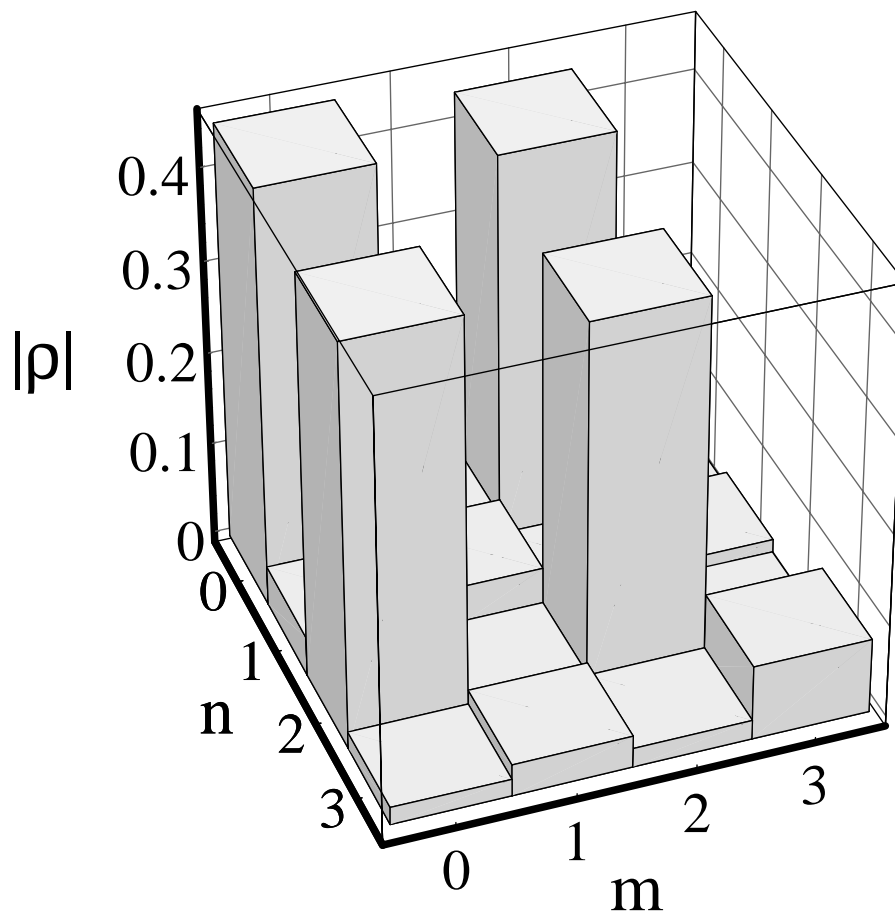


Figure 6.7: Reconstructed density matrix amplitudes of an approximate  $\frac{1}{\sqrt{2}}(|n=0\rangle - i|n=2\rangle)$  state.

In practice, we can truncate the infinite sum in Eq. (6.31) at some  $N$ . Then we can invert the matrix equation to determine  $\rho_{n,m}$ , using standard techniques.

Fig. 6.7 shows the reconstructed density matrix element amplitudes (in the Fock-state basis) for an approximate  $\frac{1}{\sqrt{2}}(|n=0\rangle - i|n=2\rangle)$  state.

## 6.4 Quantum State Engineering of Two Ions

Cirac and Zoller’s scheme for quantum computation ([40], see Sec. 7.3) calls for a collection of trapped ions, each of which may be individually addressed by laser beams. Thus far, I have discussed single-ion experiments but obviously, if we wish to work towards a quantum register along the lines of Cirac and Zoller, we need to work with multiple ions. The challenge in this task is to focus laser beams tightly enough to address the ions while simultaneously keeping the trap strong enough to allow easy manipulation of the ions’ motion and minimize the effects of background heating. Of course, these two tasks are at odds with each other: a strong trap forces the ions together, making individual addressing more of a challenge.

We have, indeed, focussed the laser beams down to a waist of  $\approx 3 \mu\text{m}$  and addressed one of two trapped ions, with negligible interaction of the other ion with the beams. This was done in the Be-electrode elliptical microtrap, with  $\omega_x \approx 6 \text{ MHz}$ . However, it was a somewhat challenging task. The AOMs used to switch the beams on and off did not produce ideal, Gaussian beams, and so there was a lot of stray light. This was reduced by sending the beam through a single mode fiber before focussing it through the trap. The fiber, however, added amplitude noise to the light (peaked around several kHz), so that it was necessary to add extra “noise-eater” circuitry to eliminate this noise. Even then, however, it was not possible to achieve high fidelity when the beams were focussed tightly. The coaxial resonator, as it turned out, was also a long mechanical lever arm, which transmitted acoustic and mechanical vibrations from the room and optical table to the trap structure, and caused it to oscillate with respect to the beam waist, reducing the fidelity of laser-induced interactions.

These technical problems are, of course, surmountable in principle. But, in the meantime, we were able to perform interesting multi-particle experiments without hav-

ing to focus the laser beams or reduce the trap strength. In particular, we were able to create entangled states of two ions' spins.

Multi-ion entangled states, such as two-particle Bell states [10, 144] or Greenberger-Horne-Zeillinger triplets [145] ( $\frac{1}{\sqrt{2}}[|\downarrow, \downarrow, \downarrow\rangle + |\uparrow, \uparrow, \uparrow\rangle]$ ), are interesting for the opportunities they provide to test quantum mechanics versus other possible theories [146] and for their illustration of quantum mechanics' seemingly paradoxical nature. But multi-ion entangled states are also of more practical and immediate interest in precision spectroscopy. For such applications, the Ramsey method of separated oscillatory fields [95] (see Sec. 3.4) is generally used to ascertain the frequency of a transition; for example, the frequency of the  $|\downarrow\rangle \rightarrow |\uparrow\rangle$  transition in our case. If all sources of technical noise are eliminated, then the fundamental limit to the Ramsey method's accuracy is the "quantum projection noise" [147] from the projection of the atoms onto one or the other basis state during the probe pulse. For uncorellated atoms, this limit is given by  $\frac{\delta\omega}{\omega} = \frac{1}{\sqrt{NT_R\tau_I}}$ , where  $T_R$  is the time between the two Ramsey zones,  $\tau_I$  is the total averaging time for the complete frequency measurement and  $N$  is the number of atoms. On the other hand, if we could replace the first  $\frac{\pi}{2}$  pulse with one that produces the state  $|\psi_{en}\rangle = \frac{1}{\sqrt{2}}(|\downarrow, \downarrow, \dots, \downarrow\rangle + e^{i\phi}|\uparrow, \uparrow, \dots, \uparrow\rangle)$ , then the fundamental precision is given by  $\frac{\delta\omega}{\omega} = \frac{1}{N\sqrt{T_R\tau_I}}$ , which is the so-called "Heisenberg limit" [148].

#### 6.4.1 Entangled States of Two Ions

The most straightforward way to produce entangled states such as the Bell states<sup>4</sup>  $|\psi_B^\pm\rangle = \frac{1}{\sqrt{2}}(|\downarrow, \uparrow\rangle \pm |\uparrow, \downarrow\rangle)$  is to address the ions differentially. In order to do so, we need some way of introducing a different interaction at each ion. One possibility is to focus the laser beams tightly so that one ion is illuminated while the other is not (i.e., has zero Rabi frequency). However, there is another way to achieve the same effect by using the micromotion.

---

<sup>4</sup> Note that  $|\psi_B^-\rangle$  is the "Einstein, Podolsky, Rosen" (EPR) pair.

Recall from Sec. 2.1 that a trapped ion's motion is made up of two parts: the slow secular motion at  $\omega_m$ , which we cool and quantize, and the fast, small amplitude, classical micromotion at  $\Omega_T$ . This micromotion can “fuzz out” the interaction with the laser beams, thereby reducing the coupling strength. Near the null of the rf trapping field, the amplitude of the micromotion is negligible. However, by applying a static potential to an additional electrode [81], we can shift the two ions such that one is near the rf null point but the other is not. In such a case, the micromotion is different for the two ions and hence so is the coupling to the laser beams [49].

In Eq. (3.4), the micromotion is ignored. To now take it into account, we write the position of the ion as

$$\hat{x}_{tot} = x_\mu + \hat{x} = x_{\mu 0} \cos(\Omega_T t) + x_0(\hat{a}_x^\dagger + \hat{a}_x), \quad (6.33)$$

where  $x_{\mu 0}$  is the amplitude of the micromotion along the  $x$ -direction (I am considering the  $x$ -direction now, as these experiments were performed in one of the elliptical traps). Thus, we may re-express Eq. (3.4) as

$$H'_{int} = \hbar\Omega \left[ S_+ e^{i\Delta k \cdot x_{\mu 0} \cos \Omega_T t} \exp\left(i\eta(\hat{a}_x^\dagger e^{i\omega_x t} + \hat{a}_x e^{-i\omega_x t}) - i\delta t\right) + H.C. \right]. \quad (6.34)$$

I have treated the micromotion as classical in Eq. (6.34). Although one may treat the complete motion of the ions quantum-mechanically [70], we still obtain an appropriate picture of the situation without doing so, as we shall see.<sup>5</sup> Expanding  $e^{i\Delta k \cdot x_{\mu 0} \cos \Omega_T t}$  [72], we find that the effect of the micromotion is that the base (carrier) Rabi frequency  $\Omega \rightarrow \Omega_j = \Omega J_0(|\delta k| \cdot x_{\mu 0, j})$ , where  $j \in \{1, 2\}$  is the  $j^{th}$  ion. That is, in the case of two trapped ions, the ion with the most micromotion is more weakly coupled to the laser beams, as discussed above. This is illustrated by the data in Fig. 6.8: as the center of mass of the two-ion system is displaced from trap center (by an applied static electric field), the ion which is moved closer to trap center experiences an increased Rabi

---

<sup>5</sup> This occurs because  $\sqrt{\frac{\hbar}{2m\omega_x}} \ll x_{\mu 0}$

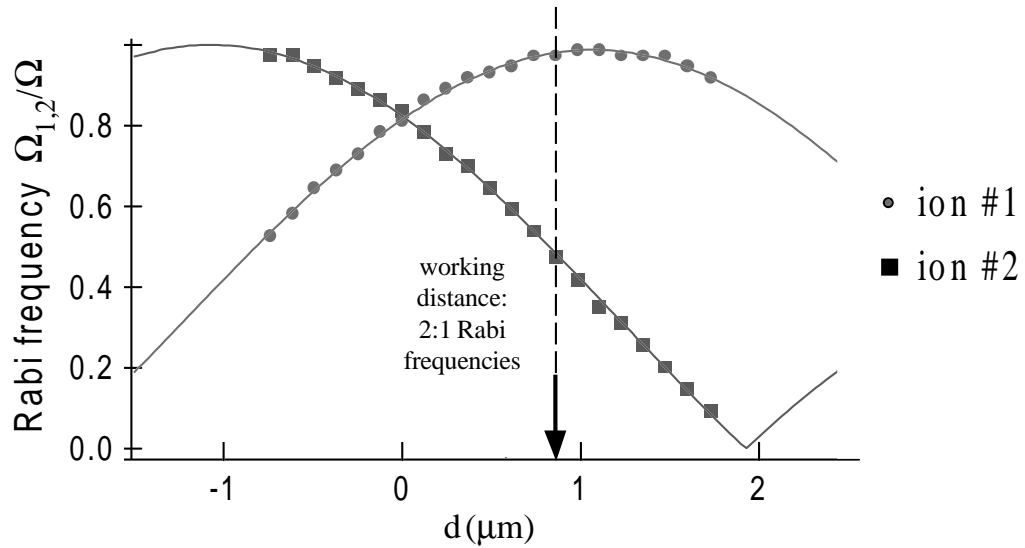


Figure 6.8: Normalized carrier Rabi frequency  $\Omega_i/\Omega$  of each of two ions as a function of center-of-mass displacement  $d$  from the rf null position  $d=0$ .  $\Omega$  is the co-propagating carrier transition Rabi frequency. The solid curves show  $\Omega J_0(|\delta k| \cdot x_{\mu 0, i})$ , where the distance between the maxima of the two curves sets the scale of the ordinate, based on the known ion-ion spacing of  $l \approx 2.2 \mu\text{m}$  at  $\omega_x/2\pi = 8.8 \text{ MHz}$ . When the center of the two-ion string is displaced by just under one micrometer from the center of the trap (arrow in graph), the two ions' Rabi frequencies are in a two-to-one ratio.

frequency while the other ion's Rabi frequency is reduced. The agreement with theory is quite good.

Using the micromotion to differentially address the two ions, we have found a way to produce the state

$$|\psi_e(\phi)\rangle = \left( \frac{3}{5} |\downarrow, \uparrow\rangle - e^{i\phi} \frac{4}{5} |\uparrow, \downarrow\rangle \right) |n=0\rangle, \quad (6.35)$$

which has an overlap  $|\langle\psi_B^-|\psi_e(\varphi=0)\rangle|^2 = |\langle\psi_B^+|\psi_e(\varphi=\pi)\rangle|^2 = 0.98$  with the Bell states [49]. (In Eq. (6.35),  $\phi$  is a controllable phase, determined by the laser beams' phases at the locations of the two ions.)

To do this, we displaced the ions' center of mass from the trap center to the point indicated by the arrow in Fig. 6.8: at this point the ions' perpendicular carrier Rabi

frequencies were in a 2:1 ratio. Thus, starting from the state  $|\psi_i\rangle = |\downarrow, \downarrow, n_{str} = 0\rangle$  we drove a  $2\pi$  pulse on one ion and a  $\pi$  pulse on the other, creating the state  $|\psi'\rangle = |\downarrow, \uparrow, n_{str} = 0\rangle$ .

From this point, we were able to use the stretch red sideband to produce the state  $|\psi_e(\phi)\rangle$ . To see how this occurred, consider the level structure shown in Fig. 6.9, which shows the various states coupled to  $|\downarrow, \uparrow, n\rangle$  by the stretch lower motional sideband, and let  $\Omega_1 = 2\Omega_2$  be the carrier Rabi frequencies on ions 1 and 2, respectively. Since we started out in  $n_{str} = 0$ , there is no  $n_{str} = n - 1$  level to which to couple. Thus, starting in  $|\psi'\rangle$ , and driving on the stretch red sideband for a time  $t_{int}$ , we produced the state:

$$\begin{aligned} |\psi(t)\rangle &= -\frac{i\Omega_{2-}}{\mathcal{G}} \sin \mathcal{G}t_{int} |\downarrow, \downarrow, 1\rangle \\ &+ \left[ \frac{\Omega_{2-}}{\mathcal{G}^2} (\cos \mathcal{G}t_{int} - 1) + 1 \right] |\downarrow, \uparrow, 0\rangle \\ &+ e^{i\phi} \left[ \frac{\Omega_{2-} - \Omega_{1-}}{\mathcal{G}^2} (\cos \mathcal{G}t_{int} - 1) \right] |\uparrow, \downarrow, 0\rangle. \end{aligned} \quad (6.36)$$

Here,  $\mathcal{G} = \sqrt{\Omega_{2-}^2 + \Omega_{1-}^2}$ ,  $\Omega_{j-} = \Omega_j \eta_{x, str} \sqrt{n+1}$  is the stretch mode red sideband Rabi frequency (recall  $\eta_{x, str} = \eta_x / \sqrt{2\sqrt{3}}$ ), and  $\phi$  is the difference of the Raman beam phases at the ions. Thus, when  $\mathcal{G}t_{int} = \pi$ , we produced the state  $|\psi_e(\phi)\rangle$ . Since the laser beams impinge on the ions at an angle to the axis along which they line up, the phase  $\phi$  depends on the ions' separation. Thus, by changing this separation, we could choose the particular state produced.

By monitoring the photon-number histograms (Ch. 3 and Appendix A), we could discriminate between  $|\downarrow, \downarrow\rangle$ ,  $|\downarrow, \uparrow\rangle$ ,  $|\uparrow, \downarrow\rangle$ , and  $|\uparrow, \uparrow\rangle$ , and extract the spin populations for the state which we produce. The optical pumping of the dark state  $|\uparrow\rangle$  into the cycling transition (Appendix A) somewhat complicated this endeavour. Were it not for this effect, we could have turned up the intensity of D2 to a point where the photon histograms allowed us to clearly distinguish between the cases  $|\downarrow, \downarrow\rangle$ ,  $|\uparrow, \downarrow\rangle$  or  $|\downarrow, \uparrow\rangle$ ,<sup>6</sup> and  $|\uparrow, \uparrow\rangle$ . However, the optical pumping precluded this. Instead, we took

<sup>6</sup> Note that, due to the different micromotions of the two ions, these two states had different scatter rates during the cycling transition

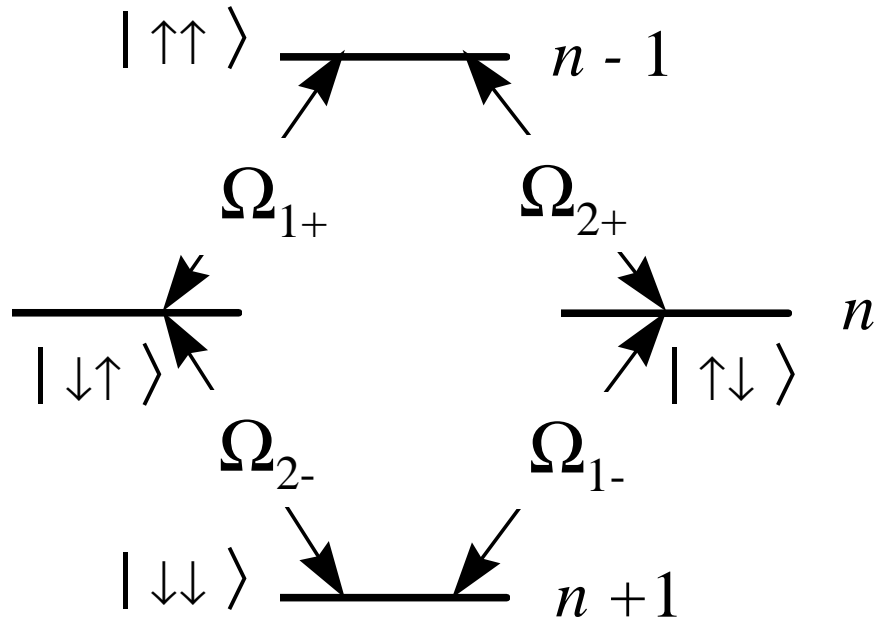


Figure 6.9: Simplified level diagram showing four levels coupled by the lower (red) motional sideband, when the lasers illuminate two trapped ions. The coupling strengths,  $\Omega_{j,\pm}$ , vary depending on which ion’s spin is being flipped, due to the ions’ different (micromotion-induced) base Rabi frequencies (see Eq. (6.36)).

“reference histograms” for the four states (see Fig. 6.10), and performed a singular-valued decomposition [96] of the measured fluorescence signal using these references as basis functions.

In order to demonstrate the coherence of the produced state, we applied the co-propagating carrier. To determine the effect of this interaction on the Bell states, it is useful to again draw the analogy between two-level systems and spin-1/2 particles. In particular, we may split the possible two-ion coupled spin states into a triplet and a singlet manifold, just as one does when treating two, coupled spin-1/2 systems. The singlet, which has spin  $J = 0$ , should be unaffected by any interaction which preserves

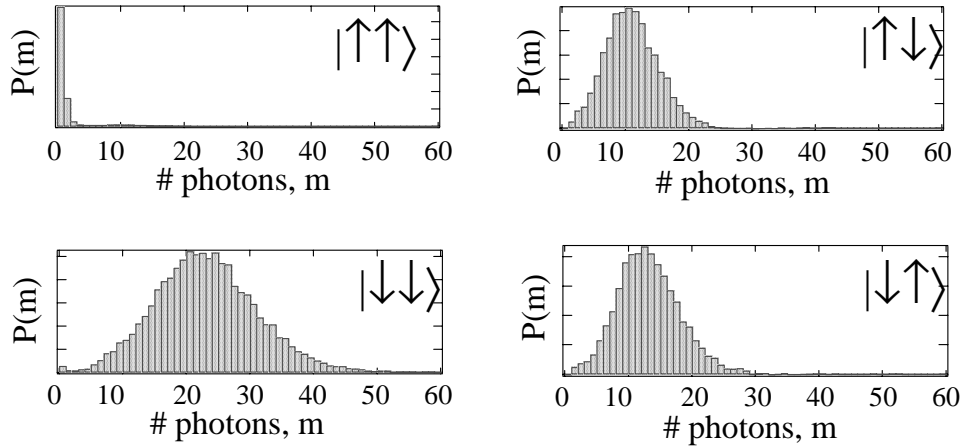


Figure 6.10: Photon-number histograms for two trapped ions. Since the ions were unequal distances from the rf null, and experience different micromotions, the mean photon numbers for the states  $|\uparrow, \downarrow\rangle$  and  $|\downarrow, \uparrow\rangle$  were different (see text). The “leak” of population from  $|\uparrow\rangle$  into the cycling transition is discussed in Appendix A.

*J.* An example of such an interaction is the co-propagating carrier which, being insensitive to motion, does not “sense” the micromotion and so interacts with both ions with the same coupling strength. On the other hand, the states  $|\psi_B^\pm\rangle \approx |\psi_e(0)\rangle$  or an incoherent mixture of  $|\downarrow, \uparrow\rangle$  and  $|\uparrow, \downarrow\rangle$  are driven to the states  $|\uparrow, \uparrow\rangle$  and  $|\downarrow, \downarrow\rangle$  by the co-propagating carrier. Thus, measuring the photon statistics after turning on the co-propagating carrier allowed us to distinguish between the coherent superposition  $|\psi_e(\pi)\rangle$  and an incoherent mixture. The data are shown in Fig. 6.11. Together with the population analysis described above, they establish that we were able to create the desired state  $|\psi_e(\phi)\rangle$  about 70% of the time [49].

Note that it is, in fact, possible to *exactly* produce the Bell states. This would require  $\Omega_1 = (\sqrt{2}+1)\Omega_2$  for the red sideband interaction, Eq. (6.36), which would create the exact Bell state from  $|\downarrow, \uparrow, 0\rangle$ . In practice, it was not possible to change the ratio of the Rabi frequencies within the course of a single experiment, and so the technique

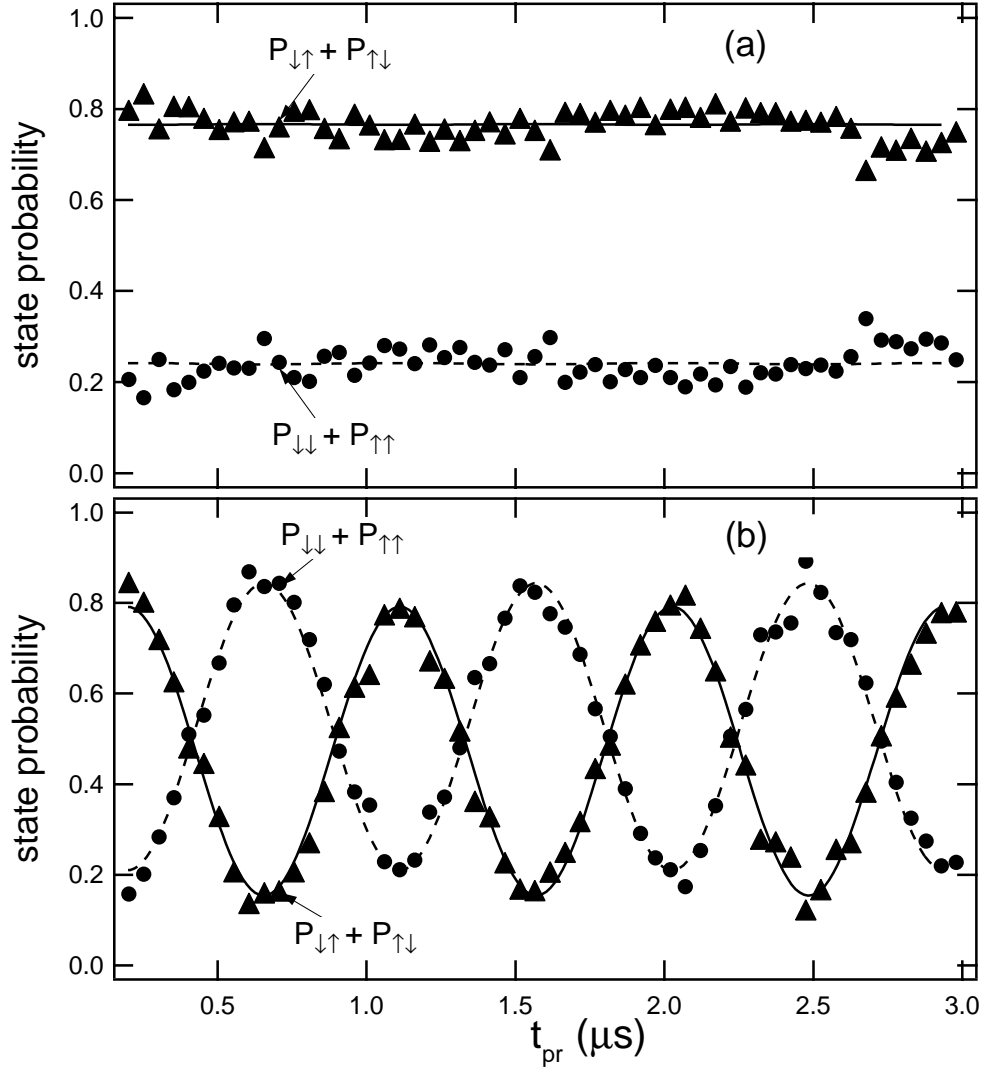


Figure 6.11: Probabilities  $P_{\downarrow,\uparrow} + P_{\uparrow,\downarrow}$  and  $P_{\downarrow,\downarrow} + P_{\uparrow,\uparrow}$  as a function of pulse length  $t_{pr}$  of the co-propagating carrier pulse applied after creation of the state  $|\psi_e(\phi)\rangle$  of Eq. (6.35). (a) For  $\phi = \pi$ , this co-propagating carrier pulse has no effect. (b) For  $\phi = 0$ , the co-propagating carrier pulse causes the various populations to change. An *incoherent* mixture would also exhibit oscillations. The data in (a) for  $\phi = \pi$  thus indicates our success in producing a coherent superposition state. The solid and dashed lines in (a) and (b) are sinusoidal fits to the data, from which we determine that we produce the desired state with a fidelity of  $|\langle\psi_{actual}|\psi_e\rangle|^2 = 0.70$ .

described above was used, instead. However, this technical difficulty is, in principle, surmountable. For example, we could change the ion-ion separation by changing the trap frequency of a linear trap in the middle of an experiment (see Sec. 7.5).

We note that, in contrast to previous experiments which have produced entangled states (see references in [49]), this present technique is *deterministic* [149]. That is, it allows production of a known and controllable quantum state of (all of) a particular set of particles, generated at a specified time. Such deterministic entanglement, along with the ability to store the states so produced, is crucial for large-scale quantum computation.

#### 6.4.2 Creating Multi-Ion Entangled States

The techniques discussed in the last section are useful for producing Bell-type states. However, they are not readily scalable to more than two ions. Sørensen and Mølmer [150] have proposed a scheme to produce maximally-entangled states which *is* scalable to multiple ions. It is also relatively insensitive to heating of the ions' motion, so long as the ions remain in the Lamb-Dicke regime.

This scheme requires one to illuminate all the ions simultaneously with the blue and red motional sidebands. The original proposal dealt with a two-photon coupling in a situation where, for example, the carrier would be driven by a single-photon interaction. In our case, where the carrier and motional sidebands are driven by two-photon transitions, Sørensen and Mølmer's scheme would require four-photon transitions. This does not change the basic physical principles of the technique. So, for the sake of simplicity, I shall use their original case to sketch out the idea of the method.

In order to understand how the technique works, consider the case of two ions. The situation is sketched out in Fig. 6.12. Here, two ions start out in the state  $|\downarrow, \downarrow, n\rangle$ . Two laser beams illuminate the ions. One is tuned to  $\omega_0 + \varepsilon$ , where  $\varepsilon \approx \omega_x$  but  $\varepsilon \neq \omega_x$  (i.e. the levels  $|\downarrow, \uparrow, n-1\rangle$  and  $|\uparrow, \downarrow, n-1\rangle$  are used as virtual levels). The other laser is tuned to  $\omega_0 - \varepsilon$ . The basic idea of the scheme is that four different two-photon

paths exist connecting  $|\downarrow, \downarrow, n\rangle$  and  $|\uparrow, \uparrow, n\rangle$ : two which “go through” a virtual level with  $n + 1$  phonons and two through a virtual level with  $n - 1$  phonons. In the Lamb-Dicke regime, the paths which “pass through” the level  $|n + 1\rangle$  have coupling strengths  $(\sqrt{n + 1}\Omega\eta)^2/(\varepsilon - \omega_x)$  whereas those passing through the  $|n - 1\rangle$  have coupling strengths  $(\sqrt{n}\Omega\eta)^2/(\omega_x - \varepsilon)$  (notice the difference in sign). When the amplitudes corresponding to the four paths are added up, the  $n$ -dependent terms cancel out, leading to an overall coupling strength

$$\Omega_{eff} = \frac{\eta^2\Omega^2\omega_x}{2(\omega_x^2 - \varepsilon^2)}. \quad (6.37)$$

Thus, the levels  $|\downarrow, \downarrow, n\rangle$  and  $|\uparrow, \uparrow, n\rangle$  are coupled, with no coupling to any other levels. In particular, levels with different  $n$  do not mix (although there is some negligible probability that the levels used as “virtual levels” will be populated — this is similar to the case considered in Sec. 3.3). So, as long as the ion is in the Lamb-Dicke regime, this scheme provides a way to make the Bell states, without requiring ground-state laser cooling. Furthermore, the technique works for an arbitrary number of ions.<sup>7</sup> For multiple ions, spin-flip transitions are driven between all possible pairs of spins, and this realizes the desired time evolution [151].

In order to implement this technique experimentally, we added a second double-pass AOM to the Red Raman beam line (see Ch. 4) so that, with the micromachined linear trap, we could illuminate two trapped ions on their upper and lower stretch sidebands at the same time. However, since the interaction strength was proportional to  $\eta^2$ , the interaction times necessary to realize Bell states were quite long. We ran into problems with fluctuating magnetic fields and with Debye-Waller factors [73] due to heating of the COM mode: these issues made it quite challenging to realize the coupling of Eq. (6.37) in a coherent fashion. As we were attempting to deal with these issues, the two-ion lifetime went down in a dramatic fashion. We hope to attempt the experiments again in a newly constructed linear trap.

---

<sup>7</sup> For an odd number of ions, an additional carrier pulse is required.

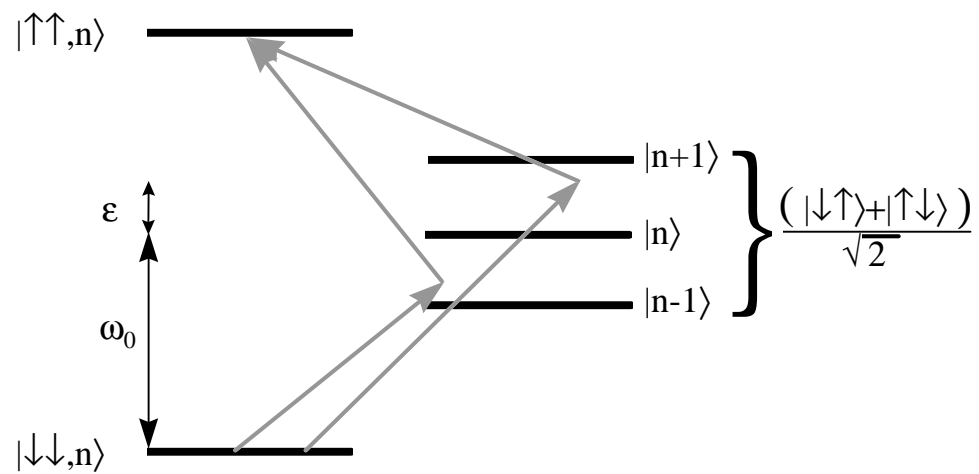


Figure 6.12: Schematic of the two-photon interaction proposed by Sørensen and Mølmer to produce maximally entangled states (two-ion case). The ions are equally illuminated by two lasers, of frequencies  $\omega_0 \pm \varepsilon$ , where  $\varepsilon \approx \omega_x$  but  $\varepsilon \neq \omega_x$ . The two ions' energy levels are shown in the triplet/singlet representation, and only the triplet levels are shown (since the singlet does not couple to the lasers). Two paths between  $|\downarrow, \downarrow, n\rangle$  and  $|\uparrow, \uparrow, n\rangle$  are possible: one path uses  $|(\uparrow\downarrow + \downarrow\uparrow), n+1\rangle$  as a virtual level, whereas the other path uses  $|(\uparrow\downarrow + \downarrow\uparrow), n-1\rangle$ . The  $n$ -dependencies of the two paths cancel out, allowing creation of maximally entangled states.

## Chapter 7

### Quantum Logic with Trapped Ions

Quantum computation, is a relatively new and thus far mostly theoretical field. It is the result of the marriage of computation theory with physical theory. Many of the pioneers of classical information and computation theory (such as Shannon, Turing, Church, and Gödel) considered information in a purely abstract manner. This led to many insights into the nature of computational complexity [152, 153]: for example, the role of the binary *bit* as a fundamental carrier of classical information, the fact that any algorithm can be implemented in terms of fundamental two-bit logic gates, the existence of complexity classes for algorithms, and the existence and significance of universal computing machines (for example, the Turing machine).

However, gradually people began to realize that information is always encoded in *physical* systems [37]and, therefore, that physics had an essential role in the theory of computation. As an example, the consideration of minimum energy dissipation for computational elements [154] led to considerations of “reversible logic gates,” and the discovery that they were computationally equivalent to the usual, irreversible logic gates (e.g. AND, NOR, etc.). On the other hand, it also became apparent that information theory was a useful point of view for considering physical law. Consider, for example, the relationship between Shannon information and the physical entropy. As another example, the realization that it costs no information to store information, but only to

erase it — an idea which arose in the aforementioned study of reversible logic — offered a resolution of the paradox of “Maxwell’s Demon” [155].

The idea that “information is *physical* [37],” along with the realization that computational elements were growing physically smaller, led Deutsch [156] to consider information elements that were inherently quantum. At the same time the realization that classical computers could not efficiently simulate quantum systems (because of the growth of the dimensionality of Hilbert space with system complexity) led Feynman [157, 158] to propose that “quantum computers” might be able to simulate such systems more efficiently.

The question of efficiency (from the point of view of computer scientists) is one of how the resources required to implement some algorithm grow with the size of the input to the algorithm. Note that, from a computational complexity point of view, “resource” refers both to the number of time-steps required to implement the algorithm and the amount of physical resources (e.g. logic gates) required to implement it. Although there are different complexity classes [152], we can obtain some idea of the divisions by noting that, for example, some algorithms scale as some polynomial of the number  $N$  of bits in the input whereas others scale exponentially with this number. Algorithms in the latter class are called “computationally hard.” For example, calculating the product of two numbers scales as a polynomial in the size of the numbers, whereas it is believed that factoring a given number into its prime factors is a “hard” problem.

This problem of factorization actually lies at the heart of much of the recent excitement about quantum computation. The computational difficulty of factoring large numbers lies at the heart of popular data-encryption schemes (such as the RSA [159] protocol). So, Shor’s [39] extension of Deutsch’s discovery [38] that quantum computers could efficiently compute algorithms that were “hard” on classical computers caused quite a stir — Shor discovered a quantum algorithm that could efficiently factorize large numbers!

In general, then, quantum computation and quantum information theory deal with information in a physical and explicitly quantum context. Although the field is new, it has caused quite a stir in several different contexts. Of course, it is still an open question as to whether a quantum computer could actually be built (for reasons I will discuss below). However, quantum computation is significant for several reasons: in general, I would make the following points.

- (1) Classical information theory showed that the difficulty of algorithms was independent of the particular logic used to implement them. So, for example, changing the hardware used to compute an algorithm, or using three-state logic instead of binary logic does not move a problem from being “hard” : (super-polynomial or exponential in the input size) to “easy” (polynomial in the input size). However, there are problems which are “hard” on *any* classical computer which are “easy” on a quantum computer. This is a revolution in information theory, and the impact of the *concept* of quantum computation on information-theoreticians may be independent of the technical issue of whether we can actually build a quantum computer in practice.
- (2) It appears that much of the “heart” of quantum mechanics (for example, the collapse or apparent collapse of the wave function) deals with the transfer of information from subsystem. The new language offered by quantum information theory may well offer new insights into these issues [42, 43]. Also, a general quantification of entanglement in many-particle quantum systems is lacking at present. The language of quantum computation may shed light on the subject. Again, the significance of this language may well be independent of the question of whether a “quantum computer code-breaker” can ever be built.
- (3) As originally pointed out by Feynman [158], the exponential growth of the Hilbert space dimensionality in quantum systems makes simulating such sys-

tems difficult. Quantum computers, if they can be built, could efficiently simulate other quantum systems. That this may be of interest is indicated by the recent Nobel prize awarded for advances in the (classical-computer) molecular dynamics approach to simulating problems in quantum chemistry. Of course, the question is often asked “why not just measure the actual system, rather than simulate it on a quantum computer?” The answer, of course, is that sometimes (e.g. biotechnology) it would be desirable to understand a complex quantum system before investing in the infrastructure necessary to realize it. A general-purpose quantum computer could enable this. In other situations (e.g. QCD), it is not possible experimentally to investigate all regions of a theory’s parameter space or to change, for example, coupling strengths or interaction Hamiltonians. In such situations, quantum computers could make significant contributions. This, of course, would depend on it being possible to construct a quantum computer!

- (4) Finally, quantum computers may enable us to implement important algorithms which would be infeasible or impossible on any classical computer. For example, since the best possible (known) classical factoring algorithm scales exponentially with the size of the number to be factored, factoring a 400-digit number would require a computer with more atoms than in the universe! On a quantum computer, it would be possible to factor a number which one could not, even in principle, factor on a classical computer. Of course, this, too, depends on it being possible to actually build a quantum computer!

In general, then, I would argue that the field of quantum information theory is here to stay, in one form or another. However, since I am an experimental physicist, I shall focus, in this Chapter, on implementing a “trapped-ion quantum computer” along

the lines proposed by Cirac and Zoller [40]. However, I shall first briefly describe the basics of quantum computation.

## 7.1 Quantum Computation

A quantum computer [35, 43, 160], like a classical one, may be considered to consist of a register of  $N$  information-carrying entities which, in correspondence to the classical case, are referred to as “qubits.” Each qubit is a two level system, with basis states  $|0\rangle$  and  $|1\rangle$ , representing logic “0” and logic “1.” However, since the qubits are quantum systems, they may exist not only in one or the other logic state, but also in *superpositions* of the form  $\alpha|0\rangle + \beta|1\rangle$  (with  $|\alpha|^2 + |\beta|^2 = 1$ ). The real power of quantum computation lies in this superposition property of qubits.

For, given an input register of  $N$  qubits, we may prepare the register in a superposition of *all* the  $2^n$  possible inputs. Furthermore, it is possible to produce this superposition (of an *exponential* number  $2^N$  of states) in a *linear* number of steps. For example, if our qubits are spins, with  $|\downarrow\rangle \equiv |0\rangle$  and  $|\uparrow\rangle \equiv |1\rangle$ , and the quantum register starts out in the state  $\prod_{n=0}^N |0\rangle$ , driving  $\pi/2$ -pulse on all the spins produces the state  $\prod_{n=0}^N (1/\sqrt{2})(|0\rangle + |1\rangle) \equiv \sum_{r=0}^N |r\rangle$ . In the last term, I have made the symbolic equivalence between a binary number  $r$  and the register state in which the individual qubits are in the appropriate state for the binary representation of  $r$ . Thus, the number  $r = 0010$  is represented by the four-qubit register state  $|0010\rangle$ . Since it is possible to efficiently initialize the quantum register in a superposition of all its possible inputs then, provided that our computation is made up of unitary operations, it is possible to process *in parallel and at once* all the possible outputs of the computation.

Of course, any attempt to read out the state of the quantum computer (or perform any type of non-unitary time evolution) will collapse it into one and only one of the

possible output states.<sup>1</sup> So, as it stands, although a quantum computer may be massively parallel, we have no way to access and utilize this parallelism. However, we may use another fundamental quantum property to overcome this obstacle: interference. Interference between different “computational paths” can enable us to distill information about global properties of computed functions (such as periodicity) [39, 161] while still preserving superposition until the very end. And such algorithms may be exponentially faster to execute than any known classical algorithm for solving the same problem.

To reiterate, although the exact mechanism by which a quantum computer may be faster than a classical computer is still not fully understood [162], it appears that this mechanism involves the interplay between “superposition” (in an exponentially large Hilbert space) and “interference” (which maps joint, or entangled, properties onto local ones). To obtain some idea of how this works in practice, consider one particular algorithm which allows a quantum computer to efficiently solve a classically hard problem: “Simon’s problem” [163]. Although this is somewhat of a “toy” problem, it is an example of the exponential speedup possible with quantum computers, and one which illustrates the ideas of quantum computation clearly.<sup>2</sup>

In Simon’s problem, we are given an unknown function  $f$  of  $N$  bits,  $f : \{0, 1\}^N \rightarrow \{0, 1\}^N$  (i.e.  $f$  maps  $N$ -bit numbers to  $N$ -bit numbers). We are told that  $f$  is 2-to-1. We are also told that  $f$  has the property that  $f(x) = f(y)$  iff  $y = x \oplus a$ , where  $\oplus$  is the bitwise Exclusive-OR operation (addition modulo 2). We are then asked to determine  $a$ . Classically, the best that we can do is to evaluate  $f$  for various  $x, y, \dots$  until we find  $x, y$  such that  $x \oplus y = a$ . If, for example, we evaluate  $f$   $2^{N/4}$  times, then the probability that  $x \oplus y = a$  is  $2^{-N}$  for any given  $x, y$ , and the number of pairs of function evaluations

---

<sup>1</sup> Here, the phrase “read out the state of the quantum computer” means an attempt to determine the computer’s logical state: that is, it refers to a qubit-by-qubit measurement in the “logical basis,”  $\{|0\rangle, |1\rangle\}$

<sup>2</sup> I shall follow the treatment given by Preskill [43].

is  $(2^{N/4})^2$ , so that the probability of success (i.e. of finding  $a$ ) satisfies:

$$P_{suc} < 2^{-N} (2^{N/4})^2 = 2^{-N/2}. \quad (7.1)$$

Thus, the problem is classically “hard,” as the probability of finding  $a$  is exponentially small as a function of  $N$ .

However, there exists an efficient quantum algorithm for finding  $a$ . Suppose that we have two,  $N$ -qubit quantum registers. We assume that the two registers start out in the state  $|0\dots 0\rangle|0\dots 0\rangle$  (i.e. all the qubits are in the state  $|0\rangle$ ). We then apply a unitary transformation  $\hat{\mathcal{H}}$  called the Hadamard transform to the first  $N$ -qubit register. I will discuss this unitary transformation shortly and, in particular, whether we can realize it in an efficient and scalable manner. However, for now, it suffices to assume that we *can* do so, and to specify its matrix representation with respect to the standard, “computation” basis,  $\{|0\rangle, |1\rangle\}$ :

$$\hat{\mathcal{H}} \equiv \frac{1}{\sqrt{2}} \begin{bmatrix} 1 & 1 \\ 1 & -1 \end{bmatrix}. \quad (7.2)$$

Let  $\hat{\mathcal{H}}^{(N)}$  represent the effect of  $N$  such Hadamard transformations acting in parallel on the  $N$  qubits. By applying Eq. (7.2) repeatedly, we can work out that

$$\hat{\mathcal{H}}^{(N)}|x\rangle = \sum_{y=0}^{2^N-1} (-1)^{x \cdot y} |y\rangle \quad (7.3)$$

where  $x \cdot y = x_0y_0 + x_1y_1 + \dots + x_Ny_N$  (i.e. if we treat the binary numbers in the binary expansion of  $x$  and  $y$  as components of a vector, then  $\cdot$  is the “dot product” of  $x$  and  $y$ ). Applying  $\hat{\mathcal{H}}^{(N)}$  to the  $N$ -qubit register leaves the quantum computer in the state:

$$|\mathcal{R}\rangle_0 = \frac{1}{2^{N/2}} \left( \sum_{x=0}^{2^N-1} |x\rangle \right) |0\dots 0\rangle, \quad (7.4)$$

Here,  $|x\rangle$  represents the state in which each qubit is in the state ( $|0\rangle$  or  $|1\rangle$ ) corresponding to the appropriate digit in the binary representation of the number  $x$ . For example, if  $x = 5 = (101)_2$ , then a register of three qubits representing this number would be in the state  $|1\rangle|0\rangle|1\rangle$ .

Starting in the state  $|\mathcal{R}\rangle_0$ , we apply the function  $f$  (which is given to us) to the second  $N$ -qubit register. Due to the superposition property of quantum mechanics, if we apply  $f$  in a unitary manner, the computer is left in the state:

$$|\mathcal{R}'\rangle = \sum_{x=0}^{2^N-1} |x\rangle |f(x)\rangle. \quad (7.5)$$

Here, we see that the superposition property allows us to compute the function  $f$  in a highly parallel manner: we compute all of its possible values in *one* computation.

Now, consider what happens if we measure the state of the second register. We collapse the state of this register into one of the  $2^{N-1}$  possible values of  $f(x)$ , say  $f(x_0)$ . But, since the states of the two registers are entangled, this also collapses the state of the first register into a superposition of the two possible states corresponding to  $f(x_0)$ : namely  $x_0$  and  $x_0 \oplus a$ . That is, the registers are left in the state

$$|\mathcal{R}''\rangle = \frac{1}{\sqrt{2}} (|x_0\rangle + |x_0 \oplus a\rangle) |f(x_0)\rangle. \quad (7.6)$$

Here, the collapse of the wave function in the second register has, through the entanglement of the two registers, produced a state in the first register which expresses information on the “periodicity” of the function  $f$ . At this point, since the second register factors out of the problem, we may ignore it and concentrate only on the first register.<sup>3</sup>

The problem now is to extract the information on  $a$  from the first register. Of course, we can't just measure the state of the register: this would give either  $x_0$  or  $x_0 \oplus a$ , but absolutely no information about  $a$ ! Instead, we may apply  $\hat{\mathcal{H}}^{(N)}$  to the register again. This produces the state:

$$\begin{aligned} \hat{\mathcal{H}}^{(N)} \left[ \frac{1}{\sqrt{2}} (|x_0\rangle + |x_0 \oplus a\rangle) \right] &= \frac{1}{2^{(N-1)/2}} \sum_{y=0}^{2^N-1} \left[ (-1)^{x_0 \cdot y} + (-1)^{(x_0 \oplus a) \cdot y} \right] |y\rangle \\ &= \frac{1}{2^{(N-1)/2}} \sum_{a \cdot y=0} (-1)^{x_0 \cdot y} |y\rangle, \end{aligned} \quad (7.7)$$

---

<sup>3</sup> In fact, it is possible to execute the algorithm without ever measuring the state of the second register! However, the ideas behind the algorithm are somewhat more clear if this step is included

In the last line of Eq. (7.7), I have collapsed the sum according to the following observation: if  $a \cdot y = 1$ , then the two terms in the coefficient of  $|y\rangle$  interfere destructively, so that only terms for which  $a \cdot y = 0$  remain. Thus, we have used destructive interference to extract information about  $a$  from the register, since when we measure the state of the register, we obtain a  $y$  for which  $a \cdot y = 0$ .

In order to determine  $a$ , we run the algorithm  $O(N)$  times, until we have found  $N$ , linearly independent values  $y_i$  for which  $a \cdot y_i = 0$ . We then solve the resulting set of linear algebraic equations to obtain  $a$ . This repetition of the algorithm  $O(N)$  times only adds linearly to the complexity of the solution. Thus, we may solve for  $a$  efficiently on our quantum computer, whereas it is not possible to do so on any classical computer.

To “flesh out” this example a bit, consider the somewhat trivial case in which  $N = 2$ . Suppose that the function  $f$  is defined by:

$$\begin{aligned} f(00) &= 00 \\ f(01) &= 01 \\ f(10) &= 00 \\ f(11) &= 01 \end{aligned} \tag{7.8}$$

(so that  $a$ , which we are to determine, is equal to 10). In order to determine  $a$ , we start out with a quantum computer consisting of two, two-qubit registers in the state

$$|\mathcal{R}\rangle_0 = |00\rangle_1 |00\rangle_2 . \tag{7.9}$$

The subscripts label registers 1 and 2. We initialize the computation by applying the Hadamard transformation to register 1, to put it in a superposition of all its possible values:

$$|\mathcal{R}\rangle_0 \longrightarrow \frac{1}{2} \left( |00\rangle + |01\rangle + |10\rangle + |11\rangle \right)_1 |00\rangle_2 . \tag{7.10}$$

Next, we apply  $f$  to the second register, taking the first register's values as  $f$ 's input.

This leaves the registers in the state

$$|\mathcal{R}'\rangle = \frac{1}{2}(|00\rangle_1|00\rangle_2 + |01\rangle_1|01\rangle_2 + |10\rangle_1|00\rangle_2 + |11\rangle_1|01\rangle_2), \quad (7.11)$$

so that now the states of the two registers are entangled.

A measurement of register 2 collapses the state into one of the possible measurement outcomes — for example, into the state:

$$|\mathcal{R}''\rangle = \frac{1}{\sqrt{2}}(|01\rangle_1 + |11\rangle_1)|01\rangle_2. \quad (7.12)$$

Now, we discard the second register, and apply the Hadamard transform to register 1, which results in

$$\begin{aligned} \hat{\mathcal{H}}^{(2)} \frac{1}{\sqrt{2}}(|01\rangle_1 + |11\rangle_1) &= \frac{1}{2\sqrt{2}}(|00\rangle_1 - |01\rangle_1 + |10\rangle_1 - |11\rangle_1 \\ &\quad + |00\rangle_1 - |01\rangle_1 - |10\rangle_1 + |11\rangle_1) \\ &= \frac{1}{\sqrt{2}}(|00\rangle_1 - |01\rangle_1). \end{aligned} \quad (7.13)$$

Note that the two values,  $x_0 = 00$  and  $x_0 = 01$ , both satisfy  $x_0 \cdot 10 = 00$ . Finally, we measure the state of register 1, obtaining *either* the result  $x_0 = 00$  or  $x_0 = 01$ .

In order to determine  $a$ , we repeat the above procedure until we obtain the *other* value<sup>4</sup> of  $x_0$ . Then, we solve the system of equations

$$\begin{aligned} 00 \cdot a &= 00 \\ 01 \cdot a &= 00 \end{aligned} \quad (7.14)$$

to obtain  $a = 10$ .

In the above example, we see some of the fundamental properties of quantum computers: the parallel computation of functions allowed through the superposition

---

<sup>4</sup>  $x_0$  is either equal to 00 or to 01 in this example, as we may check by running through the example again, this time assuming that the measurement of register 2 produces the outcome  $|00\rangle_2$  instead of the state  $|01\rangle_2$  assumed above

principle, the entanglement of two quantum registers which, through the collapse of the wave function, selects out certain properties of the function, and the use of destructive interference to “distill” this information into a form which can be effectively read out. In essence, the challenge in finding quantum algorithms is to achieve this last point; that is, to overcome the impediment of wave function collapse by using quantum interference in a clever way.

As yet, there are few concrete examples of such algorithms. Two of the most significant are those due to Shor [39] and to Grover [164] (for a pedagogical discussion of these algorithms, see Ref. [43]). Shor’s algorithm uses quantum interference to find the period of the function  $a^b(\text{mod}M)$  (where  $M$  is given and  $a$  is a randomly-chosen number co-prime with  $M$ ) and uses this information to determine the factors of  $M$ . The resources required scale as a polynomial of the size of  $M$ , whereas all known classical algorithms scale exponentially<sup>5</sup> with  $M$ . As mentioned above, factoring large numbers is of great interest to the data-encryption community.

Grover’s algorithm searches a database of qubits for a particular, marked entry. It is faster than any classical algorithm. However, the classical algorithms themselves scale as polynomials of the database size, and so Grover’s algorithm does not change the “complexity class” of the problem.

I have not yet discussed whether it is possible to implement the Hadamard transformation (or the function  $f$ ) efficiently on a given quantum computer. However, it may be shown that any unitary transformation on a set of qubits may be modelled to any desired accuracy by a fundamental set of two-qubit and one-qubit gates [165, 166]. Furthermore, the number of such gates required scales as a polynomial in the desired accuracy. This means that one may use any given quantum computer (with any given set of basic gates) to simulate any other quantum computer without changing the efficiency of the algorithms implemented on the two computers (i.e. from “easy” to “hard”).

---

<sup>5</sup> Note, however, that there is as yet no proof that an efficient classical algorithm does not exist.

Thus, one can construct a “universal quantum computer” in the sense of Turing [152]. Thus, given *some* set of universal quantum logic gates, we can efficiently implement both  $f$  and the Hadamard transformation. So, as the above example (Simon’s problem) shows, quantum computers are inherently more powerful than classical ones.

One family of universal quantum logic gates consists of one-qubit rotations and a two-qubit logic gate: the Controlled-NOT.<sup>6</sup> The effects of the Controlled-NOT quantum logic gate are prescribed by the effects of the gate on the qubit basis states; the effects of the gate in cases in which the qubits are in superposition states follows by linearity. Thus, the Controlled-NOT gate is realized by the transformation

$$|\epsilon_1\rangle|\epsilon_2\rangle \rightarrow |\epsilon_1\rangle|\epsilon_1 \oplus \epsilon_2\rangle, \quad (7.15)$$

where  $\epsilon_1, \epsilon_2$  are arbitrary elements of the two-dimensional Hilbert space and  $\oplus$  represents addition modulo 2 (or, if you prefer, the classical Exclusive-OR Boolean logic operation). Qubit 1 is referred to as the “control qubit” and qubit 2 is referred to as the “target qubit.” With the Controlled-NOT gate and single-qubit operations, we may implement any unitary transformation to the required degree of accuracy and thus perform universal quantum logic.

## 7.2 Errors and Error Correction

Since quantum computation relies on superposition states, a quantum computer is extremely sensitive to decoherence, which may be viewed as a measurement performed by uncontrolled and inaccessible degrees of freedom of the environment [15, 167]. Thus, decoherence collapses the superposition of qubits and so destroys the massive parallelism which is at the heart of quantum computation’s power. If we are to build a quantum computer, then, we must find a system where the detrimental effects of decoherence are limited.

---

<sup>6</sup> It is interesting to note that, whereas *reversible* classical logic requires at minimum a three-bit gate along with single bit operations to form a complete logic family, quantum logic requires only one- and two-qubit gates

When the construction of quantum computers was first suggested, it was argued that *no* system could be so well-isolated from the environment so as to perform the number of computational steps required for “useful” quantum computations, without suffering almost complete loss of coherence [167, 168, 169]. In particular, it was noted that [169], in atomic systems (such as trapped ions), fundamental physics would prevent performing coherent gates with an imprecision of less than  $10^{-5}$  (in fact, these arguments neglected the possibility of Raman transition, which change the limiting imprecision by two orders of magnitude — however, a fundamental limit to the precise manipulation remains, albeit however small). Aside from questions as to the length of “useful” computations, these arguments did not account for the discovery that it is possible to *correct* errors in quantum computations.

The discovery of error correction [170, 171] was a great surprise, and one of the most significant physics insights to arise from quantum information theory thus far. It is surprising because, in order to correct errors, we have to diagnose them, and this requires performing a measurement upon the quantum computer. But the effects of a measurement are to collapse quantum superpositions — which is exactly what we were trying to avoid in the first place! Furthermore, the “quantum no-cloning theorem” [43, 172, 173] precludes us from copying the state of the quantum computer onto another set of qubits, which could be measured with impunity. Nonetheless, quantum error correction *is* possible. I will briefly describe the ideas behind it here, but the reader is referred to the excellent recent article in *Physics Today* by John Preskill [174] for a more comprehensive treatment.

In fact, the ideas behind error correction in quantum computers are very similar to those behind classical error correction, with some caveats to respect the laws of quantum mechanics. So first let us consider how classical error correction works. If we have some collection of classical bits (each of which can be either in the state 0 or 1), then classical errors correspond to bit flips. In order to protect against such errors,

we may redundantly encode each bit in several: for example, we may use extra bits to store the original logical bit “0” as “000.” Then, we can protect against errors in which a single physical bit flips (i.e. “000” $\rightarrow$ “010”) by looking at the three bits, performing a majority vote, and resetting the “disagreeing” bit to the value of the other two. Of course, this error correction scheme does not protect against errors in which *two* physical bits flip, but in practice these errors are much more rare (typically, if the probability of a single bit flip is  $\varepsilon$ , then the probability of two bits flipping is  $\varepsilon^2$ ).

With qubits, the situation is more complicated. First, we can’t observe the qubit without destroying the entanglement and superposition which are necessary for quantum computation’s power. Second, we can’t simply copy the state onto extra qubits, as we could with the classical bits. Third, there are more types of errors with qubits than with classical bits. For example, given a qubit in the general state  $\alpha|0\rangle + \beta|1\rangle$ , we may certainly experience “bit flip” errors  $\alpha \leftrightarrow \beta$ . But we may also experience “phase” errors such as  $\beta \rightarrow -\beta$ . And, indeed, since we are dealing with a quantum system, we may experience a continuum of either sort of error: from no error to the “full” errors listed above. However, by being clever, we can overcome all these issues.

As an example, suppose we only want to protect against amplitude errors (i.e. the continuum of errors from no error to a complete bit flip). We may circumvent the “quantum no-cloning theorem” by redundantly encoding the information stored in a qubit without actually copying it. So, for example, if we want to protect a qubit in the state  $\alpha|0\rangle + \beta|1\rangle$  from amplitude errors, we may (using a sequence of Controlled-NOT gates) produce the state  $\alpha|000\rangle + \beta|111\rangle$ , which is *not* a “clone” of the original state (*that* would be the state  $(\alpha|0\rangle + \beta|1\rangle)^3$ ). Now, suppose a single error occurs, and the encoded state becomes  $\alpha|000\rangle + \beta|111\rangle + \varepsilon(\alpha|100\rangle + \beta|011\rangle)$ . If we were to measure the complete state of the encoded qubit, then we would destroy the superposition. However, we can still extract information about the error by making a *partial* measurement of the system; that is, we may measure collective properties of the three-qubit encoded state.

So, in order to determine whether an error has occurred (and in which qubit), we may make a measurement to determine whether qubits 1 and 2, 2 and 3, and/or 3 and 1 have the same value. Note that we do *not* determine the values of any of the qubits, but only ask whether they are the same or different. Now, assume  $\varepsilon \ll 1$  (this isn't necessary, but reflects the probable situation in a practical quantum computer). Since the error occurred in the first qubit, we will always measure that qubits 2 and 3 are in the same state. With probability  $1 - \varepsilon^2$ , our joint measurement of qubits 1 and 2 will project qubit 1 back into the state where it is identical to qubit 2 (the quantum Zeno effect [59]). On the other hand, with probability  $\varepsilon^2$ , the measurement will project qubit 1 into a state where it *definitely* is in the *opposite* logical state to qubit 2. So in this case, our joint measurement has turned a very small error into a very large one (the largest possible amplitude error!). However, this is “not a bug, it’s a feature.” Since we now know that qubit 1 is opposite to qubits 2 and 3 (but we still don't know the state of any of the three qubits), we can apply a unitary transformation to flip the logical state of the first qubit, restoring the three-qubit system to the state  $\alpha|0\rangle + \beta|1\rangle$  we started out in, without ever knowing what exactly that state was.

So, the idea behind quantum error correction is to redundantly encode the logical information of a single qubit into a system of several qubits. By making measurements of collective properties of this system, we may make “enough” of a measurement to determine that an error occurred, and how to correct it. However, we may be careful not to remove so much information from the quantum system to destroy the superposition and entanglement necessary for quantum computation. One way of looking at the situation is to view the extra qubits as an “entropy dump” which holds the extra entropy put into the quantum system by the measurements made.

The above example treated only amplitude errors. However, one may also simultaneously protect against phase errors. One way to do this [170, 174] is to further encode each three-qubit block (which protects against amplitude errors) into three, three-qubit

blocks. By comparing the relative phases of  $|000\rangle$  and  $|111\rangle$  among the three “super-blocks,” we can determine whether a phase error occurred, and in which block. We then can correct the error much like before.

Thus far, I have discussed ways to correct errors in qubits caused by interactions of the qubits with the environment. However, if the logic gates themselves are imperfect, we might imagine that this would make the situation hopeless — in trying to correct the errors, we would add *more* errors. So the question arises as to whether it is possible to come up with error correction schemes which also correct for logic gate imperfections: so-called “fault-tolerant” error correction schemes. The short answer is “yes” [170, 175, 176, 177, 178]. By using nested blocks of qubits, it is possible to perform completely faithful quantum computation even in the presence of environmentally induced decoherence and gate errors, given some minimum fidelity of the gates. This “opening bid” of fidelity lies somewhere between  $10^{-4}$  and  $10^{-6}$ , depending on the particular decoherence mechanisms which are most significant. The price to be paid is an increase in the total number of qubits and gates required to perform quantum computations (but this increase in resources grows only logarithmically with the number of steps in the algorithm). There is some possibility that error correction schemes may exist which require only a fidelity of  $10^{-2}$  for fault tolerant correction [179], using “non-concatenated” error correction codes, but ways to perform quantum computation using such codes have not yet been found.

### 7.3 Ion Trap Quantum Computers

With the advent of error correction, the question becomes not “can we find a system with so little decoherence as to allow long quantum computations?” but rather “can we find a system where the decoherence is below the threshold required for fault-tolerant error correction?” However, said system must also allow for strong interactions between different qubits so that logic gates may be implemented. Given the long spin-

coherence times observed in trapped-ion systems [180] and the success which we have had in manipulating the spin and motional degrees of freedom of trapped ions (see Ch. 6), we believe that trapped ions offer some promise, at least as far as building a rudimentary quantum information processor.

In particular, we are trying to implement a simple quantum computer of several qubits, according to the scheme proposed by Cirac and Zoller [40], and examine the technological feasibility of building even larger quantum computers along the same lines. In the Cirac-Zoller scheme, the qubits used to store information consist of two electronic levels of a collection of trapped ions, one qubit per ion. Quantum information is exchanged between qubits through two vibrational levels of one mode of the ions' quantized collective motion in the ion trap. The coupling is provided by focused laser beams that can individually address each of the ions.

In a slightly modified version of their original proposal, we can imagine a string of ions trapped in a linear trap. In our case, we may imagine that the motional modes have been laser cooled to low temperature and that one (say, the stretch mode) has been laser cooled to its ground state. In order to perform a Controlled-NOT gate between ions  $j$  and  $k$ , we illuminate ion  $j$  with a laser beam (or laser beams, for stimulated Raman transitions) on the stretch red sideband. If the ion is in  $|\downarrow\rangle \equiv |0\rangle$ , then this has no effect, and the stretch mode remains in the state  $|0\rangle$ . On the other hand, if ion  $j$  is in the state  $|\uparrow\rangle \equiv |1\rangle$ , and the interaction is left on long enough to drive a  $\pi$ -pulse, then the motional mode is left in the state  $|1\rangle$ , while ion  $j$  is left in  $|\downarrow\rangle$ . This interaction has mapped the spin state of ion  $j$  onto the motional state of the entire string, which is a joint property of all the ions. In this sense, the motional mode plays the role of a “quantum data bus,” which makes the quantum information stored in one ion's spin available to all the other ions.

With the information from ion  $j$  transferred to the motional “data bus,” it remains to implement a Controlled-NOT between the data bus and ion  $k$ . In order to do this,

we may use a third atomic level of  $k$  to put a motion- dependent phase onto the spin state of ion  $k$ , as will be described below, in Sec. 7.4. By sandwiching this transition between two  $\pi/2$ -pulses on the  $|\downarrow\rangle \leftrightarrow |\uparrow\rangle$  system, we can realize the desired interaction. Finally, we can restore the spin state of the original ion  $j$  and the motional mode by applying a final  $\pi$ -pulse on the red sideband.

Of course, the question arises as to whether it will be possible to reach the required levels of accuracy for large-scale quantum computations. We have treated many of the possible barriers (laser intensity and frequency fluctuations, magnetic field fluctuations, background electric fields, motional heating, trap imperfections, etc.) in Refs. [73, 111]; see also Refs. [36, 181]. The reader is referred to these articles for such discussion. In the end, however, there seems to be no fundamental barrier to ion-trap quantum information processors — as to the technical difficulties which must be overcome, that seems to be a question best answered by experiment.

## 7.4 Quantum Logic on One Ion

We have demonstrated a two-qubit “quantum Controlled-NOT” logic gate between the spin and motional degrees of freedom of a single trapped ion [41] (this is the important step in the general quantum computation scheme described immediately above). The qubits in our realization consisted of (i) the two-dimensional subspace of the motional Hilbert space spanned by the basis states  $|n = 0\rangle$  and  $|n = 1\rangle$ , and (ii) the two-dimensional Hilbert space spanned by the basis states  $|\downarrow\rangle$  and  $|\uparrow\rangle$ . If the motional qubit is the control and the spin the target, then the effect of the Controlled-NOT is to flip the spin if and only if the motion is in the state  $|n = 1\rangle$ .

In order to realize the Controlled-NOT, we applied the following three Raman beam pulses:

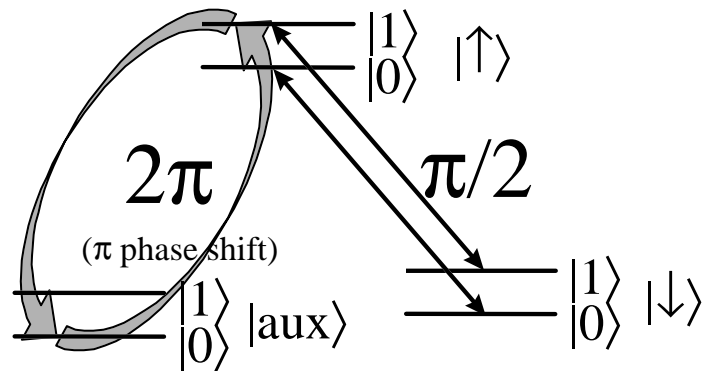
- (1) A  $\frac{\pi}{2}$  pulse on the carrier transition. By way of example,  $|\downarrow\rangle \rightarrow \frac{1}{\sqrt{2}}(|\downarrow\rangle + |\uparrow\rangle)$ .

- (2) A  $2\pi$  pulse on the first upper sideband transition between levels  $|\uparrow\rangle$  and an auxiliary level: the  $2s\ ^2S_{1/2}|F=2, m_F=0\rangle \equiv |aux\rangle$ . This transition couples  $|\uparrow, n\rangle$  and  $|aux, n-1\rangle$ . Due to the formal equivalence between two-level systems and spin-1/2 particles [2], this  $2\pi$  rotation in the two-dimensional Hilbert space spanned by  $|\uparrow, 1\rangle$  and  $|aux, 0\rangle$  changes the sign of the state vector component in  $|\uparrow, 1\rangle$ . However, since there is no lower motional state to which  $|n=0\rangle$  can couple, the pulse does not affect the component of the state vector in  $|\uparrow, n=0\rangle$ . Any component of the state vector in  $|\downarrow\rangle$  is also unaffected, due to the Zeeman shift between levels  $|aux\rangle$  and  $|\downarrow\rangle$ .
- (3) Another  $\frac{\pi}{2}$  pulse is applied on the carrier, but with a  $180^\circ$  phase shift relative to the first pulse. If there was no component of the state vector in  $|n=1\rangle$ , then this simply reverses the effects of the first  $\frac{\pi}{2}$  pulse. However, due to the minus sign introduced by Step 2, the transition started by the first pulse is *completed* by the second for any component of the state vector which was in  $|n=1\rangle$ .

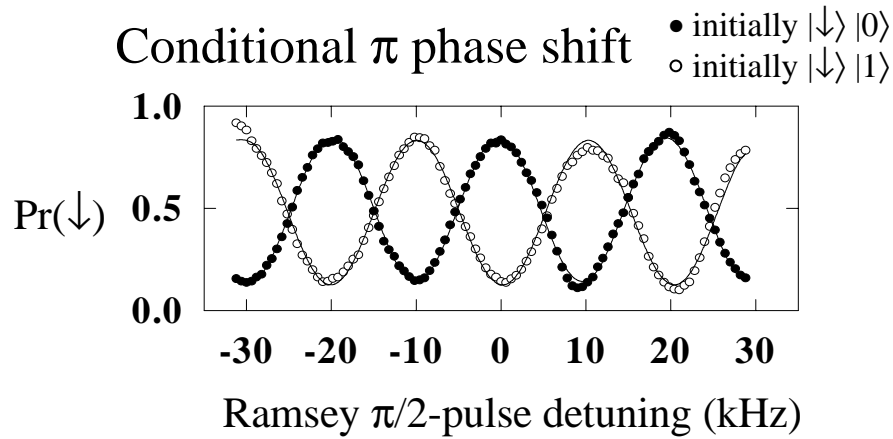
The pulse sequence is illustrated schematically in Fig. 7.1(a). The overall effect is the desired one: the spin of any component of the state vector in the motional state  $|n=1\rangle$  is flipped, while the motion is unaffected.

The effect of the Controlled-NOT gate on the computational basis states is shown in Table 7.1, which lists the probabilities for the various basis states before and after the gate. Note that a major limitation on the gate's apparent fidelity was our ability to accurately prepare the various basis states. This was primarily due to technical sources of noise (laser beam intensity fluctuations, etc.).

The conditional dynamics which are the heart of the Controlled-NOT gate are illustrated in Fig. 7.1(b). This figure shows a Ramsey spectrum in which the two  $\pi/2$ -pulses of the Controlled-NOT gate (steps 1 and 3, above) form the Ramsey zones, and the conditional dynamics occurs during what would normally be the "dark" period.



(a)



(b)

Figure 7.1: (a) Schematic representation of the Controlled-NOT gate. The crucial part of the gate is the  $2\pi$  pulse between  $|\uparrow\rangle$  and  $|\text{aux}\rangle$  on the upper motional sideband of this transition. The pulse puts a phase factor of  $-1$  in front of only the part of the motional wave function that is in  $|\uparrow, n=1\rangle$ . This produces the conditional dynamics necessary for the quantum logic gate. (b) Ramsey spectra of the Controlled-NOT (CN) gate. The detuning of the Ramsey  $\pi/2$  pulses of the gate is swept, and  $P_{\downarrow}$  is measured. The filled circles correspond to initial preparation in the  $|\downarrow, n=0\rangle$  state and the open circles to preparation in the  $|\downarrow, n=1\rangle$  state. The resulting patterns are shifted in phase by  $\pi$  radians, indicating the conditional dynamics of the gate. Similar curves result for preparation in the other two basis states.

Table 7.1: Effect of the Controlled-NOT three-pulse sequence  $\pi/2(\text{carrier}), 2\pi(\text{aux,RSb}), -\pi/2(\text{carrier})$  on the computational basis states. The initial state probabilities differ from 1 and 0 due to state preparation imperfections. The further decline in state probabilities in the “Final State” column is due to imperfections in the gate operations. Nonetheless, with high probability, the Controlled-NOT gate preserves the value of the control qubit (the motional state  $|n\rangle$ ), and flips the target qubit (the spin) if and only if  $n = 1$ .

Initial State		Final State	
P( $n = 1$ )	P( $\uparrow$ )	P( $n = 1$ )	P( $\uparrow$ )
0.02	0.01	0.09	0.16
0.03	0.99	0.04	0.88
0.92	0.05	0.77	0.88
0.94	0.98	0.88	0.19

The solid circles show the Ramsey fringes for the case when the ion started out in  $|\downarrow\rangle$  and in the motional state  $|n = 0\rangle$ : in this case, step 2 had no effect. The hollow circles show the fringes when the ion started out in the state  $|\uparrow, n = 1\rangle$ : in this case, the conditional dynamics were in effect, and caused the  $\pi$  radians phase shift with respect to the previous case. Similar fringes resulted when the ion was prepared in the other two computational basis states.

#### 7.4.1 Simplified Controlled-NOT Gate

As pointed out in Ref. [182], it is not necessary to use a third atomic level to realize a Controlled-NOT between the spin and motional degrees of freedom. Instead, we may use the nonlinear corrections to the Rabi frequencies discussed in Sec. 3.2. To do this, we set the Lamb-Dicke parameter  $\eta$  so that the  $n$ -dependent carrier frequencies (on the  $90^\circ$  carrier) result in a  $2\pi$ -pulse for one motional level when a  $\pi$ -pulse is driven on the other. For example, we have from Eq. (3.12) that

$$\Omega_{0,0} = \Omega e^{-\eta^2/2} \quad (7.16)$$

but that

$$\Omega_{1,1} = \Omega e^{-\eta^2/2} (1 - \eta^2). \quad (7.17)$$

If we choose  $\eta = 0.707$ , then  $\Omega_{0,0} = 2\Omega_{1,1}$  and so the carrier flips the ion's spin if its motion is in the state  $|1\rangle$  but only adds a trivial phase factor if the motional state is  $|0\rangle$ . This realizes an effective Controlled-NOT gate (up to phase factors) without the need for an auxiliary level. On the other hand, specific operating conditions ( $\eta$ ) are required for the trap. Other schemes have been proposed [183, 184] which do not require specific values of  $\eta$  but which do require more laser beams and/or higher-order transitions.

## 7.5 Quantum Logic on Multiple Ions

As mentioned in Sec. 6.4, the next logical step in trying to reach a quantum computer is to implement a gate between two ions. But, for the reasons discussed in that section, we have not yet done this. However, we expect that a two-ion gate will be demonstrated in the near future, most likely in a new version of the micromachined linear trap.

It is worth noting that, for two ions, the techniques used to create the Bell states (Sec. 6.4) can be used to implement a quantum logic gate [49]. To do this, we displace the two ions in an rf trap such that one ion experiences no micromotion ( $J_0(0) = 1 \neq 0$ ), whereas the other one satisfies  $\Omega J_0(|\delta k| \cdot x_{\mu 0,i}) = 0$  (see Eq. 6.34) and following discussion). In this configuration, laser-driven transitions near the carrier are only driven on the first ion. In order to allow transitions for the second ion, we may drive near the first upper or lower rf sideband. In this case, the zeroth-order Bessel functions are replaced by  $J_1(0) = 0$  and  $J_1(|\delta k| \cdot x_{\mu 0,i}) \neq 0$ , so that now the second ion interacts with the lasers while the first does not. However, it is not immediately clear how to apply a similar technique to more than two ions.

One step we have taken towards implementing multi-ion logic is demonstrating the preservation of spin coherence while moving ions back and forth in the linear trap using electric fields. Although the insensitivity of the spin degree of freedom to ion motion (in the absence of motional sideband interactions) is hardly surprising it is, nonetheless,

reassuring to observe this. Some implementations of quantum logic in ion traps [73] may require moving ions back and forth between “storage areas” and “accumulators,” in which quantum logic operations are performed between small numbers of qubits. In order to demonstrate the spin coherence, we performed a traditional Ramsey experiment (Sec. 3.4) on a single, trapped ion. Between the two Ramsey zones, we changed the voltage on the trap rods to move the ion along the  $z$ -direction some distance, and then back to its starting point. This process did not significantly degrade the contrast of the Ramsey fringes.

By shining a second, off-resonant laser beam into the trap at the position of the translated ion, we were able to map out this second laser beam’s profile, by measuring the Ramsey fringe shift due to the AC Stark effect. Fig. 7.2 shows the phase shift as a function of the displacement of the ion into the laser beam. This “laser beam” profiler indicates the approximately Gaussian beam profile at the trap. Note that the measurement occurs with negligible probability that the ion actually absorbs a photon from the second beam. The beam profile information is mapped onto the ion’s spin.

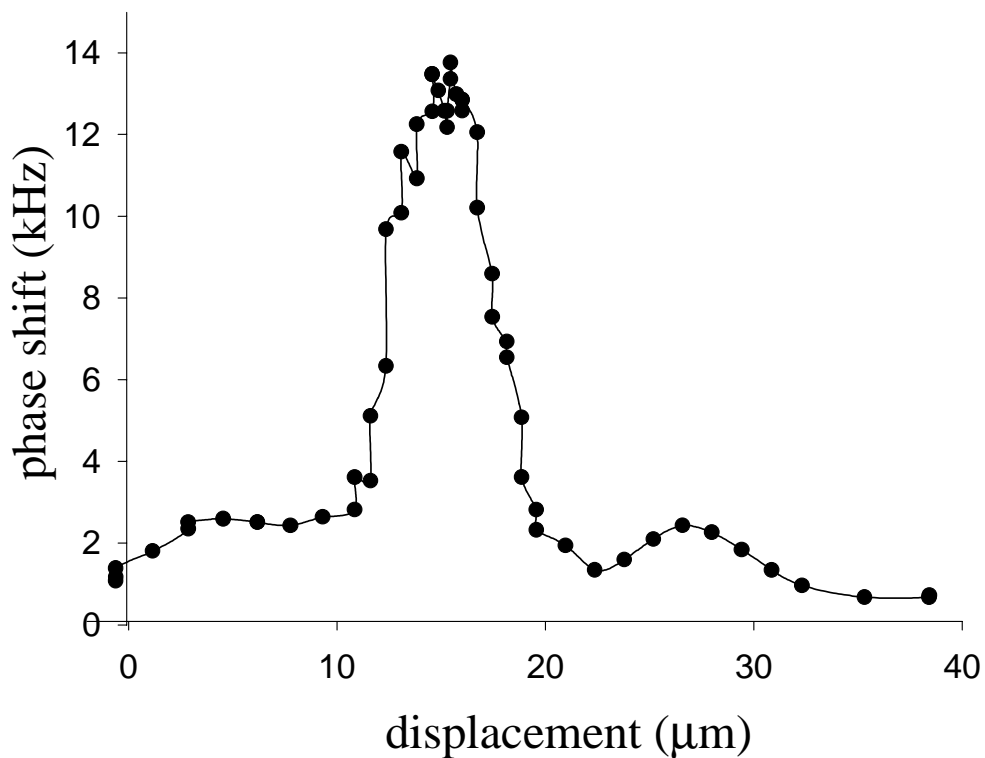


Figure 7.2: “Interaction-free” laser beam profiler. A traditional Ramsey experiment is performed on a single ion confined in the micromachined linear ion trap. In between the Ramsey zones, the trap voltages are changed so as to translate the ion into a second, nearby laser beam. By measuring the AC Stark shift phase shift of the Ramsey fringes, we can determine the second beam’s profile. Note that there is negligible probability that the ion absorbs a photon from the second beam.

## Chapter 8

### Reservoir Engineering

As we have seen, decoherence in our system is undesirable, inasmuch as it limits our ability to perform quantum state engineering and quantum logic operations. In order to do large-scale quantum computation, we must understand the sources of decoherence and be able to reduce them, at least to the levels where fault-tolerant error correction becomes possible. However, the general phenomenon of decoherence (nebulous though this title may be) is of interest in itself. The entanglement of a quantum system with inaccessible and/or uncontrollable degrees of freedom of the environment has attracted much attention [15] as a possible way of explaining how the microscopic world described by quantum mechanics transforms to the macroscopic world which we appear to inhabit. In particular, in the macroscopic world there seems to be no evidence of the superposition and entanglement behaviours which lie at the very heart of quantum mechanics.

It is therefore desirable to be able to study decoherence in a well-controlled manner. Since our trapped-ion system exhibits controllable coherent behaviour of two coupled basic quantum systems, it offers a “test bed” for examining various aspects of system-reservoir interactions leading to decoherence. Recently, we have been able to study the interaction of the ion motion with various electric-field configurations which produce theoretically well-understood reservoir interactions. Since the harmonic oscillator is often the “system of choice” for theorists (due to its simple nature), it is partic-

ularly easy to draw the correspondence between experiment and theory in this system. Furthermore, the control we have over the harmonic oscillator coupling to other degrees of freedom (see Ch. 3) allows us to explore a large region of the “parameter space” described by different theories.

In particular, we have been able to realize so-called “amplitude, “phase,” and “zero temperature” reservoir interactions with the ion’s motion. In this chapter, I will briefly overview some of the theoretical background on reservoir interactions and decoherence theory and then discuss the experiments which realized the particular reservoir interactions listed above.

## 8.1 Reservoir Interactions and Decoherence

Schrödinger’s equation is the fundamental equation of quantum mechanics: it describes the time evolution of a closed quantum mechanical system. In general, however, quantum systems are *not* closed: all systems which we can ever encounter in the real world are coupled to other parts of that real world, however weakly.<sup>1</sup> In essence, this coupling provides a route for (partial) information about the quantum state of the system under consideration to “leak” into the “rest of the world.” If we perform measurements on only the subsystem under consideration, this loss of information results in a loss of coherence.

One way to model the effects of this leak of information to uncontrollable and inaccessible degrees of freedom is through a “master equation” for the density matrix of the quantum system of interest. We may follow the approach of Carmichael [185] and others [124, 186] in order to derive a general master equation. Consider a quantum system  $S$  which interacts with its environment. I will refer to the environment as  $R$ , which stands for “reservoir:” this highlights the idea that the environment has very

---

<sup>1</sup> One may, perhaps, consider the *entire universe* as a closed quantum system. However, no matter how stimulating this may be, we will certainly never have experimental access to the *entire universe*!

many degrees of freedom and that, though the environment may have a large effect on the system  $S$ , the system will have very little effect on the overall state of the environment.

The overall Hamiltonian for the two, coupled quantum systems ( $S$  and  $R$ ), is

$$\hat{H} = \hat{H}_S + \hat{H}_R + \hat{H}_{SR}. \quad (8.1)$$

Here  $\hat{H}_S$  and  $\hat{H}_R$  are the free Hamiltonians of the system and reservoir, respectively (in the absence of any coupling between the two).  $\hat{H}_{SR}$  represents the coupling between  $S$  and  $R$ . In general,  $\hat{H}_{SR}$  will have the form:

$$\hat{H}_{SR} = \hbar \sum_i \hat{s}_i \hat{\Gamma}_i, \quad (8.2)$$

where the  $\hat{s}_i$  are operators which act only in the Hilbert space of the system and the  $\hat{\Gamma}_i$  are operators which act only in the Hilbert space of the reservoir (environment). The sum is over all the different parts (modes) of the environment: typically this sum is taken to be infinite. As a concrete example, in the case of the damping of a harmonic oscillator system's amplitude into a reservoir of harmonic oscillators, we will may take  $\hat{s}_1 = \hat{a}, \hat{s}_2 = \hat{a}^\dagger, \hat{\Gamma}_1 = \sum_i \kappa_i^* \hat{b}_i^\dagger$ , and  $\hat{\Gamma}_2 = \sum_i \kappa_i \hat{b}_i$ , where  $\hat{b}_i, \hat{b}_i^\dagger$  are the lowering and raising operator of the reservoir mode harmonic oscillators. We will return to this model later.

Let the complete density matrix for  $S \oplus R$  be  $\hat{\chi}(t)$ , and

$$\hat{\rho}(t) = \text{tr}_R[\hat{\chi}(t)] \quad (8.3)$$

be the reduced density operator of the system alone. The goal is to determine an equation of motion for  $\hat{\rho}(t)$ , since this is the state which we actually wish to, and are able to, measure.<sup>2</sup> The result of a measurement of a system operator  $\hat{O}$ , which is given by  $\langle \hat{O} \rangle = \text{tr}_{S \oplus R}[\hat{O} \hat{\chi}(t)] = \text{tr}_S\{\hat{O} \text{tr}_R[\hat{\chi}(t)]\} = \text{tr}_S[\hat{O} \hat{\rho}(t)]$ , depends only on  $\hat{\rho}(t)$  and not on the complete density matrix  $\hat{\chi}(t)$ .

---

<sup>2</sup> Even if we wished to measure the state of the environment  $R$ , we would not be able to completely determine the complete state of the rest of the universe! Thus, we cut our losses and concentrate on what we *can* measure.

In an interaction picture defined by  $\hat{U}(t) = \exp[i(\hat{H}_S + \hat{H}_R)/\hbar]$ , the equation of motion for the complete (interaction- picture) density matrix is given by:

$$\dot{\hat{\chi}}' = \frac{1}{i\hbar}[\hat{H}'_{SR}(t), \hat{\chi}'], \quad (8.4)$$

where  $\hat{H}'_{SR}$  is the interaction-picture coupling Hamiltonian.<sup>3</sup> Eq. (8.4) may be perturbatively solved [185, 124]. First, we may formally integrate the equation and plugging the result back into Eq. 8.4:

$$\hat{\chi}'(t) = \hat{\chi}'(0) + \frac{1}{i\hbar} \int_0^t [\hat{H}'_{SR}(\tilde{t}), \hat{\chi}'(\tilde{t})] d\tilde{t} \quad (8.5)$$

$$\Rightarrow \hat{\chi}'(t) = \frac{1}{i\hbar} [\hat{H}'_{SR}(t), \hat{\chi}'(0)] - \frac{1}{\hbar^2} \int_0^t [\hat{H}'_{SR}(t), [\hat{H}'_{SR}(\tilde{t}), \hat{\chi}'(\tilde{t})]] d\tilde{t}. \quad (8.6)$$

By tracing over this equation, we will obtain the reduced density matrix for the system alone. Assume that, at time  $t = 0$  (before the system-reservoir coupling is turned on), the system and reservoir are uncorrelated:  $\hat{\chi}(0) = \hat{\rho}(0)\hat{R}_0$ , where  $\hat{R}_0$  is the initial reservoir density matrix. If we assume that  $\text{tr}_R\{\hat{H}'_{SR}(t)\hat{R}_0\} = 0$ , then the first term in Eq. (8.6) drops out in tracing over the reservoir. This is the case if reservoir operators  $\hat{\Gamma}_i$  have expectation values of zero in the state  $R_0$ : we may always make this so by including the term  $\text{tr}_R\{\hat{H}_{SR}\hat{R}_0\}$  in the system Hamiltonian. Thus, the trace over the reservoir modes (with the above assumptions about the initial conditions), yields:

$$\dot{\hat{\rho}}' = -\frac{1}{\hbar^2} \int_0^t \text{tr}_R \left\{ [\hat{H}'_{SR}(t), [\hat{H}'_{SR}(\tilde{t}), \hat{\chi}'(\tilde{t})]] \right\}. \quad (8.7)$$

This equation is still exact: we have made no approximations in arriving at it. However, in general it exhibits an exceedingly complicated time dependence. Indeed, although the system and reservoir are assumed to be uncorrelated initially, (i.e. the  $t = 0$  density matrix factorizes) the interaction  $\hat{H}_{SR}$  causes them to become correlated at later times. This makes the problem very difficult to solve exactly. However, Eq. (8.7) is in a form which makes an iterative, perturbative solution relatively straightforward.

---

<sup>3</sup> As in Ch. 3, I will use a prime to denote interaction-picture operators

If we assume that the coupling between the system and the reservoir is very weak, then we may make a perturbative expansion of the complete density matrix in the coupling  $\hat{H}_{SR}$ :

$$\begin{aligned}\hat{\chi}'(t) &= \hat{\rho}'(t)\hat{R}'(t) + \mathcal{O}(\hat{H}_{SR}) \\ &= \hat{\rho}'(t)\hat{R}_0 + \mathcal{O}(\hat{H}_{SR}).\end{aligned}\tag{8.8}$$

In writing the second line in Eq. (8.8), I have replaced  $\hat{R}'(t)$  with  $\hat{R}_0$ , the initial reservoir density matrix. The reasoning behind this is that  $R$  is so large that the coupling to  $S$  should have negligible effect on  $R$ . Another way of stating this is that the back-action on  $R$  of the coupling is negligible.

Now we may make a simplifying assumption: the “Born approximation” [2, 124]. This involves dropping the higher order terms in the expansion of  $\hat{\chi}'(t)$  and substituting this approximation into Eq. (8.7). This gives us that

$$\dot{\hat{\rho}}' = -\frac{1}{\hbar^2} \int_0^t \text{tr}_R \left\{ [\hat{H}'_{SR}(t), [\hat{H}'_{SR}(\tilde{t}), \hat{\rho}'(\tilde{t})\hat{R}_0]] d\tilde{t} \right\}.\tag{8.9}$$

The Born approximation simplifies the equation of motion for the system density matrix somewhat, but Eq. (8.9) is still a complicated equation. In particular, the integral involves the value of the density matrix at all times from 0 to  $t$ . Thus, the time evolution of  $\hat{\rho}'$  exhibits “memory” of its state at all previous times, which makes solving for the evolution very difficult. However, for many systems, it is possible to make a second approximation, the “Markoff approximation,” and replace  $\hat{\rho}'(\tilde{t})$  by  $\hat{\rho}'(t)$  under the integral sign. This is possible because the integrand also contains terms with  $\hat{H}'_{SR}$  evaluated both at  $t$  and at  $\tilde{t}$ . Depending on the properties of the *reservoir*, the integrand may then be negligible except when  $\tilde{t} = t$ .

To be more specific, let us plug in the explicit form for  $\hat{H}'_{SR}(t)$  from Eq. (8.2) (transformed into the interaction picture). Then, Eq. (8.9) becomes:

$$\dot{\hat{\rho}}' = - \sum_{\{i,j\}} \int_0^t \text{tr}_R \left\{ [\hat{s}'_i(t)\hat{\Gamma}'_i(t), [\hat{s}'_j(\tilde{t})\hat{\Gamma}'_j(\tilde{t}), \hat{\rho}'(\tilde{t})\hat{R}_0]] \right\} d\tilde{t}$$

$$\begin{aligned}
&= - \sum_{\{i,j\}} \int_0^t \left\{ [\hat{s}'_i(t) \hat{s}'_j(\tilde{t}) \hat{\rho}'(\tilde{t}) - \hat{s}'_j(\tilde{t}) \hat{\rho}'(\tilde{t}) \hat{s}'_i(t)] \langle \hat{\Gamma}'_i(t) \hat{\Gamma}'_j(\tilde{t}) \rangle_R \right. \\
&\quad \left. + [\hat{\rho}'(\tilde{t}) \hat{s}'_j(\tilde{t}) \hat{s}'_i(t) - \hat{s}'_i(t) \hat{\rho}'(\tilde{t}) \hat{s}'_j(\tilde{t})] \langle \hat{\Gamma}'_j(\tilde{t}) \hat{\Gamma}'_i(t) \rangle_R \right\} d\tilde{t}. \quad (8.10)
\end{aligned}$$

In this equation, I have written:

$$\begin{aligned}
\langle \hat{\Gamma}'_i(t) \hat{\Gamma}'_j(\tilde{t}) \rangle_R &= \text{tr}_R \{ R_0 \hat{\Gamma}'_i(t) \hat{\Gamma}'_j(\tilde{t}) \} \\
\langle \hat{\Gamma}'_j(\tilde{t}) \hat{\Gamma}'_i(t) \rangle_R &= \text{tr}_R \{ R_0 \hat{\Gamma}'_j(\tilde{t}) \hat{\Gamma}'_i(t) \}, \quad (8.11)
\end{aligned}$$

which are the correlation functions of the reservoir, and used the fact that the trace operation is invariant under cyclic permutations of its argument. For many reservoir systems, the high density of reservoir states causes these correlation functions decay very rapidly. If this happens on a time scale short compared to the time evolution of  $\hat{\rho}'$ , then we may replace the (non-zero) correlation functions in Eq. (8.11) by delta functions:

$$\begin{aligned}
\langle \hat{\Gamma}'_i(t) \hat{\Gamma}'_j(\tilde{t}) \rangle_R &\rightarrow c_{ij} \delta(t - \tilde{t}) \\
\langle \hat{\Gamma}'_j(\tilde{t}) \hat{\Gamma}'_i(t) \rangle_R &\rightarrow c_{ji} \delta(t - \tilde{t}) \quad (8.12)
\end{aligned}$$

(where the  $c_{ij}$ 's are constants of proportionality). Then Eq. (8.10) becomes:

$$\begin{aligned}
\dot{\hat{\rho}}' &= \sum_{\{i,j\}} \left\{ c_{ij} [\hat{s}'_i(t) \hat{s}'_j(t) \hat{\rho}'(t) - \hat{s}'_j(t) \hat{\rho}'(t) \hat{s}'_i(t)] \right. \\
&\quad \left. + c_{ji} [\hat{\rho}'(t) \hat{s}'_j(t) \hat{s}'_i(t) - \hat{s}'_i(t) \hat{\rho}'(t) \hat{s}'_j(t)] \right\}. \quad (8.13)
\end{aligned}$$

This is the general master equation in the Born-Markoff approximation. Particular cases are obtained by choosing particular  $\hat{s}_i$ 's and  $\hat{\Gamma}_i$ 's.

I shall go on, in the next few sections, to discuss particular realizations of the master equation in our experiment. However, first, a few general comments on the above derivation are in order. This first comment is that this derivation was *general*: it dealt with the system and the reservoir modes in an explicitly quantum mechanical and somewhat abstract manner. The coupling Hamiltonian  $\hat{H}_{SR}$  was written down

in a general (though linear) form in Eq. (8.2) without specifying the particular system operators  $\hat{s}_i$  or the reservoir operators  $\hat{\Gamma}_i$ , and this general form was propagated through the entire derivation leading up to Eq. (8.13). However, careful examination of the steps leading to this equation shows that the quantum properties of the reservoir operators were never actually used in achieving the final result! The only place where the quantum nature of the reservoir becomes apparent is in writing down the  $\mathcal{C}$ -number correlation functions in Eq. (8.11), which are specifically ordered pairs of the  $\hat{\Gamma}_i$ 's. In this case, the constants of proportionality,  $c_{i,j}$ , in Eq. (8.12) may depend on the particular reservoir operators which are coupled to the system. However, since Eq. (8.12) evaluates to a constant  $\mathcal{C}$ -number, this information only feeds into the master equation in a parametric sense.

In this sense, the master equation describes quantum and “classical” reservoirs equally well! In essence, this comes about because of the approximations made in deriving the master equation: in particular, tracing over the reservoir states and making the Born and Markoff approximations. In making the Born approximation, we essentially ignore higher-order correlations in the reservoir, and in taking the trace over the reservoir state, we are reducing any functional dependence of the system reduced density matrix on the reservoir to a  $c$ -number. The Markoff approximation reduces the  $\mathcal{C}$ -number's functional form to a constant value. Because of these assumptions, the functional form of the master equation always remains the same: the most that a “non-classical” reservoir (e.g. a squeezed reservoir [124]) can “do” is to force the solutions of the equation into a region of parameter space that could never be explored by a system coupled to a classical reservoir.

### 8.1.1 Beyond the Master Equation

The idea of considering our quantum system as coupled to uncontrollable and inaccessible degrees of freedom of the “rest of the universe” marked the beginning of the

path which led to the master equation (in the Born-Markoff approximation). However, this idea has more general applications than just as a derivation of the master equation. Since these applications seem to be of some current interest, I will briefly touch on two of them.

Again, the idea is that the complete time evolution of the system plus reservoir is unitary, and governed by Schrödinger's equation. However, since we do not have information about the reservoir, we must (according to the usual prescription of quantum mechanics) trace over this part of the composite system, which leads to (apparently) non-unitary time evolution of the system considered by itself. Thus, an initial density matrix  $\hat{\rho}(t=0)$  with  $\text{tr}_S\{\hat{\rho}^2\} = 1$  evolves into a density matrix with  $\text{tr}_S\{\hat{\rho}^2\} < 1$ . However, we may still describe the system by a density matrix. Thus, although the time evolution is not described by a *unitary* operator, it is still described by a linear mapping, which maps linear operators to linear operators [43]. Such a linear mapping is referred to as a "superoperator." In particular [43, 187], we may express a superoperator  $\mathcal{M}$  as  $\mathcal{M}(\hat{\rho}) = \sum_k \hat{M}_k \hat{\rho} \hat{M}_k^\dagger$ , where the operators  $\hat{M}_k$  satisfy  $\sum_k \hat{M}_k^\dagger \hat{M}_k = \mathbf{1}_s$ .

In general, the evolution produced by this superoperator does not admit a description in terms of a differential equation. Such a description is only possible if the time evolution is *local* in time: i.e. Markovian. In this case, the reservoir (environment) does not retain a memory of the correlations between itself and the system, and so this information cannot "leak" back into the system. In this case, the dynamics of the system alone can be described by the master equation which we derived above.

In keeping with the operator/superoperator point of view, one often introduces a linear operator called the "Lindbladian." Given the Schrödinger equation,

$$\dot{\hat{\rho}} = -i/\hbar [\hat{H}, \hat{\rho}], \quad (8.14)$$

we may formally solve to obtain

$$\hat{\rho}(t) = e^{-i\hat{H}t/\hbar} \hat{\rho}(0) e^{i\hat{H}t/\hbar}. \quad (8.15)$$

We say that the Hamiltonian operator  $\hat{H}$  *generates* the time evolution. In the same way, for the non-unitary time evolution of a system in contact with a reservoir, one writes:

$$\dot{\hat{\rho}} = \mathcal{L}[\hat{\rho}] \quad (8.16)$$

$$\hat{\rho}(t) = e^{\mathcal{L}t}[\hat{\rho}] \quad (8.17)$$

and says that the linear operator  $\mathcal{L}$ , called the “Lindbladian,” generates the superoperator  $\exp(\mathcal{L}t)$  which produces the time evolution. One then re-expresses the master equation, Eq. (8.13), as:

$$\begin{aligned} \dot{\hat{\rho}}' &= \mathcal{L}[\hat{\rho}'] \\ &= - \sum_{\{i,j\}} \left\{ c_{ij} [\hat{s}'_i(t) \hat{s}'_j(t) \hat{\rho}'(t) - \hat{s}'_j(t) \hat{\rho}'(t) \hat{s}'_i(t)] \right. \\ &\quad \left. + c_{ji} [\hat{\rho}'(t) \hat{s}'_j(t) \hat{s}'_i(t) - \hat{s}'_i(t) \hat{\rho}'(t) \hat{s}'_j(t)] \right\}. \end{aligned} \quad (8.18)$$

In this context, the operators  $\hat{s}'_i$  are often referred to as “Lindblad operators.”

This more general context allows for treatment of arbitrary system-environment interactions. Indeed, in all cases, the time evolution is described by a “master equation” (non-local in time!) similar in form to Eq. (8.10) [188]. Analysis of this equation shows that, in general, system-reservoir interactions are characterized by “pointer bases” of the system’s Hilbert space. A pointer basis state is invariant under the effects of the system-reservoir coupling Hamiltonian [15, 188, 189]. (We shall see some examples of pointer bases in the next few sections). Besides providing a convenient basis for analyzing the system dynamics, the general existence of a pointer basis regardless of the particular details of the system-environment interaction may help to resolve the apparent conflict between a quantum description of the world and our everyday, macroscopic experiences.

This conflict is illustrated by the example of “Schrödinger’s cat” (see Sec. 6.2.1). Although quantum mechanics generically allows for the existence of superpositions, we never see evidence for them on the macroscopic level. However, a general analysis of system-reservoir interactions [15, 188, 189, 190, 191, 192] indicates that the pointer

basis, which is often determined by the system operators appearing in the coupling Hamiltonian [188], forms a “preferred basis.” When the density matrix is expressed in this basis, one finds (as we shall, below) that the off-diagonal terms of the density matrix vanish as an exponential in the square of the “size” of the superposition (e.g. the square of  $|m - n|$ , where the density matrix elements are  $\rho_{m,n}$ ). Since these off-diagonal terms are responsible for the interference effects which are the hallmark of superpositions [8], we never see macroscopic evidence of superpositions. Very often, the pointer states are position eigenstates, which may explain why position is a “good” classical observable. However, in some cases, energy eigenstates form the pointer basis [188]. This approach to the microscopic/macroscopic boundary is one of many, and many of its details are still being worked out. Nonetheless, it does seem to offer an attractive solution to the lack of interference effects on the macroscopic level.

In any event, the master equation, Eq. (8.13), allows us to make quantitative predictions for the behaviour of the density matrix elements for various forms of system-reservoir coupling. I will now examine some of these cases.

## 8.2 Phase Reservoir

A relatively simple example of the master equation occurs for the case of a harmonic oscillator of frequency  $\omega_z$  (system) coupled to an infinite number of other harmonic oscillators (environment/reservoir) with a “phase damping” coupling [193]<sup>4</sup> :

$$\begin{aligned}\hat{H}_{SR} &= \sum_k \hbar(\kappa_k^* \hat{b}_k^\dagger + \kappa_k \hat{b}_k) \hat{a}^\dagger \hat{a} \\ &= \hbar(\Gamma^\dagger + \Gamma) \hat{a}^\dagger \hat{a},\end{aligned}\tag{8.19}$$

Here, the  $\hat{b}_k, \hat{b}_k^\dagger$  are the lowering and raising operators for the  $k^{th}$  reservoir mode and  $\hat{\Gamma}$  is defined implicitly in the apparent manner. Making the connection with the derivation in Sec. 8.1.1, we identify  $\hat{s}_1 = \hat{s}_2 = \hat{a}^\dagger \hat{a}$ ,  $\hat{\Gamma}_1 = \Gamma^\dagger = \sum_k \kappa_k^* \hat{\Gamma}^\dagger$ , and  $\hat{\Gamma}_2 = \Gamma = \sum_k \kappa_k \hat{\Gamma}$ .

---

<sup>4</sup> Other authors (such as Ref. [185]) use a different system-reservoir coupling:  $\hat{H}_{SR} = \sum_k \hbar \kappa_k \hat{b}_k^\dagger \hat{b}_k \hat{a}^\dagger \hat{a}$ . This leads to the same master equation.

The reservoir is usually assumed to be in a thermal distribution at temperature  $T$ , so that

$$\hat{R}_0 = \prod_k \left(1 - e^{-\hbar\omega_k/k_B T}\right) e^{-\hbar\omega_k \hat{b}_k^\dagger \hat{b}_k / k_B T}. \quad (8.20)$$

This leads to the reservoir correlation functions:

$$\langle \hat{\Gamma}^{\dagger'}(t) \hat{\Gamma}^{\dagger'}(\tilde{t}) \rangle_R = 0 \quad (8.21)$$

$$\langle \hat{\Gamma}^{\dagger'}(t) \hat{\Gamma}'(\tilde{t}) \rangle_R = \sum_k |\kappa_k|^2 \overline{N}(\omega_k, T) e^{i\omega_k(t-\tilde{t})} \quad (8.22)$$

$$\langle \hat{\Gamma}'(t) \hat{\Gamma}^{\dagger'}(\tilde{t}) \rangle_R = \sum_k |\kappa_k|^2 [\overline{N}(\omega_k, T) + 1] e^{i\omega_k(t-\tilde{t})} \quad (8.23)$$

$$\langle \hat{\Gamma}'(t) \hat{\Gamma}'(\tilde{t}) \rangle_R = 0, \quad (8.24)$$

where

$$\overline{N} = \frac{e^{-\hbar\omega_z/k_B T}}{1 - e^{-\hbar\omega_z/k_B T}} \quad (8.25)$$

is the average occupation number of the reservoir mode  $k$ .

If we plug in from Eqs. (8.25) for the reservoir correlation functions and replace the sum over the reservoir modes by an integral, with density of states  $g(\omega)$ , then Eq. (8.10) becomes:

$$\begin{aligned} \dot{\rho}' &= - \int_{\omega=0}^{\infty} \int_{\tau=0}^t \\ &\left\{ 2[\hat{n}^2 \hat{\rho}'(\tilde{t}-\tau) - 2\hat{n} \hat{\rho}'(\tilde{t}-\tau) \hat{n} + \hat{\rho}'(\tilde{t}-\tau) \hat{n}^2] g(\omega) |\kappa(\omega)|^2 \overline{N}(\omega, T) e^{i\omega\tau} \right. \\ &\left. [\hat{n}^2 \hat{\rho}'(\tilde{t}-\tau) - 2\hat{n} \hat{\rho}'(\tilde{t}-\tau) \hat{n} + \hat{\rho}'(\tilde{t}-\tau) \hat{n}^2] g(\omega) |\kappa(\omega)|^2 e^{i\omega\tau} \right\} d\tilde{t} d\omega. \quad (8.26) \end{aligned}$$

In Eq. (8.26),  $\tau \doteq t - \tilde{t}$ . However, the time scales of interest to us are much longer than the time scales over which the time integrand has appreciable values. To see this, assume that  $\kappa(\omega)$  and  $g(\omega)$  are constant in Eq. (8.26). Then the integrals are just the Fourier transform of the function  $\overline{N}(\omega, T)$ ; at room temperature, the relevant reservoir time scales are on the order of  $10^{-14}$  s, much faster than the microsecond time scales of interest in our experiments. With this in mind, we can replace  $t - \tau$  with  $t$  in Eq. (8.26) (the Markoff approximation). This is sometimes referred to as ‘‘coarse graining.’’

When we make this replacement, we obtain the master equation for the density matrix:

$$\begin{aligned} \dot{\hat{\rho}}'(t) &= -\mathcal{A}[\hat{n}^2 \hat{\rho}'(t) - 2\hat{n} \hat{\rho}'(t) \hat{n} + \hat{\rho}'(t) \hat{n}^2] \\ &+ -2\mathcal{B}[\hat{n}^2 \hat{\rho}'(t) - 2\hat{n} \hat{\rho}'(t) \hat{n} + \hat{\rho}'(t) \hat{n}^2], \end{aligned} \quad (8.27)$$

where

$$\mathcal{A} = \int_{\omega=0}^{\infty} \int_{\tau=0}^t g(\omega) |\kappa(\omega)|^2 e^{i\omega\tau} d\tilde{t} d\omega \quad (8.28)$$

$$\mathcal{B} = \int_{\omega=0}^{\infty} \int_{\tau=0}^t g(\omega) |\kappa(\omega)|^2 e^{i\omega\tau} \overline{N}(\omega, T) d\tilde{t} d\omega \quad (8.29)$$

$$(8.30)$$

Again recognizing the separation of time scales between the reservoir correlation times (significant values of  $\tau$ ) and the system evolution (significant values of  $t$ ), we can extend the time integral to  $+\infty$  in Eqs. (8.30). When we do this, the integrals can be expressed as Dirac delta-functions in frequency. We also end up with terms containing the Cauchy principal values of the integrands, but these correspond to small shifts of the harmonic oscillator frequency [185] (analogous to the Lamb shift), and can be absorbed into this frequency. Tying all this together, we finally obtain the master equation for a harmonic oscillator coupled to a reservoir with a phase-damping coupling:

$$\dot{\hat{\rho}}' = \kappa \left( \hat{a}^\dagger \hat{a} \hat{\rho}' \hat{a}^\dagger \hat{a} - \frac{1}{2} (\hat{a}^\dagger \hat{a})^2 \hat{\rho}' - \frac{1}{2} \hat{\rho}' (\hat{a}^\dagger \hat{a})^2 \right), \quad (8.31)$$

where  $\kappa = 6\pi g(0) |\kappa(0)|^2$  is the effective coupling strength.

This master equation is straightforward to solve, if we express the density matrix in the Fock state basis:  $\hat{\rho}' = \sum_{n,m} \rho'_{nm} |n\rangle \langle m|$ . In this case, using the properties of the number operator  $\hat{n} = \hat{a}^\dagger \hat{a}$ , we have that

$$\begin{aligned} \dot{\rho}'_{nm} &= \kappa \left( nm - \frac{1}{2} n^2 - \frac{1}{2} m^2 \right) \rho'_{nm} \\ &= -\frac{1}{2} \kappa (n - m)^2 \rho'_{nm}. \end{aligned} \quad (8.32)$$

Thus, the density matrix is given by:

$$\rho'_{nm}(t) = \rho_{nm}(0)e^{-\frac{1}{2}\kappa(n-m)^2t}. \quad (8.33)$$

So, for example, if we make states such as  $|\psi_p\rangle = (|n\rangle + |m\rangle)/\sqrt{2}$ , then the coherences should decay like  $e^{-\kappa(n-m)^2t/2}$ . Note that the diagonal elements suffer no decay at all.

For this reservoir coupling, then, the Fock states play the role of a pointer basis<sup>5</sup>. When the density matrix is expressed in this basis, the diagonal elements do not decay, but the off-diagonal elements do. Furthermore, superpositions of widely different Fock states (i.e. “mesoscopic” superpositions) suffer extremely rapid decay of the coherences. Thus, “mesoscopic” superposition states quickly decay to mixtures.

In order to observe the effects of the coupling to the reservoir, we prepared “cat-like” states of the form  $|s\rangle(|n\rangle + |m\rangle)/\sqrt{2}$  (where  $|s\rangle \in \{\downarrow, \uparrow\}$ ) as discussed in Sec. 6.1.2. For example, the state  $|\downarrow\rangle(|0\rangle + |2\rangle)/\sqrt{2}$  was prepared by first performing a  $\pi/2$ -pulse on the blue sideband, then performing a  $\pi$ -pulse on the red sideband. After allowing the state to interact with a phase reservoir (see below), we then reversed the state preparation. Thus the experiment consisted of preparing a superposition state, allowing the state to interact with the environment for some period of time and then reversing the superposition. In this respect, it resembled a Ramsey experiment (see Sec. 3.4). Indeed, by sweeping the frequency of the  $\pi/2$ - pulses, we could sweep out Ramsey fringes. Decoherence which occurred in between the two “Ramsey zones” (superposition creation and reversal) reduced the contrast of the Ramsey fringes.

At each frequency, we repeated the experiment  $\approx 100$  times and measured the average cycling-transition photon counts, to build up a Ramsey curve. Since the Ramsey experiment connected the motional states  $|n\rangle$  and  $|m\rangle$ , it was sensitive to the off-diagonal

---

<sup>5</sup> In general, the “ideal” pointer states are eigenstates of system operators  $\hat{O}_S$ , where  $[\hat{H}_{SR}, \hat{O}_S] = 0$ . In this case, the pointer basis is exactly the Fock state basis. For the case of amplitude coupling, which we shall treat below, the coherent states are an approximate, but not exact, pointer basis.

motional density matrix elements  $\rho_{nm}$ . From the treatment above, we would then expect the contrast of the Ramsey fringes to scale as  $\exp[-\kappa(n-m)^2 t_{res}/2]$ .

The effect of a phase reservoir is to cause a random change in the ion's motional phase without affecting the ion's eigenstate distribution. One way to realize such an interaction is to change the trap frequency in a random fashion: this causes the time evolution operator  $\hat{U}(t) = e^{i\hat{n}\omega_z t} \rightarrow e^{i\hat{n}(\omega_z + \delta\omega)t/\hbar}$ . If the trap frequency is changed for a time  $t_{res}$ , then the resultant phase shift in the ion's wave function is given by:

$$\delta\phi = \int_0^{t_{res}} \delta\omega dt. \quad (8.34)$$

We changed the trap frequency by applying a noisy voltage to one of the middle segments of the linear trap's electrode structure, for a time  $t_{res} = 20 \mu\text{s}$  in between the Ramsey zones. This produced a field gradient at the ion which, according to Eq. (2.54), altered the trap frequency. We ensured that the trap frequency change was adiabatic by filtering the noise: the noise source was a 10 MHz white noise source, which was then filtered to produce a spectrum which was flat from  $\approx 1 - 100$  kHz, then rolled off at 18 dB/octave<sup>6</sup>. This filtering was necessary to reduce the frequency components at  $\omega_z$ , which would have excited the ion's motion (see Sec. 6.1.3). From studying the axial trap frequency as a function of static voltage applied to the trap electrodes, we knew that the shift in the trap frequency was 90 kHz/V, so that the expected phase shift for an applied voltage shift  $\delta V$  was:

$$\delta\phi = (90 \text{ kHz/V}) \int_0^{20 \mu\text{s}} \delta V dt. \quad (8.35)$$

Although one may use the master equation approach to deal with this situation, it is also possible to use a semi-classical model to predict the behaviour of the ion's motion in this situation. Since the trap change was adiabatic, we may view the trap strength as essentially constant in each shot of the experiment, but random from shot

---

<sup>6</sup> Additional filtering was provided by the filter network on the trap electrode structure (see Sec. 2.4.2).

to shot. The phase shift due to the differing trap strength resulted in an additional phase  $e^{i\delta\phi n}$  on the Fock state  $|n\rangle$ . Thus, the effect of the changed trap strength was to produce a phase shift  $e^{i\delta\phi(n-m)}$  in the cat-like state  $|s\rangle(|n\rangle + |m\rangle)/\sqrt{2}$ , which varied in a random fashion from shot to shot of the experiment. This phase mapped onto the Ramsey fringes, which, when averaged over the random voltage change, caused a loss of Ramsey fringe contrast. Applying this averaging procedure, one finds that the Ramsey fringe contrast should degrade exponentially in  $(n - m)^2$ .

The exponential in the square of the Fock state difference is the same as predicted by the master equation approach. In this case, the behaviour of the reservoir is classical, and so there is a semi-classical treatment of the interaction which exactly mimics the behaviour of the master equation (and vice-versa!). This is an example of the generality of the master equation approach, as discussed following Eq. (8.13). One might object that each individual experiment was describable by a state vector (i.e. unitary time evolution) and, therefore, that the situation is not one described by the master equation. However, the experiments as a whole represented an *ensemble* of identically prepared quantum systems, which correspond to a density matrix. In fact, any (non pure-state) density matrix admits any number of interpretations as an ensemble preparation [43, 187]. The behaviour of the ensemble as a whole is irrespective of the particular details of how the ensemble was realized. So the master equation is also an appropriate description of the experiment.

Of course, in principle, we could have measured the (classical) electric field gradient in each shot of the experiment, and applied a calculated phase shift to that data point, to reconstruct the Ramsey fringes with 100% contrast even in the presence of the noisy electric field. But, in fact, we did not do this and, as pointed out by Preskill [43] (for example), the situation where we have a quantum system considered by itself and one where we also have information about how that system has interacted with other

systems are fundamentally different, and have a different mathematical description. (This is illustrated by so-called “quantum eraser” experiments [194, 195, 196]).

We repeated the experiment while varying the rms voltage noise  $\mathcal{V}$ , measuring the contrast of the Ramsey fringes at each point. Fig. 8.1 shows the Ramsey fringe contrast in our experiment as a function of the applied mean squared voltage, scaled by  $(n - m)^2$ . The data are also rescaled to give unity contrast at  $\mathcal{V} = 0$ , correcting for a small loss of contrast due to sources of technical noise and due to the background source of motional heating (see Secs. 5.5, 8.3.1). All the data points fall on the universal curve predicted by theory (master equation or ensemble average).

### 8.3 Amplitude Reservoir

Another particular form of the master equation comes about by considering a harmonic oscillator of frequency  $\omega_z$  (system) coupled to an infinite number of other harmonic oscillators (environment/reservoir) in the so-called “amplitude reservoir” case. In this case, the coupling is given by

$$\begin{aligned}\hat{H}_{SR} &= \sum_k \hbar \kappa_k (\hat{a} \hat{b}_k^\dagger + \hat{a}^\dagger \hat{b}_k) \\ &= \hbar (\hat{a} \hat{\Gamma}^\dagger + \hat{a}^\dagger \hat{\Gamma}),\end{aligned}\tag{8.36}$$

where, again, the  $\hat{b}_k$ ,  $\hat{b}_k^\dagger$  are the lowering and raising operators for the  $k^{\text{th}}$  reservoir mode and  $\hat{\Gamma}$ ,  $\hat{\Gamma}^\dagger$  are the sums of these operators over the reservoir modes. Making the connection with the derivation in Sec. 8.1.1, we identify  $\hat{s}_1 = \hat{a}$ ,  $\hat{s}_2 = \hat{a}^\dagger$ ,  $\hat{\Gamma}_1 = \sum_k \kappa_k^* \hat{b}_k^\dagger$ , and  $\hat{\Gamma}_2 = \sum_k \kappa_k \hat{b}_k$ .

The derivation of the master equation is very similar to the derivation for the phase-damping case (Sec. 8.2). The resulting master equation is:

$$\dot{\rho}' = \kappa(2\hat{a}\hat{\rho}'\hat{a}^\dagger - \hat{a}^\dagger\hat{a}\hat{\rho}' - \hat{\rho}'\hat{a}^\dagger\hat{a}) + 2\kappa\overline{N}(\hat{a}\hat{\rho}'\hat{a}^\dagger + \hat{a}^\dagger\hat{\rho}'\hat{a} - \hat{a}^\dagger\hat{a}\hat{\rho}' - \hat{\rho}'\hat{a}\hat{a}^\dagger).\tag{8.37}$$

The analysis of the dynamics induced by this master equation is tedious [191]. There are two significant results. One is that the approximate pointer states for this coupling

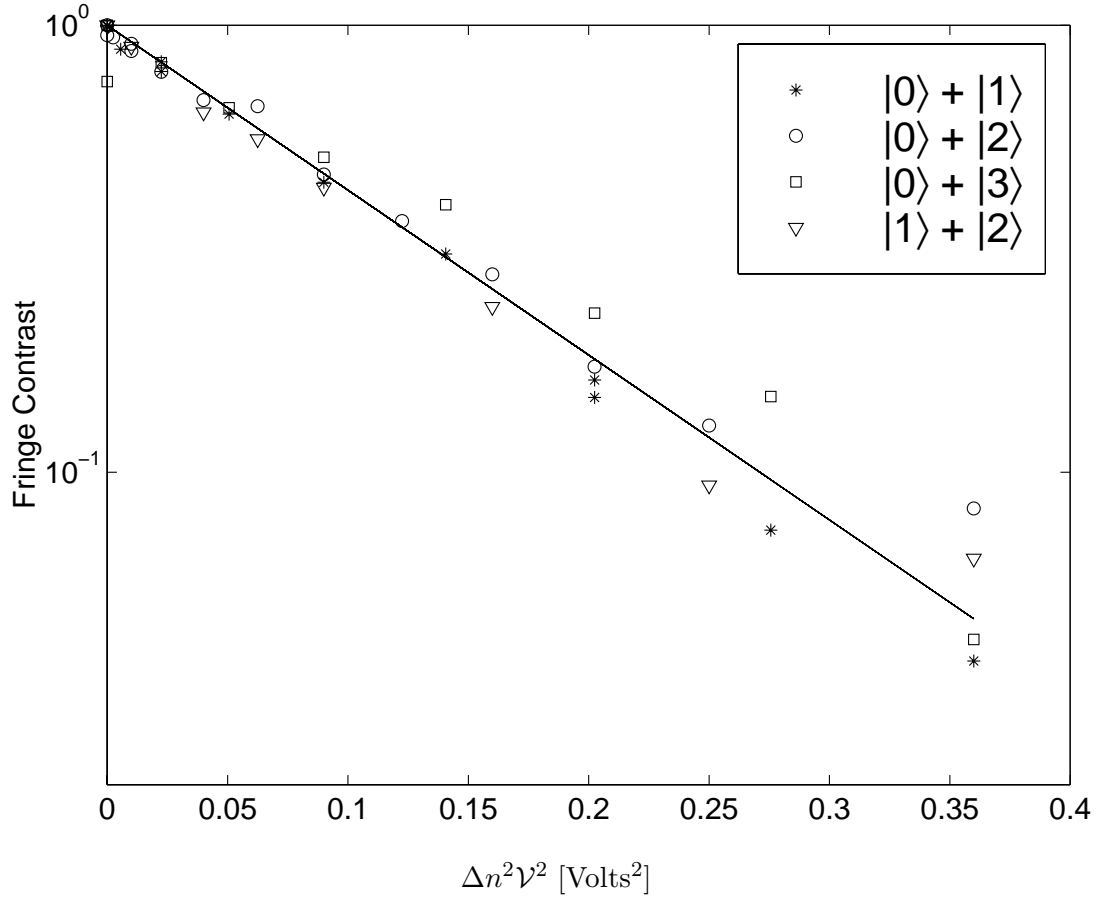


Figure 8.1: “Ramsey” fringe contrast as a function of coupling strength to phase reservoir. The  $x$ -axis is in terms of the square of the rms voltage  $\mathcal{V}$  applied to the middle electrode of the trap, scaled by the square of the “size”  $\Delta n$  of the superposition state, and the fringe contrast is normalized to unity at  $\mathcal{V} = 0$ . The solid line is a one-parameter (slope) fit to an exponential, constrained to be unity at  $\mathcal{V} = 0$ .

are the coherent states  $|\alpha\rangle$  (see Sec. 6.1.3). The second is that, again, the off-diagonal density matrix elements decay much faster than elements on the diagonal.

In order to observe the effects of the coupling to the reservoir, we prepared “Schrödinger cat” states of the form  $(|\downarrow, \alpha_\downarrow\rangle + |\uparrow, \alpha_\uparrow\rangle)/\sqrt{2}$ , as discussed in Sec. 6.2.1. Again, the cat preparation and reversal procedure can be viewed as a Ramsey-type experiment — and again, decoherence which occurred in between the two Ramsey zones reduced the contrast of the Ramsey fringes.

In our case, we obtained Ramsey fringes by sweeping the frequency of the  $\pi/2$ -pulses on the carrier transition (the first and the last pulses of the preparation/reversal pulse sequence). At each frequency, we repeated the experiment  $\approx 100$  times and measured the average intensity, to build up a Ramsey curve. A treatment following the work of Collett [191] shows that, in the high-temperature limit, we would expect Ramsey fringes of the form:

$$P_{\downarrow}(t_{res}) = \frac{1}{2} \left( 1 - e^{-2|\Delta\alpha|^2(1+\overline{N}\kappa t_{res})} \cos(\delta) \right). \quad (8.38)$$

In Eq. (8.38),  $\delta$  is the detuning of the carrier  $\pi/2$ - pulses from resonance and  $|\Delta\alpha|^2$  is the square of the separation between the two coherent states constituting the cat state.

The form of the coupling, Eq. (8.36), which contains a sum of the system operators  $\hat{a}$  and  $\hat{a}^{\dagger}$ , suggest that the effects of the reservoir may be realized by applying displacement operators to the ion. That is, indeed, the case: the reservoir may be realized by applying noisy electric fields to the ion, with a noise spectrum centred around the trap frequency  $\omega_z$ . As long as the bandwidth of the noise is large enough<sup>7</sup>, this will be a realization of the amplitude reservoir. In the experiment, we applied the noisy field to the trap electrodes for  $3 \mu\text{s}$  in between the cat creation and reversal steps. We repeated the experiment while varying the rms voltage noise  $\mathcal{V}$  and the separation  $\Delta\alpha$  between the cat wave packets, measuring the contrast of the Ramsey fringes at each point.

As with the phase reservoir case, the experiment may be analyzed either using the master equation or a semi-classical average over the shot-to-shot variations in the electric field strength (or noise voltage,  $\mathcal{V}$ ). In this latter point of view, we may view the electric field as producing a displacement  $\hat{D}(\beta)$  which varied from shot to shot of the experiment. Since the electric field affected both  $|\downarrow\rangle$  and  $|\uparrow\rangle$  the same, both components of the cat state suffered the same displacement  $\hat{D}(\beta)$ . Thus, the state

---

<sup>7</sup> In practice, if the bandwidth of the noise is large compared with  $t_{res}$ , then the bandwidth is effectively infinite

reversal still succeeded in undoing the cat creation with 100% fidelity! However, the additional displacement resulted in an additional phase between  $|\downarrow\rangle$  and  $|\uparrow\rangle$ , so that the state after the reversal was [50]:

$$|\psi\rangle' = \frac{1}{\sqrt{2}} \left( |\downarrow\rangle + e^{2i\text{Im}(\beta)\Delta\alpha^*} |\uparrow\rangle \right). \quad (8.39)$$

Thus, there was a random phase in the Ramsey fringes which was random from shot to shot of the experiment. When averaged over the random variable  $\beta$ , this caused a loss of Ramsey fringe contrast, which should have had the form  $e^{-\kappa\Delta\alpha^2\mathcal{V}^2}$  (where  $\kappa$  is a coupling constant between the applied voltage and the ion motion), as with the master-equation analysis.

Figure 8.2 shows the Ramsey fringe contrast in our experiment as a function of the applied mean squared voltage, scaled by  $|\Delta\alpha|^2$ . As with the phase noise data, the data are scaled to give unity contrast at  $\mathcal{V} = 0$ . All the data points fall on the universal curve predicted by theory (master equation or ensemble average).

### 8.3.1 Natural Amplitude Reservoir

As discussed in Sec. 5.5, an ambient heating source exists in the trap, whose exact nature is as-yet poorly understood. This source represents an ambient  $T \neq 0$  reservoir, and should produce the same behaviour in cat states as the applied amplitude reservoir. Indeed, preliminary evidence of this was reported in Ref. [47]. In order to quantify this decoherence, we varied the time between creating the cat states and reversing them, while varying the size  $\Delta\alpha$  of the cats. The Ramsey fringe visibility as a function of  $\Delta\alpha^2 t_{res}$  is shown in Fig. 8.3. Again, the fringe visibility is exponential in  $\Delta\alpha^2$ : the visibility decays as  $e^{-\gamma\Delta\alpha^2 t_{res}}$ . The decay constant, obtained by fitting a straight line to the scaled data, is  $\gamma = 6.7 \times 10^{-3}/\mu\text{s}$ , which is consistent with the heating rates in the linear trap (see Sec. 5.5 or Ref. [45]).

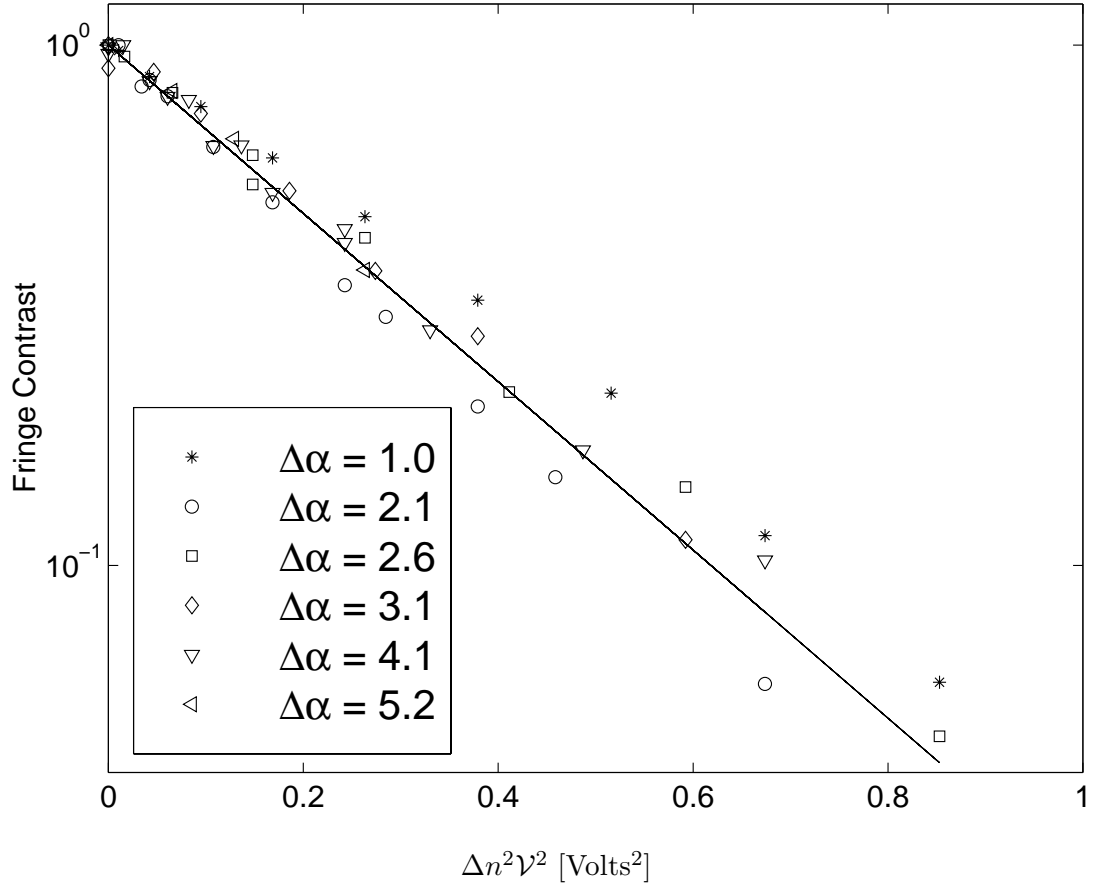


Figure 8.2: “Ramsey” fringe contrast as a function of coupling strength to an amplitude reservoir. The  $x$ -axis is in terms of the square of the rms voltage  $\mathcal{V}$  applied to the trap electrodes, scaled by  $|\Delta\alpha|^2$  (the square of the “size” of the superposition state), and the fringe contrast is normalized to unity at  $\mathcal{V} = 0$ . The solid line is a one-parameter (slope) fit to an exponential, constrained to be unity at  $\mathcal{V} = 0$ .

#### 8.4 Engineered $T=0$ Reservoir

The  $T = 0$  limit of the thermal reservoir (amplitude coupling) is not straightforward to realize with noisy, classical electric fields (which may always be expressed as an equivalent Johnson noise in a resistor at finite temperature  $T$  [114]). However, we do have ready access to a  $T = 0$  reservoir in the form of laser cooling (see Ch. 5). This connection was first pointed out by Poyatos, Cirac, and Zoller [197]. In this case, the coupling is between the laser beams (representing a  $T = 0$  reservoir) and the ion

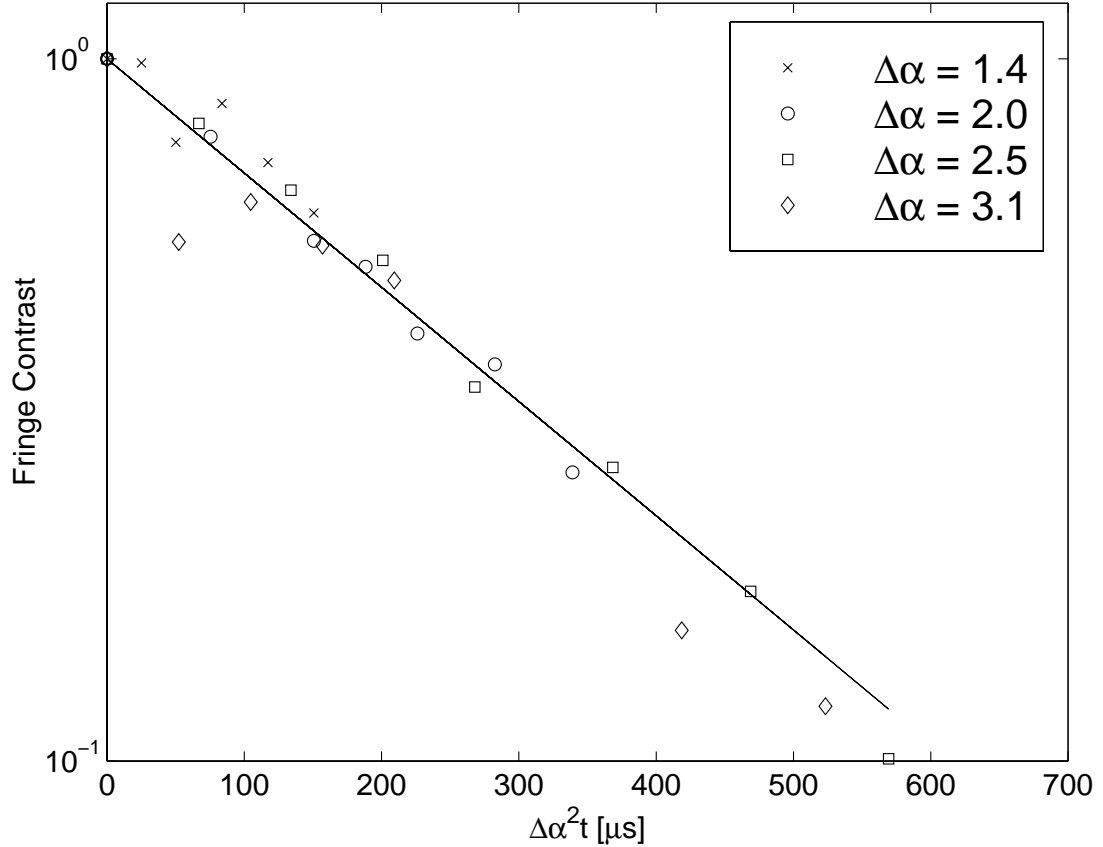


Figure 8.3: “Ramsey” fringe contrast as a function of interaction time with the “natural” amplitude reservoir due to the background heating rate in the trap. The  $x$ -axis is in terms of the interaction time  $t$ , scaled by  $|\Delta\alpha|^2$  (the square of the “size” of the superposition state, and the fringe contrast is normalized to unity at  $t = 0$ ). The solid line is a one-parameter (slope) fit to an exponential, constrained to be unity at  $t = 0$ .

motion [197]. The dissipation is due to the inherently random nature of the spontaneous emission during the recycling process. In interacting with the zero-temperature reservoir, the ion relaxes into a “dark state:” the state  $|n = 0\rangle$ , which is unaffected by the reservoir coupling. The complete reservoir interaction consists of a coherent part, which transfers the spin population from  $|\downarrow\rangle$  to  $|\uparrow\rangle$  while coherently reducing the phonon number, and an incoherent repumping from  $|\uparrow\rangle$  to  $|\downarrow\rangle$  (in this case, through the  $2p^2P_{1/2}$  level<sup>8</sup>).

<sup>8</sup> These experiments were performed with the the repumper laser resonant with transitions to the  $2p^2P_{1/2}$  level, as discussed in Sec. 4.1.3.

The decoherence of cat states into an ambient,  $T \approx 0$  reservoir has been observed before, in a Cavity-QED system [198]. However, in our case, we had the ability to “engineer” the characteristics of the reservoir interaction. By changing the relative intensities of the red sideband Raman beams and the repumping beam (the red doppler), we could change the ratio of the coherent to the incoherent pump rates. This was possible because (in contrast to the original proposal) our system actually consisted of three electronic levels:  $|\downarrow\rangle$ ,  $|\uparrow\rangle$ , and the  $2p\ ^2P_{1/2}$ . The decay rate  $\gamma$  from the  $2p\ ^2P_{1/2}$  level was much larger ( $\approx 20$  MHz) than the Rabi frequency of the  $|\uparrow\rangle \rightarrow 2p\ ^2P_{1/2}$  transition ( $\ll 1$  MHz) so that the decay from this level could be considered instantaneous. The “bottleneck” in the population transfer was thus the Rabi frequency of the repumping beam and, by varying this beam’s intensity, the ratio of coherent to incoherent pump rates could be varied. To wit, the effective decay rate of  $|\uparrow\rangle$  was given by [199]  $\Gamma = \Omega_p^2/\gamma$ , where  $\Omega_p$  was the Red Doppler (single-photon) Rabi frequency.<sup>9</sup>

In order to monitor the effects of the  $T = 0$  reservoir on the motional *populations*, we created the state  $|\psi\rangle = |\downarrow, 2\rangle$ , then applied the  $T = 0$  reservoir for a varying amount of time. Fig. 8.4 shows the motional level populations for  $n = 0, 1, 2$  (as extracted from blue sideband flopping curves) after application of the  $T = 0$  reservoir for various times  $t_{res}$ . As expected, the population in  $|n = 2\rangle$  falls monotonically to zero. The population in  $|n = 1\rangle$  initially grows from 0 as the  $|n = 2\rangle$  population trickles down into it, but then it, too, is cleared out. Eventually, all the population ends up in  $|n = 0\rangle$ .

To determine the effects of the  $T = 0$  reservoir upon the motional *coherences*, we produced the state  $|\psi\rangle_i = |\downarrow\rangle(|0\rangle + |2\rangle)/\sqrt{2}$  in the manner described above (Sec. 8.2), then applied the  $T = 0$  reservoir for a varying amount of time. We monitored the coherence (off-diagonal density matrix element)  $\rho_{20} \equiv \rho_{\{\downarrow,2\}\{\downarrow,0\}}$ . In order to determine the expected behaviour of this density matrix element, we may treat the simpler, two-level system originally proposed by Poyatos, Cirac, and Zoller [197]. However, in light

---

<sup>9</sup> This formula holds when  $\Omega_p \ll \gamma$ .

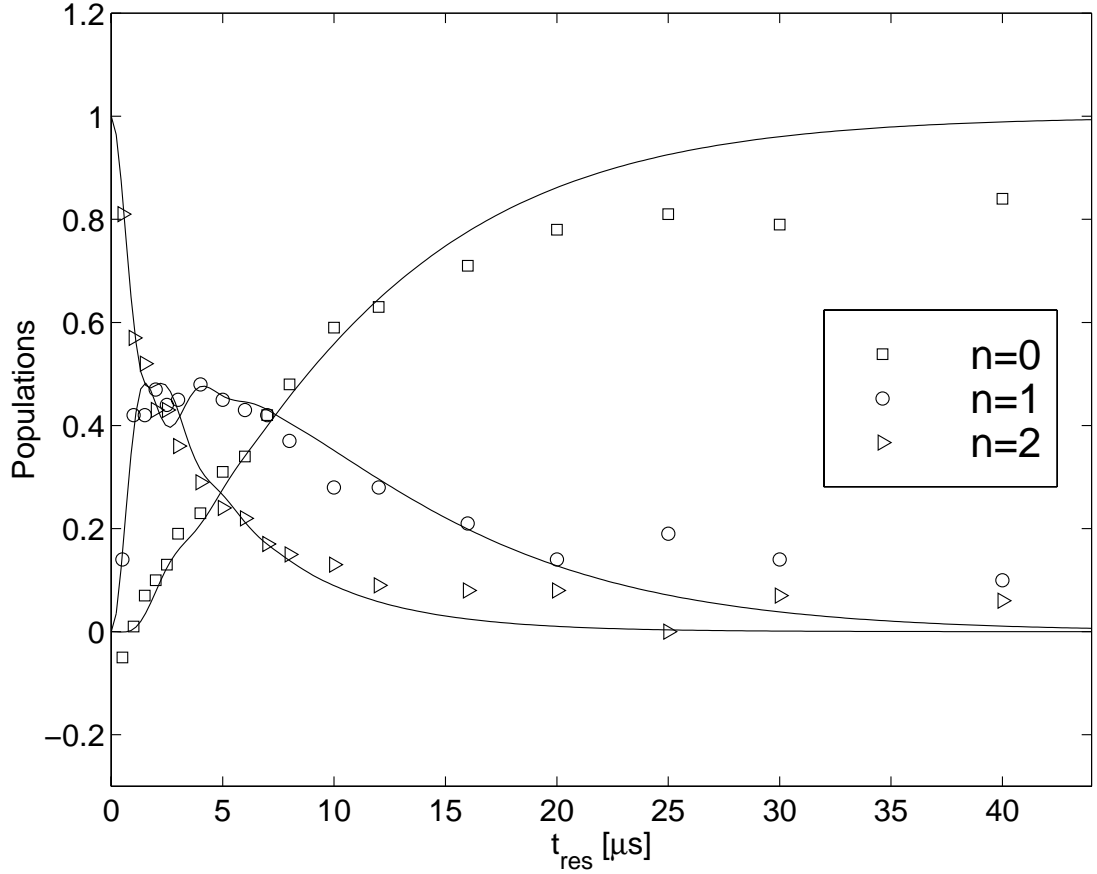


Figure 8.4: Populations of the motional levels  $|0\rangle$ ,  $|1\rangle$ , and  $|2\rangle$  as a function of the reservoir interaction time, for an initial  $|\downarrow, 2\rangle$  state. The solid lines are fits to data of the master equation solutions.

of the above discussion, the incoherent pump rate,  $\Gamma = \Omega_p^2/\gamma$ , should be considered as a controllable parameter. The level scheme is sketched out in Fig. 8.5.

The correspondence between this level scheme and the  $T = 0$  motional reservoir is worked out in Ref. [197]. However, in order to predict the results of the experiment, we may consider the master equation appropriate to the situation illustrated in Fig. 8.5(b). This master equation is:

$$\dot{\hat{\rho}} = i[\hat{\rho}, \hat{H}_S] + \frac{\Gamma}{2}(2\hat{\sigma}_- \hat{\rho} \hat{\sigma}_+ - \hat{\sigma}_+ \hat{\sigma}_- \hat{\rho} - \hat{\rho} \hat{\sigma}_- \hat{\sigma}_+), \quad (8.40)$$

where the red sideband coherent coupling Hamiltonian is given by

$$\hat{H}_S = g(\hat{a}^\dagger \hat{\sigma}_- + \hat{a} \hat{\sigma}_+), \quad (8.41)$$

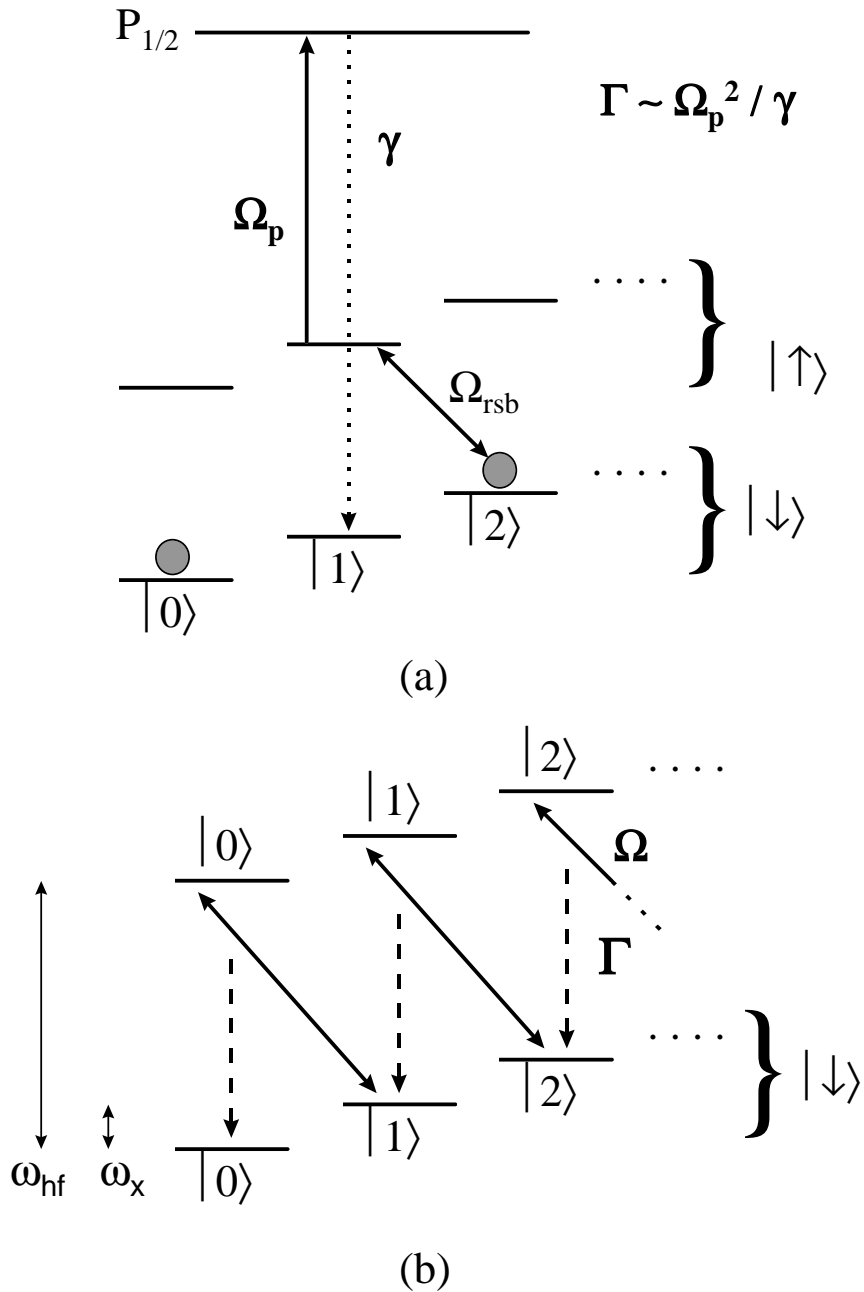


Figure 8.5: (a) Level scheme for realizing an engineered  $T = 0$  amplitude reservoir.  $|\downarrow, n\rangle$  and  $|\uparrow, n-1\rangle$  are coupled on the red sideband, with Rabi frequency  $\Omega_{rsb}$ . Repumping to  $|\downarrow\rangle$  is accomplished by coupling  $|\uparrow\rangle$  to the  $2p \ ^2P_{1/2}$  level through a single-photon transition (Rabi frequency  $\Omega_p$ ) (driven by the “repumping” Red Doppler laser), from where it decays back to  $|\downarrow\rangle$  at rate  $\gamma$ . The effective incoherent pump rate (for  $\Omega_p \ll \gamma$ ) is  $\Gamma = \Omega_p^2 / \gamma$ . This scheme is essentially Raman cooling. (b) Effective two-level system equivalent to the scheme in (a). The coherent transfer rate is  $\Omega = \Omega_{rsb}$  and the effective incoherent pump rate is  $\Gamma = \Omega_p^2 / \gamma$ .

where, from Eq. (3.7),  $g = i\eta\hbar\Omega e^{i\phi}$ . It is not hard to use Eq. 8.40 to find:

$$\dot{\rho}_{\{\downarrow 2\}\{\downarrow 0\}} = -i\sqrt{2}g\rho_{\{\uparrow 1\}\{\downarrow 0\}} \quad (8.42)$$

$$\dot{\rho}_{\{\uparrow 1\}\{\downarrow 0\}} = -i\sqrt{2}g\rho_{\{\downarrow 2\}\{\downarrow 0\}} - \frac{\Gamma}{2}\rho_{\{\uparrow 1\}\{\downarrow 0\}}. \quad (8.43)$$

The solution to this set of differential equations (given the initial state  $|\psi\rangle_i$ ) is

$$\rho_{\{\uparrow 1\}\{\downarrow 0\}} = \frac{-i\sqrt{2}g}{2(\lambda_+ - \lambda_-)} \left[ e^{\lambda_+ t} - e^{\lambda_- t} \right] \quad (8.44)$$

$$\rho_{\{\downarrow 2\}\{\downarrow 0\}} = \frac{1}{2(\lambda_+ - \lambda_-)} \left[ \left( \lambda_+ + \frac{\Gamma}{2} \right) e^{\lambda_+ t} - \left( \lambda_- + \frac{\Gamma}{2} \right) e^{\lambda_- t} \right], \quad (8.45)$$

with

$$\lambda_{\pm} = -\frac{\Gamma}{4} \pm \frac{1}{2} \sqrt{\frac{\Gamma^2}{4} - 8g^2}. \quad (8.46)$$

Again, in the experiment, we monitor  $\rho_{\{\downarrow 2\}\{\downarrow 0\}} \equiv \rho_{20}$ .

Consider two limiting cases. In the first,  $g \gg \Gamma$ , so that the  $\lambda_{\pm}$  have an imaginary part. Here we expect an exponentially decaying cosine, which is precisely what we get:

$$\rho_{20} \rightarrow \frac{e^{-\Gamma/4t}}{2} \cos(\sqrt{2}gt). \quad (8.47)$$

In the limit  $\Gamma \rightarrow 0$ , the time dependence of  $\rho_{20}$  is sinusoidal. This reflects the fact that the red sideband drives Rabi oscillations between  $|\downarrow, 2\rangle$  and  $|\uparrow, 1\rangle$  which causes the density matrix element  $\rho_{20}$  to oscillate as the population in  $|\downarrow, 2\rangle$  is driven out of that level.

In the second case  $g \ll \Gamma$ , so that  $\lambda_{\pm}$  is strictly real. In this case, it is easy to show that:

$$\rho_{20} \rightarrow \frac{1}{2}, \quad (8.48)$$

which is its initial value: the coherence never decays. This is an example of the quantum Zeno effect [59]. Before this regime is reached, the coherence exhibits exponential decay of the contrast with an extremely slow decay rate.

Figure 8.6 shows  $\rho_{20}$  (the Ramsey fringe contrast) as a function of  $t_{res}$ , for two different values of  $\Omega_p$ . For small  $\Omega_p$ , the Rabi flopping behaviour discussed above is

evident whereas, for larger incoherent pump rates (large  $\Omega_p$ ), the behaviour becomes more exponential in character. An interesting effect is that, for  $\Gamma = \Omega_p^2/\gamma > \Omega_{rsb}$ , the decay actually slows down with respect to the  $\Gamma < \Omega_{rsb}$  case: this is an example of the quantum Zeno effect [59]. The initial slope of this curve is close to zero: this is an effect of non-exponential decay [200]. Another way to look at these effects is that, by changing the effective incoherent pump rate  $\Gamma$ , we were actually changing the effective bandwidth of the reservoir. In this sense, we were able to engineer the reservoir characteristics as desired.

## 8.5 Squeezed Reservoir

The Raman beams, in combination with an incoherent repumper, may also be used [197] to simulate a so-called “squeezed reservoir” interaction [124]:

$$\begin{aligned} \dot{\hat{\rho}}' = & \kappa \left[ 2(\mu\hat{a} + \nu\hat{a}^\dagger)\hat{\rho}'(\mu\hat{a} + \nu\hat{a}^\dagger)^\dagger \right. \\ & \left. - (\mu\hat{a} + \nu\hat{a}^\dagger)^\dagger(\mu\hat{a} + \nu\hat{a}^\dagger)\hat{\rho}' - \hat{\rho}'(\mu\hat{a} + \nu\hat{a}^\dagger)^\dagger(\mu\hat{a} + \nu\hat{a}^\dagger) \right], \end{aligned} \quad (8.49)$$

where  $\mu^2 - \nu^2 = 1$ . In order to realize such an interaction, the Raman beams must simultaneously be resonant with both the red and blue sidebands [197]. In this case, the ratio of the Rabi frequencies on the red and blue sidebands is given by  $\mu/\nu$ .

This interaction is actually quite analogous to the  $T = 0$  reservoir: the only difference is that, in this case, the dark state of the interaction is a squeezed state, rather than the  $|n = 0\rangle$  Fock/coherent state. In both cases, the entropy of the ion’s motional state is reduced, and changes from that of a mixed state to that of a pure state. The only difference is the particular pure state to which the ion relaxes (i.e. the dark state of the interaction).

We illuminated the ion simultaneously with the red and blue sidebands by replacing the usual Red Raman switch AOM by two AOMs (one whose drive rf was at frequency  $80 \text{ MHz} - \omega_z$  and the other’s at  $80 \text{ MHz} + \omega_z$ ), then combining the two beams

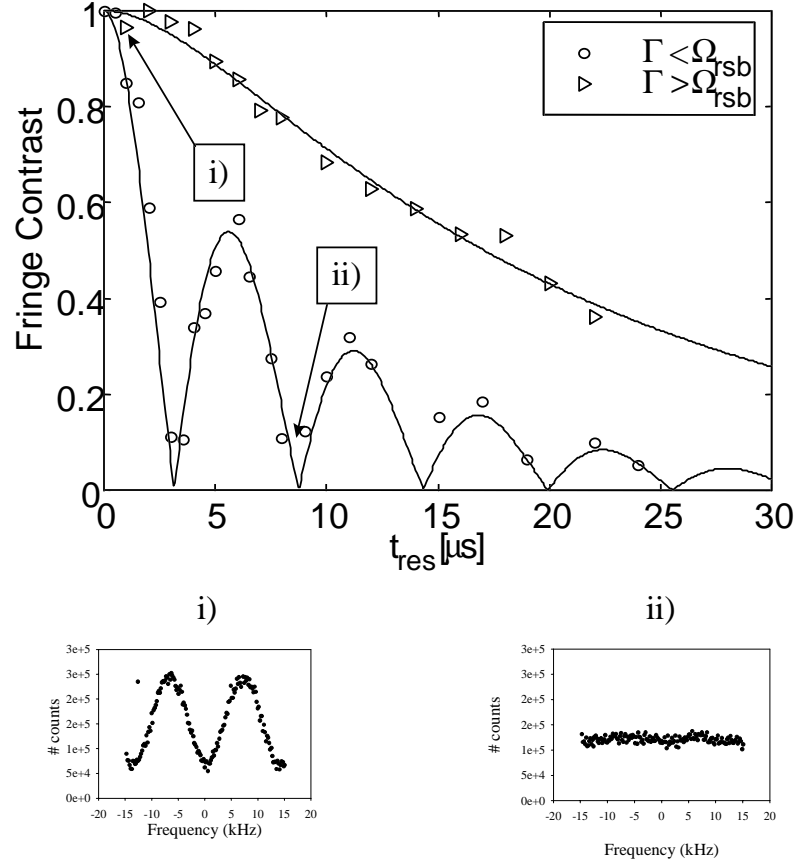


Figure 8.6: Evolution of the coherence  $\rho_{02}$  for an initial  $|\downarrow\rangle(|0\rangle + |2\rangle)/2^{1/2}$  state, as a function of the interaction time  $t_{res}$  with an engineered  $T = 0$  reservoir. Two cases are shown, indicating the two regimes of behaviour: one where the incoherent pump rate is greater than the coherent rate, and one where the opposite is true. Notice that, for the case  $\Gamma > \Omega_{rsb}$ , the decay is actually slower. This is consistent with the predicted dynamics (Eq. (8.45)), and represents a Zeno effect. The low slope near  $t_{res} = 0$  indicates non-exponential decay.

on a beamsplitter before the input lens to the trap. However, since the underlying process behind the squeezed reservoir interaction is a squeezing process, the interaction is of order  $\eta^2$ , and thus slow. At the time we tried the experiments, the heating rate in the trap overwhelmed the “cooling” rate of the squeezed reservoir interaction, preventing us from observing the effects of the reservoir.

## Chapter 9

### SU(1,1) Berry's Phase with Trapped Ions

The time evolution of a quantum system is, of course, completely described by the Schrödinger equation. However, often it is desirable to obtain some sort of intuitive feel for how a given quantum system will evolve under a specified Hamiltonian without having to completely solve the Schrödinger equation. At other times, we may wish to determine how changes in some parameter of the Hamiltonian will effect the time evolution. In such cases, an intuitive understanding of the time evolution is often necessary.

It came as somewhat of a surprise therefore when, in 1984, Berry discovered a rather counter-intuitive phase factor [201, 202] in a rather simple system: one undergoing adiabatic time evolution. This phase factor, and its generalizations, became known as “Berry’s phase.” It was first observed in 1986 [203], in the rotation of polarization of a (classical) light field in a twisted fibre. In this chapter, I will discuss a particular example of a so-called “quantum Berry’s phase” [204, 205, 206, 207] which should be observable in the motion of a trapped ion subject to squeezing operations (see Sec. 6.1.4). I will start out by describing Berry’s original observation and the subsequent generalizations of his work. Then, I will use a more modern approach to describe a Berry’s phase in a simple system: a spin-1/2 particle in a magnetic field. Finally, I will use the language which has been developed in the early part of the chapter to describe the Berry’s phase due to squeezings, and a possible future experimental implementation of the measurement.

## 9.1 Berry's Phase

In order to understand the historical context in which Berry's phase arose, let us consider, as he did, a quantum system in an eigenstate of its Hamiltonian:  $\hat{H}|\phi_n\rangle = E_n|\phi_n\rangle$ . If  $\hat{H}$  is slowly changed<sup>1</sup> then, according to the adiabatic theorem [208], the system remains in the  $n^{\text{th}}$  eigenstate of the slowly-changing Hamiltonian  $\hat{H}(t)$ . If we change the Hamiltonian so that at time  $\tau$  it returns to its initial form,  $\hat{H}(\tau) = \hat{H}(t=0)$ , it follows that the system must return to the state described by  $|\phi_n\rangle$ : that is, the system must return to its initial state. However, state vectors are arbitrary up to a phase factor of modulus unity. So in general, under the course of the system's evolution, we must write  $|\phi_n\rangle \rightarrow e^{i\theta}|\phi_n\rangle$ , where  $\theta$  is some phase. Indeed, we may express the state of the system at time  $\tau$  as:

$$|\psi_n(\tau)\rangle = e^{-\frac{i}{\hbar} \int_0^\tau E_n(t') dt'} e^{i\gamma_n(\tau)} |\phi_n\rangle. \quad (9.1)$$

The first exponential is simply the usual dynamical phase induced in the eigenstate through the time evolution operator: the time integral merely reflects the fact that the  $n^{\text{th}}$  eigenstate's energy may be (and probably is) time dependent as we vary the Hamiltonian. This is the phase factor which we would first think to write down in describing the dynamics of the system. The second phase factor,  $\gamma_n(\tau)$ , accounts for any "unexpected" phases which may crop up in the situation described: as we shall see (and as Berry first pointed out), this term is generally nonzero.

At any point in the system's evolution, we may write an equation similar to Eq. (9.1):

$$|\psi_n(t)\rangle = e^{-\frac{i}{\hbar} \int_0^t E_n(t') dt'} e^{i\gamma_n(t)} |\phi_n(t)\rangle. \quad (9.2)$$

where  $|\phi_n(t)\rangle$  is the  $n^{\text{th}}$  eigenstate of  $\hat{H}(t)$ . From the Schrödinger equation, we have that

$$i\hbar \frac{\partial |\psi_n(t)\rangle}{\partial t} = E_n(t) |\psi_n(t)\rangle. \quad (9.3)$$

---

<sup>1</sup> For example, in a magnetic system, we might slowly change the direction of the magnetic field.

Thus, writing  $\xi_n(t) = -(1/\hbar) \int_0^t E_n(t') dt'$ , differentiating Eq. (9.2), and plugging into the Schrödinger equation, we obtain:

$$i\hbar \left[ -\frac{i}{\hbar} E_n(t) e^{i\xi_n(t)} e^{i\gamma_n(t)} |\psi_n(t)\rangle + i e^{i\xi_n(t)} e^{i\gamma_n(t)} \frac{d\gamma_n(t)}{dt} |\psi_n(t)\rangle + e^{i\xi_n(t)} e^{i\gamma_n(t)} \frac{\partial}{\partial t} |\psi_n(t)\rangle \right] = e^{i\xi_n(t)} e^{i\gamma_n(t)} E_n |\psi_n(t)\rangle, \quad (9.4)$$

or,

$$\frac{\partial}{\partial t} |\psi_n(t)\rangle + i \frac{d\gamma_n(t)}{dt} |\psi_n(t)\rangle = 0. \quad (9.5)$$

Multiplying on the left by  $\langle \psi_n(t) |$ , we finally have:

$$\frac{d\gamma_n(t)}{dt} = i \langle \psi_n(t) | \frac{\partial}{\partial t} |\psi_n(t)\rangle. \quad (9.6)$$

so that, in changing the Hamiltonian adiabatically from its initial configuration and then returning it to that initial configuration (for which  $\gamma_n(0) = 0$ , by definition), we have:

$$\gamma_n(\tau) = i \int_0^\tau \langle \psi_n(t) | \frac{\partial}{\partial t} |\psi_n(t)\rangle dt. \quad (9.7)$$

Now suppose that the time dependence of the Hamiltonian arises because we are changing some parameter or parameters  $\mathcal{R}$  with time. In this case, we may re-express Eq. (9.7) as:

$$\begin{aligned} \gamma_n(\tau) &= i \int_0^\tau \langle \psi_n | \frac{\partial}{\partial t} |\psi_n\rangle dt \\ &= i \int_{\mathcal{R}_0}^{\mathcal{R}_f} \langle \psi_n(\mathcal{R}) | \nabla_{\mathcal{R}} \psi_n(\mathcal{R}) \rangle d\mathcal{R}, \end{aligned} \quad (9.8)$$

which was Berry's result. By applying Stokes' theorem to the integral of the divergence, Berry pointed out that the phase factor  $\gamma_n$  could be interpreted as a surface integral over the closed loop in parameter space traced out by the Hamiltonian in the course of its evolution. From these considerations, it becomes apparent that the phase depends *only on the path taken* in the configuration space of the parameters  $\mathcal{R}$ .<sup>2</sup> So this phase does

---

<sup>2</sup> This implies that if the Hamiltonian depends only on one parameter, then the Berry's phase vanishes, since the integral always vanishes in the one-dimensional case: the curve subtends no area.

not depend, for example, on the amount of time taken to return these parameters to their original values. This is in stark contrast to the dynamical phase, which is explicitly time-dependent. In this sense, the Berry's phase is "surprising" [201].

It is interesting to note that the Aharonov-Bohm effect [209] may be interpreted as a Berry's phase [201]. Also, the properties of a spin in a slowly-varying magnetic field may be interpreted in a similar way [201]. In particular, evaluating Berry's phase for the case in which the spin-1/2 particle adiabatically follows a magnetic field which is rotated in its direction by  $2\pi$  shows that the state vector for the spin-1/2 particle picks up a phase factor of -1 during this effective  $2\pi$ -rotation of the particle: this is an example of the well-known behaviour of fermions under rotations.

As might be expected from the above remarks, Berry's treatment may be generalized, and treated in a purely geometric manner. Some of the first steps in this generalization were made by Aharonov, Anandan, and Stodolsky [210, 211, 212]. They removed the requirement of adiabaticity in the change of the Hamiltonian, and showed that even in this case, the phase factor could be interpreted purely in terms of the inherent geometry underlying the changes in the Hamiltonian. As interest in Berry's phase (now also frequently called the "geometric phase") grew, a clearer picture of the situation arose, and a more concise language for describing the physics was developed. An overview of the geometric phase, and a "grammar" of the language, is given by Jordan [213]. In the next section, I will use this modern formulation to describe a canonical example of a geometric phase: the behaviour of a spin-1/2 particle in a magnetic field. Hopefully, this example will clarify the situation, and set the stage for discussing the geometric phase induced by squeezing operations.

It is worth noting that, after Berry's paper came out and the geometric interpretation of his result became apparent, it was pointed out that similar results existed in classical systems: in particular, the connection was drawn [214] with Panchatnaram's phase in classical polarization optics [215] and with the Hannay angle of classical me-

chanics [216, 217]. In general, such phase angles arise whenever a system’s dynamics are constrained in a non-trivial, “geometric” fashion. Such angles are examples of *anholonomies* [218]. A simple example may help to define the word. Consider a set of Cartesian coordinate axes constrained to move on the surface of a sphere, such that the  $z$ -axis is initially pointing in the direction of the north pole. Now, suppose that we translate the axes along the sphere in a parallel-transport fashion (such that we never explicitly rotate the coordinate axes about the  $z$ -direction). If we eventually bring the coordinate frame back to the north pole then, although we have *never* rotated the frame about the normal axis to the sphere, we will find that the coordinate system has undergone a net rotation about this axis! (One may try this out, using an imaginary sphere and one’s fingers as the coordinate frame — provided one is careful not to injure one’s self!) The reason for this rotation is that the coordinate frame is constrained to move on an inherently curved surface: the surface of a sphere. The rotation of a coordinate frame upon completion of a closed circuit on a curved surface is called “anholonomy.”

Of course, as the example indicates, anholonomy effects exist in classical physics. The difference with quantum systems is that quantum systems may exhibit superposition and interference effects. Such effects are phase-sensitive. So, in a single-particle quantum system, the Berry’s phase may have physical effects.

## 9.2 An Example: a Spin-1/2 Particle in a Magnetic Field

In order to introduce the terminology which I will later use to discuss the geometric phase induced by squeeze operators, let us consider a situation which may be somewhat more familiar to atomic physicists: the case of a spin-1/2 particle in a magnetic field. Of course, the time evolution in such a system may be described by the Schrödinger equation or the Bloch equations: such solutions are well known. However, here I will introduce another point of view which distinguishes the “geometric” phase

from “dynamical” phases. This will highlight the different types of evolution inherent in the dynamics. Furthermore, the language I will use is applicable to other, more complicated quantum systems.

Let the magnetic field  $\mathbf{B}(t)$  initially lie along the  $z$ -direction:  $\mathbf{B}(t = 0) = B\mathbf{e}_z$ . Thus, the initial Hamiltonian is given by

$$\hat{H}(t = 0) = -\mu_B \mathbf{B}(0) \cdot \hat{\mathbf{S}} = -\mu_B B \hat{S}_3, \quad (9.9)$$

where (as in Ch. 3),  $\hat{S}_3 = \frac{1}{2}\hbar\hat{\sigma}_3$  is the spin angular momentum operator in for the  $3 \equiv z$  direction.<sup>3</sup> Assume that the particle initially starts out in an eigenstate of  $\hat{S}_z$ . The question is then to determine what happens to the particle if the direction of the  $B$ -field is then rotated in some matter such that, at time  $t = \tau$ , the field again lines up with the  $z$ -axis.

It is somewhat easier conceptually to consider the problem in the Heisenberg picture. In particular, as we shall see, this picture admits a geometric interpretation not only of the phase, but also of the various physical observables of the system and their inter-relationship with the geometric phase. In the Heisenberg picture, the state vector remains constant while the operators evolve in time, according to:

$$\dot{\hat{O}} = -\frac{i}{\hbar}[\hat{H}, \hat{O}], \quad (9.10)$$

which is the Heisenberg equation of motion. So in order to track the changes in physical observables of an initial eigenstate of  $\hat{S}_3$  as the magnetic field is rotated, it suffices to see what happens to the operator  $\hat{S}_3$ .

The idea, then, is that we start out with the operator  $\hat{S}(t = 0) = \hat{S}(0) = \hat{S}_3 \propto \hat{H}(t = 0)$ , and apply unitary transformations  $\hat{U}(t)$  to this operator. The unitary trans-

---

<sup>3</sup> Note that I am continuing to use the notation  $\hat{S}_1, \hat{S}_2, \hat{S}_3$  as I did in Ch. 3. This is an attempt to avoid confusion with the standard use in the rest of this thesis of  $x, y,$  and  $z$  as principal directions in the trap. Of course, here there *is* a physical correspondence between the Pauli operators and physical directions:  $1 \leftrightarrow x, 2 \leftrightarrow y,$  and  $3 \leftrightarrow z$ .

formations are generated by operators which I will label  $\hat{G}(t)$ , so that:

$$i\frac{d}{dt}\hat{U}(t) = \hat{G}(t)\hat{U}(t). \quad (9.11)$$

The change in the original operator  $\hat{S}(0) = \hat{S}_3$  is then given by:

$$\hat{S}(0) \longrightarrow \hat{S}(t) = \hat{U}(t)\hat{S}(0)\hat{U}^\dagger(t). \quad (9.12)$$

In our case, we will consider rotations of the magnetic field  $\mathbf{B}$  away from the  $z$ -direction. These rotations are described by unitary operators  $\hat{U}(t)$ , and the generators of the unitary operators are just the angular momentum operators  $\hat{S}_1$ ,  $\hat{S}_2$ , and  $\hat{S}_3$ <sup>4</sup>, satisfying the usual commutation relations:

$$[\hat{S}_i, \hat{S}_j] = i\varepsilon_{ijk}\hat{S}_k. \quad (9.13)$$

So, in our situation, the operators  $\hat{G}(t)$  are the spin-1/2 angular momentum operators (and combinations of them). The unitary rotation operator,  $\hat{U}(t)$ , then generically will be of the form:

$$\hat{U}(t) = e^{i\mathbf{n}(t)\cdot\mathbf{S}} = e^{n_1(t)S_1+n_2(t)S_2+n_3(t)S_3}, \quad (9.14)$$

which is just the general expression for a rotation operator operating in the angular momentum 1/2 manifold [219].

Now, the rotation operators form a group: the rotation group. The defining property of this group is that it preserves the dot product, and hence the norm. So, for example, if rotation operators act upon a vector  $\mathbf{v} = v_1\mathbf{e}_1 + v_2\mathbf{e}_2 + v_3\mathbf{e}_3$ , then the length of the vector does not change:  $|\mathbf{v}|^2 = (v_1)^2 + (v_2)^2 + (v_3)^2 = \text{const}$ . The generators (the  $\hat{S}_i$ ) of the rotation group form a Lie algebra: in our case, the Lie algebra SU(2) of the Pauli matrices. But there is a very intimate relationship between Lie algebras and (non-Euclidean) geometry. This should not be too surprising: the Lie algebra gives the mathematical properties of infinitesimal changes under the action of some group

---

<sup>4</sup> which also happens to be our  $\hat{A}(0)$

when acting upon vectors, and so should give the “allowable” changes in the vectors with that group — in other words, a geometry. In any event, this implicit geometry will give us a picture of the various changes in phase under the action of the changing spin Hamiltonian. In this case, the picture is just another way of obtaining the Bloch sphere.

The rotation group causes rotations of vectors in any vector space, of any dimension, upon which it operates (for example, in quantum mechanics, one has the various manifolds for different values of the angular momentum). But there is one special vector space associated with the rotation group. This “special” vector space is that spanned by the three generators of the rotation group: the generators form an algebra, and an algebra is a particular example of a vector space [220]. So, although there are many different representations of the rotation group [221], the one obtained by considering a vector space whose dimension is equal to the number of group generators is special: this representation gives us the geometry associated with that group. I will now sketch out how this occurs.

Consider the operators  $\hat{S}_i$  as vectors in a three-dimensional vector space. These three vectors form a basis for that vector space: that is, any general vector may be expressed as:

$$\hat{S} = s_1\hat{S}_1 + s_2\hat{S}_2 + s_3\hat{S}_3. \quad (9.15)$$

We may construct a geometry in this vector space by examining the commutation relations, Eq. (9.13). In the language of Lie algebras, the  $\varepsilon_{ijk}$  are known as the *structure constants* of the Lie algebra [222], and these structure constants carry with them geometrical information. For example, let  $\hat{S}_a = \sum(s_a)_j\hat{S}_j$  and  $\hat{S}_b = \sum(s_b)_j\hat{S}_j$  be two vectors in our vector space. Then it is easy to verify that

$$[\hat{S}_a, \hat{S}_b] = s_1\hat{S}_1 + s_2\hat{S}_2 + s_3\hat{S}_3, \quad (9.16)$$

where

$$s_k = (s_a)_i (s_b)_j \varepsilon_{ijk} \quad (9.17)$$

(using the Einstein summation convention). This expression is identical to the usual component expansion of the vector cross product! So there is an equivalence between the commutator and a vector cross product in the vector space:

$$[\hat{S}_a, \hat{S}_b] \longleftrightarrow \hat{S}_a \times \hat{S}_b, \quad (9.18)$$

The “cross product” is induced by the structure constants of the Lie algebra (in this case, the usual Levi-Civita symbol,  $\varepsilon_{ijk}$ ).

Thus, the structure constants, the Levi-Civita symbol, induce a vector product (or, more generally, an “exterior product”) upon the vector space. The geometric implications of the Levi-Civita symbol goes further. A Lie algebra result [222] shows that this set of structure constants also induces a dot product (or “inner product”) upon the vector space, according to:

$$\hat{S}_a \cdot \hat{S}_b = (S_a)_i (S_b)_j \delta_{ij} \quad (9.19)$$

$$\delta_{ij} = -\frac{1}{2} \varepsilon_{ikl} \varepsilon_{jlk}. \quad (9.20)$$

For the rotation group,  $\delta_{ij}$  is just the usual Kronecker delta which is associated with the usual dot product.

From this, we see that the geometry induced by the group of rigid rotations upon the vector space of the Lie algebra of the group generators is just the usual Euclidean geometry which we associate with real, three-dimensional space. This is not terribly surprising: rotations are one part of the “Galilean” group of symmetries of regular, three-dimensional Euclidean space. In general, however, if we try to apply a similar “geometry-finding” procedure to other groups and their generators, the geometry which we’ll find will *not* be Euclidean. In particular, as we shall see, the group of squeezings will be generated by the Lie algebra  $SU(1,1)$ , and the geometry will be that of Minkowski spaces.

Meanwhile, let us return to our spin-1/2 particle in a magnetic field. We start out in an eigenstate of  $\hat{S}_3$ , and apply a series of rotations. In the Heisenberg picture, we start out with the operator

$$\hat{S}(0) = \hat{S}_3 = 0\hat{S}_1 + 0\hat{S}_2 + 1\hat{S}_3. \quad (9.21)$$

Because rotations preserve the norm of vectors, as the direction of the magnetic field is changed, the spin operator will undergo rotations: however, the norm

$$|\hat{S}(t)|^2 = (s_1)^2 + (s_2)^2 + (s_3)^2 = 1 \quad (9.22)$$

will be preserved (see Fig. 9.1). The vector representing the spin thus moves on the surface of a sphere: the Bloch sphere [124]. So by applying some abstract group theory and Lie algebra results, we have obtained something very familiar to atomic physicists! However, as I have pointed out before, this effort will not be for naught: the language described above will enable us to form a very clear correspondence between the Bloch sphere and the geometric phase. Furthermore, the above language is generalizable, and will enable us to construct “pictures” similar to the Bloch sphere picture for more general groups of unitary transformations. These “pictures” will be useful for the same reason that the Bloch sphere is useful: they enable us to develop an intuitive understanding of complicated system dynamics.

Now, the system Hamiltonian for our spin-1/2 particle is proportional to  $\hat{S}_3$  and the initial state is an eigenstate of this operator. For this reason, the initial Hamiltonian does not cause any movement of the vector on the Bloch sphere but, rather, causes a trivial rotation about the axis of the vector itself. Of course, we can't see the effect of this rotation on the vector. For this reason, it is useful to construct an orthonormal frame on the surface of the Bloch sphere, with the 3-axis normal to the surface, and (for example) the other two axes initially parallel to the 1- and 2-axes ( $x$ - and  $y$ -axes). The effect of the initial Hamiltonian ( $\propto \hat{S}_3$ ) is then to rotate this coordinate frame about its 3-axis.

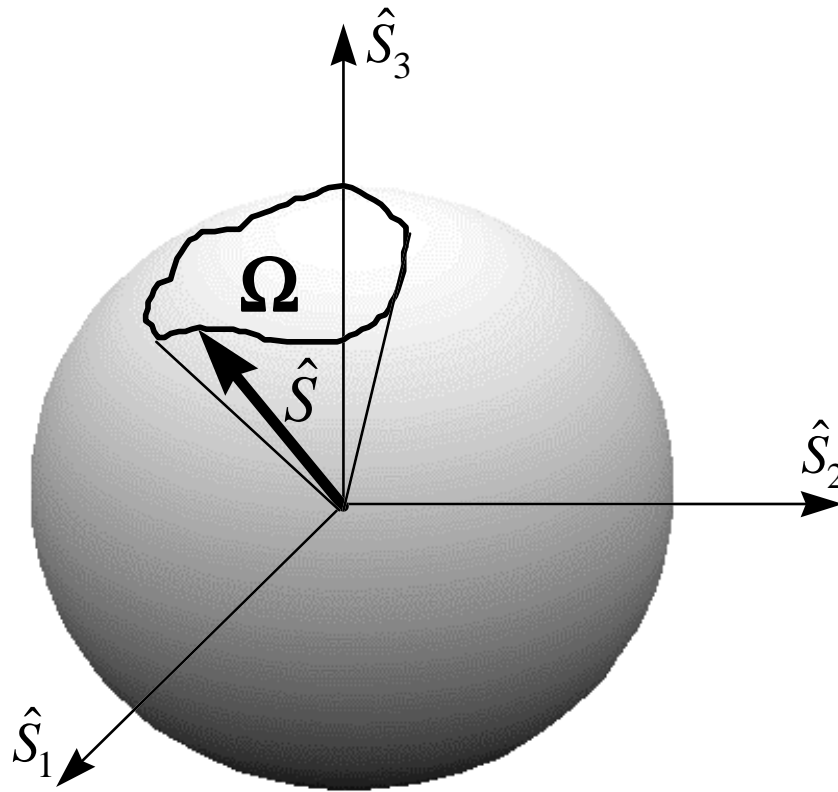


Figure 9.1: Rotations of a spin-1/2 particle in a magnetic field. The group of rotations moves  $\hat{S}_3$  on the surface of a sphere: it preserves the “length” of the vector in the three-dimensional vector space spanned by  $\hat{S}_1$ ,  $\hat{S}_2$ , and  $\hat{S}_3$ . The sphere is just the Bloch sphere.

By looking at the rotation of the coordinate axes tangent to the sphere’s surface (the 1- and 2-axes), we can keep track of the phases: for example, the “dynamical” phase due to  $\hat{U}(t) = e^{-i\hat{H}t/\hbar}$ . More generally, we shall allow the vector representing the state to move about the Bloch sphere, by changing the direction of the magnetic field. At each instant, the magnetic field will cause a rotation about its direction. However, this rotation of the state is, in some sense, trivial: it does not actually move the vector on the sphere. In general, we shall identify as a “dynamical” phase any contribution due to

an explicit rotation about the normal axis to the sphere: i.e. due to any transformation generated by an operator proportional to the vector which is representing the state. The interesting, “geometrical” phase is caused by the inherent curvature of the Bloch sphere. As in the classical, physical example of Sec. 9.1, even if we move the state-representing vector so as to eliminate any dynamical phase contribution (i.e. parallel transport it on the surface of the sphere), there will still be a net rotation of the coordinate frame, and hence a phase, due to this inherent curvature.

Thus, the distinction between dynamical and geometric phases is that the dynamical phase causes a rotation about the instantaneous direction of the vector representing the state (i.e. it is due to the instantaneous Hamiltonian). The geometric phase is the additional phase due to the rotation of coordinate frames as they are parallel-transported around the sphere, caused by the underlying geometry of the group producing the dynamics. This distinction is pointed out, in group theoretical notation and without the “picture” derived above, by Jordan [213]. So, even if the unitary rotations induce purely parallel transport of the vector around the sphere and back to the 3-axis, there can still be a net, geometrical phase, due to the inherent curvature: that is, the “anholonomy.”

To highlight the effects of the geometric phase in the system’s evolution, let us consider the case where the dynamical phase is zero: that is, in the geometric picture, we demand that

$$\hat{G}(t) \cdot \hat{S}(t) = 0. \quad (9.23)$$

From Eqs. (9.11) and (9.12), we have that

$$i \frac{d}{dt} \hat{S}(t) = [\hat{G}(t), \hat{S}(t)] \quad (9.24)$$

which, in the vector picture, can be expressed as:

$$\frac{d}{dt} \hat{S}(t) = \hat{G}(t) \times \hat{S}(t). \quad (9.25)$$

This is just the Bloch equation. In order to calculate the geometrical phase, we need to calculate the net phase in transporting the vector in a closed loop from the north

pole of the sphere back to the north pole. The way to do this is to consider a frame of coordinate axes on the surface of the sphere which moves with the state-representing vector, and to measure how much the  $x$ - and  $y$ -axes rotate in moving this frame around the closed loop. This angle will be the geometric phase.

Calculation of the rotation angle (the anholonomy) is a problem in differential geometry, but the calculation is relatively straightforward. A point on the unit sphere may be described by the triad  $(\sin \theta \cos \phi, \sin \theta \sin \phi, \cos \theta)$ , and we may prescribe a path on the sphere by appropriately specifying the parameters  $\theta$  and  $\phi$ . We may construct a coordinate frame at each point on the sphere by differentiating the  $x$ - and  $y$ -coordinates to obtain two vectors in the tangent plane, then taking the cross product of these two vectors to obtain a normal. Performing this procedure, we obtain:

$$\begin{aligned}\mathbf{f}_1 &= (\sin \theta \cos \phi, \sin \theta \sin \phi, \cos \theta) && \text{(normal vector)} \\ \mathbf{f}_2 &= (\cos \theta \cos \phi, \cos \theta \sin \phi, -\sin \theta) && \text{(direction of increasing } \theta) \\ \mathbf{f}_3 &= (-\sin \phi, \cos \phi, 0) && \text{(direction of increasing } \phi).\end{aligned}\tag{9.26}$$

So the quantity which we wish to measure is the angle  $\omega_{3,2}$  which, for example,  $\mathbf{f}_3$  moves towards  $\mathbf{f}_2$  as we go around the closed loop. From Eqs. (9.26), we have:

$$d\mathbf{f}_3 = (-\cos \phi d\phi, -\sin \phi d\phi, 0)\tag{9.27}$$

so that the desired change is

$$\omega_{3,2} = d\mathbf{f}_3 \cdot \mathbf{f}_2 = -\cos \theta d\phi.\tag{9.28}$$

The total rotation of the coordinate system is then given by the integral of  $\omega_{3,2}$  around the curve, or:

$$\gamma = \int_{\alpha} \omega_{3,2},\tag{9.29}$$

where  $\alpha$  is a parametrization of the closed curve. (Note that  $\omega_{3,2}$  already contains a differential.) In the language of modern differential geometry  $\omega_{3,2}$  is a so-called ‘‘connection one-form’’ [218], and it is a general result of differential geometry that, if  $\Theta$  is

a one-form, then

$$\oint_{\alpha} \Theta = \iint_{\mathcal{S}} d\Theta \quad (9.30)$$

where  $\mathcal{S}$  is the area on the surface enclosed by the closed path  $\alpha$  and  $d\Theta$  is the differential of the one-form  $\Theta$ . This is just the generalization of Stokes' theorem. Another result from differential geometry is that  $d\omega_{3,2} = K \Theta_3 \wedge \Theta_2$  where  $K$  is the Gaussian curvature and  $\Theta_i$  are the unit one-forms (unit differentials) in the  $i^{\text{th}}$  frame direction<sup>5</sup>. For a sphere,  $K$  is equal to the curvature  $1/r^2$  of the sphere. In our case, since we are dealing with the unit sphere,  $K = 1$ . Finally, we can put all this together to obtain:

$$\gamma = \iint_{\mathcal{S}} \sin \theta \, d\theta d\phi, \quad (9.31)$$

which is just the solid angle subtended by the circuit, as seen from the sphere's origin.

In summary, then, the Berry's phase or geometric phase due to circumscribing some path on the sphere which begins and ends on the 3-axis (north pole) of the sphere is just equal to the area on the surface of the sphere. That is, the geometric angle is equal to the solid angle subtended by the path as seen from the origin.

If, as will generally be the case, Eq. (9.23) does *not* hold — that is,  $\hat{G}(t) \cdot \hat{S}(t) \neq 0$  — then the state will also pick up a dynamical phase. This phase is just given by the integral of the component of the generator at each point along the path which is parallel to the state-representing vector at that point. That is, it is given by the integral:

$$\xi = \oint_{\alpha} \hat{G} \cdot \hat{S}. \quad (9.32)$$

### 9.3 SU(1,1) Berry's Phase with Squeeze Operators

Recall from Sec. 6.1.4 that the squeeze operator  $\hat{S}(\epsilon) = \exp[\frac{1}{2}(\epsilon^* \hat{a}^2 - \epsilon (\hat{a}^\dagger)^2)]$  (where  $\epsilon = Re^{2i\phi}$ ) squeezes the uncertainty in one rotated quadrature of the ion's motion and amplifies the uncertainty in the other. A sequence of squeezes can produce an observable geometric phase in a trapped ion's motional state, which I will now

<sup>5</sup>  $\wedge$  is the exterior product (generalized cross product)

discuss. This geometric phase arising from squeezings was first discussed by Chiao and Jordan [206]. However, in order to discuss the geometric phase, it is more convenient to express the squeeze operator using a slightly different notation. Thus, we write:

$$\hat{\mathcal{S}}(r, \theta) = e^{ir(\hat{K}_1 \cos \theta + \hat{K}_2 \sin \theta)}, \quad (9.33)$$

where

$$\hat{K}_1 = -\frac{i}{4}(\hat{a}\hat{a} - \hat{a}^\dagger\hat{a}^\dagger) \quad (9.34)$$

$$\hat{K}_2 = \frac{1}{4}(\hat{a}\hat{a} + \hat{a}^\dagger\hat{a}^\dagger). \quad (9.35)$$

Some algebra allows us to make the connection with the previous notation:

$$r = 2R \quad (9.36)$$

$$\theta = -2\phi. \quad (9.37)$$

Thus, we can see that  $\hat{K}_1$  generates squeezes along the  $z$ -axis of the  $z$ - $p$  plane, and  $\hat{K}_2$  generates squeezes at  $45^\circ$  to the  $z$  and  $p$  axes.  $\hat{K}_1$  and  $\hat{K}_2$  are, in fact, orthogonal to each other in their effect. (It is apparent that squeezes along  $z$  and  $p$  are not orthogonal to each other, since a squeeze along  $z$  is just an “anti-squeeze” along  $p$ .)

Along with

$$\hat{J}_3 = \frac{1}{4}(\hat{a}\hat{a}^\dagger + \hat{a}^\dagger\hat{a}) = \frac{1}{2}\left(\hat{n} + \frac{1}{2}\right), \quad (9.38)$$

$\hat{K}_1$  and  $\hat{K}_2$  form a Lie algebra, the algebra SU(1,1). The commutation relations which characterize this algebra are:

$$[\hat{K}_1, \hat{K}_2] = -i\hat{J}_3, \quad [\hat{K}_2, \hat{J}_3] = i\hat{K}_1, \quad [\hat{J}_3, \hat{K}_1] = i\hat{K}_2, \quad (9.39)$$

which may be written succinctly as

$$[\hat{K}_i, \hat{K}_j] = i\tilde{\varepsilon}_{ijk}\hat{K}_k \quad (9.40)$$

with

$$\tilde{\varepsilon} \doteq (-1)^{\delta_{k,3}}\varepsilon_{ijk}. \quad (9.41)$$

In this last equation, I have written  $\hat{K}_3 \equiv \hat{J}_3$ . This notation is somewhat ambiguous, but the use of  $\hat{J}_3$  is in keeping with the literature. These commutation relations are the same as for the generators of the Minkowski transformations in (2+1) dimensions (special relativity deals with Minkowski transformations in (3+1) dimensions). Thus, the group of transformations generated by these three operators, when acting on a vector  $\mathbf{v} = v_1\mathbf{e}_1 + v_2\mathbf{e}_2 + v_3\mathbf{e}_3$ , preserve the ‘‘Minkowski dot product:’’

$$-(v_1)^2 - (v_2)^2 + (v_3)^2 = \text{const.} \quad (9.42)$$

As with the SU(2) example in the last section, the group generated by the SU(1,1) operators induces a geometry on the Lie algebra, when this algebra is considered as a vector space. Again, the structure constants  $\tilde{\varepsilon}_{ijk}$  provide the means to discover this geometry. So, writing general members of the Lie algebra/vector space as

$$\begin{aligned} \hat{K}_a &= (k_a)_1\hat{K}_1 + (k_a)_2\hat{K}_2 + (k_a)_3\hat{K}_3 \\ \hat{K}_b &= (k_b)_1\hat{K}_1 + (k_b)_2\hat{K}_2 + (k_b)_3\hat{K}_3 \\ \text{etc.} \dots & \end{aligned} \quad (9.43)$$

we have:

$$\begin{aligned} \hat{K}_a \tilde{\times} \hat{K}_b &= \hat{K}_c, \\ (k_c)_m &= (k_a)_l (k_b)_l \tilde{\varepsilon}_{lmn}. \end{aligned} \quad (9.44)$$

and

$$\begin{aligned} \hat{K}_a \tilde{\times} \hat{K}_b &= (K_a)_l (K_b)_m \tilde{\delta}_{lm} \\ \tilde{\delta}_{lm} &= -\frac{1}{2} \tilde{\varepsilon}_{lst} \tilde{\varepsilon}_{mts} \\ &= -\delta_{l,m} (-1)^{\delta_{l,3}}. \end{aligned} \quad (9.45)$$

In this language, the unitary transformations generated by SU(1,1) preserve the norm  $\hat{K} \tilde{\times} \hat{K}$ . This is just another way of expressing Eq. (9.42).

Now consider that we have a harmonic oscillator, and we initially start out in an eigenstate  $|n\rangle$  of that harmonic oscillator. This is also an eigenstate of  $\hat{K}(0) = \hat{J}_3 = \frac{1}{2}\hat{H}$ . If we apply a sequence of unitary transformations generated by  $\hat{K}_1$ ,  $\hat{K}_2$ , and  $\hat{J}_3$ , then, starting with  $\hat{J}_3$ :

$$\hat{K}(0) \longrightarrow \hat{K}(t) = k_1(t)\hat{K}_1 + k_2(t)\hat{K}_2 + k_3(t)\hat{J}_3. \quad (9.46)$$

That is, the unitary transformations take the vector  $\hat{J}_3$  into a linear combination of the basis vectors  $\hat{K}_1$ ,  $\hat{K}_2$ , and  $\hat{J}_3$  of the vector space. Since the unitary operators are generated by the SU(1,1) algebra, we have that, in the course of this evolution:

$$\hat{K}(t)\tilde{\hat{K}}(t) = -k_1(t)^2 - k_2(t)^2 + k_3(t)^2 = 1, \quad (9.47)$$

since we initially have  $-k_1(0)^2 - k_2(0)^2 + k_3(0)^2 = -0^2 - 0^2 + 1^2 = 1$ . So, in the course of the system's evolution, the vector which starts out as  $\hat{J}_3$  (i.e. along the  $k_3$  or  $\hat{J}_3$  axis) moves along the surface of the unit hyperboloid, as shown in Fig. 9.2.

As before, we may describe the time evolution of  $\hat{U}(t)$  and hence of  $\hat{K}(t)$ , given some sequence of generators  $\hat{G}(t) = g_1(t)\hat{K}_1 + g_2(t)\hat{K}_2 + g_3(t)\hat{J}_3$ . We have that

$$\hat{K}(t) = \hat{U}(t)\hat{K}(0)\hat{U}^\dagger(t) = \hat{U}(t)\hat{J}_3\hat{U}^\dagger(t), \quad (9.48)$$

$$i\frac{d}{dt}\hat{U}(t) = \hat{G}(t)\hat{U}(t), \quad (9.49)$$

and hence:

$$i\frac{d}{dt}\hat{K}(t) = [\hat{G}(t), \hat{K}(t)]. \quad (9.50)$$

In the vectorial picture, Eq. (9.50) becomes

$$\frac{d}{dt}\hat{K}(t) = \hat{G}(t)\tilde{\times}\hat{K}(t), \quad (9.51)$$

which is the equivalent of the Bloch equation.

If we apply a sequence of such transformations such that, at time  $t = \tau$ , we end up with  $\hat{K}(\tau)$  again along the positive  $\hat{J}_3$  axis (at the nadir of the hyperboloid), then,

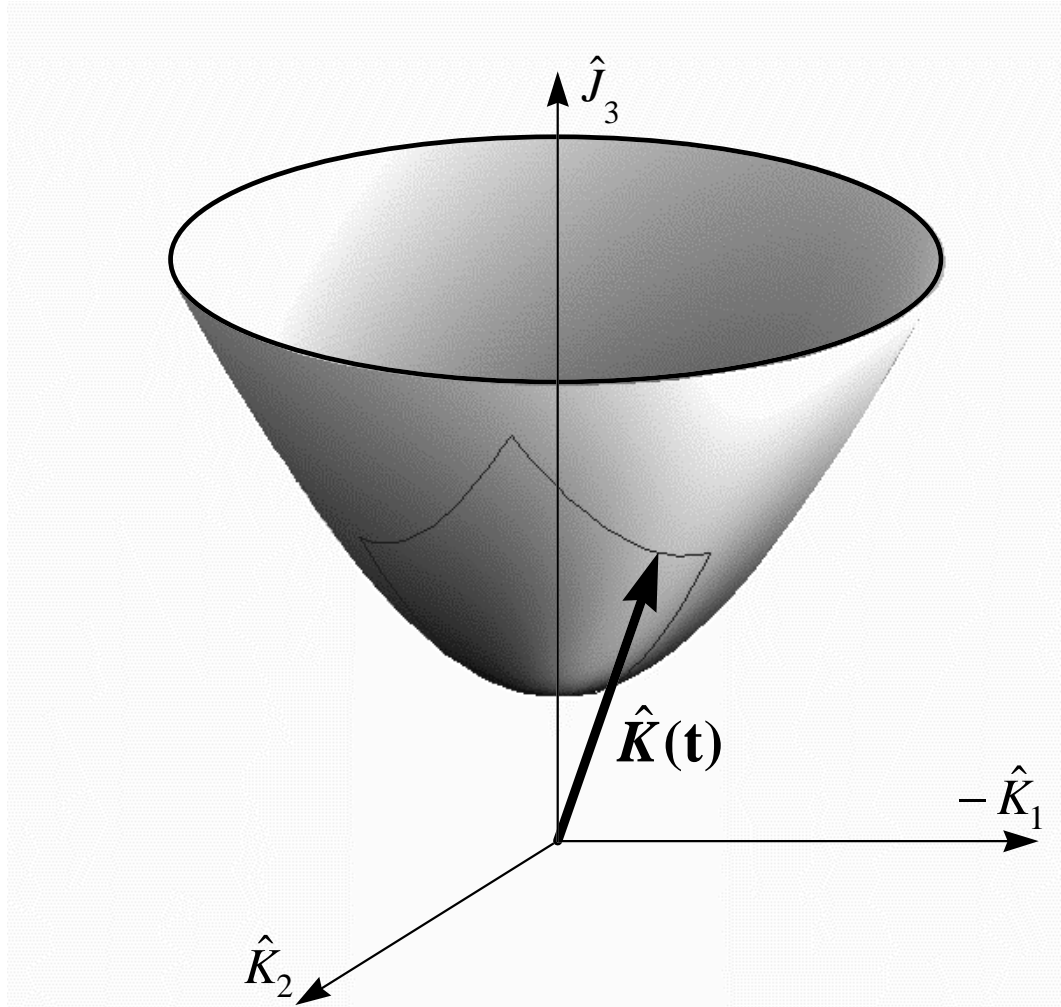


Figure 9.2: Unit hyperboloid in the vector space spanned by  $\hat{J}_3 = \frac{1}{4}(\hat{a}\hat{a}^\dagger + \hat{a}^\dagger\hat{a})$ ,  $\hat{K}_1 = -\frac{i}{4}(\hat{a}\hat{a} - \hat{a}^\dagger\hat{a}^\dagger)$ , and  $\hat{K}_2 = \frac{1}{4}(\hat{a}\hat{a} + \hat{a}^\dagger\hat{a}^\dagger)$ . An initial state  $\hat{J}_3$  moves on the surface of this hyperboloid under the (squeezing and rotation) operations generated by these three operators. This hyperboloid is a useful tool for visualizing the effects of these transformations upon an eigenstate of  $\hat{J}_3$  (i.e. of  $\hat{n}$ ), just as the Bloch sphere is useful in visualizing spin rotations. The path indicated on the surface of the hyperboloid is that traced out in the experiment discussed in the text.

in the course of that evolution,

$$\hat{J}_3 \longrightarrow e^{i\phi\hat{J}_3} \hat{J}_3 \quad (9.52)$$

and, just as in the spin/magnetic field case, we pick up a phase factor:

$$|\psi\rangle_0 = |n\rangle \longrightarrow |\psi\rangle_\tau = e^{i\phi\hat{J}_3} |n\rangle = e^{i(n+\frac{1}{2})\phi/2} |n\rangle. \quad (9.53)$$

We may calculate the dynamical and geometric contributions to the phase  $\phi = \xi + \gamma$  as in the last section, if we merely replace the dot and cross products there by their Minkowski space equivalents. Thus,

$$\xi = \int_0^\tau \hat{G}(t') \cdot \hat{K}(t') dt' . \quad (9.54)$$

In order to calculate the geometric phase, we need to calculate the surface area on the hyperboloid enclosed by the path traced out by  $\hat{K}(t)$ , in the Minkowski metric. Using  $k_1$ ,  $k_2$ , and  $k_3$  as our coordinates, and applying the constraint that  $-(k_1)^2 - (k_2)^2 + (k_3)^2 = 1$ , we have that the element of surface area on the unit hyperboloid is given by

$$d\mathcal{S} = \frac{dk_1 dk_2}{k_3} = \frac{dk_1 dk_2}{\sqrt{1 + k_1^2 + k_2^2}} \quad (9.55)$$

and so

$$\gamma = \oint_{\mathcal{S}} \frac{dk_1 dk_2}{\sqrt{1 + k_1^2 + k_2^2}}, \quad (9.56)$$

where  $\mathcal{S}$  is the surface enclosed by the path traced out by  $\hat{K}(t)$ .

The geometric phase induced by  $SU(1,1)$  dynamics has been measured before. Kitano and Yabuzaki [223] measured the net rotation in the polarization of light passed through a network of linear polarizers. This net rotation can be expressed in terms of the geometric phase<sup>6</sup>. Svensmark and Dimon [224] measured a phase shift in a series of connected, nonlinear oscillators. However, in both these cases, the measurements were performed on *classical* electric fields. It is, therefore, of some interest to measure

---

<sup>6</sup> if one ignores the losses in the polarizers, which induce non-unitary, rather than unitary, evolution.

the geometric phase in the *wave function* of a material oscillator. Furthermore, in our system, we have the unique ability to prepare Fock states and thus to measure the  $(n + \frac{1}{2})/2$  Fock state dependence of the geometry phase.<sup>7</sup>

The basic idea for measuring the geometric phase in our system is to perform a Ramsey experiment on the spin, and perform a sequence of squeeze operations in between the Ramsey zones. The Ramsey experiment maps any relative motional phase between  $|\uparrow\rangle$  and  $|\downarrow\rangle$  onto the spin phase, which manifests itself as a shift in the Ramsey fringes. So, for example, if we do not squeeze or otherwise affect  $|\downarrow\rangle$ , but apply a sequence of operations on the motional state in  $|\uparrow\rangle$  corresponding to a closed path on the unit hyperboloid, we could measure Berry’s phase as the phase shift between  $|\uparrow\rangle$  and  $|\downarrow\rangle$ . In the rotating frame, any contribution to the phase shift from the “natural” motional time evolution drops out, and the only contribution comes from the effects of the operators applied between the Ramsey zones.

There are, of course, many possible closed paths on the unit hyperboloid. For instance, we might imagine applying a squeeze generated by  $\hat{K}_1$ , rotating the vector by  $\pi/2$  radians by applying  $e^{i\pi\hat{J}_3/2}$ , then undoing the squeeze by applying a squeeze generated by  $\hat{K}_2$  [225]. However, we do not (in the rotating frame) have an experimental implementation of a pure “phase space rotation” ( $\hat{J}_3$ ) operator. The most straightforward procedure<sup>8</sup> is to apply a sequence of four squeezes [206]:

$$e^{ir\hat{K}_2}e^{is\hat{K}_1}e^{-is\hat{K}_2}e^{-ir\hat{K}_1}. \quad (9.57)$$

Of course, in order to circumscribe a closed area on the unit hyperboloid,  $r$  and  $s$  must satisfy some relationship between each other. One might expect that we require  $r = s$ , but this is not the case. The reason for this is that the effects of a squeeze operator

<sup>7</sup> Since  $\exp(-i\gamma\hat{J}_3)\hat{a}\exp(i\gamma\hat{J}_3) = \exp(i\gamma/2)\hat{a}$ , all coherent states pick up the same phase  $\exp(i\gamma/2)$ .

<sup>8</sup> Actually, one may trace out a closed path on the unit hyperboloid with a sequence of *three* pure squeezes: for example  $\exp(ir\hat{K}_1)\exp[i(a\hat{K}_1 + b\hat{K}_2)]\exp(-is\hat{K}_2)$ . However, the algebraic relations between  $r$ ,  $s$ ,  $a$ , and  $b$  are somewhat complex (though numerically soluble). In fact, as we shall see, there are reasons for performing a sequence of *four* squeezes: simplicity and the ability to “split the job up” between  $|\uparrow\rangle$  and  $|\downarrow\rangle$ .

depend on where on the hyperboloid it is applied. An analogous effect happens with a vector whose tip is constrained to move on the surface of a sphere: near the north pole, a rotation of  $\pi/2$  radians about the 3-axis moves the vector's tip only a small arc length. Further from the north pole, however, a rotation by the same angle moves the tip of the vector by a much greater arc length. In our case, on the unit hyperboloid, the condition for the four squeezes listed above to move the vector in a closed path is that [206]

$$\sinh s = \tanh r. \quad (9.58)$$

Under the above evolution, the dynamical phase is given by:

$$\xi = \int_0^\tau \hat{K}(t') \hat{G}(t') dt' = 2 \operatorname{arcsinh}[\tanh r] \sinh r. \quad (9.59)$$

The geometric phase is given by:

$$\gamma = - \int_{k_1=0}^{\sinh r} \int_{k_2=0}^{\sinh r} \frac{dk_1 dk_2}{k_3} = -2 \operatorname{arcsinh}[\tanh r] \sinh r + \arcsin[\tanh^2 r] \quad (9.60)$$

(some details of the integration, which involves some obscure integrals, are given in Appendix C). The dynamical phase cancels out some of the geometric phase, and the net phase shift induced by the sequence of four squeezes is:

$$\phi = 2 \arcsin[\tanh^2 r]. \quad (9.61)$$

The dynamic, geometric, and net phase shift are shown in Fig. 9.3. Note that the net phase shift reaches its maximum value for  $r \approx 3$ , corresponding to  $R \approx 1.5$ .

## 9.4 Experimental Issues

Ideally, then, we would perform an experiment in which we prepared an equal superposition of  $|\uparrow\rangle$  and  $|\downarrow\rangle$ , performed the sequence (9.57) of four squeezings on the  $|\uparrow\rangle$  part of the motional state only, and then compare the phase of the  $|n=0\rangle$  state in  $|\downarrow\rangle$  with the  $|n=0\rangle$  result of squeezing  $|\uparrow\rangle$ , by recombining the  $|\uparrow\rangle$  and  $|\downarrow\rangle$  wave

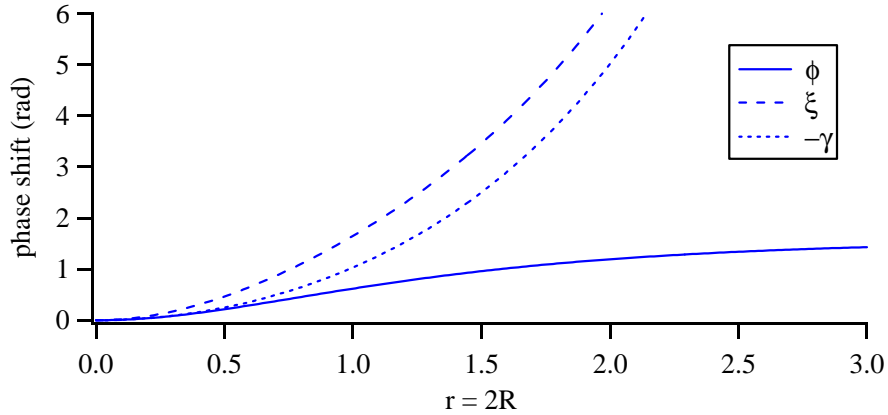


Figure 9.3: (a) Predicted phase shift for an initial  $|n = 0\rangle$  state subject to a sequence of four squeezings constituting a closed path on the unit hyperboloid.  $\gamma$  is the geometric contribution to the phase, due to the inherent curvature of the hyperboloid upon which moves the vector which represents the state.  $\xi$  is the dynamical phase. The net phase is  $\phi$ .

packets. The net phase shift  $\phi$  resulting from the residual geometric phase (Eq. (9.61)) would then result in a net phase shift of the Ramsey fringes with respect to the usual Ramsey experiment in which the four squeeze pulses were absent. This experiment is attractive, since we may “peak up” the four squeeze operators by applying them to the state  $|\uparrow\rangle$  and confirming that we return to the motional state  $|n = 0\rangle$ .

However, the squeeze operators which are produced by the “walking standing wave” interaction with the laser beams (Sec. 6.1.4) are of second order in the Lamb-Dicke parameter  $\eta$  and so, the squeezing operations are relatively slow. We attempted to measure the SU(1,1) Berry’s phase in the micromachined linear ion trap. Unfortunately, the background heating rate precluded performing four sequential squeeze operations: the decoherence washed out any signal. This did not present an insurmountable barrier, however. As pointed out by Chiao and Jordan [206] in a different context, it suffices to perform two squeezes on one part of the spin wave packet and the other two on the other part. Thus, an equivalent experiment consists of a  $\pi/2$  carrier pulse, simultaneously

performing the operations:

$$|\downarrow, 0\rangle \longrightarrow e^{-is\hat{K}_2} e^{-ir\hat{K}_1} |\downarrow, 0\rangle \quad (9.62)$$

$$|\uparrow, 0\rangle \longrightarrow e^{-is\hat{K}_1} e^{-ir\hat{K}_2} |\uparrow, 0\rangle. \quad (9.63)$$

Then the Ramsey experiment measures the overlap

$$\langle 0 | e^{ir\hat{K}_2} e^{is\hat{K}_1} e^{-is\hat{K}_2} e^{-ir\hat{K}_1} | 0 \rangle, \quad (9.64)$$

just as in the original experiment. The trick, however, is to arrange that a squeeze  $e^{ir\hat{K}_1}$  on  $|\downarrow\rangle$  should be a squeeze  $e^{ir\hat{K}_2}$  on  $|\uparrow\rangle$ . It is possible to do this, by appropriately setting the polarization of the Raman beams, as described below.

#### 9.4.1 Differential Squeezing Using Polarization

Recall from Sec. 6.1.4 that the squeeze parameter for “walking standing wave” production of squeezed states is given by  $\epsilon = R e^{2i\phi} = \frac{r}{2} e^{i\theta} = i\eta^2 \Omega t e^{i\phi_L}$  (where I have now explicitly written the laser phase). But, as discussed in Sec. 6.2.1, the effective Rabi frequencies for  $|\uparrow\rangle$  and  $|\downarrow\rangle$  for the “walking standing wave” interaction depend on the polarizations of the two Raman beams creating the interaction. As discussed there,  $R_{co}$  must have the polarization  $\frac{1}{\sqrt{2}}(\sigma^+ + \sigma^-)$ , but we may alter the polarization of the  $RR_{\perp}$  beam. Recall Eqs. (6.19) and (6.20):

$$\begin{aligned} \Omega_{\downarrow} &= \frac{g^2}{\Delta_R + \omega_0} \frac{2\Upsilon}{3} + \frac{g^2}{\Delta_R + \delta_{FS} + \omega_0} \left( \Lambda + \frac{\Upsilon}{3} \right) \\ \Omega_{\uparrow} &= \frac{g^2}{\Delta_R} \left( \frac{\Lambda}{2} + \frac{\Upsilon}{6} \right) + \frac{g^2}{\Delta_R + \delta_{FS}} \left( \frac{\Lambda}{2} + \frac{5\Upsilon}{6} \right), \end{aligned}$$

where the  $RR_{\perp}$  beam has polarization  $\Lambda\sigma^- + \Upsilon\sigma^+$ . In Sec. 6.2.1, we ignored the hyperfine splitting when deriving Eq. (6.21) for the ratio of  $\Omega_{\downarrow}$  to  $\Omega_{\uparrow}$ . Now, if we take this into account, we obtain:

$$\frac{\Omega_{\downarrow}}{\Omega_{\uparrow}} = \frac{\Delta_R (\delta_{FS} + \Delta_R) \left( \frac{4\Upsilon}{\omega_0 + \Delta_R} + \frac{2(3\Lambda + \Upsilon)}{\delta_{FS} + \omega_0 + \Delta_R} \right)}{3\Lambda + \delta_{FS}\Upsilon + 6(\Lambda + \Upsilon)\Delta_R}. \quad (9.65)$$

By placing a  $\frac{\lambda}{4}$  followed by a  $\frac{\lambda}{2}$  plate in the  $\overline{\text{RR}}_{\perp}$  beam line immediately before the input lens to the trap envelope, we can choose any value for  $\Lambda$  and  $\Upsilon$ . We want to realize the operator  $\hat{S}(r, \theta = 0) = e^{ir\hat{K}_1}$  in one spin state, and the operator  $\hat{S}(r, \theta = \pi/2) = e^{ir\hat{K}_2}$  in the other. It follows from Eq. (6.17), therefore, that we want to have

$$\frac{\Omega_{\downarrow}}{\Omega_{\uparrow}} = \pm i. \quad (9.66)$$

The values of  $\Lambda$  and  $\Upsilon$  are somewhat complicated functions of the angles of the  $\frac{\lambda}{4}$  and  $\frac{\lambda}{2}$  plate angles, and the dependence of the Rabi frequency ratio, through Eq. (9.65), even more complicated. Nonetheless, the resulting equation can be solved numerically (for a given Raman beam detuning  $\Delta_R$ ) to obtain the angles. For example, at a detuning of  $\Delta_R = 12.33$  GHz, the the slow axis of the quarter-wave plate should be at  $-6.1^\circ$  from the vertical and the slow axis of the half-wave plate at  $-31.9^\circ$  from the vertical (assuming a vertically polarized input beam).

Figure 9.4(a), (b), and (c) show the dependence of the absolute value and argument of the ratio  $\frac{\Omega_{\downarrow}}{\Omega_{\uparrow}}$  as a function of  $\Delta_R$ , the  $\frac{1}{4}$ -wave plate angle, and the  $\frac{1}{2}$ -wave plate angle, the other parameters being held fixed at their nominal values. These figures indicate that, although care must be taken in setting the wave plate angles, the requirements for appropriate squeezing of  $|\uparrow\rangle$  and  $|\downarrow\rangle$  are not impracticable.

Unfortunately, birefringence in the vacuum envelope windows added a random change in the polarization of the  $\overline{\text{RR}}_{\perp}$  beam after the polarization optics. This birefringence also varied from spot to spot on the windows. Since the “peaking up” procedure involved comparing squeezed state flopping curves for initial  $|\uparrow, n = 0\rangle$  and  $|\downarrow, n = 0\rangle$  curves,<sup>9</sup> a time-consuming procedure, it was not practical to perform the experiment, given the unknown birefringence of the windows. Unfortunately, since there was one window between the polarization optics and the ion, but two windows before the beam

---

<sup>9</sup> Other meters of the relative squeezing in  $|\uparrow\rangle$  and  $|\downarrow\rangle$  exist — for example, variants of the Ramsey experiment. Several such techniques were tried: however, the heating-induced decoherence made them essentially useless with the ion heating at the rate it did when the experiments were tried.

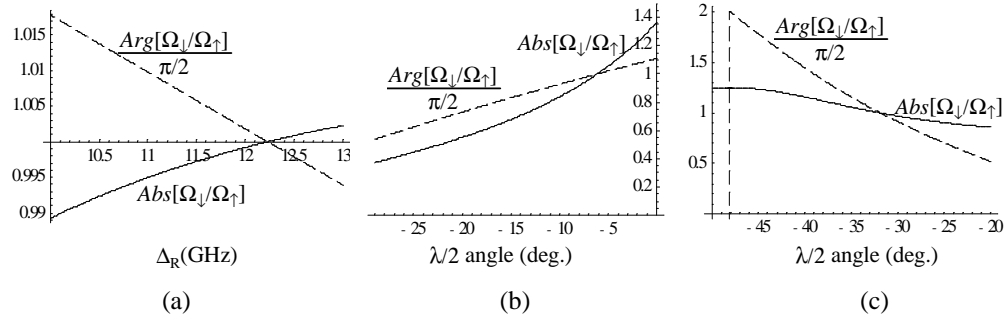


Figure 9.4: Sensitivity of  $\Omega_{\downarrow}/\Omega_{\uparrow}$  to errors in experimental parameters. Nominal values for  $\Omega_{\downarrow}/\Omega_{\uparrow} = i$  are  $\Delta_R = 12.333$  GHz,  $\frac{\lambda}{4}$  plate at  $-6.1^\circ$  from the vertical, and  $\frac{\lambda}{2}$  plate at  $-31.9^\circ$  from the vertical. (a) Dependence of  $\Omega_{\downarrow}/\Omega_{\uparrow}$  on the detuning  $\Delta_R$  of the Raman beams from the  $2p^2P_{1/2}$  virtual level, with the quarter- and half-wave plate angles held at their nominal values. The detuning affects the relative importance of transitions driven through the  $^2P_{1/2}$  and  $^2P_{3/2}$  (virtual) levels. (b) Dependence of  $\Omega_{\downarrow}/\Omega_{\uparrow}$  on the angle of the quarter-wave plate, with  $\Delta_R = 12.333$  GHz and the half-wave plate held at its nominal value. (c) Dependence of  $\Omega_{\downarrow}/\Omega_{\uparrow}$  on the angle of the half-wave plate, with  $\Delta_R = 12.333$  GHz and the quarter-wave plate held at its nominal value. In (a), (b), and (c), the dashed lines show the argument of the complex Rabi frequency ratio, while the solid lines show its magnitude.

passed out the other side of the vacuum envelope, it was not possible to determine the polarization state at the ion.

Were the heating rate lower, all four squeezes could be performed on only one of the spin states. In this case (neglecting the fine-structure contributions, which is a small perturbation for small  $\Delta_R$ ), as with the original Schrödinger cat experiment, pure  $\sigma^-$  light in the  $RR_{\perp}$  beam line would affect only  $|\downarrow\rangle$ . Despite the birefringence in the windows, there are rapid diagnostics which could allow us to determine when the light at the ion is pure  $\sigma^-$ : for example, the cycling transition (see Appendix A). Thus, if the heating rate were low enough to allow four sequential squeeze operations, the experiment would be possible.

### 9.4.2 The Effect of Small Errors on Berry's Phase

It is worthwhile to examine the effects of small errors in the squeeze operations on the measured residual geometric phases. For example, the magnitude of the Rabi frequencies in  $|\uparrow\rangle$  and  $|\downarrow\rangle$  might not be equal, or the argument between the two might not be exactly  $\pi/2$  radians. Alternatively, in a four-squeeze implementation, there might be slight errors in the magnitudes of the squeezes. In general, since the geometry of the unit hyperboloid (see above) is smooth, we would not expect a small imperfection in the path of the vector representing the state to translate into very large changes in the observed phase. Of course, if the path on the hyperboloid is not closed, it is not possible to talk of the solid angle enclosed by that path. However, different approaches to the issue are possible.

One approach which facilitates the determination of the effects of small errors uses yet another description of the phase shifts which occur in applying sequential squeezings. This approach arises from considering the action of two sequential squeezing operations, as was considered in Refs. [226, 227]. Before writing down the result, it is worthwhile to reiterate the effects of the group elements generated by the  $SU(1,1)$  algebra. The operator

$$\hat{R}(\zeta) = e^{i\zeta\hat{J}_3} = e^{i\zeta(\hat{a}\hat{a}^\dagger + \hat{a}^\dagger\hat{a})/4} \quad (9.67)$$

produces “rotations” in phase space. (In our case, since there is only one “dimension” in which rotations may occur, rotation operators commute.) The operator

$$\hat{S}(r, \vartheta) = e^{ir(\hat{K}_1 \cos \vartheta + \hat{K}_2 \sin \vartheta)} \quad (9.68)$$

generates a squeeze along the direction  $\vartheta/2$ . In general, we may re-express Eq. (9.68) as:

$$\hat{S}(r, \vartheta) = \hat{R}^\dagger(\vartheta)\hat{S}(r, 0)\hat{R}(\vartheta). \quad (9.69)$$

The result of two squeezes is then a squeeze plus a rotation. Specifically [226, 227],

$$\hat{\mathcal{S}}(p, \zeta)\hat{\mathcal{S}}(q, 0) = \hat{R}(\Phi)\hat{\mathcal{S}}(r, \vartheta'), \quad (9.70)$$

where

$$r = \operatorname{arccosh} [\cosh p \cosh q + \cos \zeta \sinh p \sinh q], \quad (9.71)$$

$$\vartheta' = \arctan \left\{ \frac{\sin \zeta \sinh p}{\sinh q \cosh p + \cos \zeta \sinh p \cosh q} \right\}, \quad (9.72)$$

$$\Phi = 2 \arctan \left\{ \frac{-\sin \zeta \sinh(p/2) \sinh(q/2)}{\cosh(p/2) \cosh(q/2) + \cos \zeta \sinh(p/2) \sinh(q/2)} \right\}. \quad (9.73)$$

Note that this result also holds true when considering the special relativity (in 2+1 dimensions) interpretation of the transformations generated by SU(1,1). In this language, rotations are rotations, squeezes are boosts, and the product of two boosts is a net boost *plus* a rotation. This is the origin of the Thomas precession (see Ref. [89]§11.8).

Recall from Eq. (9.57) that the experiment consists of the four operations

$$e^{ir\hat{K}_2} e^{is\hat{K}_1} e^{-is\hat{K}_2} e^{-ir\hat{K}_1} \equiv \hat{\mathcal{S}}(r, \frac{\pi}{2})\hat{\mathcal{S}}(s, 0)\hat{\mathcal{S}}(s, \frac{3\pi}{2})\hat{\mathcal{S}}(r, \pi). \quad (9.74)$$

Using Eq. (9.70) to combine the left two and right two squeeze operators, we may re-express this as:

$$\hat{\mathcal{S}}(r, \frac{\pi}{2})\hat{\mathcal{S}}(s, 0)\hat{\mathcal{S}}(s, \frac{3\pi}{2})\hat{\mathcal{S}}(r, \pi) = \hat{R}(\Phi_1)\hat{\mathcal{S}}(R_1, \vartheta_1)\hat{R}(\Phi_2)\hat{\mathcal{S}}(R_2, \vartheta_2), \quad (9.75)$$

where  $R_1, R_2, \vartheta_1, \vartheta_2, \phi_1,$  and  $\phi_2$  are obtained from Eq. (9.73). In fact, it is straightforward to show that  $R_1 = R_2 \doteq R$  and  $\Phi_1 = \Phi_2 \doteq \Phi$  for the prescribed sequence of squeezes, although  $\vartheta_1 \neq \vartheta_2$ . Thus,

$$\begin{aligned} \hat{\mathcal{S}}(r, \frac{\pi}{2})\hat{\mathcal{S}}(s, 0)\hat{\mathcal{S}}(s, \frac{3\pi}{2})\hat{\mathcal{S}}(r, \pi) &= \hat{R}(\Phi)\hat{\mathcal{S}}(R, \vartheta_1)\hat{R}(\Phi)\hat{\mathcal{S}}(R, \vartheta_2) \\ &= \hat{R}(\Phi)\hat{\mathcal{S}}(R, \vartheta_1)\hat{R}(\Phi - \vartheta_2)\hat{\mathcal{S}}(R, 0)\hat{R}(\vartheta_2) \\ &= \hat{R}(2\Phi - \vartheta_2)\hat{\mathcal{S}}(R, \vartheta_1 + \Phi - \vartheta_2)\hat{\mathcal{S}}(R, 0)\hat{R}(\vartheta_2). \end{aligned} \quad (9.76)$$

Now, if  $\vartheta_1 - \vartheta_2 + \Phi = \pi$ , the two squeezes on the last line cancel, and the net effect is a rotation operator

$$\hat{R}(2\Phi - \vartheta_2)\hat{R}(\vartheta_2) = \hat{R}(2\Phi). \quad (9.77)$$

This occurs if  $\tanh r = \sinh s$ , which is the same as Condition (9.58).<sup>10</sup> So another way of looking at the experiment is that, if we choose the squeeze parameters correctly, the resultant squeeze of the first two squeeze operators cancels with that of the second two, and we are left only with the net rotation (the equivalent of the Thomas precession). Of course, with this approach, we cannot distinguish between dynamical and geometric contributions to the resultant phase, which is the advantage of the approach taken in Sec. 9.3.

If we now assume that there are small errors in the experimental pulses, then the two squeeze operators will not exactly cancel. For example, suppose that the angles  $(0, \pi/2, \pi, \text{ and } 3\pi/2)$  of the various operations are correct, but that there are errors in the magnitude of the various squeezes. This is a reasonable model of the errors, since the phase between the squeezes will either be set by an rf phase or a polarizer setting — either of which may be well controlled. The squeeze amplitudes, however, may be harder to calibrate and keep constant. We may model this situation by assuming  $s$ , and letting  $r \rightarrow r + \varepsilon$  (where still  $\tanh r = \sinh s$ ). In this case, Eq. (9.76) becomes

$$\hat{S}(r + \varepsilon, \frac{\pi}{2})\hat{S}(s, 0)\hat{S}(s, \frac{3\pi}{2})\hat{S}(r + \varepsilon, \pi) = \hat{R}(2\Phi' - \vartheta'_2)\hat{S}(R', \vartheta'_1 + \Phi' - \vartheta'_2)\hat{S}(R', 0)\hat{R}(\vartheta'_2). \quad (9.78)$$

Note that combining the leftmost and rightmost pairs of squeeze operators still results in the same squeeze amplitude and rotation angle, as was the case before. Explicitly:

$$R' = \operatorname{arccosh} [\cosh(r + \varepsilon) \cosh s] \doteq R + \alpha \quad (9.79)$$

$$\Phi' = -2\arctan \{ \tanh[(r + \varepsilon)/2] \tanh[s/2] \} \doteq \Phi + \beta. \quad (9.80)$$

---

<sup>10</sup> It is extremely challenging to prove this algebraically. On the other hand, we can plug the result from Eq. (9.58) into the combined expressions for  $\vartheta_1 - \vartheta_2 + \Phi$  from Eq. (9.73) and verify the truth of the statement.

$\vartheta'_1$  and  $\vartheta'_2$  also differ from their values above. Explicitly:

$$\vartheta'_1 = \arctan \left[ \frac{\tanh(r + \varepsilon)}{\sinh s} \right] \doteq \vartheta_1 + \delta \quad (9.81)$$

$$\vartheta'_2 = \arctan \left[ \frac{\tanh s}{\sinh(r + \varepsilon)} \right] \doteq \vartheta_2 + \kappa. \quad (9.82)$$

One result is that  $\vartheta'_1 - \vartheta'_2 + \Phi' \neq \pi$ . Thus, the two squeeze operators resulting from the combination of the left pair and right pairs of squeezes no longer cancel. The result, according to Eq. (9.70), is an additional squeeze and an additional rotation over the ideal case. The phase shift which we measure then differs from the theoretical prediction, Eq. (9.61), for two reasons. First, the arguments of the outermost rotation operators in Eq. (9.78) no longer have the correct values. Second, the fact the the two squeeze operators in the middle of Eq. (9.78) no longer cancel introduces an *additional* rotation operator and, hence, an additional phase shift error. As well, the squeeze operator causes a reduction in the Ramsey fringe contrast.

The experiment measures, for example,  $\langle 0 | \hat{U} | 0 \rangle$  which, in the presence of the error is given by:

$$\begin{aligned} \langle 0 | \hat{R}(2\Phi' - \vartheta'_2) \hat{S}(R', \vartheta'_1 + \Phi' - \vartheta'_2) \hat{S}(R', 0) \hat{R}'(\vartheta'_2) | 0 \rangle \\ = e^{i\Phi'/2} \langle 0 | \hat{R}(\Lambda) \hat{S}(v, \nu) | 0 \rangle \\ = e^{i\Phi'/2} e^{i\Lambda/4} \frac{1}{\sqrt{\cosh v}} \\ = e^{i\Phi'/2} e^{i(\Lambda+\alpha)/4} \frac{1}{\sqrt{\cosh v}}. \end{aligned} \quad (9.83)$$

Here,  $v$  and  $\nu$  (which doesn't enter into the final result) are the parameters of the squeeze resulting from  $\hat{S}(R', \vartheta'_1 + \Phi' - \vartheta'_2) \hat{S}(R', 0)$  and  $\Lambda$  is the rotation angle.

Now, in the ideal case, we have  $\Phi + \vartheta_1 - \vartheta_2 = \pi$ . Thus, from Eqs. (9.80), (9.81), and (9.82), we have

$$\Phi' + \vartheta'_1 - \vartheta'_2 = \pi + \alpha + \delta - \kappa \quad (9.84)$$

so that

$$\sin(\Phi' + \vartheta'_1 - \vartheta'_2) = -\sin(\beta + \delta - \kappa)$$

$$\cos(\Phi' + \vartheta'_1 - \vartheta'_2) = -\cos(\beta + \delta - \kappa). \quad (9.85)$$

Using the above information in Eq. (9.70), we obtain:

$$\begin{aligned} v &= \operatorname{arccosh} \left[ \cosh^2(R + \alpha) - \cos(\beta + \delta - \kappa) \sinh^2(R + \alpha) \right] \\ \Lambda &= 2 \arctan \left\{ \frac{\sin(\beta + \delta - \kappa) \sinh^2[(R + \beta)/2]}{\cosh^2(R + \alpha)/2 - \cos(\beta + \delta - \kappa) \sinh^2[(R + \alpha)/2]} \right\} \end{aligned} \quad (9.86)$$

which we can plug back into Eq. (9.83) to determine the effect on the measured signals. Of course, if we do this, we only express the error in terms of  $\alpha$ ,  $\beta$ ,  $\delta$ , and  $\kappa$ : the errors in the parameters  $R$ ,  $\Phi$ ,  $\vartheta_1$ , and  $\vartheta_2$  of the combined squeezes. In order to express the error in terms of  $\varepsilon$  (the error in the squeeze parameter  $r$ ), we need to use the full expressions in Eqs. (9.80), (9.81), and (9.82). This is straightforward. However, the algebra is complicated enough that performing this final step adds little to the information content of this description. I shall, therefore, merely quote the result.

Figure 9.5 plots the net phase for the ideal Berry's phase experiment and with  $\varepsilon = 0.05r$  — that is to say,  $r \rightarrow 1.05 \operatorname{arctanh}[\sinh s]$ . For small squeeze parameters, small errors in the squeeze operations should result in small errors in the measured phase shift.

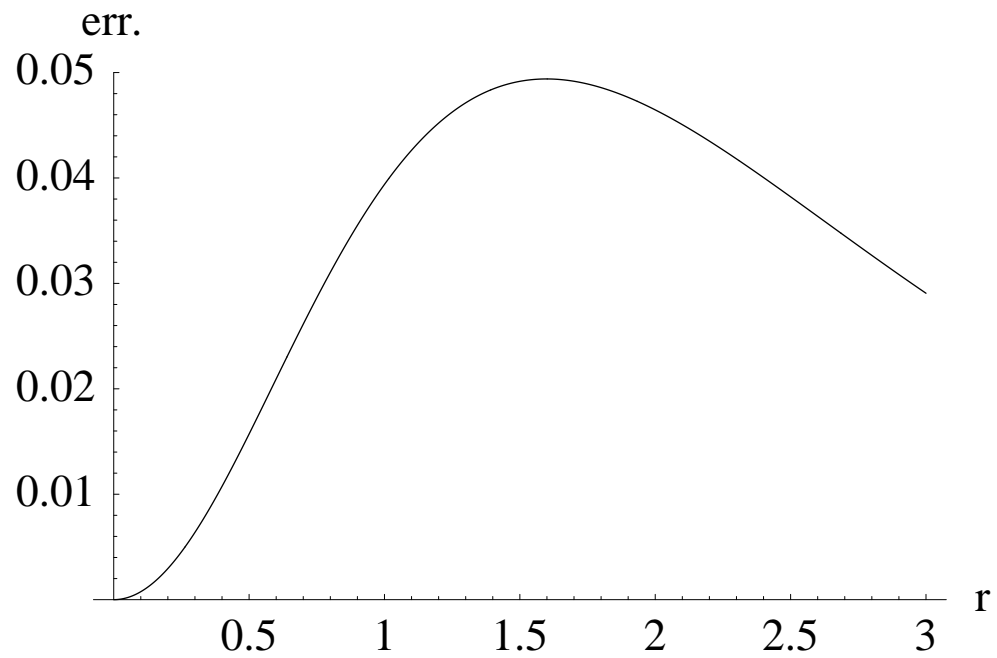


Figure 9.5: Effect of small imperfections of the squeezing pulses on the measured geometric phase shift. The curve shows the absolute error, assuming a five percent error in  $r$ , the amplitude of the first squeeze. The ordinate axis shows  $r$ , but in the various formulae for the phase shift,  $r \rightarrow 1.05 r$ . However, the amplitude  $s$  of the second squeeze satisfies  $\tanh r = \sinh s$ , where  $r$  is read off the ordinate axis of the graph.

## Appendix A

### Photon Statistics and “Peaking Up” the Experiment”

In this appendix, I will discuss some of the details of the cycling transition ( $|\downarrow\rangle \rightarrow |2p\ ^2P_{3/2}\rangle$ ). The statistics of the photons from this transition provide a sensitive guide to various aspects of the experiment. So, I will try to provide a recipe for “peaking up” the experiment, as well as discuss some of the limits to the cycling transition.

Basically, the peaking up based on the photon statistics falls into two categories: those methods based on the average number of photons detected per experiment (i.e. the mean count rate) and those based on the histogram of photon numbers per experiment. I shall deal with these in order. First, I will catalogue the various peak-up procedures based on average photon number, and then I will discuss what information can be gleaned from the histograms, as well as discussing the limit of the cycling transition’s quantum efficiency for discriminating  $|\downarrow\rangle$  from  $|\uparrow\rangle$  (due to off-resonant transitions from  $|\uparrow\rangle$  into the cycling transition).

#### A.1 Peaking Up the Experiment With the Mean Photon Number

To recap, the typical experiment lasts anywhere from 0.5 – 1ms. At the end of each experiment, we turn on the Blue Doppler beam for typically 200  $\mu$ s, and measure the number of photons collected by the photodetection system (which has an overall quantum efficiency of  $\approx 10^{-3}$  due to detector efficiency and solid angle). Typically, we detect photons with the imager tube while loading the trap, then switch to the

photomultiplier tube for peaking up the experiment and for taking data. The pulses output by these detectors are sent to a scalar (Ortec Model #9349), which produces a current proportional to the count rate (# of photons detected per second). This current is then used to drive galvanometers. Although using needle dials to indicate the average count rate may strike some as old-fashioned, this is, in fact, a very useful tool, as it seems to be the easiest way for people to assimilate the information. In particular, it is *much* easier to determine the maximum count rate while peaking up using the needle dials than using a digital count rate indicator. The time constant of the scalar is adjustable. We typically use a time constant of 0.3 s.

All the following peak-ups should be performed with the Blue and Red Doppler beams on continuously, and with the Raman and Repumper beams off (i.e. blocked!). Note that, if the Repumper beam is going into the trap, it will be impossible to peak up the Doppler beam lines, as the count rate becomes very “jumpy.”

After loading an ion and centering it in the imager tube, the first task is to maximize the count rate by adjusting the Doppler beam input lens. To do this, block the Repumper beam line and the Red Doppler, and maximize the count rate. Next, set the Blue Doppler polarization. With the Red Doppler still blocked (or, if the ion is flakey without the Red Doppler, attenuated to well below the saturation intensity), iterate between adjusting the angle and orientation of the quarter-wave plate, and adjusting the currents in the  $\mathbf{B}$  field shim coils. This procedure aligns the wave vector of the Doppler beam with the magnetic field.

Once the Blue Doppler beam is adjusted, let the Red Doppler in again (or, if it had only been attenuated, remove the attenuation). Unplug one of the shim coil current supplies. The count rate should drop, since the polarization has been effectively degraded. Then adjust the Red Doppler input beamsplitter to maximize the count rate.

In order to peak up the Repumper, it is usually best to turn Raman cooling on, then disable the Raman probe. The count rate should be considerably lower (20-30%)

lower than before Raman cooling was turned on. Next, allow the Repumper beam into the trap, and maximize the count rate. It is often useful to observe the photon number histogram (see below) to ensure that one has the Repumper beam position optimized.

## A.2 Photon-Number Histograms

The histogram of the distribution of detected fluorescence photons is produced on the PC. A variable number of experiments are binned together (typically, 1000), and the resulting histogram is displayed on-screen. In addition, the mean number and the variance are calculated for the binned experiments and displayed. The variance should be exactly 1.00 for a Poisson distribution (which is the expected distribution). In practice, the number varies between 0.97 and 1.08 when 1000 experiments are binned together. If the variance creeps up much beyond 1.10, then something is wrong (usually, it's a problem with intensity or frequency fluctuations on the Doppler laser).

It is also useful to set a discriminator between  $|\uparrow\rangle$  and  $|\downarrow\rangle$  in terms of the number of photons received per experiment. The program calculates the percentage of experiments in which a number of photons corresponding to  $|\uparrow\rangle$  was received, and displays this information as well. In practice, due to background light, scatter off the trap electrodes, and the limitation of the cycling transition in  ${}^9\text{Be}^+$ , the discriminator is usually set such that experiments in which two or less photons are received are binned as  $|\uparrow\rangle$ , and those in which more photons are received are binned as  $|\downarrow\rangle$ . The “limit” mentioned above is due to off-resonant pumping of population in  $|\uparrow\rangle$  into the cycling transition, and will be further explained below.

In practice, a canonical  $|\downarrow\rangle$  state is that which results from optical pumping at the beginning of the experiment. A canonical  $|\uparrow\rangle$  state is produced by starting out in  $|\downarrow\rangle$  and applying a  $\pi$ -pulse on the co-propagating carrier. With the discriminator set to two photons,  $|\uparrow\rangle$  produces counts in the “ $|\downarrow\rangle$ ” channel 2-4% of the time. A  $|\downarrow\rangle$  state typically produces no counts in the “ $|\uparrow\rangle$ ” channel. Typical histograms for

$|\downarrow\rangle$  and  $|\uparrow\rangle$  are reproduced in Fig. A.1(a). Fig. A.1(b) shows a typical carrier Rabi flopping curve with photon number histograms shown for several interesting parts of the curve. In particular, note that the photon distribution for  $\frac{1}{\sqrt{2}}(|\downarrow\rangle + |\uparrow\rangle)$  is the appropriately weighted sum of the  $|\downarrow\rangle$  and  $|\uparrow\rangle$  (Poissonian) histograms, rather than being a Poissonian at the average of the  $|\downarrow\rangle$  and  $|\uparrow\rangle$  average photon numbers.

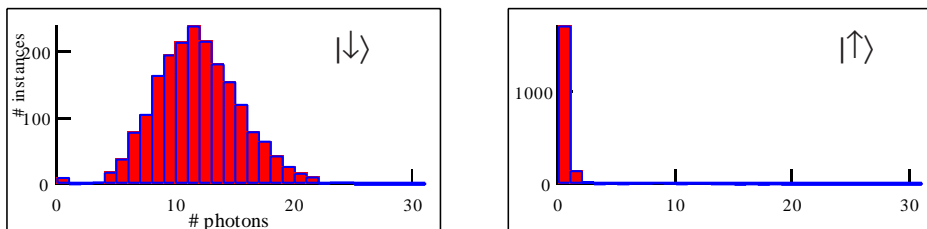
### A.2.1 Discrimination Limits: Off-Resonant Pumping

The 2-4% “leak” of  $|\uparrow\rangle$  into  $|\downarrow\rangle$  bins is due to the finite hyperfine splitting of  ${}^9\text{Be}^+$ : the linewidth of the  $2p^2P_{3/2}$  level is 19.4 MHz while the hyperfine splitting is only 1.25 GHz. Thus the state  $|\uparrow\rangle$  occasionally scatters photons, rather than being truly dark — indeed, once  $|\uparrow\rangle$  scatters a photon, it is likely that it will end up in  $|\downarrow\rangle$ , and hence participate in the cycling transition.

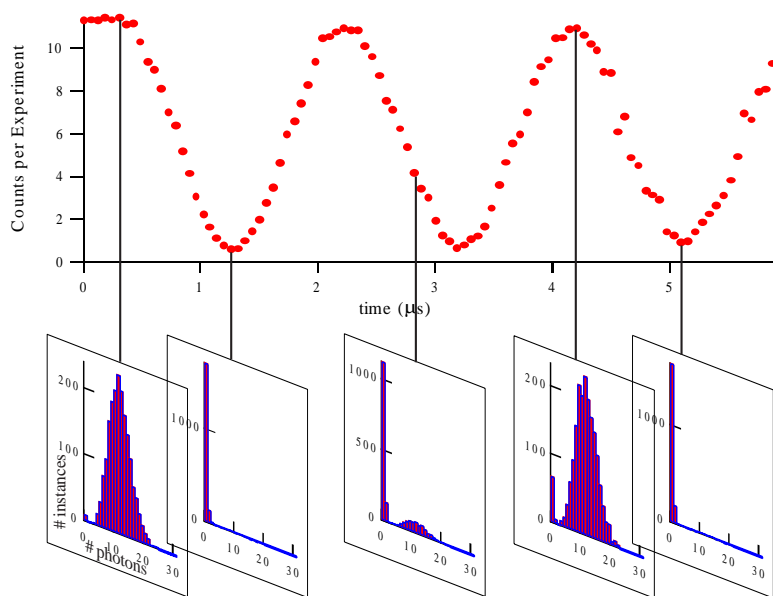
If the ion is in  $|\downarrow\rangle$ , then the photon number distribution is truly Poissonian, with  $\bar{m} = \bar{m}_0 = \zeta\beta_2 t_{DG}$ , where  $\beta_2$  is the scatter rate in  $|\downarrow\rangle$ ,  $t_{DG}$  is the length of the detection time gate, and  $\zeta$  is the detection efficiency ( $\zeta \approx 8 \times 10^{-3}$ ). The challenge is to calculate the photon number distribution if the ion is in  $|\uparrow\rangle$  at the beginning of  $t_{DG}$ . In this case, the photon distribution is a spike at  $\bar{m} = 0$  for some time  $t_p$  (related to the scatter rate  $\beta_2$  due to off-resonant transitions) until the ion enters the cycling transition, at which point the photon distribution becomes a Poissonian with  $\bar{m} = \bar{m}_0(1 - \frac{t_p}{t_{DG}})$ . The complication occurs because  $t_p$ , being related to the excited state lifetime, is a random variable.

To be more quantitative, let

$$\beta_1 = \frac{\frac{I}{I_S} \frac{1}{2\tau}}{1 + \frac{I}{I_S} + 4 \left( \frac{\omega_0 + \delta}{\gamma} \right)^2} \approx \frac{\frac{I}{I_S} \frac{1}{2\tau}}{1 + \frac{I}{I_S} + 4 \left( \frac{\omega_0}{\gamma} \right)^2} \quad (\text{A.1})$$



(a)



(b)

Figure A.1: (a) Photon number histograms for  $|\downarrow\rangle$  and  $|\uparrow\rangle$ . 1000 experiments were binned together for each histogram, and Detection Gate was  $200\ \mu\text{s}$ . The counts in the nonzero  $|\uparrow\rangle$  bins are due to background and to off-resonant pumping of  $|\uparrow\rangle$  population into the cycling transition. (b) Carrier flopping curve with photon number histograms at select points. Note that halfway down the flopping curve, when the ion is in  $1/\sqrt{2}(|\downarrow\rangle + |\uparrow\rangle)$ , the photon distribution is the sum of the  $|\downarrow\rangle$  and  $|\uparrow\rangle$  distributions, and not a Poissonian centred at the average of the  $|\downarrow\rangle$  and  $|\uparrow\rangle$  average count rates.

be the base off-resonant scatter rate of photons when the atom is in  $|\uparrow\rangle$  (neglecting the laser polarization and atomic matrix elements, for the moment) and

$$\beta_2 = \frac{\frac{I}{I_S} \frac{1}{2\tau}}{1 + \frac{I}{I_S} + 4 \left(\frac{\delta}{\gamma}\right)^2} \quad (\text{A.2})$$

be the scatter rate of photons when the atom is in  $|\downarrow\rangle$  (i.e. the cycling transition scatter rate). In these equations,  $\tau$  is the  $2p^2P_{3/2}$  lifetime and  $\gamma$  its linewidth,  $I$  is the laser intensity,  $I_S$  is the saturation intensity, and  $\delta$  is the detuning from resonance. (In practice,  $\delta$  will be negative to allow laser cooling with the Doppler beams.)

Now, the atomic levels of interest, along with the appropriate transition strengths, are shown in Fig. A.2(a). Eliminating the excited state levels, we get the simplified level structure of Fig. A.2(b), which guides us in writing down the following rate equation for the population in  $|\uparrow\rangle$ :

$$\begin{aligned} \dot{P}_\uparrow &= - \left[ \frac{1}{6}\beta_1 + \frac{5}{24}\beta_1 \frac{\frac{1}{18}\beta_2}{\frac{1}{18}\beta_2 + \frac{5}{24}\beta_2} \right] P_\uparrow \\ &= \frac{4}{19}\beta_1 P_\uparrow. \end{aligned} \quad (\text{A.3})$$

Thus,  $P_\uparrow(t) = P_\uparrow(0)[1 - \exp(-\frac{4}{19}\beta_1 t)]$ . Of course, this equation reflects the *average* dynamics of  $|\uparrow\rangle$ : in a single experiment, the atom follows a probability distribution of decay times. Guided by Eq. (A.3), we write:

$$p(t_p) = \frac{1}{\tau_p} e^{-\frac{t_p}{\tau_p}}, \quad (\text{A.4})$$

where  $\tau_p = \frac{19}{4\beta_1}$ .

To reiterate, we see no photons until the atom off-resonantly pumps into the cycling transition at (random) time  $t_p$ . Then, we see a Poissonian distribution with  $\bar{m} = \bar{m}_0(1 - \frac{t_p}{t_{DG}})$ . Thus, the probability distribution for the number of photons observed in an experiment may be written as the conditional probability distribution:

$$P(m|\bar{m}) = \frac{e^{-\bar{m}} \bar{m}^m}{m!}. \quad (\text{A.5})$$

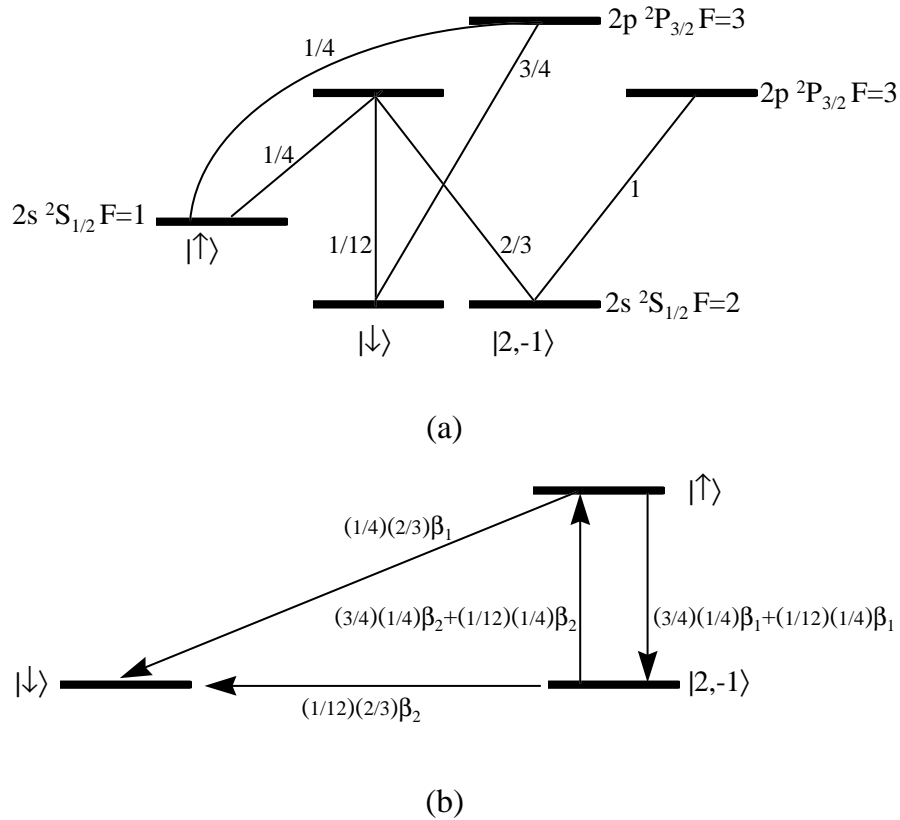


Figure A.2: (a) Relevant energy levels in  ${}^9\text{Be}^+$  for discussing off-resonant pumping of  $|\uparrow\rangle$  population into the cycling transition. The numbers are the relative transition strengths. See Appendix B for a complete diagram of transition strengths. (b) Simplified effective level diagram, showing the various rates of population transfer.

It follows that the probability of observing  $m$  photons in an experiment is given by:

$$P(m) = \int P(m|\bar{m})\rho(\bar{m})d\bar{m}, \quad (\text{A.6})$$

where  $\rho(\bar{m})$  is the probability distribution for  $\bar{m}$  (due to the random nature of  $t_p$ ).

In order to calculate  $\rho(\bar{m})$ , we can write down the cumulative distribution of  $\bar{m}$ :

$$F_M(\bar{m}) = \text{Prob.}(M \leq \bar{m}) = \int_{\{t_p: M(t_p) < \bar{m}\}} p(t_p) dt_p, \quad (\text{A.7})$$

where  $M$  is the number of photons detected. From the expression  $\bar{m} = \bar{m}_0(1 - \frac{t_p}{t_{DG}})$ , we may rewrite the domain of integration as  $t_p > (1 - \frac{\bar{m}}{\bar{m}_0})t_{DG}$ . Putting this into the

above integral, and plugging in for  $p(t_p)$  from Eq. (A.4), we may evaluate the integral:

$$\begin{aligned} F_M(\bar{m}) &= \int_{(1-\frac{\bar{m}}{\bar{m}_0})t_{DG}}^{\infty} \frac{1}{\tau_p} e^{-\frac{t_p}{\tau_p}} dt_p \\ &= e^{-\frac{t_p}{\tau_p}(1-\frac{\bar{m}}{\bar{m}_0})}. \end{aligned} \quad (\text{A.8})$$

Then, we may calculate the probability distribution for  $\bar{m}$ :

$$\rho(\bar{m}) = \frac{\partial F_M(\bar{m})}{\partial \bar{m}} = \frac{t_p}{\bar{m}_0 \tau_p} e^{-\frac{t_p}{\tau_p}(1-\frac{\bar{m}}{\bar{m}_0})} + e^{-\frac{t_p}{\tau_p}} \delta(\bar{m}). \quad (\text{A.9})$$

The  $\delta$ -function is due to the discontinuity of the integral at  $t_p = 0$ .

Finally, plugging back into Eq. (A.6), we have that the probability of observing  $m$  photons in a given experiment, given that we start out in  $|\uparrow\rangle$ , is:

$$P(m) = e^{-\frac{t_{DG}}{\tau_p}} \delta_{m,0} + \frac{t_{DG} e^{-\frac{t_{DG}}{\tau_p}}}{\tau_p \bar{m}_0 m!} \int_{0+\epsilon}^{\bar{m}_0} e^{(\frac{t_{DG}}{\tau_p \bar{m}_0} - 1)\bar{m}} \bar{m}^m d\bar{m}. \quad (\text{A.10})$$

With some minor tweaking, the integral can be put into the form of an incomplete Gamma function ([72]§6.5), and we finally have:

$$P(m) = e^{-\alpha \bar{m}_0} \left[ \delta_{m,0} + \frac{\alpha}{(1-\alpha)^{m+1}} P(n+1, (1-\alpha)\bar{m}_0) \right], \quad (\text{A.11})$$

where  $\alpha = \frac{t_{DG}}{\tau_p \bar{m}_0}$  and  $P(m+1, (1-\alpha)\bar{m}_0)$  is the incomplete Gamma function. Note that this function is the cumulative distribution for the Chi-square distribution.

The important fact to draw from Eq. (A.11) is that  $P(0)$ , which should ideally be equal to 1, is given by  $P(0) = \exp(-\frac{t_{DG}}{\tau_p} \bar{m}_0) = e^{-\alpha \bar{m}_0}$ , where  $\alpha \approx \frac{4}{19\zeta} (\frac{\gamma}{2\omega_0})^2$ . For  ${}^9\text{Be}^+$ , we have that  $\alpha \approx \frac{1.35 \times 10^{-5}}{\zeta}$ . This is the fundamental limit to the accuracy of discriminating  $|\uparrow\rangle$  from  $|\downarrow\rangle$ . Thus, with  $\zeta \approx 8 \times 10^{-3}$ , we have  $P(0) \approx 0.98$  under typical operating conditions, rather than  $P(0) = 1$ . Fig. A.3 shows photon number histograms for optimum conditions and for the case in which the Blue Doppler intensity is high enough that power broadening exacerbates the leak out of  $|\uparrow\rangle$ .

In terms of the cycling transition,  ${}^9\text{Be}^+$  is actually one of the worst alkali-like ions, due primarily to its small hyperfine splitting. For example,  $\alpha = \frac{3.7 \times 10^{-7}}{\zeta}$  for  $\text{Cd}^+$

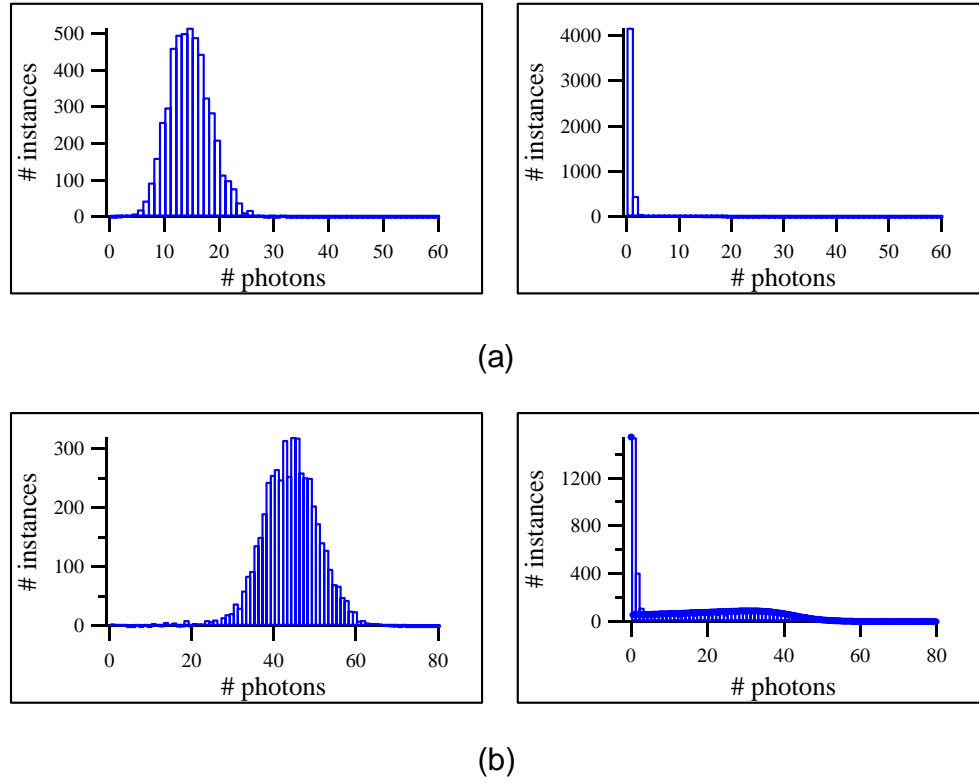


Figure A.3: Photon number histograms versus power broadening. (a) Photon number histograms for optimum Blue Doppler intensity. In particular, note that the number of photons in “ $|\downarrow\rangle$ ” channels for the  $|\uparrow\rangle$  state is only 6% of the total. (b) Photon number histograms when the Blue Doppler intensity is large enough that power broadening pumps population from  $|\uparrow\rangle$  into the cycling transition. 59% of the counts for the state  $|\uparrow\rangle$  are in “ $|\downarrow\rangle$ ” channels. The dots are a fit to Eq. (A.11). The fit gives 3188 as the total number of instances (the actual number is 5000 — this reflects the excess experimental counts in Channels 1 and 2, due to background),  $\alpha = 0.017$ , and  $\bar{m} = 43$  (compare with the average photon number in the  $|\downarrow\rangle$  histogram).

on the  $S_{1/2} \leftrightarrow P_{3/2}$  cycling transition, and  $\alpha = \frac{5.3 \times 10^{-7}}{\zeta}$  for  $^{199}\text{Hg}^+$  on the  $S_{1/2} \leftrightarrow P_{1/2}$  cycling transition. For these ions, the cycling transition thus allows almost perfect discrimination between the bright and dark states, for the photon detection efficiency available in our experiment.

### A.2.2 Fine-Tuning the Resonant Beam Intensities

The histograms can be used to fine-tune the Blue Doppler, Red Doppler and the Repumper intensities, and are also useful in setting the Repumper beam position. To set the Blue Doppler intensity, vary the attenuation (rf and optical) in the Blue Doppler line to get as many counts as possible per experiment without exacerbating the off-resonant pumping of  $|\uparrow\rangle$  into the cycling transition. In practice, with our solid angle, a  $200\ \mu\text{s}$  Detection Gate, and the Blue Doppler beam detuned roughly halfway down the resonance curve (i.e. 10 MHz detuned), this corresponds to  $\bar{m} \approx 10$  for  $|\downarrow\rangle$ . This gives less than 2% discrimination error between  $|\uparrow\rangle$  and  $|\downarrow\rangle$ .

The Red Doppler intensity may be set in much the same way. If the intensity is too low, then optical pumping is not efficient, and state preparation suffers. So, for example, if we drive a co-propagating carrier  $\pi$ -pulse to prepare the state  $|\uparrow\rangle$  then any population which was left in  $|\uparrow\rangle$  after optical pumping gets transferred to  $|\downarrow\rangle$ . Rather than producing a dark state, we produce a mixture of photon counts corresponding to  $|\uparrow\rangle$  and  $|\downarrow\rangle$ . On the other hand, if Red Doppler is too intense, then the efficiency of optical pumping becomes much more sensitive to imperfections in the Red Doppler polarization due to off-resonant pumping *out* of  $|\downarrow\rangle$ .

Finally, the histograms may be used to line up the Repumper beam on the ion. This beam is typically wider than the Blue and Red Doppler beams before the input lens. Thus it is more tightly focussed at the ion, and so is harder to align. Also, this beam is less intense than the Doppler beams. However, once Raman cooling is turned on, the multiple recyclings from  $|\uparrow\rangle$  to  $|\downarrow\rangle$  produce a large probability that the ion will fall into the  $2s\ ^2S_{1/2}F = 2, m_F = -1$  state. If we try to make the state  $|\downarrow\rangle$  with Raman cooling on and the Repumper off then we get a pile-up of counts in the first few bins of the photon number histogram. Fig. A.4(a) illustrates this (compare with Fig. A.4(b), where the Repumper beam is aligned on the ion). Note that, with the

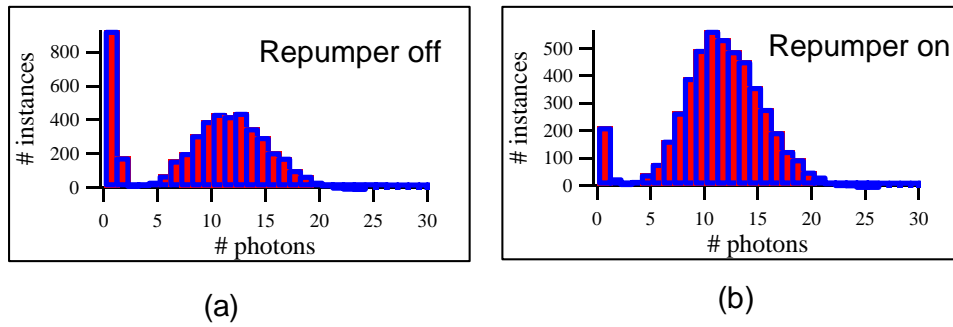


Figure A.4: (a) Photon number histogram with the ion nominally in  $|\downarrow\rangle$ , but Raman cooling on and no Repumper. 23% of the counts fall in bins which correspond to  $|\uparrow\rangle$ . (b) Photon number histogram for the same conditions as in (a), but with the Repumper aligned on the ion. Now, only 5% of the counts fall in channels corresponding to  $|\uparrow\rangle$ .

Repumper blocked, 23% of the counts for a nominal  $|\downarrow\rangle$  state fall into the first three channels.

In order to peak up the Repumper, sit off-resonance with the Probe oscillator (or turn the Probe off), and maximize the count rate (looking at the needle gauge) by playing with the input optics for the Repumper beam line. Once the Repumper is optimized, there shouldn't be more than 4-8% of the counts in the first three bins of the photon number histogram.

## Appendix B

### Matrix Elements

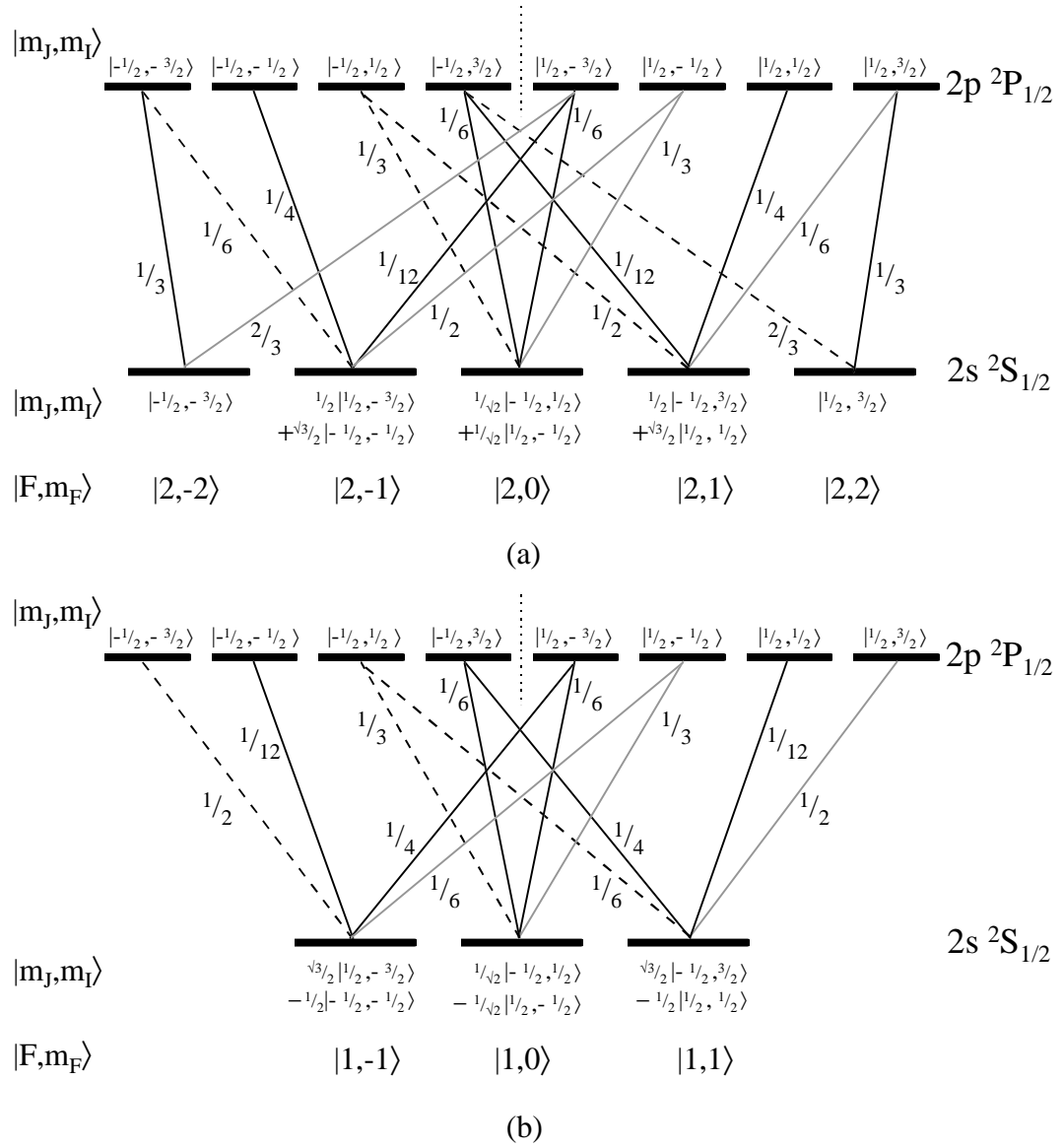


Figure B.1: Relative transition strengths for transitions between  $|\downarrow\rangle$  and the  $2p\ ^2P_{1/2}$  level. The states are labelled in the  $|m_J, m_I\rangle$  basis in the ground and excited states. In addition, for the ground state  $2s\ ^2S_{1/2}$ , the quantum numbers  $F$  and  $m_F$  are indicated. Transitions which are driven by  $\sigma^+$ -polarized light are shown in solid gray, those driven by  $\pi$ -polarized light in solid black, and those driven by  $\sigma^-$ -polarized light in dashed black. (a) Matrix elements between the ground state,  $F = 2$  hyperfine and  $2p\ ^2P_{1/2}$  levels. Note that  $|F = 2, m_F = -2\rangle \equiv |\downarrow\rangle$ . (b) Matrix elements between the ground state,  $F = 1$  hyperfine and  $2p\ ^2P_{1/2}$  levels.  $|F = 2, m_F = -1\rangle \equiv |\uparrow\rangle$ .

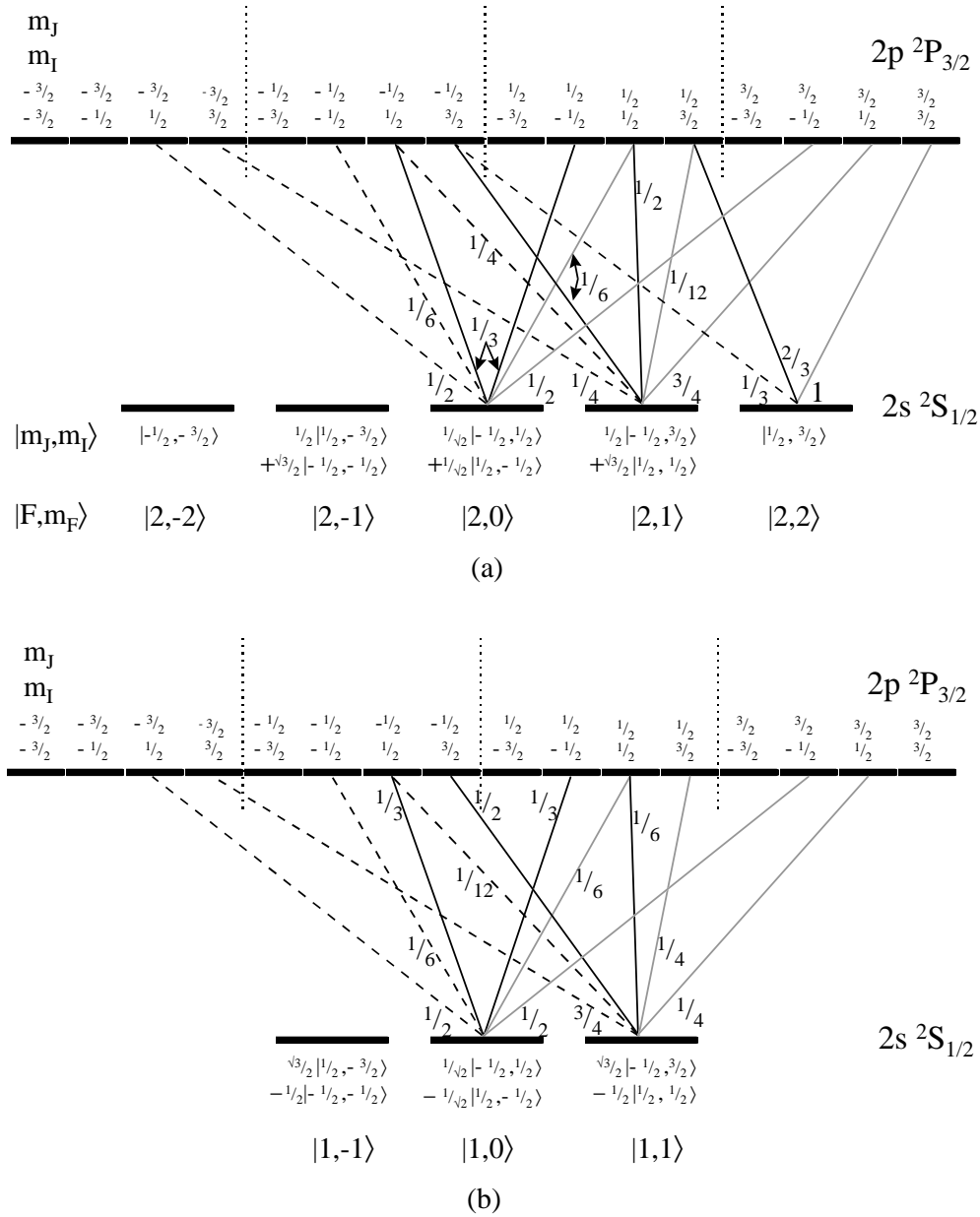


Figure B.2: Relative transition strengths for transitions between  $|\downarrow\rangle$  and the  $2p \ ^2P_{3/2}$  level. The states are labelled in the  $|m_J, m_I\rangle$  basis in the ground and excited states. In addition, for the ground state  $2s \ ^2S_{1/2}$ , the quantum numbers  $F$  and  $m_F$  are indicated. For the sake of clarity, the transition strengths are only indicated for the ground states with  $m_I \geq 0$ . The transition strengths are the same for the states  $|m_J, m_I = -|m_I|\rangle$ . Transitions which are driven by  $\sigma^+$ -polarized light are shown in solid gray, those driven by  $\pi$ -polarized light in solid black, and those driven by  $\sigma^-$ -polarized light in dashed black. (a) Matrix elements between the ground state,  $F = 2$  hyperfine and  $2p \ ^2P_{3/2}$  levels. Note that  $|F = 2, m_F = -2\rangle \equiv \downarrow$ . (b) Matrix elements between the ground state,  $F = 1$  hyperfine and  $2p \ ^2P_{3/2}$  levels.  $|F = 2, m_F = -1\rangle \equiv \uparrow$ .

## Appendix C

### Mathematical Miscellany for SU(1,1) Berry's Phase

#### C.1 Calculation of SU(1,1) Berry's Phase Integral

We wish to calculate the integral

$$-\gamma = \int_{k_1=0}^{\sinh r} \int_{k_2=0}^{\sinh r} \frac{dk_1 dk_2}{\sqrt{1+k_1^2+k_2^2}}, \quad (\text{C.1})$$

which gives the geometric (anholonomic) contribution to the phase produced by a sequence of four squeezings constituting a closed loop on the unit hyperboloid (see Sec. 9.3). The first integral is straightforward, and so we immediately obtain:

$$-\gamma = \int_{k_2=0}^{\sinh r} \operatorname{arcsinh} \left[ \frac{\sinh r}{\sqrt{1+k_2^2}} \right] dk_2. \quad (\text{C.2})$$

With the substitution  $k_2 = \sinh x$ , this becomes

$$-\gamma = \int_0^r \operatorname{arcsinh}[\sinh r \operatorname{sech} x] \cosh x dx. \quad (\text{C.3})$$

Identifying  $dv = \cosh x dx$  and  $u = \operatorname{arcsinh}[\sinh r \operatorname{sech} x]$  and integrating by parts, this becomes:

$$\begin{aligned} -\gamma &= \operatorname{arcsinh}[\tanh r] \sinh r - \int_0^r \frac{\sinh r \sinh^2 x}{\cosh x \sqrt{\sinh^2 r + \cosh^2 x}} dx \\ &= \operatorname{arcsinh}[\tanh r] \sinh r - \mathcal{I}. \end{aligned} \quad (\text{C.4})$$

In order to integrate  $\mathcal{I}$ , let  $y = \cosh x$ . In this case, the integral becomes:

$$\mathcal{I} = \sinh r \int_1^{\cosh r} \frac{1}{y} \sqrt{\frac{1-y^2}{\sinh^2 r + y^2}} dy. \quad (\text{C.5})$$

This integral is somewhat obscure. However, rewriting it as

$$\mathcal{I} = i \sinh r \int_1^{\cosh r} \frac{1}{y} \sqrt{\frac{1-y^2}{y^2 - (i \sinh r)^2}} dy \quad (\text{C.6})$$

puts it in a form found on pg. 362 of Ref. [228]. Thus,

$$\mathcal{I} = -\sinh r \operatorname{arctanh} \left[ \frac{\sinh r}{\sqrt{\cosh^2 r + \sinh^2 r}} \right] - i \operatorname{arctanh} \left[ \frac{i \sinh^2 r}{\sqrt{\cosh^2 r + \sinh^2 r}} \right]. \quad (\text{C.7})$$

Using the identities  $\operatorname{arctan}(ix) = i \operatorname{arctanh}(x)$ ,  $\operatorname{arctanh}(x) = \operatorname{arcsinh}\left(\frac{x}{\sqrt{1-x^2}}\right)$ , and  $i \operatorname{arcsinh}(x) = \operatorname{arcsin}(ix)$ , this may finally be put in the form:

$$\mathcal{I} = -\operatorname{arcsinh}[\tanh r] \sinh r + \operatorname{arcsin}[\tanh^2 r], \quad (\text{C.8})$$

which gives

$$-\gamma = 2 \operatorname{arcsinh}[\tanh r] \sinh r + \operatorname{arcsin}[\tanh^2 r], \quad (\text{C.9})$$

which is Eq. (9.60).

## Appendix D

### Glossary of Symbols

A prime (') generally denotes interaction-picture operators.

$V_0$	rf voltage amplitude
$\Omega_T$	rf drive frequency
$d_0$	characteristic trap dimension
$Q$	ion charge
$m$	ion mass
$z_{tot}$	ion position, including secular motion and micromotion
$z$	secular motion
$z_\mu$	micromotion
$x_{\mu 0, j}$	micromotion amplitude of $j^{th}$ ion in $x$ -direction (2-ion entanglement)
$\omega_m$	secular frequency of mode $m$
$\omega_z$	$z$ secular frequency $\approx \frac{2\sqrt{2}QV_0}{md_0^2\Omega_T}$
$\omega_r$	radial secular frequency (spherical quadrupole trap) $\omega_r = \omega_z/2$
$\bar{D}_z$	pseudopotential well depth ( $z$ -direction) $\approx \frac{QV_0^2}{md_0^2\Omega_T^2}$
$U_0$	static quadrupole voltage on trap electrodes
$q$	Mathieu q-parameter
$a$	Mathieu a-parameter

$\beta$	$\frac{2\omega_m}{\Omega_T} \approx \sqrt{a + \frac{g^2}{2}}$
	<i>also</i> displacement parameter due to noisy electric fields
	<i>also</i> qubit coefficient
$\hat{a}$	harmonic oscillator lowering operator = $\sqrt{\frac{m\omega_z}{2\hbar}}(\hat{z} + \frac{i}{m\omega_z}\hat{p})$
$\hat{a}^\dagger$	harmonic oscillator raising operator = $\sqrt{\frac{m\omega_z}{2\hbar}}(\hat{z} - \frac{i}{m\omega_z}\hat{p})$
$\hat{n}$	harmonic oscillator number operator = $\hat{a}^\dagger\hat{a}$
<i>H.C.</i>	Hermitian conjugate
$z_0$	ground state wave packet spread = $\sqrt{\frac{\hbar}{2m\omega_z}}$
$\mathcal{Q}$	resonator quality factor
$Z_0$	resonator characteristic impedance
$\alpha$	atomic polarizability of neutral background gas atoms
	<i>also</i> coherent state amplitude
	<i>also</i> qubit coefficient
$\mu_{red}$	reduced mass for ion/neutral collisions
$\nu$	relative velocity in ion/neutral collisions
$b$	impact parameter for ion/neutral collisions
$b_{crit}$	critical impact parameter for spiralling ion/neutral collisions
$k_{Langevin}$	Langevin rate constant
$\gamma_{Langevin}$	reaction rate due to background neutral gas particles/spiralling collisions
$\gamma_{el}$	background gas reaction rate based on total elastic cross section
$\rho$	background gas density
$\hat{\rho}, \rho_{n,m}$	density matrix, matrix elements
$\sigma_{el}$	total elastic collision cross section
$\mathbf{e}_x, \mathbf{e}_y, \mathbf{e}_z$	unit vectors in the $x$ -, $y$ -, and $z$ - directions

$e$	electron charge
$ \downarrow\rangle$	${}^9Be^+$ , $2s\ 2S_{1/2}$ , $ F=2, m_F=-2\rangle$ state (sometimes $ F=2, m_F=2\rangle$ )
$ \uparrow\rangle$	${}^9Be^+$ , $2s\ 2S_{1/2}$ , $ F=1, m_F=-1\rangle$ state (sometimes $ F=1, m_F=1\rangle$ )
$ v\rangle$	“virtual level” for Raman transitions: ${}^9Be^+$ , $2s\ 2S_{1/2}$ level
$\gamma$	excited state ( $2p$ ) linewidth $\approx 19.4$ MHz for ${}^9Be^+$ <i>also</i> Berry’s (geometrical) phase
$\delta_{FS}$	${}^9Be^+$ fine-structure splitting $\approx 197$ GHz
$\tau$	excited state lifetime ( $= 1/2\pi\gamma$ )
$\hat{\sigma}_1, \hat{\sigma}_2, \hat{\sigma}_3$	Pauli matrices (one also sees the notation $\hat{\sigma}_x, \hat{\sigma}_y, \hat{\sigma}_z$ )
$\hat{S}_1, \hat{S}_2, \hat{S}_3$	atomic spin operators $= \frac{1}{2}\hbar\hat{\sigma}_j$
$\hat{S}_+, \hat{S}_-$	$\hat{S}_\pm = \frac{1}{2}(\hat{S}_1 \pm \hat{S}_2)$
$\hat{\mu}$	electric dipole moment of the atom $= e\hat{\mathbf{r}}_{el}$
$\mathbf{k}, k$	laser wave vector, magnitude
$\Delta\mathbf{k}$	laser wave vector difference (Raman transitions)
$\omega_L$	laser frequency
$\Delta\omega_L$	laser frequency difference
$\phi$	laser phase <i>also</i> general phase
$\omega_0$	carrier resonance frequency ( ${}^9Be^+$ hyperfine splitting plus Zeeman shift difference)
$\delta$	laser detuning from resonance
$\Delta_R$	Raman laser detunings from virtual level $v$

$\Omega$	carrier Rabi frequency
$\Omega_{n,m}$	sideband Rabi frequency
$\Omega_d$	effective displacement amplitude for applied electric fields
$\hat{g}_i$	single-photon coupling operators (Raman transitions) $= E_i e^{-i\phi_i} \boldsymbol{\epsilon}_i \cdot \hat{\mathbf{x}}/2\hbar$
$g_1$	single-photon coupling strength (Raman transitions) $= \langle \downarrow   \hat{g}_1   v \rangle$
$g_2$	single-photon coupling strength (Raman transitions) $= \langle \uparrow   \hat{g}_2   v \rangle$
$g$	general Rabi frequency (e.g. if $g_1 = g_2 = g$ ) <i>also</i> red sideband coupling strength for engineered $T = 0$ reservoir $= i\eta\hbar\Omega e^{i\phi}$
$\eta$	Lamb-Dicke parameter ( $= kz_0$ , 1D)
$\bar{n}$	average phonon number
$\zeta$	overall detection efficiency <i>also</i> dimensionless time in Mathieu equation
$t_{DG}$	length of Detection Gate
$t_{pr}$	length of probe pulse
$T_R$	length of free evolution time in Ramsey experiment
$I$	laser intensity
$I_S$	saturation intensity ( $\approx 85$ mW/m <sup>2</sup> for ${}^9\text{Be}^+$ )
$\bar{m}$	avg. number of photons detected
$\hat{D}(\alpha)$	displacement operator $= e^{(\alpha\hat{a}^\dagger - \alpha^*\hat{a})}$
$L_n^m$	associated Laguerre polynomial
$P_\downarrow$	probability that the ion is in $ \downarrow\rangle$

$C_n, C_{\downarrow,n}, C_{\uparrow,n}$	motional state probability amplitude
$C_i^{(k)}(t)$	$k^{\text{th}}$ -order perturbative expansion of $C_i(t)$
$P_n$	prob. that the ion is in motional Fock state $ n\rangle$
$r$	ratio of red to blue sideband sizes  <i>also</i> squeeze amplitude in $\hat{K}_1, \hat{K}_2$ formalism
$p_r$	recoil momentum = $\hbar k$
$E_r$	recoil energy = $\frac{p_r^2}{2m}$
$\mathcal{B}$	background counts
$S_E(\omega)$	electric field noise spectral density (V/m <sup>2</sup> )
$\Gamma_0$	rate at which ion is heated out of ground state  of motion
$k_B$	Boltzmann's constant $\approx 1.38 \times 10^{-23}$ J/K
$g(t)$	time-dependent laser coupling strength (“walking standing wave” generation of coherent states)  $= \langle \downarrow   \mathbf{e}_x \cdot \mathbf{r}_{el} \frac{eE}{2\hbar} \cos[\frac{1}{2}(\Delta kz - \delta t + \delta\phi)]   v \rangle$
$\hat{S}(\epsilon)$	squeeze operator = $\exp[\frac{1}{2}(\epsilon^* \hat{a}^2 - \epsilon(\hat{a}^\dagger)^2)]$
$\epsilon$	squeeze parameter $\epsilon = R e^{2i\phi}$  <i>also</i> energy
$\hat{\epsilon}$	laser polarization vector
$\Omega_{\downarrow}$	Rabi frequency for $ \downarrow\rangle$ (including laser polarization/matrix elements)
$\Omega_{\uparrow}$	Rabi frequency for $ \uparrow\rangle$ (including laser polarization/matrix elements)
$W(\alpha) \equiv W(z, ip)$	motional Wigner function
$Q_n(\alpha) \equiv  \mathcal{C}_n(\alpha) ^2$	Fock state probabilities for displaced motional state (density matrix reconstruction) = $\langle n   \hat{D}^\dagger(\alpha) \hat{\rho} \hat{D}(\alpha)   n \rangle$

$ \psi_B^\pm\rangle$	Bell states = $\frac{1}{\sqrt{2}}( \downarrow, \uparrow\rangle \pm  \uparrow, \downarrow\rangle)$
$ \psi_e(\phi)\rangle$	approximate Bell state = $\left(\frac{3}{5} \downarrow, \uparrow\rangle - e^{i\phi\frac{4}{5}} \uparrow, \downarrow\rangle\right) n=0\rangle$
$\Omega_i$	Rabi frequency of ion $i$ (Bell state production)
$\varepsilon$	detuning in “Sørensen and Mølmer” entangled-state production scheme  <i>also</i> small error in Berry’s phase squeeze operators  <i>also</i> error
$\oplus$	Exclusive-OR operator (addition modulo 2)  <i>also</i> Hilbert space direct sum
$ \mathcal{R}\rangle$	state of qubit register
$\mathcal{R}$	parameters upon which Berry’s phase depends  <i>also</i> reservoir
$\hat{\mathcal{H}}, \hat{\mathcal{H}}^{(N)}$	Hadamard transform
$ aux\rangle$	auxilliary level for Controlled-NOT logic gate  $=  2s^2 S_{1/2}, F=2, m_F=0\rangle$
$\hat{s}_i$	system operator (reservoir interactions)
$\hat{\Gamma}_i$	reservoir operator of mode $i$ (reservoir interactions)
$\hat{\chi}$	complete density matrix of system + reservoir
$\hat{R}_0$	initial reservoir density matrix
$\mathcal{M}$	superoperator
$\mathbb{1}$	identity operator
$\hat{b}_k, \hat{b}_k^\dagger$	lowering and raising operators for reservoir  (harmonic oscillator) mode $k$
$\bar{N}$	average reservoir occupation number (for given mode or frequency)
$\kappa$	coupling strength (to reservoir mode)

$\mathcal{V}$	rms voltage noise
$\Gamma$	effective decay rate ( $T = 0$ reservoir engineering)
$\Omega_p$	Rabi frequency of Red Doppler beam ( $T = 0$ reservoir engineering)
$\xi$	dynamical phase
$\hat{U}(t)$	(Ch. 9) unitary operator which changes quantum state to produce Berry's phase
$\hat{G}(t)$	(Ch. 9) operator which generates $\hat{U}(t)$
$\hat{S}(t)$	spin operator for spin- $\frac{1}{2}$ Berry's phase
$\mathbf{f}_i$	$i^{th}$ frame field unit vector
$\omega_{i,j}$	differential "one form" which measures rotation of frame field
$\hat{K}_1$	generator of squeezes along $z$ $= -\frac{i}{4}[\hat{a}^2 - (\hat{a}^\dagger)^2]$
$\hat{K}_2$	generator of squeezes along $z + ip$ $= \frac{1}{4}[\hat{a}^2 + (\hat{a}^\dagger)^2]$
$\hat{J}_3 \equiv \hat{K}_3$	generator of rotations in $(z, ip)$ -plane $= -\frac{1}{2}(\hat{n} + \frac{1}{2})$
$\hat{K}(t)$	state operator for SU(1,1) Berry's phase
$\tilde{\times}$	Minkowski cross product (see Eq. (9.44) )
$\tilde{\cdot}$	Minkowski dot product (see Eq. (9.45) )
$\tilde{\varepsilon}_{ijk}$	$\doteq (-1)^{\delta_{k,3}} \varepsilon_{ijk}$

## Bibliography

- [1] J. R. Gribbin, *In search of Schrödinger's cat: Quantum Physics and Reality* (Bantam Books, Toronto, ON, 1984).
- [2] C. Cohen-Tannoudji, B. Diu, and F. Laloë, *Quantum Mechanics* (John Wiley & Sons, New York, 1977).
- [3] R. S. Van Dyck, Jr., P. B. Schwinberg, and H. G. Dehmelt, *Phys. Rev. Lett.* **59**, 26 (1987).
- [4] A. J. Lichtenberg and M. A. Lieberman, *Regular and Stochastic Motion* (Springer-Verlag, New York, 1983).
- [5] M. C. Gutzwiller, *Chaos in Classical and Quantum Mechanics* (Springer-Verlag, New York, 1990).
- [6] B. G. Klappauf, W. H. Oskay, D. A. Steck, and M. G. Raizen, *Phys. Rev. Lett.* **81**, 4044 (1998).
- [7] P. Jensen, *Phys. Today* **51**, 58 (1998).
- [8] R. P. Feynman, R. B. Leighton, and M. Sands, *The Feynman Lectures on Physics* (Addison-Wesley, Menlo Park, CA, 1964), Vol. 3.
- [9] E. Schrödinger, *Naturwissenschaften* **23**, 807 (1935).
- [10] A. Einstein, B. Podolsky, and N. Rosen, *Phys. Rev.* **47**, 777 (1935).
- [11] N. Bohr, *Phys. Rev.* **48**, 696 (1935).
- [12] D. Lindley, *Where Does the Weirdness Go?* (Basic Books (Harper Collins), New York, 1996).
- [13] H. Everett, *Rev. Mod. Phys.* **29**, 454 (1957).
- [14] J. A. Wheeler, *Rev. Mod. Phys.* **29**, 463 (1957).
- [15] W. H. Zurek, *Phys. Today* **44**, 36 (1991).
- [16] S. Goldstein, *Phys. Today* **51**, 42 (1998).
- [17] R. B. Griffiths and R. Omnès, *Phys. Today* **52**, 26 (1999).

- [18] G. C. Ghirardi, A. Rimini, and T. Weber, *Phys. Rev. D* **34**, 470 (1986).
- [19] S. Goldstein, *Phys. Today* **51**, 38 (1998).
- [20] J. S. Bell, *Speakable and Unspeakable in Quantum Mechanics* (Cambridge University Press, New York, 1993).
- [21] D. J. Wineland and W. M. Itano, *Phys. Today* **40**, 2 (1987).
- [22] S. Chu, *Rev. Mod. Phys.* **70**, 685 (1998).
- [23] C. N. Cohen-Tannoudji, *Rev. Mod. Phys.* **70**, 707 (1998).
- [24] W. D. Phillips, *Rev. Mod. Phys.* **70**, 721 (1998).
- [25] R. Eisberg and R. Resnick, *Quantum Physics of Atoms, Molecules, Solids, Nuclei, and Particles* (John Wiley & Sons, Toronto, ON, 1974).
- [26] D. J. Wineland and W. M. Itano, *Phys. Rev. A* **20**, 1521 (1979).
- [27] E. T. Jaynes and F. W. Cummings, *Proc. IEEE* **51**, 89 (1963).
- [28] C. A. Blockley, D. F. Walls, and H. Risken, *Europhys. Lett.* **17**, 509 (1992).
- [29] J. I. Cirac, R. Blatt, A. S. Parkins, and P. Zoller, *Phys. Rev. Lett.* **70**, 762 (1993).
- [30] W. Vogel and R. L. de Matos Filho, *Phys. Rev. A* **52**, 4214 (1995).
- [31] B. Hayes, *American Scientist* **83**, 304 (1995).
- [32] S. Lloyd, *Scientific American* **273**, 140 (1995).
- [33] D. P. DiVincenzo, *Science* **270**, 255 (1995).
- [34] C. H. Bennett, *Physics Today* **48**, 24 (1995).
- [35] A. Ekert and R. Jozsa, *Rev. Mod. Phys.* **68**, 733 (1996).
- [36] A. Steane, *Appl. Phys. B* **64**, 623 (1997).
- [37] R. Landauer, *IBM J. Res. Dev.* **5**, 183 (1961).
- [38] D. Deutsch, *Proc. R. Soc. Lond. A* **439**, 553 (1992).
- [39] P. W. Shor, in *Proceedings of the 35th Annual Symposium on the Foundations of Computer Science*, IEEE Computer Society (IEEE Computer Society Press, New York, 1994), p. 124.
- [40] J. I. Cirac and P. Zoller, *Phys. Rev. Lett.* **74**, 4091 (1995).
- [41] C. Monroe *et al.*, *Phys. Rev. Lett.* **75**, 4714 (1995).
- [42] W. Zurek, [quant-ph/9805065](http://arxiv.org/abs/quant-ph/9805065) (1998).
- [43] J. Preskill, <http://www.theory.caltech.edu/people/preskill/ph229/#lecture> (1999).

- [44] C. Monroe *et al.*, Phys. Rev. Lett. **75**, 4011 (1995).
- [45] B. E. King *et al.*, Phys. Rev. Lett. **81**, 1525 (1998).
- [46] D. M. Meekhof *et al.*, Phys. Rev. Lett. **76**, 1796 (1996).
- [47] C. Monroe, D. M. Meekhof, B. E. King, and D. J. Wineland, Science **272**, 1131 (1996).
- [48] D. Leibfried *et al.*, Phys. Rev. Lett. (1996).
- [49] Q. A. Turchette *et al.*, Phys. Rev. Lett. **81**, 3631 (1998).
- [50] C. J. Myatt *et al.*, in *Proceedings of the 14 International Conference on Laser Spectroscopy* (World Scientific, New Jersey, 1999).
- [51] H. G. Dehmelt, Phys. Rev. **103**, 1125 (1962).
- [52] W. Paul, O. Osberghaus, and E. Fischer, Forschungsber. Wirtsch. Verkehrsminist. Nordrhein-Westfalen **415**, (1958).
- [53] R. F. Wuerker, H. Shelton, and R. V. Langmuir, J. Appl. Phys. **30**, 342 (1958).
- [54] H. G. Dehmelt, Adv. in At. and Mol. Phys. **5**, 109 (1969).
- [55] in *Proceedings of the Fifth Symposium on Frequency Standards and Metrology*, edited by J. C. Bergquist (World Scientific, New Jersey, 1995).
- [56] W. Nagourney, J. Sandberg, and H. G. Dehmelt, Phys. Rev. Lett. **56**, 2797 (1986).
- [57] T. Sauter, W. Neuhauser, R. Blatt, and P. E. Toschek, Phys. Rev. Lett. **57**, 1696 (1986).
- [58] J. C. Bergquist, R. G. Hulet, W. M. Itano, and D. J. Wineland, Phys. Rev. Lett. **57**, 1699 (1986).
- [59] W. M. Itano, D. J. Heinzen, J. J. Bollinger, and D. J. Wineland, Phys. Rev. A **41**, 2295 (1990).
- [60] D. J. Wineland, R. E. Drullinger, and F. L. Walls, Phys. Rev. Lett. **40**, 1639 (1978).
- [61] W. Neuhauser, M. Hohenstatt, P. Toschek, and H. Dehmelt, Phys. Rev. Lett. **41**, 233 (1978).
- [62] D. J. Berkeland *et al.*, in *Methods for Ultrasensitive Detection*, edited by B. L. Fearey (SPIE, Bellingham, WA, 1998), p. 138.
- [63] G. Wuerth, in *Progress in Atomic Spectroscopy*, edited by H. J. Beyer and H. Kleinpoppen (Plenum Press, New York, 1984), Vol. C.
- [64] P. K. Ghosh, *Ion Traps* (Clarendon Press, Oxford, 1995).
- [65] P. Lorrain, D. R. Corson, and F. Lorrain, *Electromagnetic Fields and Waves*, 3 ed. (W. H. Freeman and Company, New York, 1988).

- [66] W. Paul, *Angew. Chem. Int. Ed. Engl.* **29**, 739 (1990).
- [67] P. L. Kapitsa, *Zh. Eksp. Teor. Fiz.* **34**, 242 (1951).
- [68] H. G. Dehmelt, *Adv. in At. and Mol. Phys.* **3**, 53 (1967).
- [69] J. Mathews and R. L. Walker, *Mathematical Methods of Physics*, 2 ed. (Benjamin/Cummings, Menlo Park, CA, 1970).
- [70] J. I. Cirac *et al.*, *Phys. Rev. A* **49**, 421 (1994).
- [71] P. J. Bardroff, C. Leichtle, G. Schrade, and W. P. Schleich, *Phys. Rev. Lett.* **77**, 2198 (1996).
- [72] M. Abramowitz and I. A. Stegun, *Handbook of Mathematical Functions* (U.S. Gov't. Printing Office, Washington, D.C., 1964).
- [73] D. J. Wineland *et al.*, *J. Res. of the NIST* **103**, 259 (1998).
- [74] H. Walther, in *Advances in Atomic, Molecular and Optical Physics* (Academic Press, Inc., New York, 1993), Vol. 31, pp. 137–182.
- [75] J. A. Hoffnagle and R. G. Brewer, *Physica Scripta* **159**, 380 (1995).
- [76] R. Alheit *et al.*, *Appl. Phys. B* **61**, 277 (1995).
- [77] R. J. Cook, D. G. Shankland, and A. L. Wells, *Phys. Rev. A* **31**, (1985).
- [78] M. Combescure, *Ann. Inst. Henri Poincaré* **44**, 293 (1986).
- [79] R. J. Glauber, in *Proceedings of the International School of Physics “Enrico Fermi”*, edited by E. Arimondo, W. D. Phillips, and F. Strumia (North-Holland, New York, 1992), Vol. CXVIII, pp. 643–660.
- [80] A. B. Murphy, *J. Appl. Phys.* **70**, 2880 (1991).
- [81] S. R. Jefferts, C. Monroe, E. Bell, and D. J. Wineland, *Phys. Rev. A* **51**, 3112 (1995).
- [82] C. J. Myatt *et al.*, in *Methods for Ultrasensitive Detection*, edited by B. L. Fearey (SPIE, Bellingham, WA, 1998), pp. 131–137.
- [83] R. G. DeVoe, *Phys. Rev. A* **58**, 910 (1998).
- [84] R. H. Dicke, *Phys. Rev.* **89**, 472 (1953).
- [85] J. D. Prestage, G. J. Dick, and L. Maleki, *J. Appl. Phys.* **66**, 1013 (1989).
- [86] M. G. Raizen *et al.*, *J. Mod. Opt.* **39**, 233 (1992).
- [87] R. W. Hasse and J. P. Schiffer, *Ann. Phys. N.Y.* **203**, 419 (1990).
- [88] H. G. Dehmelt, in *Proceedings of the Fourth Symposium on Frequency Standards and Metrology*, edited by A. De Marci (Springer-Verlag, Berlin, 1996).

- [89] J. D. Jackson, *Classical Electrodynamics*, 2 ed. (John Wiley & Sons, New York, 1975).
- [90] J. B. Hasted, *Physics of Atomic Collisions*, 2 ed. (Elsevier, New York, 1972).
- [91] L. D. Landau and E. M. Lifshitz, *Quantum Mechanics (Non-relativistic Theory)*, 3 ed. (Pergamon, New York, 1977).
- [92] *Cavity Quantum Electrodynamics*, edited by P. R. Berman (Academic Press, Inc., New York, 1994).
- [93] C. Cohen-Tannoudji, J. Dupont-Roc, and G. Grynberg, *Atom-Photon Interactions* (John Wiley & Sons, New York, 1992).
- [94] R. J. Glauber, in *Quantum Optics and Electronics, Les Houches Lectures 1964*, edited by C. deWitt, A. Blandin, and C. Cohen-Tannoudji (Gordon and Breach, New York, 1965).
- [95] N. F. Ramsey, *Molecular Beams* (Oxford University Press, London, 1963).
- [96] W. H. Press, B. P. Flannery, S. A. Teukolsky, and W. T. Vetterling, *Numerical Recipes* (Cambridge University Press, New York, 1986).
- [97] J. L. Hall and S. A. Lee, *Appl. Phys. Lett.* **29**, 367 (1976).
- [98] P. J. Fox, R. E. Scholten, M. R. Walkiewicz, and R. E. Drullinger, *Am. J. Phys.* **67**, 624 (1999).
- [99] W. Demtröder, *Laser Spectroscopy* (Springer-Verlag, New York, 1981).
- [100] P. Horowitz and W. Hill, *The Art of Electronics* (Cambridge University Press, Cambridge, MA, 1983).
- [101] S. Gerstenkorn and P. Luc, *Atlas du Spectre D'Absorption de la Molecule D'Iode* (Laboratoire Aime-Cotton, CNRS II, Orsay, France, 1978).
- [102] T. W. Hänsch and B. Couillaud, *Opt. Comm.* **35**, 441 (1980).
- [103] A. Yariv, *Quantum Electronics*, 2 ed. (John Wiley & Sons, New York, 1975).
- [104] A. V. Smith, *SNLO nonlinear optics code* (available from A.V. Smith, Sandia National Laboratories, Albuquerque, NM 87185-1423, 1999).
- [105] D. F. Walls and G. J. Milburn, *Quantum Optics* (Springer-Verlag, New York, 1994).
- [106] D. J. Wineland and H. Dehmelt, *Bull. Am. Phys. Soc.* **20**, 637 (1975).
- [107] T. W. Hänsch and A. L. Schawlow, *Opt. Comm.* **13**, 68 (1975).
- [108] F. Diedrich, J. C. Bergquist, W. M. Itano, and D. J. Wineland, *Phys. Rev. Lett.* **62**, 403 (1989).

- [109] H. Goldstein, *Classical Mechanics*, 2 ed. (Addison-Wesley, Reading, Massachusetts, 1980).
- [110] D. J. Wineland, J. J. Bollinger, W. M. Itano, and D. J. Heinzen, *Phys. Rev. A* **50**, 67 (1994).
- [111] D. J. Wineland *et al.*, *Fortschritte der Physik* **46**, 363 (1998).
- [112] T. A. Savard, K. M. O'Hara, and J. E. Thomas, *Phys. Rev. A* **56**, R1095 (1997).
- [113] M. E. Gehm, K. M. O'Hara, T. A. Savard, and J. E. Thomas, *Phys. Rev. A* **58**, 3914 (1998).
- [114] H. G. Dehmelt, *Advances in Atomic and Molecular Physics* **3**, 53 (1967).
- [115] D. J. Wineland and H. G. Dehmelt, *J. of Appl. Phys.* **46**, 919 (1975).
- [116] A. J. Dahm and D. N. Langenberg, *Am. J. Phys.* **43**, 1004 (1975).
- [117] F. Reif, *Fundamentals of Statistical and Thermal Physics* (McGraw-Hill, Toronto, 1965).
- [118] J. B. Camp, T. W. Darling, and R. E. Brown, *J. Appl. Phys.* **69**, 7126 (1991).
- [119] C. Kleint, *Annalen der Physik* **10**, 309 (1963).
- [120] G. W. Timm and A. Van der Ziel, *Physica* **32**, 1333 (1966).
- [121] C. K. Law and J. H. Eberly, *Phys. Rev. Lett.* **76**, 1055 (1996).
- [122] T. vonFoerster, *J. Phys. A* **8**, 95 (1975).
- [123] J. H. Eberly, N. B. Narozhny, and J. J. Sanchez-Mondragon, *Phys. Rev. Lett.* **44**, 1323 (1980).
- [124] P. Meystre and M. Sargent, III, *Elements of Quantum Optics*, 2 ed. (Springer-Verlag, New York, 1991).
- [125] D. J. Heinzen and D. J. Wineland, *Phys. Rev. A* **42**, 2977 (1990).
- [126] J. F. Poyatos, J. I. Cirac, and P. Zoller, *Phys. Rev. Lett.* **77**, 4728 (1996).
- [127] O. Carnal and J. Mlynek, *Phys. Rev. A* **66**, 2689 (1991).
- [128] D. W. Keith, C. R. Ekstrom, Q. A. Turchette, and D. E. Pritchard, *Phys. Rev. A* **66**, 2693 (1991).
- [129] M. Kasevich and S. Chu, *Phys. Rev. A* **67**, 181 (1991).
- [130] J. L. et al, *Phys. Rev. A* **75**, 4194 (1995).
- [131] L. Marton, J. Arol Simson, and J. A. Suddeth, *Phys. Rev.* **90**, 490 (1954).
- [132] H. Maier-Leibnitz and T. Springer, *Z. Physik* **167**, 368 (1962).

- [133] L. D. Noordam, D. I. Duncan, and T. F. Gallagher, *Phys. Rev. A* **45**, 4734 (1992).
- [134] R. R. Jones, C. S. Raman, D. W. Schumacher, and P. H. Bucksbaum, *Phys. Rev. A* **71**, 2575 (1993).
- [135] M. W. Noel and C. R. Stroud, Jr., *Phys. Rev. A* **75**, 1252 (1995).
- [136] D. L. Leibfried, T. Pfau, and C. Monroe, *Phys. Today* **51**, 22 (1998).
- [137] E. P. Wigner, *Phys. Rev.* **40**, 749 (1932).
- [138] S. Stenholm, *Annals of Physics (New York)* **218**, 233 (1992).
- [139] A. Royer, *Phys. Rev. Lett.* **52**, 1064 (1984).
- [140] H. Moya-Cessa and P. L. Knight, *Phys. Rev. A* **48**, 2479 (1993).
- [141] S. Wallentowitz and W. Vogel, *Phys. Rev. A* **53**, 4528 (1996).
- [142] K. Banaszek and K. Wodkiewicz, *Phys. Rev. Lett.* **76**, 4344 (1996).
- [143] M. Freyberger, *Phys. Rev. A* **55**, 4120 (1997).
- [144] J. S. Bell, *Physics* **1**, 195 (1964).
- [145] D. M. Greenberger, M. A. Horne, A. Shimony, and A. Zeilinger, *Am. J. Phys.* **58**, 1131 (1990).
- [146] A. Aspect, P. Grangier, and G. Roger, *Phys. Rev. Lett.* **49**, 91 (1982).
- [147] W. M. Itano *et al.*, *Phys. Rev. A* **47**, 3554 (1993).
- [148] J. J. Bollinger, W. M. Itano, D. J. Wineland, and D. J. Heinzen, *Phys. Rev. A* **54**, R4649 (1996).
- [149] C. K. Law and H. J. Kimble, *J. Mod. Opt.* **44**, 2067 (1997).
- [150] K. Mølmer and A. Sørensen, *Phys. Rev. Lett.* **82**, 1835 (1999).
- [151] B. C. Sanders, *Phys. Rev. A* **40**, 2417 (1989).
- [152] C. H. Papadimitriou, *Computational Complexity* (Addison-Wesley, Reading, MA, 1995).
- [153] N. Abramson, *Information Theory and Coding* (McGraw Hill, New York, 1963).
- [154] C. H. Bennett, *IBM J. Res. Dev.* **17**, 525 (1973).
- [155] C. H. Bennett, *Int. J. Theor. Phys.* **21**, (1982).
- [156] D. Deutsch, *Proc. R. Soc. Lond. A* **400**, 97 (1985).
- [157] R. P. Feynman, *Int. J. Theor. Phys.* **21**, 467 (1981).
- [158] R. P. Feynman, *Optics News* **11**, 11 (1985).

- [159] R. L. Rivest, A. Shamir, and L. M. Adleman, *Comm. ACM* **21**, 120 (1978).
- [160] A. Steane, *Reports on Progress of Physics* **61**, 117 (1998).
- [161] L. K. Grover, *Phys. Rev. Lett.* **79**, 4709 (1997).
- [162] E. Knill and R. Laflamme, *Phys. Rev. Lett.* **81**, 5672 (1998).
- [163] D. Simon, in *Proceedings of the 35th Annual Symposium on Foundations of Computer Science* (IEEE Press, Los Alamitos, CA, 1994), pp. 124–134.
- [164] L. K. Grover, *Phys. Rev. Lett.* **79**, 325 (1997).
- [165] D. Deutsch, A. Barenco, and A. Ekert, *Proc. R. Soc. Lond. A* **449**, 669 (1995).
- [166] D. P. DiVincenzo, *Phys. Rev. A* **51**, 1015 (1995).
- [167] W. G. Unruh, *Phys. Rev. A* **51**, 992 (1995).
- [168] R. Landauer, *Proc. R. Soc. Lond. A* **353**, 367 (1995).
- [169] S. Haroche and J. M. Raymond, *Phys. Today* **49**, 51 (1996).
- [170] P. Shor, *Phys. Rev. A* **52**, 2493 (1996).
- [171] A. M. Steane, *Phys. Rev. Lett.* **77**, 793 (1996).
- [172] D. Dieks, *Phys. Lett. A* **92**, 271 (1982).
- [173] W. K. Wootters and W. H. Zurek, *Nature* **299**, 802 (1982).
- [174] J. Preskill, *Phys. Today* **52**, 24 (1999).
- [175] A. Y. Kitaev, *Russian Mathematical Surveys* **52**, 1191 (1997).
- [176] D. Aharonov and M. Ben-Or, in *Proceedings of the 29th Annual ACM Symposium on the Theory of Computing* (ACM, New York, 1997), p. 176.
- [177] J. Preskill, *Proc. R. Soc. Lond. A* **454**, 385 (1998).
- [178] E. Knill, R. Laflamme, and W. Zurek, *Proc. R. Soc. Lond. A* **454**, 365 (1998).
- [179] E. Dennis, *quant-ph/9905027* (1998).
- [180] J. J. Bollinger *et al.*, *IEEE Transactions on Instrumentation and Measurement* **40**, 126 (1991).
- [181] R. J. Hughes *et al.*, *Fortschritte der Physik* **46**, 329 (1998).
- [182] C. Monroe *et al.*, *Phys. Rev. A* **55**, R2489 (1997).
- [183] J. Steinbach and C. C. Gerry, *Phys. Rev. Lett.* **81**, 5528 (1998).
- [184] K. Mølmer and A. Sørensen, *Phys. Rev. Lett.* **82**, 1971 (1999).

- [185] H. Carmichael, *An Open Systems Approach to Quantum Optics* (Springer-Verlag, New York, 1993).
- [186] W. H. Louisell, *Quantum Statistical Properties of Radiation* (John Wiley & Sons, New York, 1973).
- [187] A. Peres, *Quantum Theory: Concepts and Methods* (Kluwer Academic, Boston, 1993).
- [188] J. P. Paz and W. H. Zurek, *Phys. Rev. Lett.* **82**, 5181 (1999).
- [189] W. H. Zurek, *Phys. Rev. D* **26**, 1862 (1982).
- [190] D. F. Walls and G. J. Milburn, *Phys. Rev. A* **31**, 2403 (1985).
- [191] M. J. Collett, *Phys. Rev. A* **38**, 2233 (1988).
- [192] S. J. D. Phoenix, *Phys. Rev. A* **41**, 5132 (1990).
- [193] C. W. Gardiner, *Quantum Noise* (Springer-Verlag, New York, 1991).
- [194] M. O. Scully, B. G. Englert, and H. Walther, *Nature* **351**, 111 (1991).
- [195] Z. Y. Ou, L. J. Wang, X. Y. Zou, and L. Mandel, *Phys. Rev. A* **41**, 1597 (1990).
- [196] P. G. Kwiat, A. M. Steinberg, and Y. Chiao, *Phys. Rev. A* **45**, 7729 (1992).
- [197] J. F. Poyatos, J. I. Cirac, and P. Zoller, *Phys. Rev. Lett.* **77**, 4728 (1996).
- [198] M. Brune *et al.*, *Phys. Rev. Lett.* **77**, 4887 (1996).
- [199] I. Marzoli, J. I. Cirac, R. Blatt, and P. Zoller, *Phys. Rev. A* **49**, 2771 (1994).
- [200] S. R. Wilkinson *et al.*, *Nature* **387**, 575 (1997).
- [201] M. V. Berry, *Proc. R. Soc. Lond. A* **392**, 45 (1984).
- [202] B. Simon, *Phys. Rev. Lett.* **51**, 2167 (1983).
- [203] A. Tomita and R. Y. Chiao, *Phys. Rev. Lett.* **57**, 937 (1986).
- [204] S. Chaturvedi, M. S. Sriram, and V. Srinivasan, *J. Phys. A* **20**, L1071 (1987).
- [205] F. Hong-Yi and H. R. Zaidi, *Can. J. Phys.* **66**, 978 (1988).
- [206] R. Y. Chiao and T. F. Jordan, *Phys. Lett. A* **132**, 77 (1988).
- [207] C. C. Gerry, *Phys. Rev. A* **39**, 3204 (1989).
- [208] A. Messiah, *Quantum Mechanics* (North-Holland, Amsterdam, 1958), Vol. 1.
- [209] Y. Aharonov and D. Bohm, *Phys. Rev.* **115**, 485 (1959).
- [210] Y. Aharonov and J. Anandan, *Phys. Rev. Lett.* **58**, 1593 (1985).
- [211] J. Anandan and L. Stodolsky, *Phys. Rev. D* **35**, 2597 (1987).

- [212] J. Anandan, Phys. Lett. A **129**, 201 (1988).
- [213] T. F. Jordan, J. Math. Phys. **29**, 2042 (1988).
- [214] S. Ramaseshan and R. Nityananda, Curr. Sci. **55**, 1225 (1986).
- [215] S. Pancharatnam, Proc. Ind. Acad. Sci. **A44**, 247 (1956).
- [216] J. H. Hannay, J. Phys. A **18**, 221 (1985).
- [217] M. V. Berry, J. Phys. A **18**, 15 (1985).
- [218] B. O'Neill, *Elementary Differential Geometry* (Academic Press, Toronto, 1966).
- [219] J. J. Sakurai, *Modern Quantum Mechanics* (Benjamin/Cummings, Reading, MA, 1985), S. F. Tuan, *ed.*
- [220] K. Hoffman and R. Kunze, *Linear Algebra*, 2 ed. (Prentice-Hall, Englewood Cliffs, NJ, 1971).
- [221] J. F. Cornwell, *Group Theory in Physics: an Introduction* (Academic Press, Toronto, ON, 1997).
- [222] B. Rosenfeld, *Geometry of Lie Groups* (Kluwer Academic, Dordrecht, The Netherlands, 1997).
- [223] M. Kitano and T. Yabuzaki, Phys. Lett. A **142**, 321 (1989).
- [224] H. Svensmark and P. Dimon, Phys. Rev. Lett. **73**, 3387 (1994).
- [225] G. Milburn, private communication.
- [226] D. Han, E. E. Hardekopf, and Y. S. Kim, Phys. Rev. A **39**, 1269 (1989).
- [227] P. K. Aravind, Phys. Rev. A **42**, 4077 (1990).
- [228] *Handbook of Mathematical, Scientific and Engineering Formulas, Tables, Functions, Graphs, Transforms* (Research and Education Association, New York, 1984).